Sheffield Hallam University | Materials and Engineering Research Institute

Radiation Damage Effects on the Structure and Properties of Radioactive Waste Glasses

Prince Rautiyal

B.Sc.(H), M.Tech.

A Thesis Submitted to

Materials & Engineering Research Institute (MERI)

Sheffield Hallam University

in partial fulfilment of its requirements for

The Degree of Doctor of Philosophy

College of Business, Technology and Engineering

Materials & Engineering Research Institute

Sheffield Hallam University

March 2021

Candidate’s Declaration:

I hereby declare that:

1. I have not been enrolled for another award of the University, or other academic or professional organisation, whilst undertaking my research degree.

2. None of the material contained in the thesis has been used in any other submission for an academic award.

3. I am aware of and understand the University's policy on plagiarism and certify that this thesis is my own work. The use of all published or other sources of material consulted have been properly and fully acknowledged.

4. The work undertaken towards the thesis has been conducted in accordance with the SHU Principles of Integrity in Research and the SHU Research Ethics Policy.

5. The word count of the thesis is 35,451.

Name	*Prince Rautiyal*
Date	*March, 2021*
Award	*PhD*
Faculty	*College of Business, Technology and Engineering*
Director(s) of Studies	*Professor Paul A. Bingham*

Content

Acknowledgements

Firstly, I would like to thank my supervisor Prof Paul Bingham, for his guidance, support, and encouragement. This work would not have been possible without your valuable support. Thanks for giving me this opportunity to come to Sheffield and pursue a PhD.

I would like to thank my second supervisor Dr Hywel Jones. I would like to give a big thank to Dr Shuchi Vaishnav who introduced me to Paul before starting this PhD and who helped me throughout this journey in numerous ways. I would also like to massively thank Dr Tony Bell, Deeba Zahoor, Amy McNally, Clare Mills Roberts, Rachael Toogood, Gail Hallewell, Jane Wright, Dr Francis Clegg, Dr Alex Scrimshire, Dr Daniel Backhouse, Dr Wei Deng, Dr Erhan Kilinc, Gloria Wie-Addo, Jessica Rigby, Katrina Love, Daniel James, Alex Stone, Masoud Bigharaz, Dr Gaurav Gupta.

I would also like to thank my research collaborators: Dr Laura Leay, Dr Ruth Edge, Dr Maulik Patel, and Aaron Daubney. You guys have been very helpful.

I would like to thank my loving parents for providing me numerous opportunities to study, for their endless sacrifices, and for their love and support. Without them and their encouragement this thesis would not have been possible. I would like to thank my friends and relatives back in India. I am truly blessed to have many wonderful people in my life who are like my extended family. And finally, I would like to thank the Government of India, the Ministry of Social Justice and Empowerment for funding my PhD. I would also like to thank the High Commission of India, London, for all the help and support you have provided over the course of my PhD.

Abstract

The performance assessment of glass matrices currently being used in different nuclear energy producing countries to contain and immobilise high-level waste (HLW) waste is crucial for safe and economic disposal. During the first ~500 years of geological disposal fission products will me the main source or radiation and they decay by beta-gamma emission. We studied different borosilicate glasses used in different countries to immobilise HLW, such as Indian glass (NaBaBSi), UK glasses (LiNaBSi), also called MW- Mixture Windscale, UK-CaZn a modified version of MW, French glass (SON68) and a glass proposed by six collaborating nations, called the International Simple Glass (ISG), to see whether / how irradiation defects are dependent on glass composition. Glasses were externally irradiated using a ^{60}Co gamma source to study the effects of beta-gamma radiation (a gamma emitter loses it energy to atomic electrons they then further interact via coulombic interactions); and by He^{2+} ion implantation to study the effects of alpha particles. A multi-spectroscopic approach was used to characterise glass specimens before and after irradiation. NaBaBSi and LiNaBSi glasses were irradiated using ^{60}Co gamma photons and we found boron-oxygen hole centres (BOHC), electrons trapped at alkali cations or ET centres and peroxy-radicals (PORs) as common defect in these glasses. In addition, E^- or polaron centres which may be related to formation of elemental / metallic sodium colloids formed in NaBaBSi glass. Time-dependent thermal annealing of the irradiated glasses revealed that POR's are the most thermally stable of the defect centres. BOHC and ET centres were common to SON68, ISG and CaZn glasses. In NaBaBSi, LiNaBSi and SON68 glasses loaded with non-active simulated HLW no sharp and intense signals indicative of radiation-induced paramagnetic defect centres was observed. In the study of NaBaBSi and LiNaBSi glasses doped with 0.19. 0.99, and 4.76 mol% Fe_2O_3 prepared in an oxidising melting environment, electron paramagnetic resonance (EPR) spectroscopy showed that gamma irradiation induced sharp and intense signals exist for only the 0 and 0.19 mol% Fe_2O_3 doped samples and disappeared for samples containing higher molar concentrations of Fe_2O_3. It is postulated that, upon gamma irradiation, in LiNaBSi glass Fe^{2+} is oxidised to Fe^{3+} by the capture of holes, whereas in NaBaBSi glass Fe^{3+} is reduced to Fe^{2+} due to capture of electrons. Further research is needed to understand the reasons behind these different behaviours.

Published Work and Conferences

Contribution to Conferences – Proceedings

P. Rautiyal*, R. Edge, L. Leay, A. Daubney, M. Patel, P.K. Kulriya, A.H. Jones, P.A. Bingham, *Effects of He Ion Irradiation in Simple Borosilicate Glasses for HLW Immobilisation – 20324*, in: Waste Management Symposium, 2020: pp. 1–10.

Contribution to Conferences – Posters

P. Rautiyal*, A. Daubney, R. Edge, L. Leay, A.H. Jones, P.A. Bingham, *Effects of gamma irradiation on high and intermediate-level radioactive waste glasses*, 5th Nuclear Materials Conference, 2019, Seattle, USA, 2019.

P. Rautiyal*, A.H. Jones, P.A. Bingham *Towards improvement of radiation stability in high-level nuclear waste (HLW) glasses*, Sheffield Hallam University, UK, 2018.

Contribution to Conferences – Talks

P. Rautiyal*, R. Edge, L. Leay, A. Daubney, M. Patel, P.K. Kulriya, A.H. Jones, P.A. Bingham, *Effects of He Ion Irradiation in Simple Borosilicate Glasses for HLW Immobilisation – 20324*, in: Waste Management Symposium, 2020: pp. 1–10.

P. Rautiyal*, P.K. Kulriya, R. Edge, L. Leay, A.H. Jones, P.A. Bingham, *Effects of gamma and alpha irradiation on iron-free and iron-containing high-level nuclear waste base glasses*, XXV International Congress on Glass, Boston, USA, 2019.

P. Rautiyal*, A. Daubney, R. Edge, L. Leay, A.H. Jones, P.A. Bingham, *Electron paramagnetic resonance (EPR) spectroscopic study of nuclear waste glasses*, Society of Glass Technology Annual Meeting, Cambridge, UK, 2019.

P. Rautiyal*, A. Daubney, R. Edge, L. Leay, A.H. Jones, P.A. Bingham, *Electron paramagnetic resonance (EPR) spectroscopic study of nuclear waste glasses*, Joint ICTP-IAEA International School on Nuclear Waste Vitrification, Trieste, Italy, 2019

P. Rautiyal*, A.H. Jones, P.A. Bingham, *A study of irradiation effects in high-level radioactive waste glasses,* Society of Glass Technology Annual Meeting, Cambridge, UK, 2018.

P.A. Bingham*, P. Rautiyal, and B. Allsopp, *Redox in glasses: interactions with radiation*, PNCS-ESG, Saint-Malo, France, 2018.

P. Rautiyal*, A.H. Jones, P.A. Bingham, *Irradiation effects in Indian and UK high-level radioactive waste glasses*, Society of Glass Technology Annual Meeting, Cambridge,UK, 2017.

Published Work – Co-authored

A.M.T. Bell*, D.J. Backhouse, W. Deng, J.D. Eales, E. Kilinc, K. Love, P. Rautiyal, J.C. Rigby, A.H. Stone, S. Vaishnav, G. Wie-Addo, P.A. Bingham, *X-ray fluorescence analysis of feldspars and silicate glass: Effects of melting time on fused*

bead consistency and volatilisation, Minerals. 10 (2020). https://doi.org/10.3390/min10050442.

T.Y. Chen*, P. Rautiyal, S. Vaishnav, G. Gupta, H. Schlegl, R.J. Dawson, A.W. Evans, S. Kamali, J.A. Johnson, C.E. Johnson, P.A. Bingham, 2020*, Composition structure-property effects of antimony in soda-lime-silica glasses*, J. Non. Cryst. Solids. 544 (2020) 120184. https://doi.org/10.1016/j.jnoncrysol.2020.120184

Published Work – First author

P. Rautiyal, G. Gupta, R. Edge, L. Leay, A. Daubney, M.K. Patel, A.H. Jones, P.A. Bingham, *Gamma irradiation-induced defects in borosilicate glasses for high-level radioactive waste immobilisation*, J. Nucl. Mater. (2020) 152702. https://doi.org/10.1016/j.jnucmat.2020.152702.

List of Tables

List of Figures

Chapter 2

Chapter 3

Chapter 4

Chapter 5

Chapter 6

Appendix C

Appendix D

Appendix E

Chapter 1. Introduction

1.1 Overview

Today about 10% of the world's total electricity comes from nuclear power plants operating in 30 countries [1]. Nuclear energy is the second-largest source of low-carbon power and contributes about one-third of all low carbon power [2]. There are more countries embarking (considering, planning or starting) on nuclear power programmes in the future [2]. With the growing energy demands and increasing greenhouse gas emissions, nuclear power is considered as one of the main candidates to meet the energy demands with very low or negligible carbon footprints [3]. A huge inventory (about 104,150 m^3 as estimated on 1 April 2019 withing UK's government records) of high-heat generating waste [4,5] (HHGW), waste with high heat output and potentially significant fissile nuclide content, such as high-level waste (HLW), spent nuclear fuel (SNF), and low heat generating waste (LHGW), waste with limited but potentially significant heat output and fissile nuclide content such as intermediate level waste (ILW) and low-level waste (LLW) is produced during the operations, maintenance and decommissioning of nuclear power plants (waste classification based on radioactivity content is discussed in Section 2.1.2). This inventory of waste requires safe, effective and economic management for the sustainable utilisation of nuclear energy [3,6,7].

HHGW is categorised further into high-level liquid waste (HLLW) (referred to as highly active liquor (HAL) in the UK) arising from reprocessing of spent fuel and spent fuel itself from nuclear power reactors. Initial cooling (3-5 years) [8] precedes reprocessing, HLLW is treated, to reduce its volume and made into a more stable form which can be concentrated and immobilised in a solid matrix. This is achieved in many countries (USA, UK, France, India, Germany, Belgium, Sweden, Switzerland, Japan) [9,10] by vitrifying HLW in a borosilicate glass matrix (waste form) which is poured into stainless steel canisters (waste container). The waste forms and the waste containers will further be contained overpack container. This waste package which will be transported and disposed in geological repositories for permanent disposal [4].

About 97% of the waste arising from various processes and activities during an entire nuclear fuel cycle is made up of resins, filters, valves, fabrics/clothes, scraps,

metals etc., and has low or intermediate level radioactivity [7,11,12]. The remaining ~3% of the waste is HLW which contains about 98% of the total radioactivity present in all nuclear fuel cycle wastes [7,11,12]. HLW is composed of fission products and minor actinides (discussed in detail in Chapter 2). The half-life of the many radionuclides present in HLW can range from a few years to several tens of thousands of years and therefore, to avoid any dispersal of radioactivity to the biosphere, HLW is immobilised in a physically and chemically stable waste form. The global method of choice for HLW immobilisation is vitrification in a borosilicate glass matrix followed by planned geological disposal in a repository over geological time scales. The borosilicate glass matrix, which is the first barrier to the dispersal of radioactivity to the biosphere will be subjected to self-irradiation damage and resulting radiogenic heat, in addition to contact with its surrounding environment (canister, overpack materials and, potentially, groundwater) [7,9,13,14].

Over time, metallic canisters in a geological disposal repository are expected to corrode due to water-canister interaction and other extreme environments presented to them (temperature, loads, pH etc.) within the repository, which will then expose the vitrified HLW to water [15]. It is believed that degradation of the glass matrix will be responsible for the release of radionuclides to the biosphere however, there is multi-barrier (glass matrix, waste container, waste overpack container, buffer material, and use of 500 m of rock) concept to prevent / limit its release [7,9,13,14]. Thus, it is of highest importance to understand the long-term behaviour and evolution of glass due to the self-irradiation damage, and its impacts on glass leaching and alteration mechanisms. To accurately predict the degradation of glass and forecast the release of radionuclides, it is imperative to understand fundamentally the structural evolution of HLW waste forms when subjected to self-irradiation, i.e. the effects of alpha, beta and gamma irradiation over long time scales so that their relationships with long-term stability and dissolution of the waste form can be understood, established and more accurately predicted [16]. This has led to several studies on self-irradiation damage on simpler and more complex surrogate waste loaded glasses to address these issues [17–35].

Radiation arising from radionuclide decay in HLW is a complex scenario. There are alpha particles, alpha recoil nuclei, and gamma photons which originate from the decay of minor actinides. Beta particles and gamma photons originate from the

decay of fission products. During beta-decay, e.g., when ^{137}Cs decay, a neutron gets converted to a proton and ^{137}Ba nuclei is formed with the release of an electron. These complexities present incredible challenges to accurately simulate and study the effects of radiation damage in HLW glasses and consequently many different approaches, methods and techniques have been employed to simulate and study the effects of self-irradiation damage in HLW glasses [3]. These include ion beams from accelerators or TEM to simulate the electronic energy losses of alpha, beta particles and gamma photons, as well as losses due to elastic collisions or ballistic interactions of alpha recoil nuclei [17–35]. These studies are essentially accelerated studies, meaning that an equivalent integrated dose of longer period is delivered in a short time. Typically, the individual effects of electronic interactions due to beta/gamma and alpha particle or nuclear interactions due to alpha recoil nuclei are studied. A few reports, however, have presented the effects of mono-, simultaneous and sequential ion irradiations [3,36,37]. These studies have given great insight and provide motivation to review self-irradiation damage in nuclear waste glasses by considering the effects of dose and dose rate, and effects of mass and energy in accurately predicting the evolution of nuclear waste glasses [3,36–38]. Another method to study the effects of radiation damage which is reported in the literature is doping of HLW glass with a short-lived actinide such as ^{244}Cm or ^{238}Pu [13,24,30,39]. This method is impractical for most laboratories due to the obvious risks associated with handling of radionuclides. However, it is one of the most representative methods to study self-irradiation damage in nuclear waste glasses to simulate the damage of alpha decay.

It has been established that electronic effects due to interactions with beta/gamma from the decay of fission products will be responsible for self-irradiation damage in the first ~ 500 years of geological disposal [3,24,40]. The decay of fission products will also produce radiogenic heating which will increase the temperature (as high as 670 K for the UK HLW form) of the waste form ([37,41]. Whilst this increase in the temperature could have several detrimental effects on waste form performance, one potential benefit is that this may also “heal” at least some of the damage caused by electronic interactions (discussed in detail in Chapter 2). Atomistic simulations to study nuclear or ballistic damaging effects have contributed significantly to our understanding of long-term waste form evolution. Based on these studies it has been

reported that nuclear collision or ballistic damage due to alpha recoil nuclei will be the primary source of irradiation damage over longer periods [7,42–44]. A recent study, however, highlighted that electronic irradiation cannot be neglected as it may play a role in repairing the damage in HLW glass [36,45].

Whilst there have been a considerable number of studies performed on simple glasses and nuclear waste glasses to study the aqueous corrosion and chemical durability in geological repository or related conditions [16,46–54], self-irradiation damage of nuclear waste glasses has received less attention. Furthermore, self-irradiation - induced paramagnetic defects, structural changes associated with them and their relationships with glass composition, temperature, macroscopic changes, and impact on glass dissolution requires an enhanced understanding to be able to predict the long-term performance of HLW waste forms in geological repository conditions [15,17,37,55].

Beta/gamma and alpha particles interact with HLW glass and transfer energy to the atoms therein via ionisation and excitation [37,45]. This primary interaction produces electron and hole pairs in the glass [37,45,56]. These mobile charge carriers can be trapped at different sites within the glass structure, forming radiation-induced paramagnetic defects [28,33,56,57]. These paramagnetic defects can be healed by allowing trapped charge carriers to recombine when external energy is supplied [31,57,58]. This energy can be supplied in the form of heat or by coulombic forces [31,57,58]. Electrons can be trapped by multivalent cations such as transition metals and lanthanides which are present in HLW glasses and thus they may change their oxidation state [30,59–66]. A few studies in the literature have reported that the radiation-induced defects due to electronic interactions can be healed or mitigated, due to the presence of multivalent cations in HLW glass via defect hopping [29,60,63,67,68]. Furthermore, studying radiation-induced paramagnetic defects in simulated HLW glasses may be challenging since there are few techniques which can be utilised to identify the radiation-induced paramagnetic defects. One of the most widely used techniques to measure and identify paramagnetic defects is electron paramagnetic resonance (EPR) spectroscopy also known as electron spin resonance (ESR) spectroscopy. EPR can be used to probe materials such as glasses which have been irradiated; which have multivalent cations present therein; or both (the presence of unpaired electrons is an essential criterion for EPR).

However, even EPR has limitations: for example, resonance absorption signals can saturate and overlap, since it is a very sensitive technique (small concentrations can give a high-intensity absorption signal). EPR measurements can be useful when supported with information from complimentary techniques such as UV-Vis-nIR optical absorption and Raman spectroscopies. Alternatively, simpler glasses doped with probe cations such as transition metals can be utilised for developing fundamental understanding.

1.2 Objectives

Some of the questions and required studies to enhance the fundamental understanding of radiation induced defects in simple (without waste) and simulated HLW nuclear glasses discussed in the previous section forms the basis of this PhD. These are addressed in the PhD work presented in this thesis.

Three simple borosilicate representative glasses from India, UK (MW) and France (SON68) are studied. A fourth glass known as the International simple glass (ISG) and a modified version of the UK glass, called CZMW (Calcium-Zinc MW) are also studied. All of these glasses have been irradiated with gamma photons from a ^{60}Co source. EPR, UV-Vis-nIR and Raman spectroscopies are used to study pristine and irradiated glasses to study radiation-induced effects. A comparative study based on how / whether radiation-induced defects vary with glass composition has also been undertaken.

Time and temperature dependent study of gamma-induced paramagnetic defects for Indian and UK (MW) simple glasses is carried out. This was performed with the objective to study the stability / healing of the defects with time and temperature. The two glass types are also irradiated with two different doses of gamma radiation to study the effects of dose. A comparison based on how / whether radiation-induced defects vary in two glasses is also carried out. EPR, Raman and UV-Vis-nIR optical absorption spectroscopies were employed to carry out this study.

Effects of alpha particle implantation (simulated by He-ion) are studied using EPR and Raman spectroscopies on Indian and UK (MW) simple glasses. This study was carried out to study the irradiation effects of He-ions used as simulants for alpha particles. Structural changes and paramagnetic defects based on compositions and varying doses are illustrated through Raman and EPR, respectively.

Indian and UK simple glasses were doped with different concentrations of Fe_2O_3 in oxidised, reduced and controlled redox states to study their effects on gamma irradiation-induced paramagnetic defect concentration. Mössbauer spectroscopy was employed to study the oxidation states and local environments of Fe. EPR and Raman spectroscopies were employed to characterise the pristine and irradiated glasses.

Indian, UK and French glasses were doped with inactive surrogates of their respective HLW waste compositions. These glasses were irradiated using gamma and characterised using EPR and Raman spectroscopies.

X-ray diffraction analyses were carried out on all the glasses to identify any crystalline phases present. Density measurements were performed for pristine and all gamma irradiated glasses.

1.3 Structure of the thesis

This thesis is organised in 7 chapters, as follows:

Chapter 1. This chapter presents a brief overview of current understanding of HLW nuclear waste glasses, disposal strategies, self-irradiation damage and chemical durability over geological time scales. Methods to study self-irradiation damage are briefly discussed. Key important questions which have led to this work are raised and highlighted. Finally, the aims and objectives of this PhD study are specified.

Chapter 2. This chapter begins with an introduction on the importance of the nuclear energy and the need to manage radioactive waste safely and economically. Then sources of nuclear waste, classification of nuclear waste, a global picture of waste immobilisation strategies and methods are presented and discussed. Further, a brief theory of glass, its structure and defining properties are discussed. Finally, radiation sources in HLW glass and a literature review of irradiation-induced microstructural and macroscopic effects from both electronic and nuclear interactions are presented and discussed.

Chapter 3. This chapter presents the experimental methodology which begins with information and categorisation of the several types of glasses synthesised in this work. The compositions of all glasses are also presented. Then a brief discussion of the different steps involved in glass synthesis and methods used is given. Then a

background of all characterisation and analysis techniques used, and sample preparation requirements for them, is explained. Finally, a record of the different irradiation techniques employed is presented.

Chapter 4. This chapter presents the details of the investigation carried out to study the effects of alpha particle (simulating the self-irradiation effects of alpha particle in alpha decay of minor actinides) in Li_2O-Na_2O-B_2O_3-SiO_2 (LiNaBSi) and Na_2O-BaO-B_2O_3-SiO_2 (NaBaBSi) glasses using a He-ion implantation method. The chapter sets the objective in the beginning, then gives a brief account of experimental method of glass synthesis, methods employed for sample preparation and then presents technique employed for He-ion implantation. Finally, it discusses the results obtained in this investigation.

Chapter 5. This chapter presents the details of the investigation carried out to study the effects of gamma irradiation (to simulate the self-irradiation effects of beta-gamma damage in actual HLW glass) in LiNaBSi and NaBaBSi glasses using external irradiation from ^{60}Co gamma source. It also discusses the methods for glass synthesis and sample preparation. The chapter then presents all spectroscopic and other methods used to characterise the samples. Results from characterisation before and after irradiation, and from thermal treatment experiments are presented. Finally, all the important key results are discussed, and a comparison has been made for the different glasses under investigation.

Chapter 6. This chapter discusses the beta-gamma radiation effects in three simple glasses: SON68, International Simple Glass (ISG) and CaZn. Results from EPR, UV-Vis-nIR absorption and Raman spectroscopies are presented and discussed. This chapter also presents EPR and Mössbauer spectroscopic studies on varying concentrations of Fe_2O_3 doped pristine and gamma irradiated glass specimens. It also presents EPR studies for NaBaBSi, LiNaBSi and SON68 non-active waste simulated glasses.

Chapter 7. This chapter presents the summary of the conclusions from several studies in this thesis. A list of future work is also presented in towards the end of this chapter.

Chapter 2. Background and Literature Review

2.1 Introduction

Since the 1950s, when nuclear energy was first produced in an experimental breeder reactor-I (EBR) in Idaho [69], nuclear energy has been considered one of the top candidates for sustainable and environment friendly source of energy The international Atomic Energy Agency's (IAEA) Nuclear Energy Basic Principles describe the vision and rationale for using nuclear energy and covers aspects including benefits, and the responsible and sustainable use of nuclear energy to meet the world's growing energy demand [70]. These basic principles are to be complied with and followed by all essential elements of nuclear energy systems.

The Nuclear Energy basic principles also describe the objectives of radioactive waste management at different stages while complying with safety standards set for humans and the environment and maintaining security and non-proliferation. The benefits from nuclear electricity should outweigh the cost associated with the management of the radioactive waste by reducing the generation of the waste and optimising the processes to manage it.

The total number of operational nuclear reactors at the end of 2018 was 450, with 396 GW(e) as the net installed power capacity [71]. The total electricity generation from nuclear power reactors increased by about 2.4% in 2018 and reached 2563 TW.h.

For the sustainable use of nuclear energy, the safe, reliable, and economic management of nuclear waste is crucial. This includes all the technological and engineering challenges related to storage, transportation, and disposal (interim and permanent) of spent nuclear fuel (SNF) and high-level waste (HLW) arising from reprocessing [72]. Since the operation of the first nuclear power plant, 370,000 tonnes of heavy metal (tHM) in the form of used fuel has been discharged, as estimated by IAEA [73]. The IAEA estimates that the 120,000 tHM has been reprocessed from this total discharged used fuel [73].

2.1.1 Nuclear waste generation

This section discusses the sources from which nuclear waste is generated. Electricity is produced from uranium in nuclear power reactors through a series of

industrial processes which involve different activities. These activities are described under what is called as ‘the nuclear fuel cycle’ [74]. Radioactive waste is generated from the following activities [75]:

- Mining and milling of uranium.
- Processes involved in production of nuclear fuel,
- Nuclear power production by the operation of nuclear power plants.
- Operation of the nuclear research reactors.
- Remediation of contaminated areas, weapons and testing sites, and nuclear accident sites
- Reprocessing of spent nuclear fuel.
- Decommissioning of nuclear reactors and facilities.

This cycle starts from the mining of uranium ore through electricity production from nuclear reactor operation and ends with disposal of spent nuclear fuel [76]. The front end of the nuclear fuel cycle includes mining and milling, conversion, enrichment, and fabrication. The back end comprises of reprocessing and reuse of spent nuclear fuel, and disposal [77] (Figure 2.1).

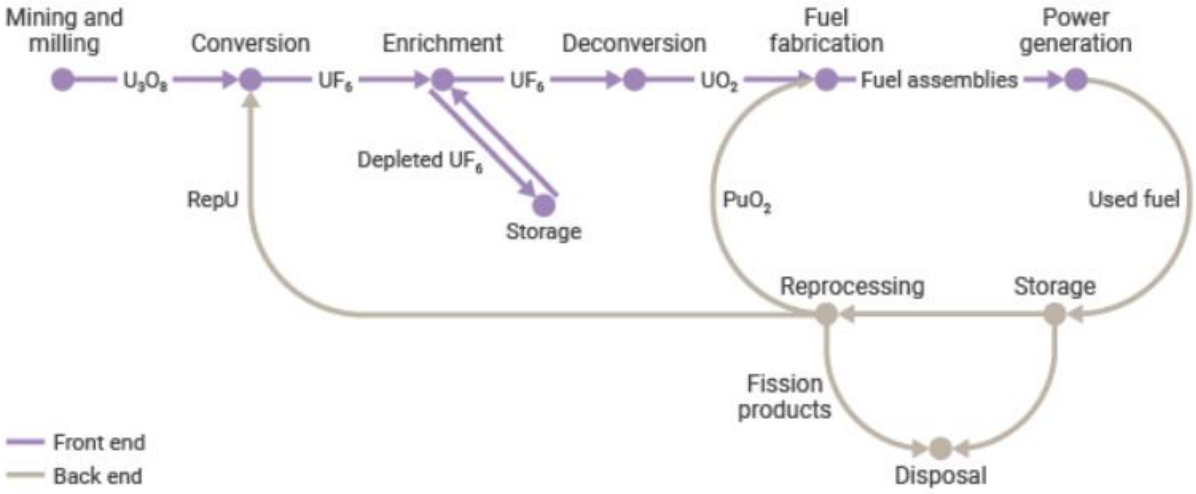

Figure 2. 1 The Nuclear Fuel Cycle (Source: [78])

2.1.1.1 Mining and milling

Uranium (U) is a naturally occurring element which can be found in rocks and soils, in many rivers and in the sea [74,79,80]. Its average concentration in the Earth’s crust varies from 1.8 to 2.8 ppm [80]. Uranium content in its ores varies in the range

from 20% U for example, in some Canadian mines, to as low as 0.02% [81]. The uraninite ore, also called pitchblende, is extracted or recovered using different methods such as in-situ leaching or from open cast mines [79]. It is then crushed, milled, and then leached in sulphuric acid to separate out the undissolved minerals, rock and to dissolve uranium oxides. It is then further processed to recover uranium oxide, also known as yellowcake (U_3O_8) [82](Figure 2.2).

Figure 2. 2 U_3O_8 or Yellowcake (Source: [79])

2.1.1.2 Conversion

Conversion is a process in which yellowcake (uranium concentrate) is converted to UF_6 (uranium hexafluoride) by fluorinating the oxide using a combination of fluorine and hydrogen fluoride (HF). To enable increasing the fissile content of ^{235}U in natural uranium (^{238}U is 99.3% and ^{235}U is 0.7%), conversion of yellow cake is carried out to form uranium hexafluoride, UF_6.

2.1.1.3 Enrichment

The process by which the fissile content, that is the proportion of ^{235}U, in natural uranium is increased above the levels present in natural uranium is called enrichment [83]. The mass difference between $^{238}UF_6$ and $^{235}UF_6$ is utilised in enrichment technologies such as gaseous diffusion and gas centrifuge that separate the two isotopes of gaseous UF_6 [74,76,83]. Nuclear fuel used in civilian nuclear power reactors is generally enriched to 3-5% ^{235}U [76]. Figures 2.3 and 2.4 show

schematics of the gaseous diffusion unit and gas centrifuge diffusion technology, respectively.

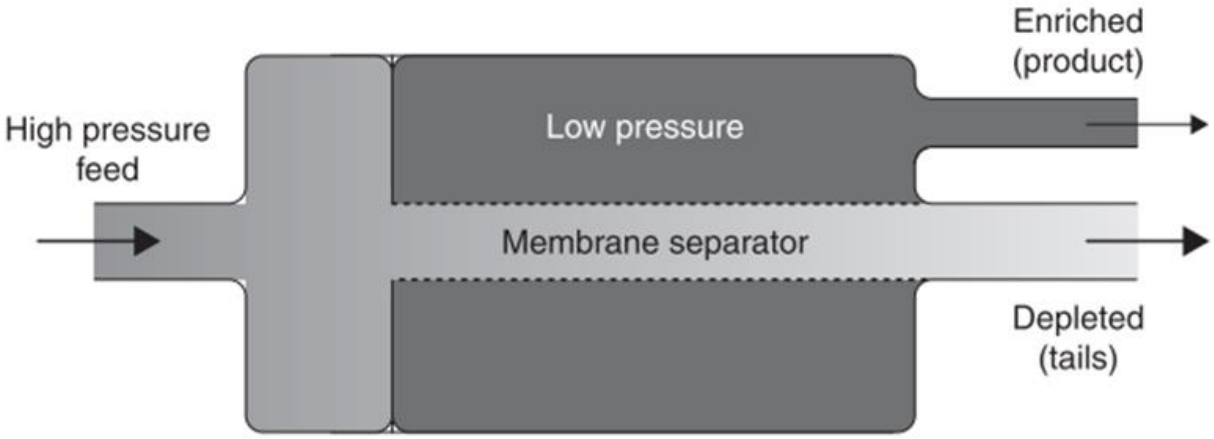

Figure 2. 3 Gaseous diffusion unit (Source:[83])

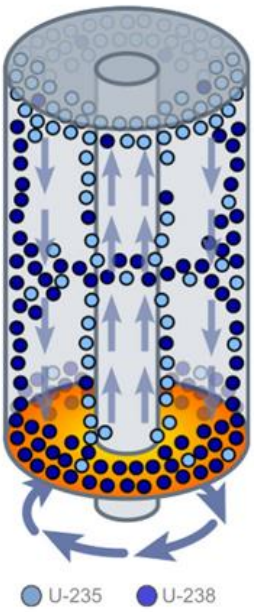

Figure 2. 4 Gas Centrifuge (Source:[79])

2.1.1.4 Fabrication

Fabrication of nuclear fuels is done by the conversion of enriched uranium to uranium oxide powder (UO_2) [79,83]. UO_2 powder is compressed to form fuel pellets and then sintered and machined to very tight tolerances. Nuclear fuel pellets are generally around 1 cm in diameter, but their exact dimensions vary with reactor type. The ceramic fuel pellets are then loaded into fuel rods and once rods are fabricated,

they are inserted into fuel assemblies [76]. The configuration of fuel assemblies also varies from one reactor to another type.

2.1.1.5 Reprocessing of spent nuclear fuel

Irradiated fuel from a nuclear reactor is discharged / removed after a target burnup is reached. This is done because fission products accumulated in the irradiated fuel start consuming neutrons which do not allow the chain reaction to sustain, as well as to avoid any potential fuel-cladding rupture due to swelling which may be caused by gaseous fission products and also due to higher burnup [84]. It is then stored at an interim storage facility for a cooling-off period (short-lived fission products decay, generating heat) followed by eventual disposal. This is called open cycle or the once-through cycle [85]. USA (civil nuclear power plants), Sweden and Finland are examples of nuclear power producing countries which have adopted open fuel cycles [86,87].

The closed fuel cycle approach is adopted by France, United Kingdom, Japan, Russia, China, and India [84,88]. In this approach reprocessing of spent nuclear fuel is done to chemically separate the fissile uranium and plutonium for recycling and reusing them as nuclear fuel [87]. Reprocessing has been considered an attractive choice since it helps in reducing overall volumes of waste and in utilising resource which would have gone to waste otherwise, as well as being an attractive option from sustainability and economic points of view [84,89]. Each year about 10,000 metric tonnes of heavy metal (MtHM) is produced from nuclear power reactors, globally [90].

SNF is transported from interim storage facilities to reprocessing plants, where it may be stored for further cooling for 3 to 5 years, until it is cooled sufficiently [87]. This helps in the reduction of activity which facilitates processing. There are two options available for reprocessing. The first is the conventional method based on aqueous solutions. This liquid-liquid extraction / separation method is based on hydrometallurgical separation of uranium (^{235}U) and plutonium (^{239}Pu formed by neutron capture by ^{238}U) from transuranic elements (neptunium, plutonium, americium and curium), fission products and activation products, and it is commonly known as the PUREX (Plutonium URanium EXtraction) process [87,91–93]. Figure 2.5 shows a flowsheet of the PUREX process. The first step in this process is to mechanically de-clad / cut / shear the fuel elements. The resulting sections of fuel

rod and debris of fuel pellets are dissolved in a nitric acid (HNO_3) solution. The concentration of HNO_3 is maintained in the 2-4 M range to adjust the oxidation state of plutonium to the tetravalent state since this is the most extractable state [89]. The organic phase, which is the tri-*n*-butyl phosphate (TBP), extracts metal ions from aqueous phase which is the nitric acid solution, when both are mixed [89,91,94]. The extracted Pu and U can then be used in mixed oxide (MOX) fuel fabrication. MOX fuel will be used in Generation IV reactors - pressurised water reactors (PWRs) and fast breeder reactors (FBRs). After extraction of Pu and U, the acidic aqueous raffinate or acidic liquor is known as high-level liquid waste (HLLW). It consists of impurities and remaining fines from cladding removal, fission products (FPs), minor actinides formed by neutron capture during reactor operation, activation products, and inactive process additives used for reprocessing [89,95]. The cladding materials such as stainless steel and Zircaloy (cladding hulls) and some insoluble fission products such as ruthenium, molybdenum, rhodium, palladium, and technetium do not dissolve in nitric acid. The nitric acid solution consisting of these is filtered or centrifuged to remove the insoluble fission products, cladding hulls, and fines This step is called clarification. These are separated and washed to recover uranium and plutonium, fission products and transuranic elements, however, they still end up in the waste Besides this some of the gaseous fission products (krypton, xenon, iodine, C-14) do not get dissolved and gases (NO and NO_2) which are produced by the reaction of nitric acid and spent fuel are routed to a treatment unit called as ‘head gases’ unit.

The cladding hulls and solids are dried and packaged (discussed in section 2.1.2) as low-level radioactive waste (LLW) [91]. The fission products and minor actinides are concentrated into a solid high-level waste form, also explained in section 2.1.2. The nitric acid and TBP are recycled which reduces the volume of the final waste substantially. The high-level liquid waste liquor (HLLW) is then stored in stainless steel cylinders. Prior to concentrating and immobilising HLLW into a solid waste form these cylinders containing HLLW are either stored in water pools called wet storage or pool storage; or in concrete casks which are surrounded by noble gas above ground, called dry storage [86].

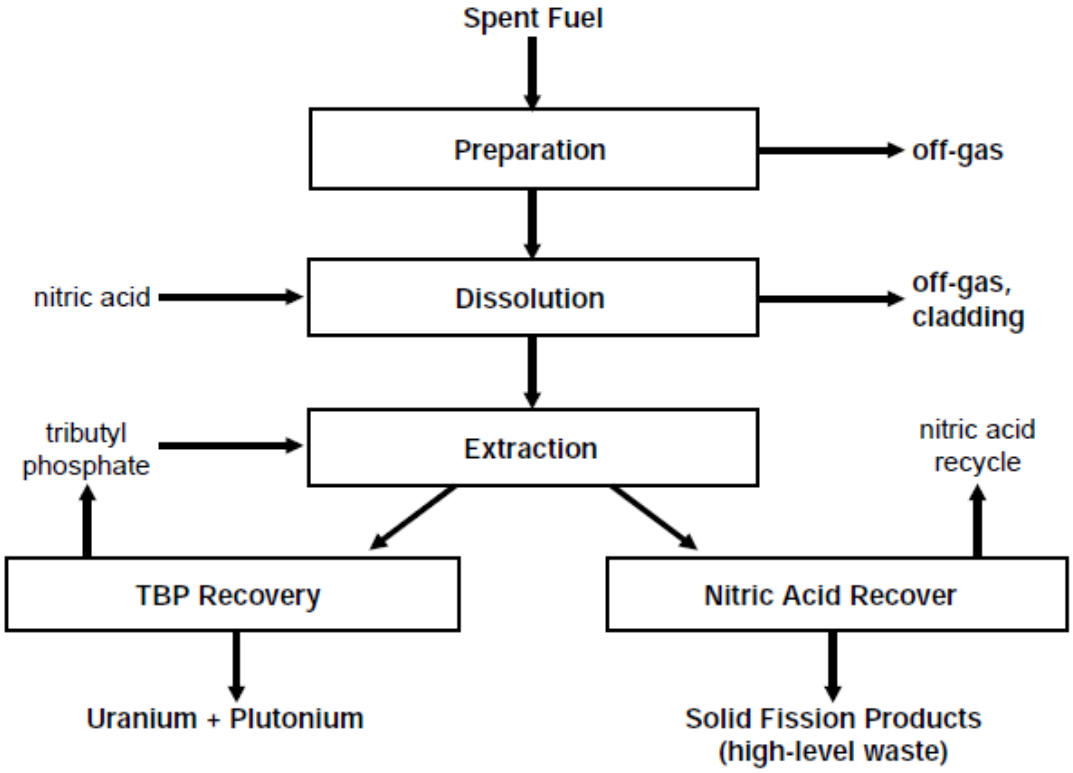

Figure 2. 5 Flowsheet of the PUREX process (source:[91])

The other route is pyrochemical reprocessing, also known as the electrometallurgical technique, and this is based on the electrolytic separation of uranium (^{235}U) and plutonium (^{239}Pu formed by neutron capture by ^{238}U) from transuranic elements (neptunium, plutonium, americium, and curium), fission products and activation products [96]. However, methods based on pyrochemical reprocessing are small scale and / or in development phase [87,97].

2.1.2 Nuclear waste classification

This section discusses the categories of nuclear waste. Radioactive waste is classified into various categories by different countries either based on the half-lives of radionuclides present or by activity content [5]. It also depends on the origin of the waste (e.g., reactor types) as well as criticality aspects [98]. IAEA classifies radioactive waste into six categories. Figure 2.6 provides the summary of nuclear waste classification in UK.

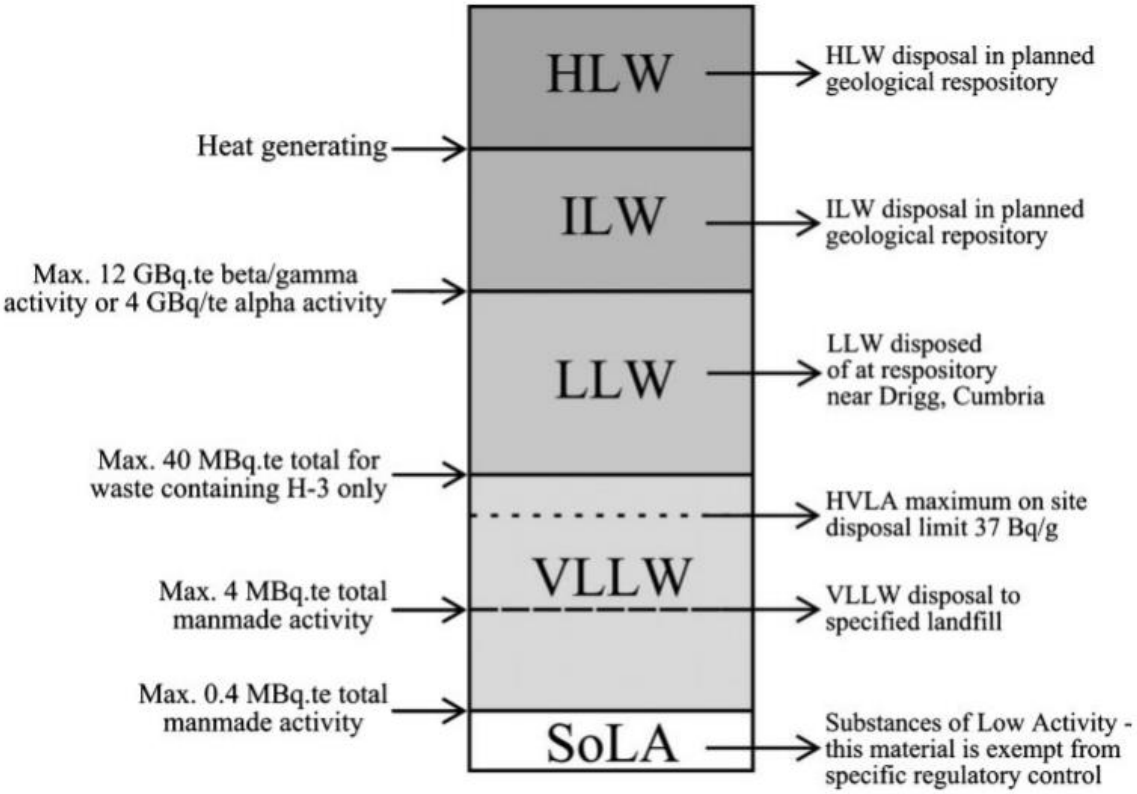

Figure 2. 6 Summary of nuclear waste classification in UK. (Source:[99])

1) Exempt waste (EW): The waste which does not require provisions for radioprotection, or the waste which is cleared, exempted or excluded as per the criteria set by radiation protection regulation board for clearance, exemption or exclusion [5].
2) Very short-lived waste (VSLW): This category of waste contains radionuclides with very short half-lives. Their radioactivity concentrations are higher than the levels set by the regulation board for clearance. This waste is stored for short times of up to a few years to decay so that it can be cleared as per the provisions set by the regulatory board. This category of waste often arises from the radionuclides used in research and medical purposes, for example VLLW arising from ^{192}Ir and ^{99m}Tc.
3) Very low-level waste (VLLW): This category of waste does not require special containments and isolation, but it does not fall in the category of exempted waste either and, therefore, it is disposed of in near-surface landfill sites with consideration of regulatory and safety provisions set for this kind of waste [5,100,101]. Waste in this category may arise from rehabilitation and

dismantling of industrial sites and the mining or processing of ores and minerals.

4) Low level waste (LLW): This category of waste contains limited amounts / numbers of long-lived radionuclides and requires containment for up to a few hundred years. It arises from nuclear power plants, nuclear and medical research laboratories and includes soil, concrete, steel, packaging etc. This is usually compacted and contained in steel canisters/drums and stacked into large containers which are then disposed in near-surface engineered facilities [12,100,102,103].
5) Intermediate level waste (ILW): This category of waste contains a greater amount of activity due to the long-lived radionuclides present and requires a greater degree of isolation and containment than that is required for LLW. However, it does not require provisions for radiogenic heating. ILW may require significant shielding, and may arise from fuel cladding, chemical sludge from the treatment of radioactive effluents. It is usually contained (discussed later in section 2.1.3.2) in bituminite (in the UK currently) and disposed at a greater depth from the surface (tens to a few hundred meters) [12,100,102,103].
6) High level waste (HLW): This category of waste contains mainly fission products arising from spent fuel reprocessing, along with minor actinides generated from neutron capture, corrosion products generated from the materials of storage tanks in which HLW is stored prior to vitrification, and process additives used during processing. These fission products produce a significant amount of radiogenic heating, such that it requires many years of cooling, multi-level shielding, immobilisation (discussed in section 2.1.3.2 in detail) and disposal in multi-engineered barrier systems in geological repositories [5,100,103–105]. High-level waste contains ~98 % of the total radioactivity in nuclear waste [100,102]. The UK defines HLW as the waste with maximum activities in the region of 4×10^5 GBq m^{-3} α-activity and 8×10^7 GBq m^{-3} β- and γ-activities [101][106]. In India HLW is classified as the waste type with concentration of activity greater than 3.7×10^2 GBq/L [98].

2.1.3 Nuclear waste immobilisation

This section discusses the different immobilisation and containment methods and strategies for different categories of waste. The differences in classification of the wastes put forward by different countries and different regulatory and environmental agencies (e.g., International Atomic Energy Agency (IAEA), US Nuclear Regulatory Commission (NRC), National Decommissioning Authority (NDA), Atomic Energy Regulatory Board (AERB) and so on) involve different immobilisation and disposal strategies and technologies [5,12,104,107,108]. The primary objectives set by nuclear energy producing nations to manage nuclear waste are reduce, reuse, and recycle [104,109–111]. This strategy has been followed to reduce the volume of waste for disposal by separating out reusable and recyclable fuel materials. The immobilisation of waste with primary objectives to convert nuclear waste into a more stable form which can eventually be stored in geological repositories has been in practice and adopted by many countries including France, Russia, Belgium, India, Japan, UK, Germany, Canada, Italy and USA [92,102,112]. This would prevent the waste from entering the biosphere and at the same time help to support non-proliferation.

2.1.3.1 Low and intermediate level waste immobilisation

For LLW and ILW, together known as LILW, bituminisation and cementation are two immobilisation techniques widely used by many countries including UK, France, Belgium, USA and Finland [100]. Cements are a relatively cheaper option than, for example, vitrification, to immobilise LLW and ILW. The cement-based waste form is produced using Ordinary Portland cement (OPC) and blast furnace slag (BFS) or pulverised fuel ash (PFA) [102,113,114]. Cement-based waste forms have low processing temperatures, which is beneficial in terms of reduced volatilisation of radionuclides. It also has reduced solubility in high pH water (pH 11-12) but swelling due to radiolysis, instabilities in inert environments, and durability are some of disadvantages of cement-based waste forms [112–114]. Cementation and cement composites are also used in India for immobilising low level and intermediate level liquid waste. Low level aqueous waste in treated by several methods employed in operations such as ion-exchange, evaporation or chemical treatment in India prior to their conditioning in cement and polyester styrene (polymerization) [98,115]. Figure. 2.7 shows an image of a cone mixer for conditioning of ILW in a cement matrix.

Figure 2. 7 A cone mixer at Waste Immobilisation plant, Trombay (Source:[98])

2.1.3.2 HLW immobilisation - vitrification

As discussed in preceding sections of this chapter, the majority of radioactivity (about 98 % or greater) in the entire nuclear fuel cycle in concentrated in the high-level liquid waste produced from either reprocessing of commercial spent nuclear fuel or processing / reprocessing of spent fuel from reactor fuels for generating plutonium or from defence research activities (e.g., nuclear weapons or naval reactors) [92,104,112]. The desirable characteristics and requirements for a waste form to immobilise and contain HLW for safe and economic disposal are as following:

- High waste loading: the waste form must be able to accommodate sufficiently high proportions of waste, to reduce waste form volumes, to reduce the number of containers to be disposed of in geological repositories, and to reduce the costs associated with manufacturing, transport, storage and disposal [116–118].
- Ease of processing: the process of fabrication of waste forms should be efficient and readily accomplished. The processing temperature should be

sufficiently low (to avoid volatilisation of radionuclides such as ^{134,137}Cs and ^{131}I), which has several advantages including lower off-gas emissions, reduction in the fabrication cost, longer life of plant etc.

- Self-irradiation stability: the waste form should be able to maintain its integrity under self-irradiation due to the radionuclides present in the HLW (the study of irradiation induced changes in the microstructure, properties and performance is central to this thesis, and is discussed later in detail). It should be tolerant to potential irradiation induced changes which may lead to detrimental effects (e.g., swelling, cracking etc.) [116–119]. Radiation effects in nuclear waste glasses are central to this thesis and are discussed in detail in the next chapters.
- Chemical durability: since HLW contains radionuclides which can have very long-half lives, a waste form should be resistant to extreme conditions (ground water, corrosive gases and vapor, aqueous solutions etc.) over geological disposal periods. It should be resistant to aqueous dissolution to prevent any dispersal of radionuclide to the ground water and biosphere [6,10,102,116,120].
- Solubility: all components of HLW should be homogenously concentrated within the waste form structure (with < 10wt% inhomogeneities). This also means that the waste form should be able to incorporate and accommodate all the radionuclides and other components of HLW with minimum formation of secondary phases [10,102,116].
- Good mechanical and thermal stability: the waste form should have good mechanical strength to maintain integrity against all potential disintegrating environments such as radiogenic heating, corrosion etc.

Vitrification has been the globally accepted technology for the immobilisation and incorporation of HLW and has been researched since the 1950s by the nuclear power producing or nuclear weapon producing states [10,102,112,121,122]. Vitrification is defined as a process of incorporating radionuclides in a solid glassy waste form by melting at suitable temperatures [100]. This provides the HLW in a suitable solid form which can be stored and transported for eventual geological disposal. Vitrification technology is used by many countries including USA, France, UK, India, Germany, Japan, China, Russia, South Korea for immobilising mainly

HLW, however, countries such as USA, Russia and S. Korea have been using it to treat certain LLW and ILW [21,24,100,123]. Borosilicate glasses have been the globally preferred choice for the vitrification of HLW and some LAW since they meet the maximum desirable characteristics of a suitable waste form for long term safe and economic storage while many countries are researching and pursuing alternative waste forms such as glass ceramics (borosilicate glasses are discussed later in this thesis in detail) [10,63,93,112,118,124,125].

2.1.3.3 HLW vitrification in France

The research on solidification of fission products started at Saclay in the 1950s and was led by Roger Bonniaud [125]. Research began by attempting to incorporate fission products into synthetic mica but soon the first radioactive glass was produced at Saclay in 1957. From the 1960s to 1980, fission products were immobilised into silicate glasses and synthetic mica. Larger scale (10 kg) radioactive glass production was achieved at a pilot vitrification facility called Gulliver in Marcoule in the 1960s. In 1968 semi-industrial scale (200 kg) production of vitrified high-activity solutions was achieved in the Marcoule Pilot Plant, called PIVER. The high-activity solutions were fission products arising from graphite gas reactors running on natural uranium as well as from Phenix fast reactors [102,125–127].

The two pilot facilities in Marcoule opened the way for the successor AVM (Marcoule vitrification facility) which was commissioned by COGEMA (name changed to AREVA and now ORANO) in 1978. The confidence gained through the operation of AVM led to the possibility of vitrification of the fission product solutions produced at the reprocessing plant at La Hague. This reprocessing plant was built to reprocess spent fuel from 58 French PWRs (pressurised water reactors). This led to the start-up of two vitrification units at La Hague: R7 in 1989 and T7 in 1992, since AVM did not have sufficient capacity to vitrify the fission products solutions from the reprocessing of spent fuel from all the power plants. The AVM is a two-step process: calcination and vitrification, this same process was purchased by BNFL (British Nuclear Fuels Ltd.) for Sellafield Ltd. (UK's reprocessing, vitrification site)[125]. Figure 2.8 shows the French hot induction crucible melting process. The R7 and T7 reprocessing plants have been producing borosilicate glass waste forms immobilising HLW [127]. The composition of the non-active version of R7T7, known as SON68 borosilicate glass, which is studied in this thesis, is given in Table 3.2 [23]

in Section 3.2.2. The simulated waste composition (nominal) synthesised in this thesis is adapted from Karakurt *et al.* [128] and is given in Table 3.7 in Section 3.2.2.

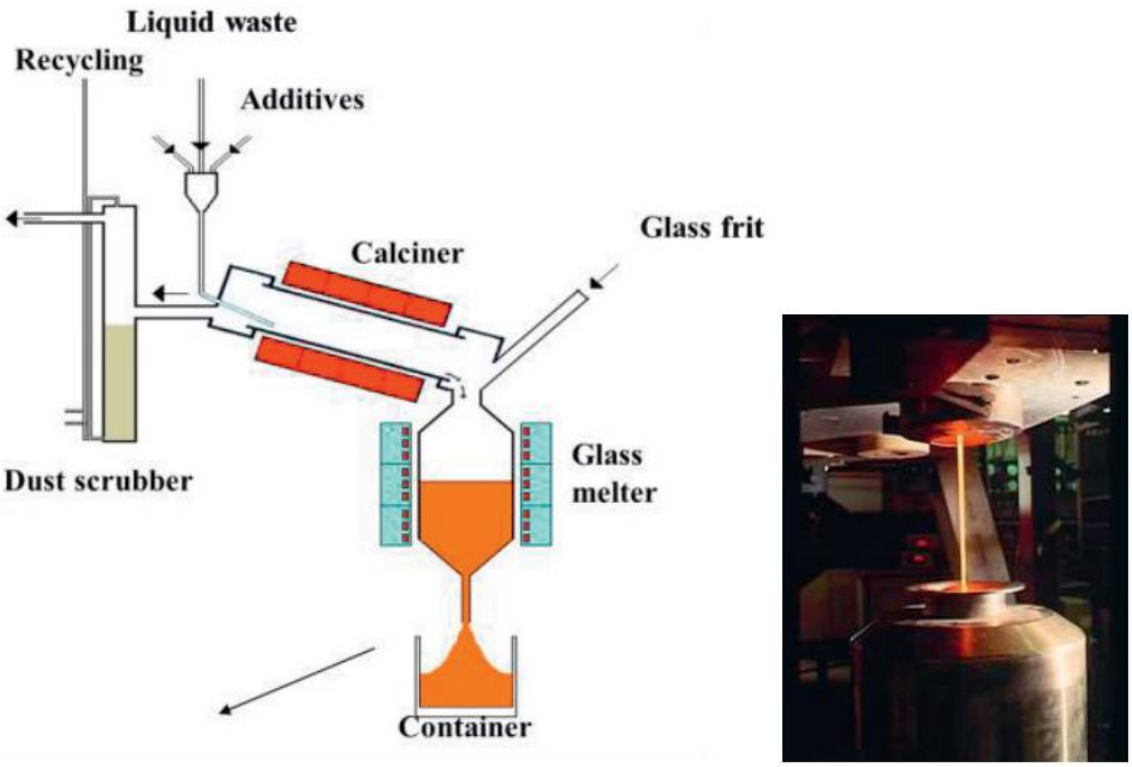

Figure 2. 8 Two-step French vitrification process using hot induction melting furnace (Source:[125])

2.1.3.4 HLW vitrification in UK

In the UK HLW arises as a highly active liquor (HAL) by-product from the reprocessing of spent nuclear fuel from the Magnox reprocessing plant which reprocessed the natural uranium metal fuel from UK's first-generation Magnox reactors and THORP (Thermal Oxide Reprocessing Plant) which reprocessed enriched oxide fuels from AGRs (Advanced Gas cooled Reactors) and LWRs (Light Water reactors) [129].

The UK's spent fuel is reprocessed at the reprocessing facilities at Sellafield Ltd. and produces two distinct (different chemical and isotopic concentrations) HAL streams from the reprocessing of spent nuclear fuel from Magnox and AGRs/LWRs. Magnox HAL is rich in magnesium and aluminium coming from residual cladding material. Oxide HAL does not contain Mg or Al but contains higher concentrations of fission products and actinides owing to higher fuel burnup of. It also contains higher content

of gadolinium which is a reprocessing additive (used as a neutron poison). Oxide HAL is never vitrified by itself and was historically mixed with Magnox HAL in a 75:25 Oxide:Magnox blend to meet the vitrified product requirements [129]. THORP completed reprocessing in 2018 and MAGNOX reprocessing is coming to an end and will conclude in 2021 [130,131]. This will end the production of civil plutonium and HAL production at Sellafield. Sellafield will then move towards completion of HLW vitrification followed by POCO (Post-Operational Clean Out), decommissioning and remediation [130,131]. HAL waste streams have been categorised into seven groups (Table 2.1).

Table 2. 1 Chemical components present in UK Magnox and Oxide HAL waste streams and 'Magnox' and 'Oxide' in the subscript denotes the components specifically found in Magnox or Oxide HAL, respectively. (Source:[41])

Fission Products	Ge	As	Se	Rb	Y
	Sr	Zr	Mo	Ru	Te
	Nb	Ag	Cd	In	Sn
	Cs	Ba	La	Ce	Pr
	Sb	Dy	Eu	Gd	Tb
	Nd	Sm	Tc	Rh	Pd
	Pm				
Unextracted elements	U	Pu			
Actinides	Cm	Am	Np	Th	
Corrosion products	Fe	Cr	Ni	Nb (Magnox)	Mn (Oxide)
Cladding	Mg	Al	Fe	Si (Magnox)	Zr (Magnox)
	Ni (Oxide)	Cr (Oxide)			
Fuel additives and impurities	Fe	Al	Si	Mo	Cr
	Ni	Mg	Mn	P_2O_5	Zn
	Ca (Oxide)				
Anions	SO_4^{2-}	PO_4^{2-}			
Poisons	Gd				

‘Magnox’ and ‘Oxide’ in the subscript in Table 2.1 denotes the components specifically found in Magnox or Oxide HAL, respectively.

The AVM vitrification technology bought from France was further developed and a Full-Scale Inactive Facility (FSIF) at Sellafield in 1981 was constructed. In 1982 the second-generation French AVH (Atelier de Vitrification La Hague) process was implemented, and the UK’s waste vitrification plant’s (WVP) construction began. It had a higher throughput (25 kg vs 15 kg per hour) and was using an elliptical melter instead of the cylindrical melter used in AVM. The WVP lines 1, 2 and 3 were commissioned in 1989, 1990 and 2002, respectively. A research facility known as the Vitrification test rig (VTR) was constructed in 2001 for performing research for the improvement of the process (HAL volume reduction, higher waste loading etc.) and underpinning the technology of vitrification in a non-active waste vitrification facility [129]. Figure 2.9 illustrates the schematic of the HLW vitrification process on the Sellafield site.

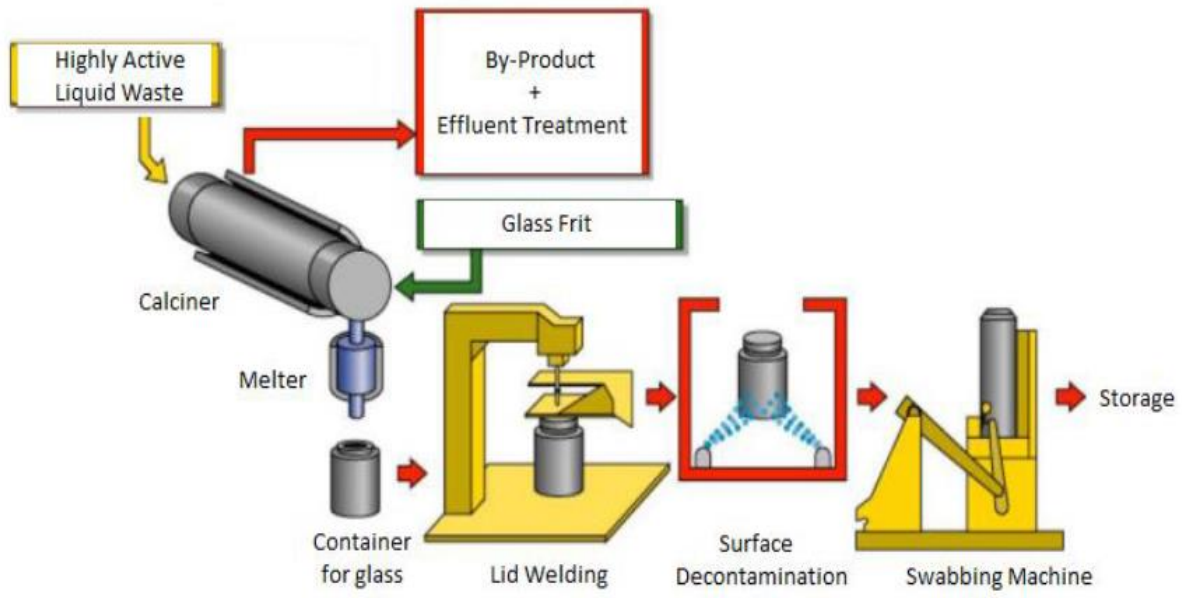

Figure 2. 9 Schematic of UK HLW vitrification process at Sellafield site.(Source:[129])

Vitrification process technology in the UK is based on the French two-stage vitrification process and can be simplified into three main steps:

1. Calcination- HAL is transferred from storage tanks to one of the feed tanks in the WVP where it is combined with sugar solution and fed into a rotary calciner. The HAL feed is heated electrically which partially denitrates the feed and produces a powder called calcine.
2. Melting- Calcine is fed along with metered quantities of base glass frit (MW borosilicate glass) into an induction heated melter crucible, where it is heated to ~1060 ˚C. The resulting product is a combination of calcined waste and base glass frit which produces a homogenous melt. This melt is poured into product containers.
3. Cooling- The melt is allowed to cool before the containers are welded with a lid. These product containers are stored at a short-term local storage facility called the Vitrified Product Store (VPS).

Whilst implementing the French two-stage AVH process, the MW (Mixture Windscale) glass composition was selected. MW is a mixed alkali borosilicate glass which met the requirements of a suitable waste form to immobilise HLW in the UK. In the original MW base glass composition (see Table 3.2) Li and Na were present in equimolar amounts. However, $LiNO_3$ was added to the HAL feed, so as to improve the reactivity of the calcine and as a suppressing agent for the formation of refractory oxides in the melter. Hence, to balance out the amount of Li_2O in the final 25% standard waste product, the original MW glass composition was reformulated with half of the original lithium content, and it is known as 'MW-1/2 Li' [129]. Another glass composition was developed, called Ca-Zn MW or MWCZ to immobilise the post operational clean out wastes (POCO) stored in highly active storage tanks (HAST) at the Sellafield site [106,121,132]. This waste has high molybdenum contents (up to 60 wt%). Studies on non-active simulated waste in the Ca/Zn MW glass matrix have shown that Ca can preferentially form a more durable phase with Mo called as $CaMoO_4$ (powellite) than the alkali molybdate phase which is more water soluble (Na_2MoO_4). This led to development of the MWCZ glass for immobilising high Mo containing POCO waste in future [106,121,132].

2.1.3.5 HLW vitrification in India

In India borosilicate glass matrix development for HLW waste immobilisation started in the 1970s. Before that nephelinite based glasses were considered in the 1950s but were not pursued further since their processing temperatures were very high,

1400-1500 ˚C [133] and hence were not suitable for the hot-wall induction melters used in the Waste Immobilisation Plant during that time. Thus, the replacement of Al_2O_3 with B_2O_3 was undertaken, which reduced the synthesis temperature to 950-1000 ˚C [133].

A few sodium borosilicate glass compositions were selected which showed acceptable product requirements such as durability, viscosity, pouring temperature ~950 ˚C or lower etc., however, the processing temperature of ~ 950 ˚C was too high to retain Cs and Ru at plant scale [104,117,133]. Addition of Ti^{4+} removed the problem of volatilisation [133], however, this increased crystallisation and/or immiscibility either during melting or thermal treatment. Since sodium borosilicate glass was not suitable due to the phase separation and liquid-liquid immiscibility due to the high sulphate contents of Indian HLW, new compositions based on alkali earth borosilicate glasses were researched [134,135].

The PbO-B_2O_3-SiO_2 glass system was studied extensively since this system was known to be more leach resistant and have low synthesis temperature, however, due to poor solubility limits of sulphate, the search for a newer glass system was started [135]. Barium doped sodium borosilicate glass was then studied and pursued since it has a high sulphate incorporation capacity and also above the solubility limit it forms $BaSO_4$ which is a leach resistant phase [98,104,136,137].

Vitrification in India consists of pre-concentrated waste and glass forming additives/slurry being added to the process pot. The three main components of the furnace are the process pot, susceptor and induction coils (see Figure 2.10). The furnace is a multizone induction furnace consisting of three zones, namely top dish, cell and bottom dish [98,133]. The cell is made of a high Ni-Cr alloy, Inconel-690. This alloy can withstand high temperatures and both oxidising and corrosive conditions. The cell is joined to the top and bottom dishes by welding. The susceptor is heated by induction heating zones, it then radiates heat to the process pot. HLW in aqueous nitric acid and glass additive slurry are added to the process pot using different channels. The level of HLLW is measured by thermocouples which are located at different heights [104,133]. The complete vitrification process is a multi-stage process which consists of feeding (100-105 ˚C), evaporation (105-120 ˚C), calcination (300-700 ˚C), melt formation (700-850 ˚C) and soaking (950-1000 ˚C). The homogenous melt is poured into stainless steel canisters which are cooled in air and are closed by a welding a lid on them. The canisters are then put inside a

stainless steel overpack and stored in underground multi-engineered barrier storage remote facility for eventual geological disposal.

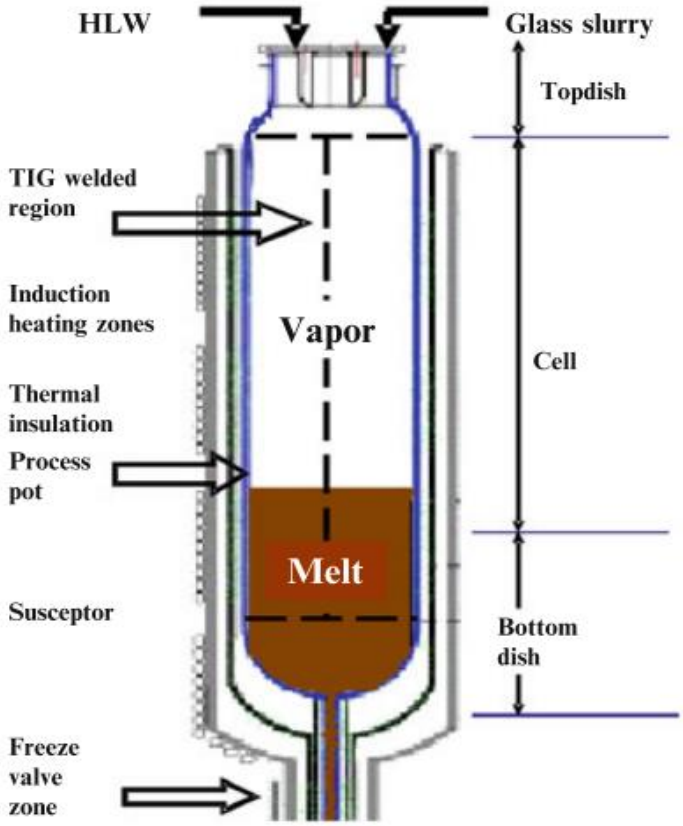

Figure 2. 10 A diagram of a typical hot wall induction melting furnace.(Source:[133])

2.1.3.6 International Simple Glass

The International scientific community (Japan, USA, UK, Germany, France, Belgium) working on nuclear waste management developed and agreed upon a glass which is called the International Simple Glass (ISG) [23,55]. This glass was essentially a simplified version of French SON68 glass, and it was chosen as a reference glass for aqueous leaching and durability studies. It was decided that this glass will be studied by all the collaborating nations and provide a benchmark for experimental data and compositional analyses. The composition of ISG glass is given in Table 3.2. This glass comprises of components which are common to boroaluminosilicate glasses.

2.2 Glass definition, structure, and properties

2.2.1 Defining glass.

Over a period of many decades, different theories and definitions of glass as a material have been provided by researchers and scientists. There has been an evolution of the fundamental understanding of the nature of glass and therefore its definition kept changing, despite being a ubiquitous material.

Varshneya [138] defined glass as an amorphous solid which can be formed by rapid melt quenching that exhibits a glass transition phenomenon at glass transition temperature T_g. Nieuwenhuizen [139,140] defined - “The glassy state is inherently a non-equilibrium state; a substance that is a glass in daily life (time scale of years) would behave as a liquid on geological time scale.” and stressed the idea that equilibrium thermodynamics does not work for glasses, because there is no equilibrium. A more recent and comprehensive definition by Zanotto and Mauro [141] is - “Glass is a non-equilibrium, non-crystalline state of matter that appears solid on a short time scale but continuously relaxes towards the liquid state. Their fate, in the limit of infinite time, is to crystallise.” For a general understanding a glass can be defined as a non-crystalline solid which lacks long range order and periodic arrangement of atoms. It is synthesised by rapid cooling a liquid such that it passes the nucleation and crystallisation. Glass transformation occurs over a range of temperature or transition range which is the onset of departure from the supercooled liquid state to the rigid glassy state [138].

2.2.2 Thermodynamics of glass

The glass transition or glass transformation region is defined as a range of temperatures over which a transition from a supercooled liquid state to a non-equilibrium, non-crystalline metastable solid state occurs (see Figure 2.11). The structure of glass depends on its thermal history as well as on composition.

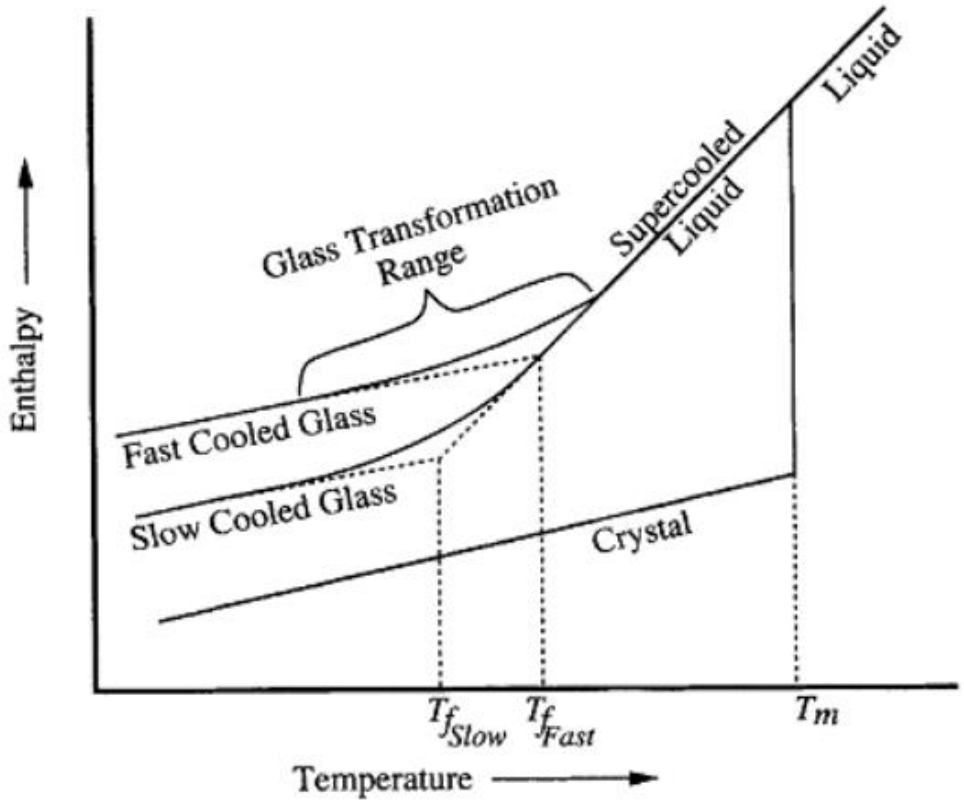

Figure 2. 11 Enthalpy versus Temperature curve showing effects of rate of cooling and temperature on enthalpy (Source:[142]).

A liquid in the supercooled state, if cooled for more slowly the glass transition temperature, will form a more relaxed system with low enthalpy and is expected to have a lower volume and high density since slow cooling allows the structure to rearrange itself. The enthalpy of a system can be affected by thermal treatments. Rapid cooling of the liquid will increase the enthalpy and fictive temperature (T_f) of the system. T_f is the equilibrium temperature at which the structure of the glass is considered that of the equilibrium liquid.

2.2.3 Oxide glasses

The components of oxide glasses are categorised into glass network forming, network modifying, and those which can act both as network forming and network modifying species, also called as intermediates, such as Al, Mo, Zr [106,138,142–145]. Glass network forming components are generally elements with small ionic radii and high valences such as Si, B, Ge, and P. These elements form the oxide glass network by forming covalent bonds with the oxygen atoms. Glass modifying components are cations such as alkalis, alkaline earths, and rare earths. They act as

modifiers and convert bridging oxygens into non-bridging oxygen by breaking covalent bonds between glass forming species (Si,B) and oxygens. Each mole of alkali oxide can create two NBOs by breaking Si-O-Si in an alkali silicate glass [138,142]. Under certain conditions glass modifier can also act as charge compensator as explained later in this section [146]. The abundance for NBOs is higher for large modifier cations such as Ba^{2+} [147]. The network of the oxide glasses determines the role of the cations and properties which depend on the cation such as, for example, viscosity [148,149].

2.2.4 Structure of vitreous silica and silicate glasses

The earliest discussions of structural theories of glasses began with discussions on the structure of vitreous silica and alkali silicate glasses. Several theories were developed (Greaves *et al.,* [150], Greaves *et al.,* [151] Wright [152]) but the one theory which is most widely accepted was developed by Zachariasen [153]. Zachariasen wrote a paper entitled 'The Atomic Arrangement in Glass' and presented a theory called 'random network theory'. He used the crystal structure terminology and proposed that glass may be characterised by an infinitely large unit cell containing an infinite number of atoms. His XRD experiments suggested that the glass network lacks periodicity and symmetry, unlike crystals [153] and this is how a glass and crystal can be distinguished. Due to a lack of symmetry in the glass network, glass has an isotropic character [153] meaning that the atomic arrangement in a glass will be statistically the same in all directions unless external fields are present. Zachariasen-Warren [153] formulated the following set of rules to describe the conditions required for glass formation:

1. Each oxygen atom is linked to no more than two atoms A (silicon or boron atom/cation).
2. The coordination of oxygen atoms surrounding atom A must be small.
3. The oxygen polyhedra must share corners with each other and not edges or faces.
4. If the network is required to be a three-dimensional network, each oxygen polyhedron must share at least three of the four corners.
5. Sample must contain a high percentage of cations which are surrounded by oxygen tetrahedra or triangles.
6. Oxygen tetrahedra or triangles share only corners with each other.

7. Some oxygen atoms are linked to only two network cations, and do not form further bonds with any other cations.

Figure 2.12 shows the glass structure as described by the first three rules, with a tetrahedron labelled MO_4. These rules were formulated for glasses made from simple oxides [100,106,145,153].

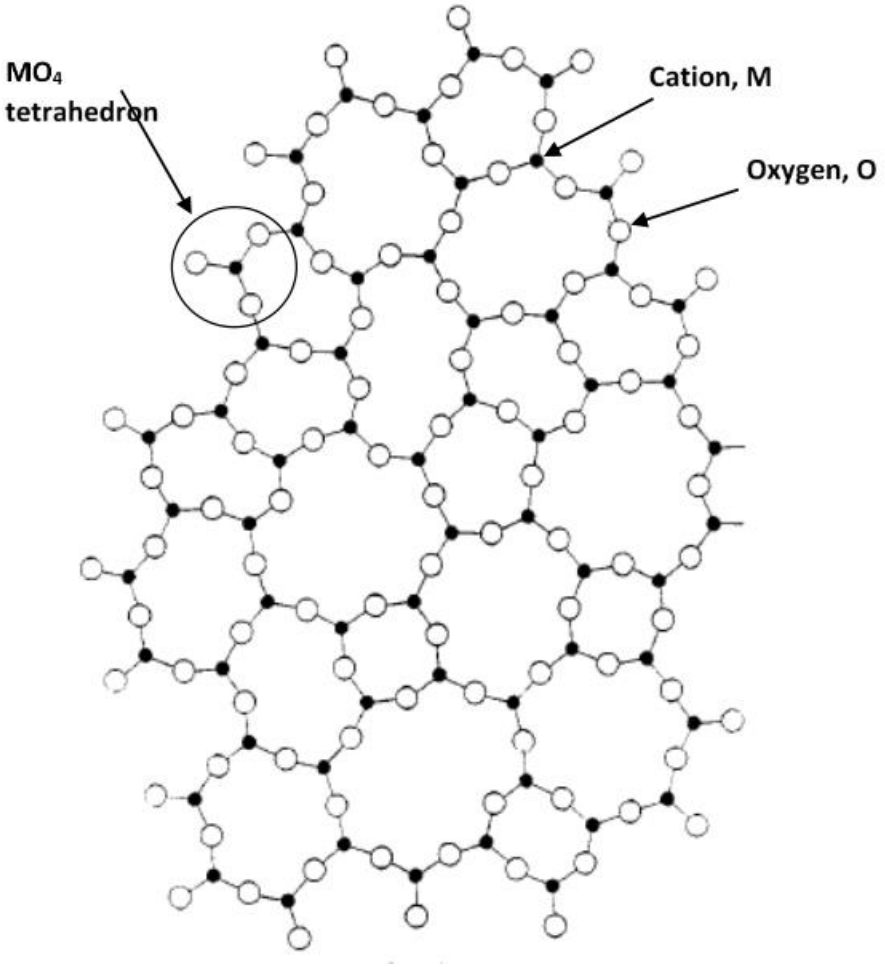

Figure 2. 12 Illustration of the structure of a simple oxide glass in two dimensions as proposed by Zachariasen. (Source:[145,153])

Zachariasen's rules described the condition required for formation of a glass but several theories and models to explain glass structure took these as their basis [106,154,155]. An extension to Zachariasen's theory was proposed by Warren in 1941 which is known as the Zachariasen-Warren model [154]. This model postulates that the alkali cations (can also be applied to alkaline earth cations) randomly occupy spaces within rings of tetrahedron in the glass, as illustrated by Figure 2.13.

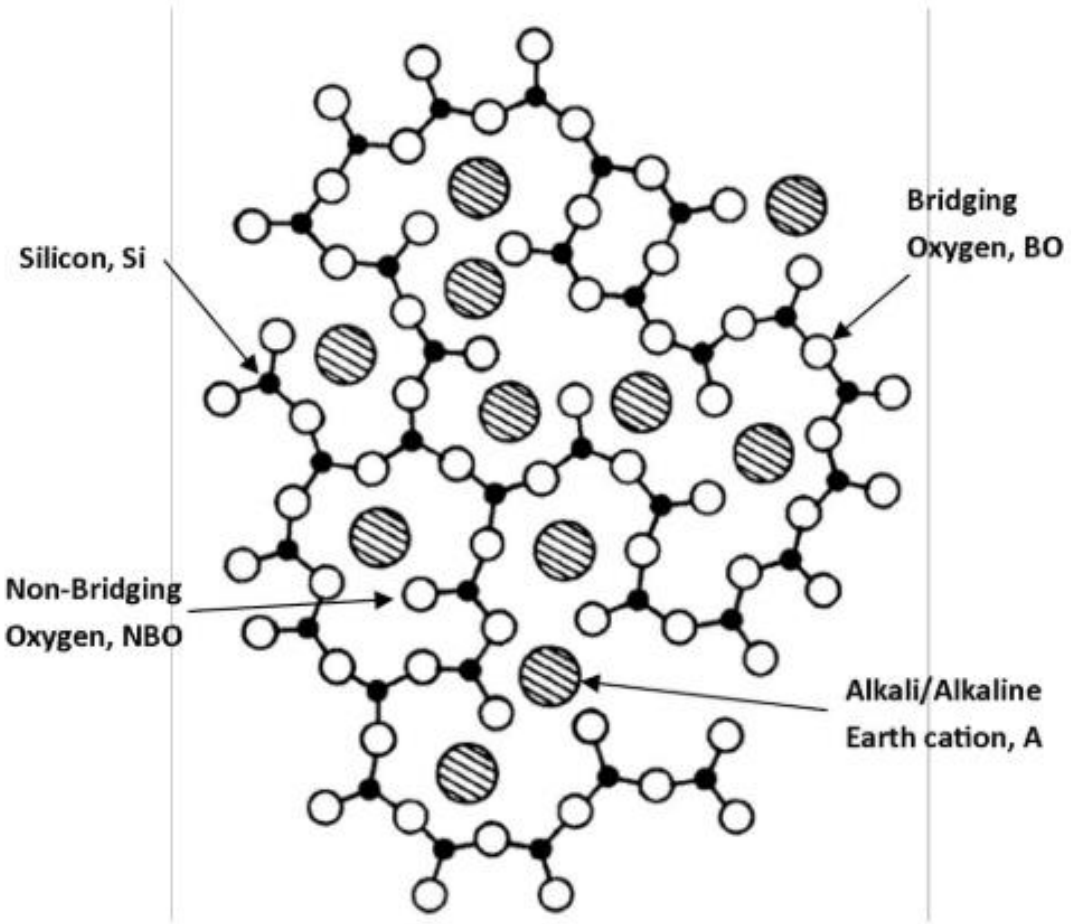

Figure 2. 13 Zachariasen-Warren model showing structure of soda-silica glass in two-dimensions. (Source:[154])

2.2.5 Structure of borate and borosilicate glasses

In silicate, alkali silicate, alkaline earth silicate and borosilicate glass systems, silicon is covalently bonded to oxygen atoms, forming tetrahedra. . Furthermore, oxygen atoms (bridging oxygens) are responsible for linking the structural units and thus define network polymerisation. The coordination of SiO_4 tetrahedral units can be represented as Q^n speciation or entities, where *n* defines the number of bridging oxygens. A network modifier breaks the silica network and thus creates non-bridging oxygens (NBOs). Charge compensation of a NBO is carried out by a cation by forming an ionic bond with it. A schematic of Q^n speciation is given in Figure 2.14.

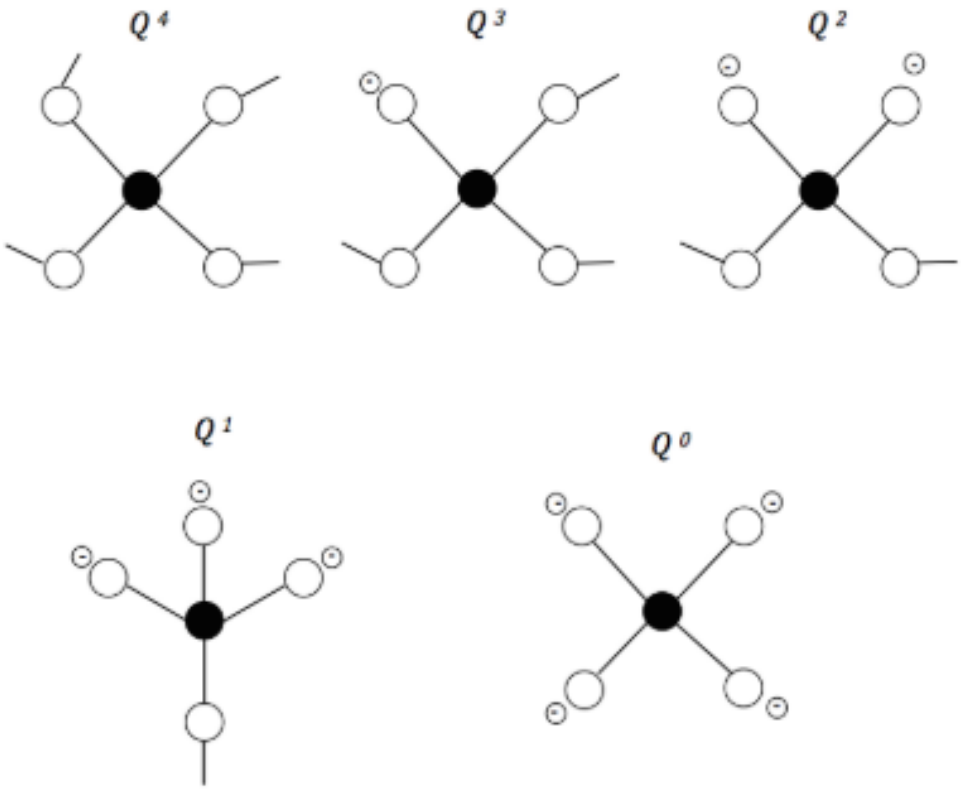

Figure 2. 14 Illustration of the Q^n speciation of SiO_4 tetrahedral structural units (Source: [156]).

The theories for alkali/alkaline earth silicate glasses cannot be directly applied to borate or borosilicate glasses, as silicon can exist only in the 4-coordinated state in these glass networks, whereas boron can exist both in trigonal (3-fold coordinated, BO_3 triangles) and tetrahedral (4-fold coordinated BO_4 tetrahedra) structural units within the glass network [100,106,145]. Before understanding the structure of borosilicate glasses, it is therefore helpful to briefly discuss the structure of borate glasses.

In 1962, [157] Krogh-Moe proposed a model which suggested that with the change in the content of alkali, boron changes its speciation through different boron groupings. These groupings are structural units (BO_3 and BO_4) and superstructural units (units which are made up of more than one BO_3 / BO_4 structural unit) with no internal degrees with respect to bond and torsion angles are the primary units of borate glasses [63,145]. This model predicts the structure of borate glasses through the relative proportions of boroxol (3 x 3-coordinated units, B_3O_6), tetraborate (6 x 3-coordinated and 2 x 4-coordinated units, B_8O_{16}) and diborate (2 x 3-coordinated and

2 x 4-coordinated units) superstructural units [106,145,157]. In Figure 2.15, f1- ilustrates symmetrical trigonal planar born unit with all BOs, f2 - symmetrical tetrahedral boron unit with all BOs and one alkali ion, f3 - non-symmetrical trigonal planar with one NBO and one alkali associated with it, f4- trigonal planar boron unit with two NBOs and two alkali ions and f5 illustrates trigonal planar boron unit with three NBOs and three alkali ions.

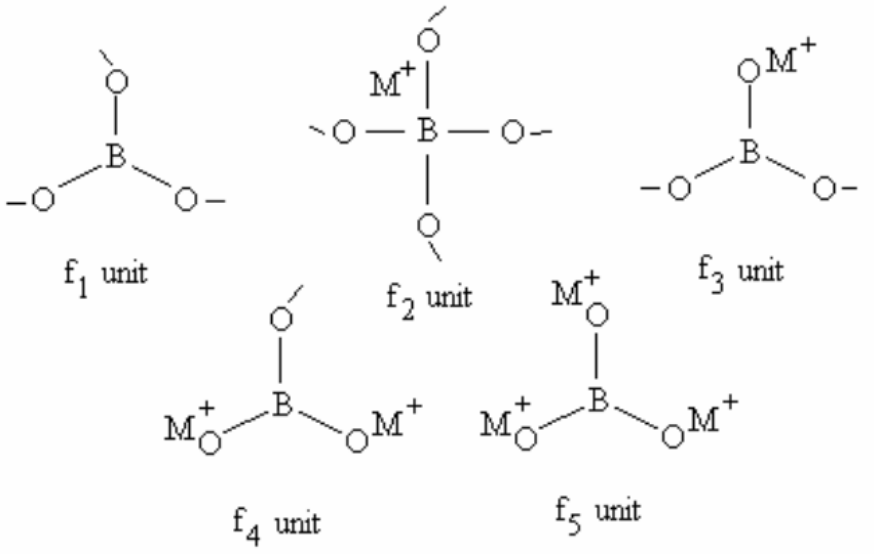

Figure 2. 15 Illustration of the possible borate units within an alkali borate and borosilicate glasses (Source: [158])

In a borosilicate glass, addition of network modifiers such as alkali cations can convert the network-forming symmetrical trigonal BO_3 structural units to BO_4 tetrahedral units, and a further addition of network modifier alkali cation converts BO_4 to non-symmetric BO_3 units with a cation associated with NBO [100]. This behaviour is called the 'boron-anomaly' [100,159]. In 1958, Silver and Bray [160] defined the concentration of BO_4 in terms of N_4 fraction (ratio of BO_4 to the total concentration or borate units) in the glass network. A N_4 maximum was observed by them at about~ 30mol% alkali oxide. Yun & Bray in 1978 and Dell *et al.,* in 1983 [161,162] proposed a model which suggested that for R<0.5, where R is the ratio of modifier content to the B_2O_3 content, preferably a conversion of BO_3 units to BO_4 happens. The model also demonstrated that an increase in alkali content up to R = 0.5 destroyed diborate groups. This modelled system was similar to a borate glass system where the silicate network is unaffected by the alkali ions. Figure 2.16 illustrates change in the N_4 fraction with respect to R for a sodium borosilicate glass [100,162]. The Dell-Bray

describes structural changes in borosilicate glass with the addition of alkali content in more detail in [162], however, a general consensus seems that alkali cations are more randomly distributed between the silicate and borate networks than what is assumed under the model [100,159–162].

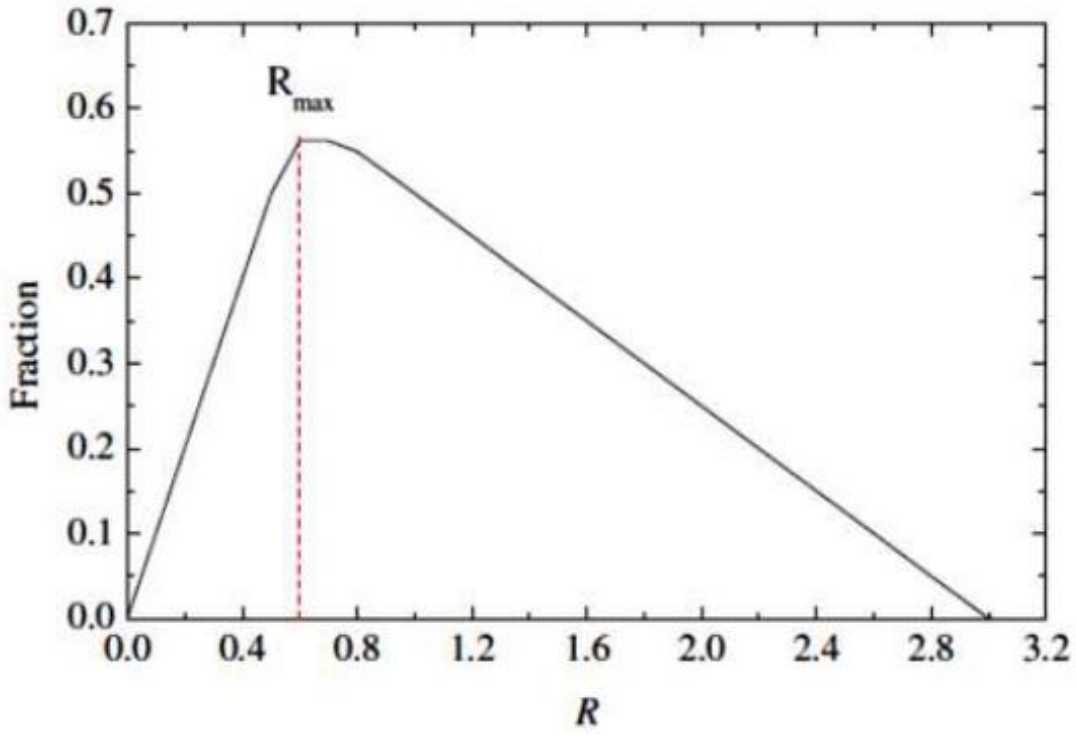

Figure 2. 16 Plot for N_4 versus R (ratio of modifier content to the B_2O_3 content) (Source:[162])

2.2.6 Structural defects in borosilicate glasses due to irradiation

Due to the presence of radionuclides as the sources of high activity in HLW, the immobilisation matrices (borosilicate glasses) will be subjected to radiation damage (explained in the following sections in detail). Borosilicate glasses will undergo structural changes upon self-irradiation [27,57]. These structural changes form defect centres, voids or disorders which can lead to volume changes, phase separation or gas (helium, oxygen) accumulation [27,57,163]. These macroscopic changes are initiated due to microstructural changes upon irradiation and may affect the long-term chemical durability of the glass [38,127,156,163–165]. DeNatale *et al.* [166] reported formation of oxygen bubbles and suggested mechanisms by which microstructural changes led to their formation in gamma irradiated alkali-silicate glasses. Peuget *et al.* [167] have reported changes in the density and mechanical properties following alpha irradiation in R7T7-type borosilicate glass. Delaye *et al.,*

[42] also reported an increase in the disorder and internal energy of a sodium borosilicate glass system when ballistic effects study was performed using molecular dynamics simulations (MD). In a recent study by Peuget *et al.,* [55] demonstrated that due to alpha self-irradiation (simulated in this study using ^{244}Cm doping and external irradiation using gold ions) ISG glass water alteration at high-reaction progress is impacted by glass structural damage. Some of the common radiation-induced electronic defects or paramagnetic defect centres formed in glasses upon irradiation in the literature [18,25,26,30–34,57,60,61,68,165,168–174], their definition and structure are presented as follows:

(1) Boron oxygen hole centre or BOHC (≡B-O• or =B-O•): This paramagnetic defect centre is defined as a hole trapped on a non-bridging oxygen in a trigonal borate unit or in a tetrahedral borate unit.
(2) E' centre (≡Si·): an electron trapped on a three-fold coordinated Si atoms.
(3) Peroxy radical (≡Si-O-O a hole trapped on a non-bridging oxygen or O_2^- bonded to one Si atom in the glass matrix.
(4) HC1 centre (≡Si-O• Na^+): a hole trapped on non-bridging oxygen bonded with three-fold Si tetrahedron near a Na cation

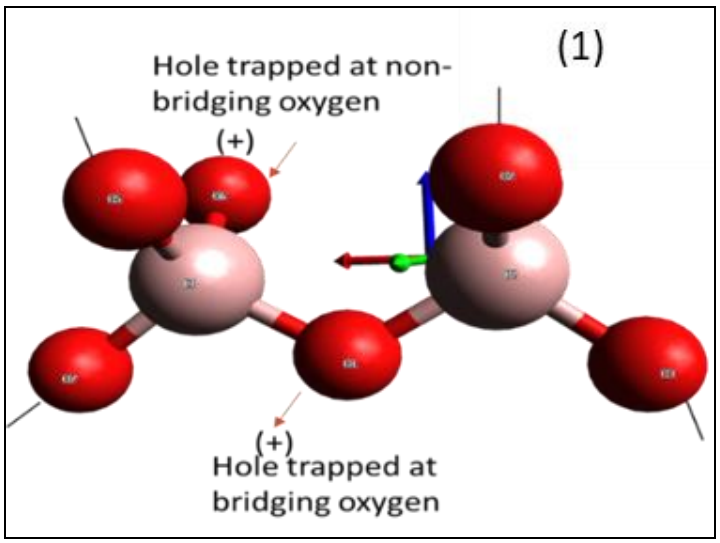

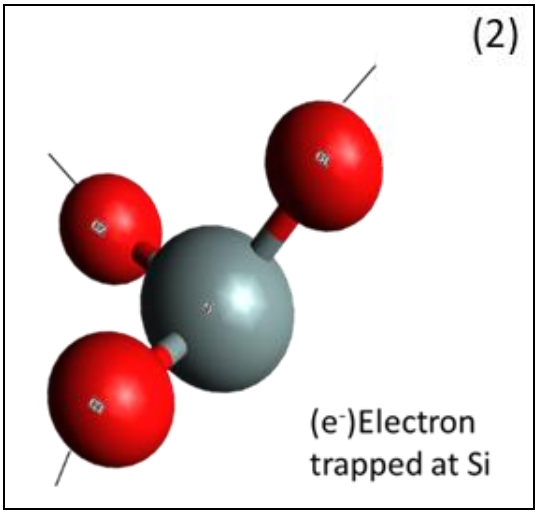

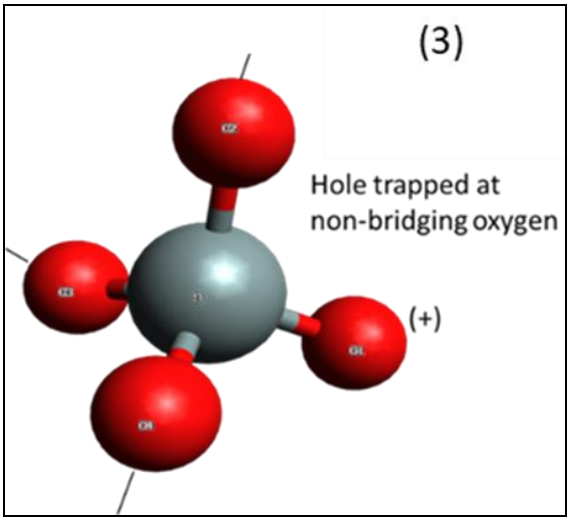

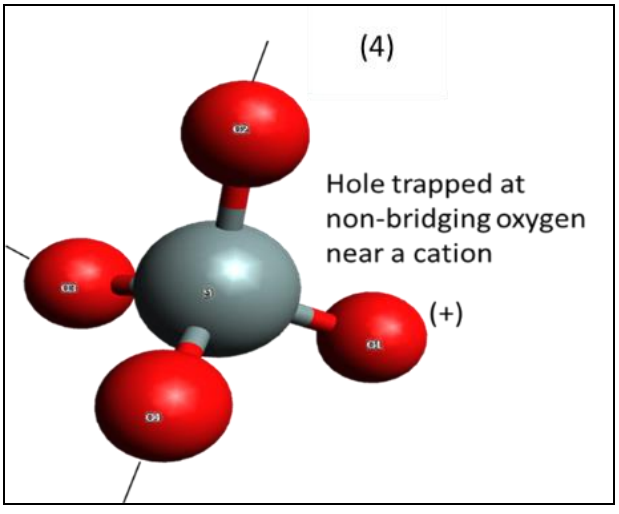

Figure 2. 17 Structure of 1) BOHC, 2) E' centres, 3) peroxy radicals, and 4) HC1 paramagnetic centres.

Weeks in 1956 [175], reported using magnetic susceptibility and and paramagnetic resonance measurements, electron and hole resonace in silica glass and natural andd synthetic crystals which were irradiated by neutrons at temperatures of 523 and 573 K. Frieble et al., [56] reported peroxy radical or O_2^- in high-purity synthetic silica using EPR spectroscopy at 110 K. Cases and Griscom [33] reported interstiitial O_2^- ions, O_2^- bonded to the glass network, and interstitial ozonide ions O_3^- by room temperature EPR study of γ-irradiated potassium silicate glasses. Griscom [169] reviewed EPR studied of around 25 years in glasses.

There are more defects which are less common in the literature, such as non-bridging oxygen hole centres (NBOHCs), and silicon base hole centres (SHCs) and aluminium based hole centres (AlOHCs) in alumino borosilicate glasses [25,27,142]. Different mechanisms through which they can form in glasses upon irradiation or how/whether they can have deteriorating effects on the performance in terms of durability and their thermal stability is dicussed in detail in the following section [28,32,165,173,174,176–178].

2.3 Self-irradiation effects in glasses for HLW immobilisation

This section discusses the sources of radiation and heat in HLW waste matrices and their effects, which may have undesirable (or, in some cases, desirable) effects on stability, structure, properties, and performance of HLW waste forms in a closed system. Both macroscopic and microscopic changes in terms of the long-term storage are discussed. This section also discusses and reviews the different methods, techniques, strategies, and current understanding to study the radiation effects in nuclear waste glasses at laboratory scale (smaller scale).

The interaction of radiation with glass results in the transfer of energy to the glass matrix. This transferred energy can appear as heat, some of it can appear as X-rays or light via atomic transitions (transfer of energy to the orbital electrons: ionization and excitation) and some can induce structural changes by interacting directly with the atoms and displacing them from their initial sites or changing their chemical state [39,119].

2.3.1 Radiation sources in HLW

The principal sources of radiation in a high-level nuclear waste glass are beta decay of short-lived fission products (e.g. ^{90}Sr,^{137}Cs) and alpha decay of long-lived minor

actinides (e.g. e.g. ^{237}Np, ^{241,243}Am, ^{244,245}Cm) [6,10,13,39,129] Beta-decay of fission products produce energetic beta particles, low energy recoil nuclei and gamma rays. The typical energies for beta particles vary in the range of a few hundred keV to about 1 MeV. Alpha-decay of actinides produces energetic alpha particles with energies that range between 4 to 5 MeV, energetic recoil nuclei with energies in the range between 80-120 keV and gamma rays [13,22] Fission fragments and neutrons can also be produced from spontaneous fission and alpha-neutron reactions in HLW; however, their production rates are very low [24].

2.3.2 Radiation effects

In HLW glass, radiation damage primarily occurs because of beta-decay of fission products and alpha-decay of actinides comprising HLW via transfer of energy to the atoms of the material. Thus, the different ways of energy transference on radiation-glass interactions can be categorised as follows [13,40]:

1. The loss of energy to electrons which results in excitation or ionization of the atoms.
2. The loss of energy directly to the atoms by elastic collisions, causing them to displace.
3. The nuclear reactions or transmutation of unstable parent nuclei into a different more stable nuclei [13,22]

Thus, the radiation effects can be categorised into two main categories: (i) ballistic, which is the displacement of atomic nuclei in the glass network upon elastic collisions, and (ii) electronic, which are ionisation and excitation processes, producing electron-hole pairs. The dominant mode of interaction and energy transfer for beta-gamma radiation is through excitation and ionisation [37]. There are only very few atomic displacements that are caused by beta interaction with the glass [24,37]. On the other hand, an alpha particle interacts mainly through ionisation and excitation, however, towards the end of its range, the energy loss is via elastic interaction resulting in about 400 atomic displacements [24]. Figure 2.18, top plot illustrates the cumulative absorbed dose over the storage time, a saturation of the absorbed dose can be seen for electronic interactions (beta and gamma) at around 100 years, whereas for nuclear interactions a saturation plateau begins at around 1000 years [24]. These saturation plateaus change and occur at higher doses and storage times for high waste loading (fission product and minor actinide increase) as

illustrated bottom plot in Figure 2.18. In addition to the energy transferred via ionisation, electronic excitation and ballistic processes, transmutation of fission products and actinides after emitting the radiation can also lead to the formation of different chemical elements and neutrons. These elements may also influence the chemistry, structure and thus properties of the glass (discussed later in this section) [13,21,22]

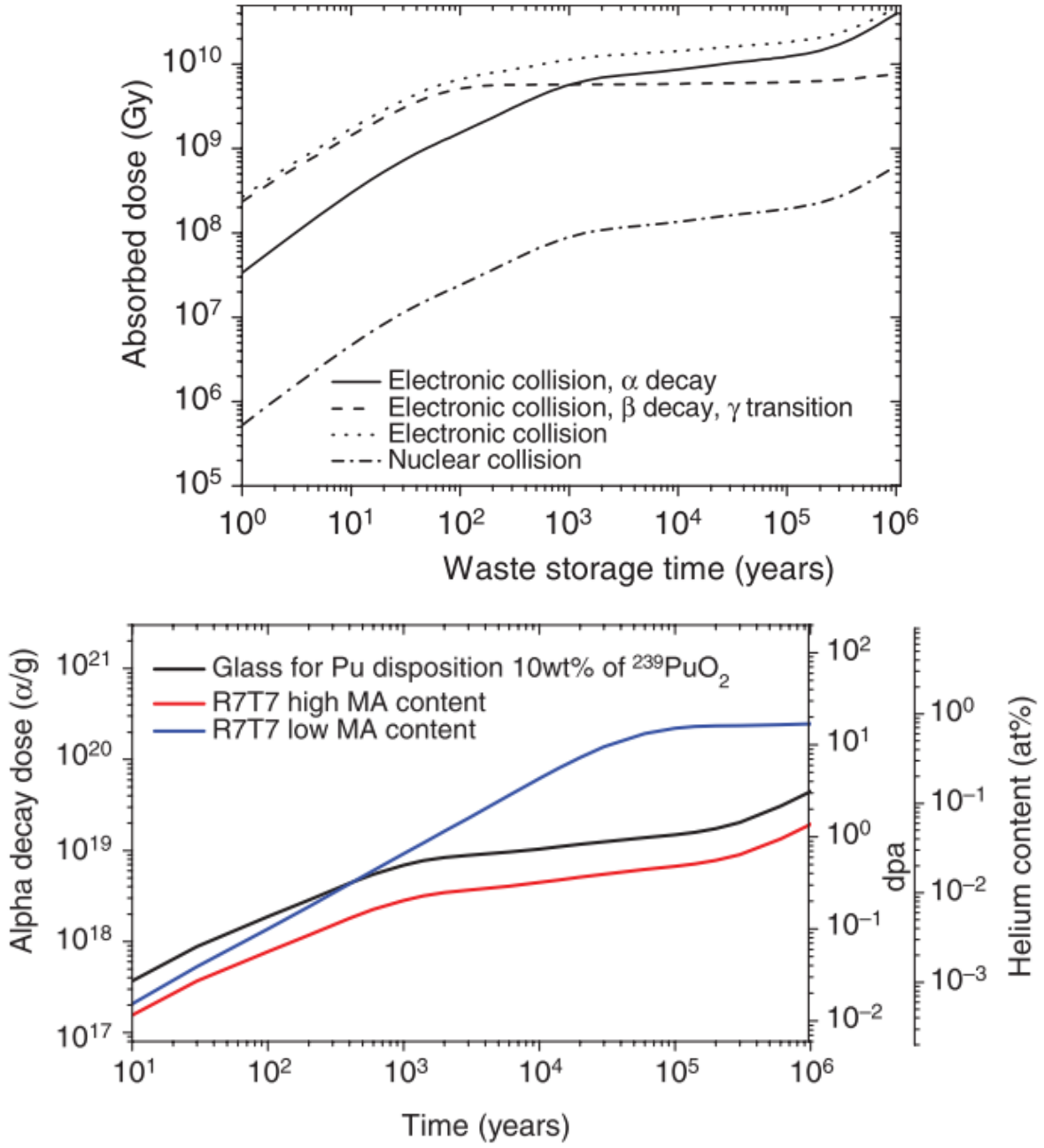

Figure 2. 18 Top, cumulative absorbed dose versus storage time for a typical R7T7 type nuclear and bottom figure illustrates the ballistic damage for different concentrations of minor actinides and fission products (Source:[24])

In the first few hundred years (~500 years) of geological disposal a glass waste form will experience heat generation, causing an increase in the temperature of the glass waste form (see Figure 2.19) and associated radiation damage (absorbed dose ~ 5 GGy) due to the decay of short-lived beta / gamma radionuclides present in HLW (e.g., $t_{1/2}$ for ^{137}Cs = 30.2 years and ^{90}Sr = 28.8 years).

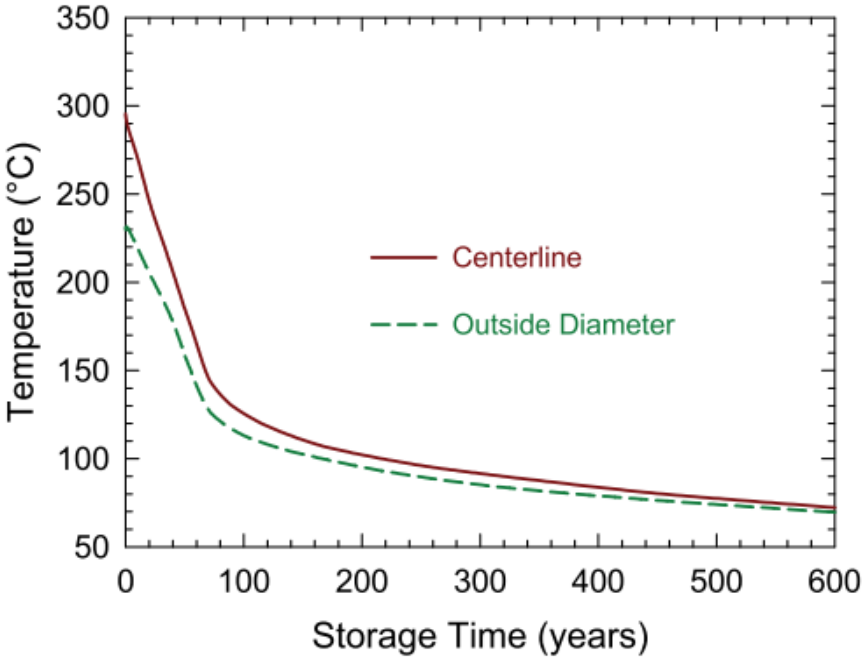

Figure 2.19 Temperature variation in a 0.32 m diameter canister containing HLW glass (25 wt% waste loading) from Savannah River Plant, USA, as a function of storage time (source:[13,22])

Thereafter, alpha emitting radionuclides (e.g. ^{240}Pu,^{241},^{243}Am, ^{237}Np and ^{244}Cm) due to their very long half-lives (~10-10^6 years, e.g. 2.15 million years for ^{237}Np) will be responsible for radiation damage (absorbed dose of tens of GGy in 1 million years of geological storage) in HLW glass waste forms (see Figure 2.18) [13,24,37,39,40,119,122].

2.3.3 Effects of electronic interactions in glass

2.3.3.1 Primary defects

During long-term storage, HLW borosilicate glass will accumulate a dose of the order of ~10^9 Gy from beta-irradiation. This dose can cause several structural changes as well as macroscopic changes to the glass. The primary changes reported in different borosilicate and other glasses are as follows:

i. **Irradiation-induced paramagnetic defects** – electronic or Coulombic interactions create electron and hole pairs by ionisation and excitation. The electronic structure and atomic arrangements after irradiation at the defect-site have been studied and reported by many authors using different spectroscopic and other complimentary techniques such as electron paramagnetic resonance spectroscopy and UV-Vis-nIR optical absorption spectroscopy [169,175,179,180]. Several radiation-induced paramagnetic defects in glasses are reported in the literature, such as boron oxygen hole centres or BOHCs ((=B-O•), peroxy radicals or PORs ((≡Si-O-O•), E' centres (≡Si^{-}), hole centres of the type HC1 (≡Si-O•Na^{+}) and others [28,32,165,173,174,176–178].

ii. **Reduction of rare earths and transition metals** – it has been suggested that transition metals and rare earths / lanthanides, when present in glasses in different redox states, can mitigate or prevent the formation of point defects and thus the associated structural transformations [30,59–66]. Electrons and hole pairs created by irradiation in the glass can be trapped by rare earth elements, e.g., Eu, Sm, Gd, Yb and transition metals, e.g. Fe, Mn, Cr present in the HLW glass as by-products of fission, corrosion during storage in waste tanks or as process additives during reprocessing [59,61,62,173].

iii. **Migration, segregation, and clustering of alkali and other charge compensators** – electronic interactions can result in significant structural changes in glasses subjected to irradiation [156,171,178]. These structural changes are attributed to the motion of network modifying cations such as Na ions [171]. It is reported by many authors[23] that low electron energies (from simulating electronic damage using TEM) can result in negative space energy build-up: this results in alkali migration in the direction of travel of the electrons. Non-bridging oxygens (NBOs) are created by modifier cations or by radiation. Electronic interactions can disrupt the ionic bonds between NBOs and modifier cations, resulting in the formation of alkali ions which can either act as electron trap or migrate under the influence of electric field produced locally due to electron space charge or by external irradiation [6,26,166,171,181]. These alkali-ions may undergo clustering [179]. Alkali

ions can also trap electrons and form elemental colloids via a phenomenon similar to that which has been observed in alkali halide crystals [26,39,182].

iv. **Glass network modification** – beta-gamma irradiations causing structural changes such as boron coordination changes, oxygen bubble formation, network polymerisation, have been reported by many authors in the literature [6,24,25,60,164,183,184]. Increase in the molecular oxygen content, increase in the network polymerisation, and densification due to decreases in the Si-O-Si bond angle is attributed to alkali migration and aggregation under beta-gamma irradiations. It has been suggested that aggregation of alkalis is related to cation mobility (Li>Na>K) [25,28,172,179,183].

v. **Phase separation** – glass-in-glass phase separation resulting in microscale heterogeneities such as segregated silicon-rich and boron-rich regions is also reported in the literature for beta doses exceeding 4 x 10^{11} Gy [20].

vi. **Macroscopic properties** – to the author's knowledge, only one study has reported a decrease in hardness and Young's modulus in borosilicate glass when irradiated with electrons in the range of 10^{7}-10^{9} Gy [185].

2.3.3.2 Thermal stability of radiation-induced defects

The waste form canister centreline cooling (CCC) temperature is a function of time and dimensions and depends on activity content and thermal history of the waste form [40]. CCC temperatures may range from 370 K – 570 K and may go as high as 670 K [37,41]. Thermal stability of glass waste forms is an important consideration and plays a crucial role in defining the long-term durability of the waste glass. Self-irradiation effects, mainly from the ionising sources during first few hundreds of years (~500 years), will cause structural changes which are associated with the creation of paramagnetic defects within the glass [33,165,171,186]. Since glass waste forms will experience temperature rises (radiogenic heating) due to the decay of short-lived radionuclides such as ^{137}Cs and ^{90}Sr, it is therefore important to study the effects of temperature on radiation-induced paramagnetic defects.

Boizot *et al.* [25] showed that when 5- and 6- oxide glasses are irradiated at 323 K and annealed at 573 K, peroxy radicals (POR's) and some other hole centres remained, whereas when irradiations were done at higher temperatures, BOHCs are still present at higher temperatures. They suggested that due to the increase in irradiation temperature some paramagnetic defects stabilise that are normally

annealed-out that those temperatures. They proposed that temperature during irradiation and annealing temperature for irradiated samples both play a crucial role in defining the stability of radiation-induced paramagnetic defects. Mohapatra *et al.* [57] investigated the temperature stability of gamma irradiation-induced paramagnetic defects in sodium barium borosilicate glass doped with 0.1 mol% Fe_2O_3 and reported that upon annealing at 500 K most of the EPR signals disappeared due to possible electron hole recombination. The only defect type which was stable after annealing was the peroxy radical or O_2^- radical on threefold-coordinated Si atoms, as illustrated in Figure 2.20.

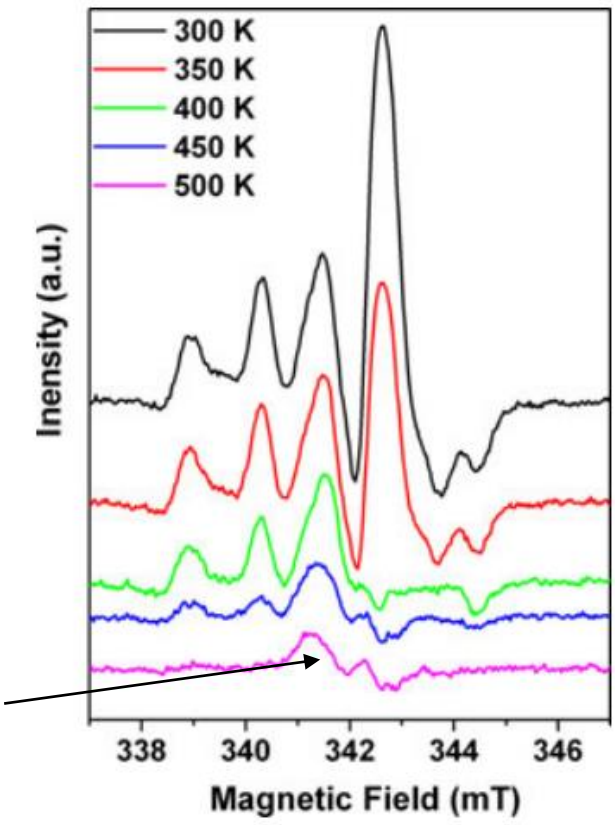

Figure 2. 20 EPR double derivative spectra for gamma irradiated sodium barium borosilicate glass doped with 0.1 mol% Fe and annealed at different temperatures. (Source: [57])

Griscom *et al.* [187] studied several boron containing HLW glass simulants irradiated with gamma or He^+ ion implantation and reported the production of BOHCs and complementary trapping of electrons on Ti^{4+} impurities. Upon annealing at about 573 K all of these trapped carriers were recombined, and this revealed the underlying PORs or O_2^- interstitial ions, as illustrated by Figure 2.21.

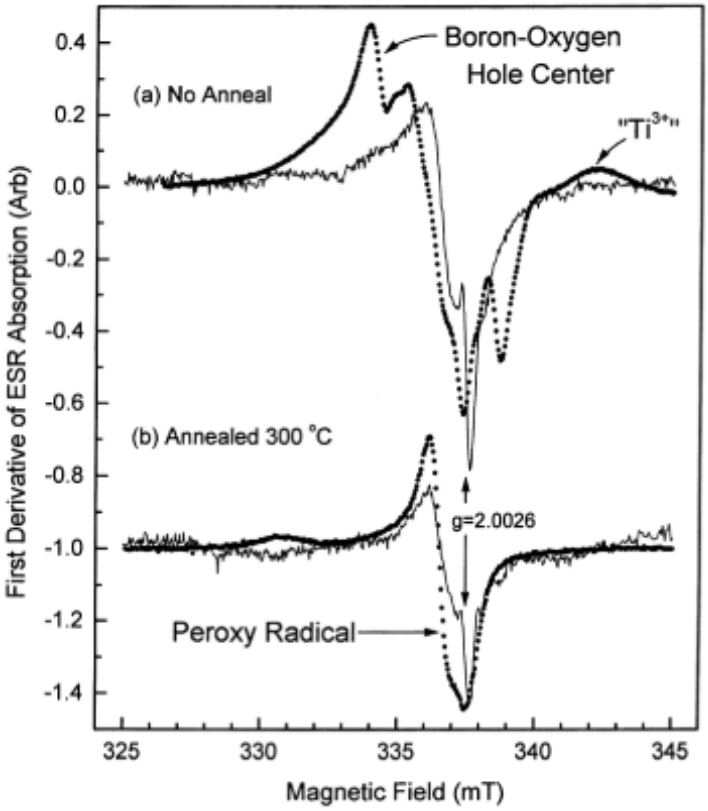

Figure 2. 21 X-band EPR spectra recorded at 77 K for HLW glass simulant CSG irradiated with gamma (dotted curves) and 160 KeV He^+ (thin solid curve) before and after annealing. (Source: [187])

2.3.3.3 Devitrification

Thermal stability of the glass matrix is crucial since glasses are metastable and under some conditions for crystal growth can partially convert to crystalline materials [188]. Each HLW storage canister is filled with molten waste glass by pouring several times. This causes a temperature difference between the centre and surface of the canister which retards the cooling rate which requires several hours for the glass to cool below the softening point. It can also generate cracking of the glass within the canister due to rapid (re)heating at the interfaces between different “pours” [189].

After pouring of a HLW glass, devitrification (formation of crystalline phases) can potentially occur due to the radiogenic heat retarding the cooling rate of the glass. The saturation plateau for beta-gamma cumulative dose in HLW glass occurs at about ~ 5 GGy in a typical nuclear waste matrix (this depends on the initial waste loading) [37]. This means that radiation damage due to beta-gamma interactions will occur at elevated temperatures (due to radiogenic heating) [37]. Devitrification could

be more probable near the glass transition temperature, as radiogenic heating provides additional energy to overcome any activation barrier. Weber *et al.,* [39], suggested that radiation-induced devitrification is less likely in geological repository conditions, however, precipitation of alkali metal crystals such as Na as discussed in Chapter 5, due to radiolytic decomposition, can occur [39]. Glass crystallisation begins with crystal nucleation due to the presence of nucleation sites such as insoluble particles (e.g., platinoids) or pre-existing surfaces such as melter walls and glass melt and atmosphere interface. Crystal nucleation is followed by subsequent crystal growth [118,164]. Radiation-induced heating of the glass wasteform can produce internal stresses, the magnitude of which depends on the thermal conductivity and thermal expansion. These residual stresses can cause internal cracking of the glass waste form if they are high enough. The difference in the thermal expansion properties of crystalline phases and glass may lead to the growth of cracks. The internal cracking can lead to a higher surface area and increased rates of corrosion and decrease in chemical durability [94,102].

2.3.3.4 Bubble formation

Electronic effects can lead to the formation of molecular oxygen, which can also form bubbles. As discussed previously, migration of sodium ions can result in the formation of molecular oxygen [163,190]. This creates a region rich in molecular oxygen but depleted in sodium. Molecular oxygen formation is inhibited by the mixed-alkali effect [163]. It has been reported that there is a threshold electron flux for a given temperature, below which bubbles will not form. That study suggested that simultaneous sample heating and irradiation is required for oxygen bubble formation in nuclear waste glasses [170].

2.3.4 Effects of nuclear interactions in glasses

Alpha decay of actinides produces alpha particles within an energy range of 4.5 to 5.5 MeV [24,38], energetic recoil nuclei in the energy range 80 to 120 keV and some gamma rays which are transitional by-products of alpha decay. Alpha particles predominantly lose their energy via electronic interactions as beta-particles, as discussed in the previous section. Electronic or Coulombic interactions of alpha particles within glasses cause similar primary defects to beta-gamma particles, such as point-defects, modification of boron coordination, changes in the glass network, or changes in the density, hardness, and Young's modulus, as previously discussed in

Section 2.3.3.1. All of these microstructural and macroscopic changes are highly dependent on the glass [7,15,43,55,185,191] On the other hand, recoil nuclei from alpha-decay interact via elastic collisions with glass atoms, causing them to displace from their original sites [7]. Recoil nuclei possessing low energy and high mass induce maximum damage in terms of atomic displacements per atom, in comparison to alpha particles and beta-gamma irradiation [7].

Several approaches and methods have been adopted to study the effects of alpha decay from minor actinides and Pu in waste glasses during disposal. These mainly consist of spectroscopic techniques including MAS-NMR, Raman, EPR, X-ray absorption (XAS) and optical absorption spectroscopy [23]. The methods used to simulate the damage from alpha decay are as follows:

-Simulating the damaging effects of alpha decay (both alpha particles and recoil nuclei) by doping glasses with short lived minor actinides such as ^{244}Cm, ^{238}Pu. This is the most representative technique but with disadvantage of fabricating and characterising radionuclide doped glasses [13,30,39,93,127,192]. These studies have shown that there is an increase in the stored energy (accumulation of an excess of latent energy due to build-up of defects and local changes in the glass structure) with the increasing dose, that saturates at values of 90-140 J/g at doses of 10^{17}-10^{18} α/g (compositional dependent). Peuget *et al.* [127] reported up to 30% decrease in glass hardness and modulus of elasticity and about 60% increase in fracture toughness in the R7T7 when irradiated with alpha dose of 2 x10^{18} α/g. In another report from Peuget *et al.,* [167] the saturation of density and mechanical properties was seen for integrating dose of 4 x 10^{18} α/g in the French SON68 glass. It was also reported in [38,127] that density change and swelling evolution occurs due to combined effects of recoil nuclei and alpha particles. There are discrepancies [24,163] in the reports presenting results related to formation of He bubbles in the glasses as they are believed to be dependent on helium content, irradiation temperature and homogeneities up to nm level.

- Simulating the damaging effects of alpha decay by irradiation with light and heavy ions. This enables simulation of the radiation effects of electronic and nuclear stopping separately and individually. This is done in particle accelerators or using electron beam facilities (TEM) [36,128,172,185,186,190,193–195]. It can simulate

the dose of many years in a short time (in one or several days). Multi-ion beam facilities have enabled the study of synergistic effects of alpha and recoil nuclei. Multi-ion beam studies have shown that while nuclear collisions are mainly responsible for the damage, electronic interactions cannot be neglected; they can partially repair the damage created by heavy ions [36,45].

- Glasses are irradiated in research reactors using ^{10}B (n, α)^{7}Li reactions. This is another method to simulate the damage of electronic and nuclear stopping from alpha decay in the glass. This method has shown very high generation of He content (~0.5 at%) along with similar macroscopic changes as discussed previously, in the glass [24,167,196,197].

- Molecular dynamics (MD) simulation techniques have been used to model the damage from alpha decays. MD simulation studies on simple borosilicate glass systems have reported volume increase, Young's modulus decrease, change in the coordination, and network depolymerisation when subjected to displacement cascades. These changes saturate after 4 x 10^{20} keV cm^{-3} (30 MGy) [42,43,167,198].

2.3.5 Effects of radiation on glass corrosion

It has been estimated that underground water may breach the waste package and come into contact with HLW glass after a few thousand years in a geological repository (exact time is unknown) [7,199]. Therefore, it becomes imperative to study the alteration mechanisms of the glass in a complex environment, especially in an aqueous medium, which will be present in a geological disposal repository, to demonstrate the safe disposal of HLW waste packages. Since water will be the main medium for transport of radionuclides to the biosphere, numerous studies have been conducted since the 1980s, to understand the alteration mechanisms of glass in aqueous media [7,199,200]. Different models have been proposed and studied to study the glass corrosion during their interaction with water. The basic mechanisms and kinetics behind glass corrosion are reasonably well established. However, there are only a few studies which have considered the impacts of self-irradiation on the corrosion of the glass. Mougnaud *et al.* [201] studied two simple borosilicate glasses irradiated with Au ions (0.5 to 3.5 MeV) and reported a substantial increase in the alteration layer of the glass sample which was pre-irradiated. Another recent study by Mir *et al.* [52] highlighted the importance of glass composition and radiation

damage's crucial role in the microstructural evolution of glasses during corrosion. They showed the formation of mesoporous C-S-H (calcium-silica-hydrate) gels in Ca-bearing borosilicate glasses and a microporous microstructure in Al-bearing glasses after corrosion period of 21 years. The porous corroded glasses were healed when they were irradiated with heavy ions using in-situ TEM. The healing effects of ballistic collisions by heavy ions to simulate the damage of recoil nuclei turned corroded glasses to glasses with pore-free homogenous glasses [52].

2.4 Summary

Structural evolution under self-irradiation is less well understood in glasses for HLW waste immobilisation and yet of primary importance. This study aims to contribute to developing an enhanced fundamental understanding of the nature of radiation-induced defects, the mechanisms of their creations, abundance, thermal stability and how / whether they differ with different glass compositions, dopants, and wastes. Therefore, this study investigates radiation (gamma and alpha) effects in simple, Fe_2O_3 (multivalent ion) doped, and non-active HLW waste loaded representative glasses using a multi-spectroscopic approach including EPR, UV-Vis-nIR optical absorption and Raman spectroscopies.

Chapter 3. Experimental Procedures

3.1 Introduction

This chapter presents detailed information about the types of glasses synthesised with their chemical compositions, methods of synthesis and their melting conditions. A detailed background of all the characterisation techniques employed to study the different glass systems pre-and-post irradiation, their principles, and the sample preparation for each characterisation technique is also presented. A brief record of the different irradiation methods employed, and the experiments carried out, is given towards the end of this chapter.

3.1.1 Glass categories

This PhD study is focussed on mainly three categories of glasses which are explained in the following sections.

3.1.1.1 Base or simple glasses

The first group of glasses synthesised for this study are called ‘simple’ or ‘base’ glasses and are henceforward referred to as simple or base glasses interchangeably. The first glass in this group is a sodium barium borosilicate (4-oxide) glass, Na_2O-BaO-B_2O_3-SiO_2 (NaBaBSi) and it is used as a glass matrix for Indian high-level waste immobilisation. The modification of commonly used sodium borosilicate glass matrices by the addition of barium was carried out to enhance the solubility of sulphate bearing Indian high-level nuclear waste [136,137,202]. The sodium barium borosilicate matrix has been used to immobilise Indian sulphate-bearing high-level waste at the Waste Immobilisation Plant, Bhabha Atomic Research Centre, Trombay [137].

The second glass is called as ‘MW’ (Mixture Windscale). This is a sodium lithium (mixed-alkali) borosilicate 4-oxide, Li_2O-Na_2O-B_2O_3-SiO_2 (LiNaBSi) glass. Mixed alkali compositions were developed in UK for maximising the waste loading and to optimise the process requirements such as ease of manufacture and viscosity whilst meeting the chemical durability requirements. The MW glass composition was selected for vitrification of highly active UK liquor (HAL) [129] at the Sellafield site.

The third glass is the International Simple Glass [23], which is a reference glass proposed by six nations addressing the key scientific problems particularly related to

glass dissolution and durability. This glass is based on SON68, which is the inactive version of French R7T7 glass [23].

The fourth glass in the group of simple glasses is SON68 which is the inactive version of French R7T7 glass, and it is one of the widely most studied radioactive waste glasses for radiation stability as well as chemical durability [24]. Both ISG and SON68 are inactive version of R7T7 but they both have slightly different compositions and therefore we decided to study both of them.

The fifth and final glass in this group is the modified version of MW glass containing Ca and Zn and it is called as MWCZ/CaZn [132,203–205]. This glass was designed to immobilise POCO (Post Operational Clean Out) wastes. The waste streams from POCO contain significant quantities of MoO_3 which forms a non-durable or soluble phase with alkali, such as Na_2MoO_4. The formation of this alkali soluble phase also known as yellow phase is suppressed by addition of Ca as it forms $CaMoO_4$ (powellite) which is a more durable crystalline phase [132,203,204].

3.1.1.2 Base glasses doped with Fe_2O_3 (oxidised and reduced)

The second group of glasses is Fe_2O_3 doped glasses. NaBaBSi and LiNaBSi glasses were loaded with 0.19, 0.99, 4.76 and 9.09 mol% Fe_2O_3. Iron doped glasses were synthesised in the oxidising conditions and characterised to study the effects of iron on irradiation-induced defects. This study follows previous work done by Bingham and co-workers [63,206] which indicates the potential mitigation or even self-healing of radiation-induced defects in glasses doped with Fe or other multivalent elements. These glasses were also synthesised in reducing melting conditions using graphite (≥99%) batch additions as a reducing agent.

3.1.1.3 Non-active waste simulated glasses

The third and final category consists of glasses that were doped with inactive simulated HLW wastes or surrogate waste components. NaBaBSi, LiNaBSi and SON68 base glasses were doped with simulated non-active wastes. The composition for NaBaBSi with ~18 wt% waste loading adapted from [207], LiNaBSi with ~25 wt% adapted from [63] and SON68 with ~14 wt% waste loading adapted from [128] is given in Table 3.5. The surrogates/simulants non-active waste components for HLW from India, UK and France are given in Table 3.6. To simulate oxides in a glass batch (see Section 3.2.1) mainly carbonates were used (Table 3.6)

as surrogates/simulants since they are relatively cheap, easily available, mostly less hygroscopic and can be handled in a laboratory settings [138,142] Some of the oxides were used as it is (in the oxides form). The decomposition of a carbonate forms oxide and carbon dioxide gas is evaporated. To make sure we get the desired oxide quantity from raw materials we take in to account the batch or gravimetric factor. Batch factors or gravimetric factor [208] is also given in Table 3.6. It is defined as follows:

G_f = Molar weight (raw material)/ Molar weight (oxide)

The choice of surrogates/simulants is based on electronegativity, valence and the ion radii for a given coordination [209]. Keeping these in mind and availability, WO_3 was used as a surrogate for UO_3, CeO_2 for Pr_6O_{11} and Al_2O_3 was used for Y_2O_3.

3.2 Glass synthesis

3.2.1 Batch preparation

The Indian glass, **Na_2O-BaO-B_2O_3-SiO_2 (NaBaBSi)** was produced using high purity (≥99.9%) sand (SiO_2), sodium carbonate (Na_2CO_3), procured from Better Equipped with >99.9%, barium carbonate ($BaCO_3$) procured from Alfa Aesar with purity > 99.9%, and boric acid (H_3BO_3) procured from Better Equipped with purity > 99.9%. The composition for this glass was adopted from Mishra *et al.* [137].

The UK-MW glass, **Li_2O-Na_2O-B_2O_3-SiO_2 (LiNaBSi)** was produced using high purity (≥99.9%) sand (SiO_2), sodium carbonate (Na_2CO_3), lithium carbonate (Li_2CO_3) procured from Better Equipped with purity > 99.9%, and boric acid (H_3BO_3). The composition for this glass is adopted from Harrison [129].

The **ISG** glass was synthesised using high purity (≥99.9%) sand (SiO_2), sodium carbonate (Na_2CO_3), boric acid (H_3BO_3), aluminium hydroxide ($Al(OH)_3$) procured from Better Equipped with purity > 99.9%, calcium carbonate ($CaCO_3$) procured from Better Equipped with purity > 99.9%, and zirconium dioxide (ZrO_2) procured from Sigma Aldrich with purity > 99.9% metal basis. The composition was adopted from Karakurt *et al.* 2016 [128].

The French **SON68** glass was synthesised using high purity (≥99.9%) sand (SiO_2), sodium carbonate (Na_2CO_3), lithium carbonate (Li_2CO_3), boric acid (H_3BO_3), aluminium hydroxide ($Al(OH)_3$), calcium carbonate ($CaCO_3$), zirconium dioxide

(ZrO_2), and zinc oxide (ZnO) procured from Sigma Aldrich with purity > 99.9%. The composition was adopted from Marples [93].

The UK-MW glass modified with Ca and Zn, or **MWCZ**, was produced using high purity (≥99.9%) sand (SiO_2), sodium carbonate (Na_2CO_3), lithium carbonate (Li_2CO_3), boric acid (H_3BO_3), calcium carbonate ($CaCO_3$), and zinc oxide (ZnO). The composition for this glass is adopted from Cassingham *et al.* [203].

Iron oxide (Fe_2O_3) procured from Alfa Aesar with purity >99% metals basis, was used for the Fe doped Indian and UK-MW glass. To synthesise reduced Fe samples, graphite was used. The glass compositions for the reduced Fe_2O_3 doped are given in Appendix A.

All the raw materials/chemicals were dried in an electric heating oven at 110 ˚C for at least 24 hours, except H_3BO_3 as it has a decomposition temperature less than 100 ˚C. Appropriate amounts of chemicals based on the batch calculations to make a glass batch of 180 g were weighed out using a 3-decimal place balance into zip-lock bags. Zip-lock bags were then sealed and mixed thoroughly to attain a good mixture for melting. Melting was done in an electric furnace using melt-anneal-pour method in recrystallised alumina crucibles. The melting parameters for all the glass samples are given in the following Table 3.1.

Table 3. 1. Melting parameters for all the glass samples

Glass	Melting Conditions	Annealing Conditions
NaBaBSi	RT to 1050˚C at 3 ˚C/min, dwell 2 hours	2 hrs at 470 ˚C, 470 ˚C to RT at 1 ˚C/min
LiNaBSi	RT to 1150 ˚C at 4 ˚C/min, dwell 2 hours	2 hrs at 480 ˚C, 480 ˚C to RT at 1 ˚C/min
ISG	RT to 1350 ˚C at 4 ˚C/min, dwell 3 hours	2 hrs at 480 ˚C, 480 ˚C to RT at 1 ˚C/min
SON68	RT to 1080 ˚C at 3 ˚C/min, dwell 2 hours	2 hrs at 480 ˚C, 480 ˚C to RT at 1 ˚C/min
MWCZ	RT to 1150 ˚C at 4 ˚C/min, dwell 2 hours	2 hrs at 480 ˚C, 480 ˚C to RT at 1 ˚C/min
NaBaBSi + Fe_2O_3	RT to 1050 ˚C at 3 ˚C/min, dwell 2 hours	2 hrs at 470 ˚C, 480 ˚C to RT at 1 ˚C/min
LiNaBSi + Fe_2O_3	RT to 1150 ˚C at 4 ˚C/min, dwell 2 hours	2 hrs at 480 ˚C, 480 ˚C to RT at 1 ˚C/min
NaBaBSi waste loaded	RT to 1050˚C at 3 ˚C/min, dwell 2 hours	2 hrs at 470 ˚C, 470 ˚C to RT at 1 ˚C/min
LiNaBSi waste loaded	RT to 1150 ˚C at 4 ˚C/min, dwell 2 hours	2 hrs at 480 ˚C, 480 ˚C to RT at 1 ˚C/min
SON68 waste loaded	RT to 1080 ˚C at 3 ˚C/min, dwell 2 hours	2 hrs at 480 ˚C, 480 ˚C to RT at 1 ˚C/min

3.2.2 Glass compositions

Table 3. 2. Nominal composition (mol%) of Indian, MW, ISG (International Simple Glass) and SON68 base glasses

Oxide	Indian	MW	ISG	SON68	MW-Ca/Zn
SiO_2	41.67	60.50	60.12	56.37	57.13
B_2O_3	20.83	18.50	16.01	14.97	18.90
Na_2O	21.88	10.49	12.62	11.89	11.33
Al_2O_3	-	-	3.82	3.57	-
CaO	-	-	5.71	5.31	2.11
BaO	15.62	-	-	-	-
Li_2O	-	10.50	-	4.98	5.97
ZrO_2	-	-	1.70	0.60	-
ZnO	-	-	-	2.28	4.533
Total	100	100	100	100	100

Table 3. 3. Nominal composition (mol%) of NaBaBSi base glass loaded with 0, 0.19, 0.99, 4.76, and 9.09 mol% Fe_2O_3

Oxide	NaBaBSi base glass + Fe_2O_3				
SiO_2	41.67	41.58	41.25	39.68	37.88
B_2O_3	20.83	20.78	20.62	19.38	18.93
Na_2O	21.88	21.83	21.66	20.83	19.89
BaO	15.62	15.58	15.46	14.87	14.20
Fe_2O_3	0	0.19	0.99	4.76	9.09
Total	100	99.96	99.98	99.52	99.99

Table 3. 4. Nominal composition (mol%) of LiNaBSi base glass loaded with 0, 0.19, 0.99, 4.76, and 9.09 mol% Fe_2O_3

Oxide	LiNaBSi base glass + Fe_2O_3				
SiO_2	60.50	60.38	59.90	57.62	55.00
B_2O_3	18.50	18.46	18.31	17.62	16.81
Na_2O	10.49	10.47	10.39	9.99	9.54
Li_2O	10.50	10.47	10.39	10.00	9.54
Fe_2O_3	0	0.19	0.99	4.76	9.09
Total	99.99	99.97	99.98	99.99	99.98

Table 3. 5 Nominal compositions in mol% for NaBaBSi (18 wt% waste loaded), LiNaBSi (25 wt% waste loaded) and SON68 (14 wt% waste loaded) glasses loaded with HLW simulated waste.

Oxide (mol%)	Doped NaBaBSi	Doped LiNaBSi	Doped SON68
SiO_2	35.20	53.65	53.11
B_2O_3	17.59	16.44	14.13
Na_2O	18.48	9.36	11.47
Li_2O	-	9.28	4.63
BaO	13.19	0.13	0.28
CaO	-	-	5.05
ZnO	-	-	2.16
Fe_2O_3	0.34	0.50	1.32
Cr_2O_3	0.09	0.11	0.24
Na_2O	11.32	-	-
Gd_2O_3	-	0.64	-
K_2O	0.22	-	-
MnO	0.61	-	-
WO_3	2.52	-	-
SrO	0.02	0.44	0.23
ZrO_2	0.003	1.72	1.55
MoO_3	0.11	1.19	0.86
Cs_2O	-	-	0.27
TeO_2	0.01	0.15	0.10
BaO	0.03	-	-
La_2O_3	0.01	0.20	0.19
Y_2O_3	-	-	0.06
CeO_2	0.08	-	-
CeO_2	0.002	0.82	-
Nd_2O_3	0.03	0.94	0.19
Pr_2O_3	-	-	0.09
Sm_2O_3	0.01	-	-
Ag_2O	-	-	0.009
CdO	-	-	0.01
Al_2O_3	0.03	1.31	3.41
MgO	-	2.85	-
NiO	-	0.14	0.40
P_2O_5	-	0.05	0.14
SnO	-	-	0.009
Total	99.895	99.92	99.908

Table 3. 6 Simulants/surrogates (non-active) for Indian (NaBaBSi), UK (LiNaBSi) and French (SON68) HLW.

Oxide	Non-active Simulant Indian HLW	Non-active Simulant UK HLW	Non-active Simulant French HLW	Weighing /batch factor
SiO_2	SiO_2	SiO_2	SiO_2	1
B_2O_3	H_3BO_3	H_3BO_3	H_3BO_3	1
Na_2O	Na_2CO_3	Na_2CO_3	Na_2CO_3	1.7101
Li_2O		Li_2CO_3	Li_2CO_3	2.473
BaO	$BaCO_3$	$BaCO_3$	$BaCO_3$	1.287
CaO			$CaCO_3$	1.7848
ZnO			ZnO	1
Fe_2O_3	Fe_2O_3	Fe_2O_3	Fe_2O_3	1
Cr_2O_3	Cr_2O_3	Cr_2O_3	Cr_2O_3	1
Na_2O	Na_2CO_3		Na_2CO_3	1.7101
Gd_2O_3		Gd_2O_3		1
K_2O	K_2CO_3		KH_2PO_4	1.917
MnO	MnO			1
UO_3	WO_3			1
SrO	$SrCO_3$	$SrCO_3$	$SrCO_3$	1.4247
ZrO_2	ZrO_2	ZrO_2	ZrO_2	1
MoO_3	MoO_3	MoO_3	MoO_3	1
Cs_2O			Cs_2CO_3	1.1561
TeO_2	TeO_2	TeO_2	TeO_2	1
BaO	$BaCO_3$			1.287
La_2O_3	La_2O_3	La_2O_3	La_2O_3	1
Y_2O_3	$Al(OH)_3$			1
CeO_2	CeO_2	CeO_2		1
CeO_2				1
Nd_2O_3	Nd_2O_3	Nd_2O_3	Nd_2O_3	1
Pr6O11	CeO_2			1
Sm_2O_3	Sm_2O_3			1
Ag_2O			Ag_2O	1
CdO				
Al_2O_3		$Al(OH)_3$	$Al(OH)_3$	1..5301
MgO		$MgCO_3$		2.0919
NiO		NiO	NiO	1
P_2O_5		$NH_4H_2PO_4$		1.6207
SnO			SnO_2	1

3.2.3 Glass casting and annealing

Glasses were cast in the form of discs by pouring the melts into a pre-heated circular iron mould on a pre-heated steel plate using pouring tongs, Figure 3.1. The mould was removed, and glasses were then carefully transferred to annealing furnaces at the appropriate annealing temperatures as given in Table 3.1.

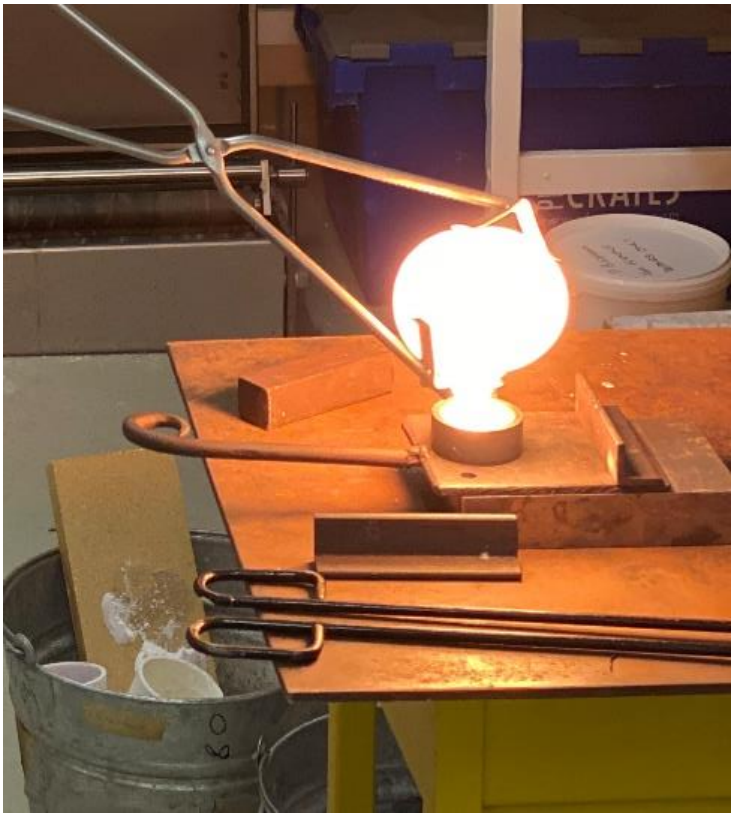

Figure 3. 1 Glass melt pouring and casting in disc-shaped mould onto a pre-heated steel plate (image captured at Glass and Ceramics Lab, Sheffield Hallam University)

3.3 Glass characterisation

3.3.1 X-ray Diffractometry (XRD): background

X-ray diffraction is a phenomenon in which X-rays (electromagnetic waves) are diffracted from regularly spaced atoms in a crystal or lattice planes when the wavelength of the X-rays is of the same order as the distance between two lattice planes [100,210]. Constructive interference of the rays after scattering from the lattice planes is produced when Bragg's condition is satisfied, which is given by:

$$n\lambda = 2d\,sin\theta \qquad \text{(Equation 3.1)}$$

where λ is the wavelength of the incident X-rays, d is the interplanar spacing, θ is the angle of incidence of X-rays and n is the order of reflection. This technique is less useful for amorphous materials since they do not have a regular periodic arrangement as in crystals. Thus, XRD patterns for amorphous materials cannot provide detailed information about their molecular structure but it indicates whether they are X-ray amorphous or whether there are any crystalline phases present [211]. If there are any crystalline phases present there will be sharp peaks present in XRD pattern.Figure 3.2 shows the image of a X-pert PRO X-ray diffractometer. XRD measurements were taken using an X-pert PRO diffractometer with 40kV and 40mA Cu-$K_{\alpha 1}$ tube as an X-ray generator. It is equipped with a PIXcel 3D detector. Data was collected in theta-theta geometry in a 2θ range of 10-70 ˚ with a step size of 0.016 ˚.

Figure 3. 2 Image of X-pert PRO X-ray diffractometer (image captured at Glass and Ceramics Lab, Sheffield Hallam University)

3.3.1.1 XRD: sample preparation

Bulk glass samples were ground to form powder using a vibration mill at a speed of 600 rpm. Glass powders were then pressed into specific XRD sample holders (Figure 3.3) and then mounted on a sample spinner stage.

Figure 3. 3 Image of sample holder for powdered samples for XRD measurements (image captured at Glass and Ceramics Lab, Sheffield Hallam University)

3.3.2 Raman spectroscopy: background

Raman spectroscopy is based on the scattering phenomenon of monochromatic light from the chemical bonds of the material under study [100,212,213]. It is a non-destructive technique spectroscopic technique which is used to analyse internal chemical structure, contamination/impurity, and molecular interactions within the material. Monochromatic light is incident from a high-intensity laser source interacts with sample. Most of the light elastically scatters meaning that wavelength and frequency remains the same as of the incident light. This is called as Rayleigh scattering. When light scatters inelastically from the vibrations of the molecule, it either shifts up called Stokes scattering or shifts down which is called Anti-stokes scattering. At room temperature Stokes scattering is dominant, anti-Stokes scattering can be measured at high temperatures [100,212,213].

3.3.2.1 Raman spectroscopy: experimental details

Raman spectroscopic measurements were performed using a Thermo-Scientific DXR^2 imaging microscope (Figure 3.4). Figure 3.5 shows the schematics of a typical Raman spectrometer. This setup was equipped with a 532 nm laser powered to 10 mW. Raman spectra were recorded on glass monolith samples in the spectral range 100 - 2000 cm $^{-1}$. Elastically scattered light is filtered out using a notch filter.

Figure 3. 4 Image of Thermo-Scientific DXR2 Raman spectrometer (image captured at Glass and Ceramics Lab, Sheffield Hallam University)

The detector used to collect the inelastically scattered photons was CCD detector and grating was set to 900 lines / mm to disperse the signal onto the CCD. The data collection and background corrections were done using an in-built software package OMNIC. To obtain the optimum focus a 50x objective lens and 50 µm aperture was used and 30 accumulations of 15 seconds each were recorded. The corrections for temperature and excitation line effects were performed using the method by Long (1977) [214].

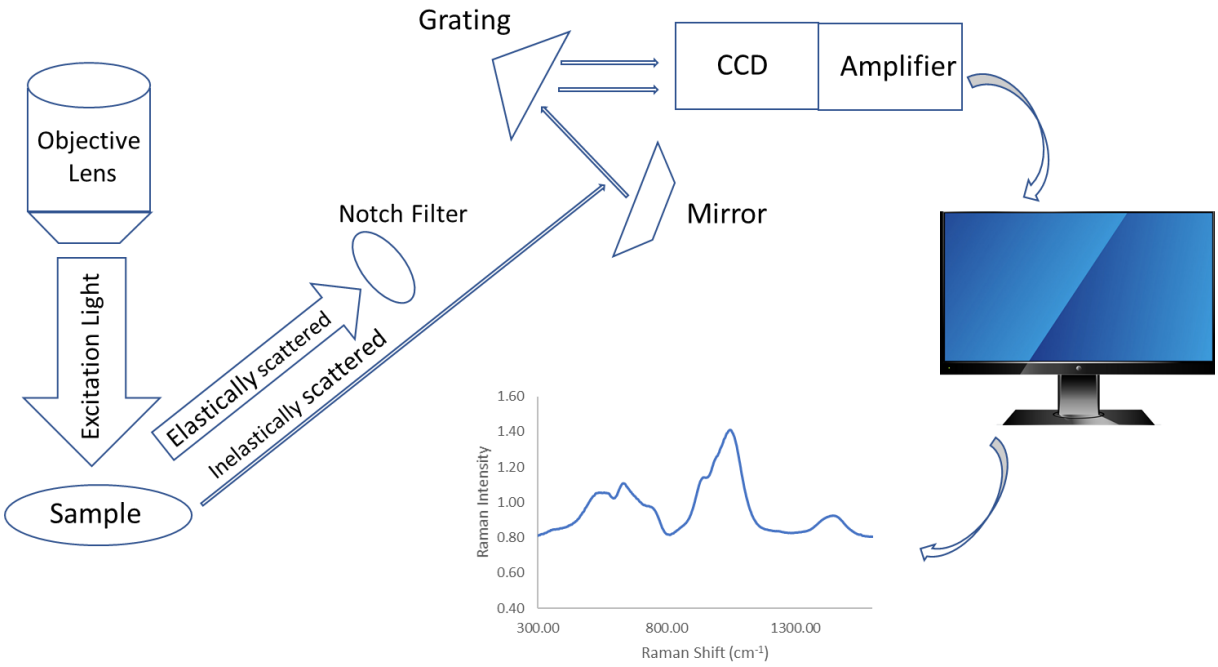

Figure 3. 5 Schematic diagram of a Raman spectrometer (modified from [215])

3.3.3 Density measurements

Density measurements were done for different monolithic pristine glass samples as well as irradiated samples using Archimedes' method. This method uses a solid sample which is to be measured, a densimeter balance and a displacement fluid. The glass monoliths were first weighed in the air and then in the displacement fluid which was distilled water. The densimeter used was a Mettler Toledo balance which has an accuracy of 0.0001 g. The density of the glass sample is given by the relation (Equation 3.2) between mass of the sample in the air (M_{air}), mass of the sample in the fluid (M_{fluid}) and density of the fluid (ρ_{fluid}) at room temperature. Averages of five independent measurements were taken to minimise the uncertainties. Figure 3.6 shows the image of the densimeter balance used to measurements.

$$\rho_{sample} = \frac{\rho_{fluid}\,(T) M_{air}}{(M_{air} - M_{fluid})} \qquad \text{(Equation 3.2)}$$

Figure 3. 6 Mettler Toledo densimeter (Source:[216])

3.3.4 Electron paramagnetic resonance spectroscopy: background

Zavoisky (1945) [217] was the first scientist to report the phenomenon of electron paramagnetic resonance. Electron paramagnetic resonance (EPR) spectroscopy is a non-destructive analytical technique to study species with unpaired electrons, such as radicals, radical cations, and excited states with non-zero spin e.g., triplet states. It is also called as electron spin resonance (ESR) spectroscopy. It is based upon the absorption of microwave photons by unpaired electrons in the presence of an externally applied magnetic field. It is a technique which studies interaction of electromagnetic radiation (microwaves) with magnetic moment produced by the electron spin. Since the net magnetic moment of paired electrons is zero, it can only be utilising to study systems with unpaired spin that the systems having a net spin moment [218].

Electrons in an atom are characterised by four quantum numbers: n, l, m_l, m_s where n is the principle quantum number, l is the azimuthal or orbital angular momentum quantum number, m_l is the magnetic quantum number and m_s is the spin quantum number [219]. The magnetic moment due to orbital angular momentum ($\hbar L$) of an electron in an atom is given by:

$$\mu_L = -\frac{|e|\hbar L}{2m} = -\mu_B L \qquad \text{(Equation 3.3)}$$

where μ_B is the Bohr magneton and $-\frac{e}{2m}$ is the gyromagnetic ratio and the constant of proportionality. The magnetic moment associated due to spin angular momentum ($\hbar S$) of an electron in an atom is given by:

$$\mu_S = -g_e \frac{|e|\hbar S}{2m} = -g_e \mu_B S \quad \text{(Equation 3.4)}$$

where g_e is the spectroscopic splitting factor or Landé factor or *g*-factor and has a value ≈ 2.002319 for a free electron. In the presence of a magnetic field, the energy *E* experienced by an individual particle is proportional to the magnetic moment and is given by:

$$E = \mu B \qquad \text{(Equation 3.5)}$$

As per quantum mechanics the energy levels of a magnetic dipole are quantized due to the quantization of spin angular momentum in a specified direction in the presence of magnetic field. Using Equation 3.4 in 3.5 we obtain:

$$E = -g_e \mu_B B S \qquad \text{(Equation 3.6)}$$

Thus, when a system with unpaired electrons is subjected to an external magnetic field the energy levels (which were degenerate in the absence of a magnetic field) associated with the electrons aligns themselves parallel (β-lower energy level) or antiparallel (α-higher energy level) to the direction of magnetic field and this is called Zeeman splitting and it is shown in Figure 3.7. The two possible energy states are $\pm\frac{1}{2} g_e \mu_B B$ since S can take two values $\pm\frac{1}{2}$.

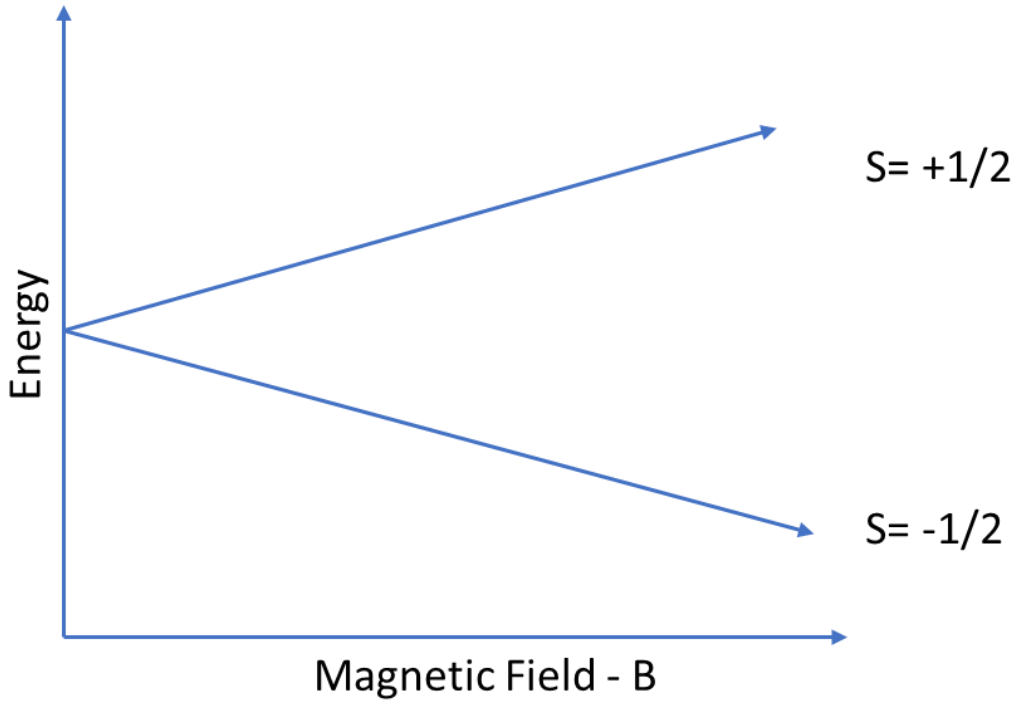

Figure 3. 7 Zeeman splitting for S = $\pm 1/2$ (modified from [220])

The energy difference between the two energy levels is given by:

$$\Delta E = h\nu = E_\alpha - E_\beta = g_e \mu_B B \qquad \text{(Equation 3.7)}$$

The resonance absorption and hence resonance transition of electromagnetic radiation (microwave) from lower energy level to higher energy level can happen only when the energy of the photon $(h\nu)$ matches the difference between the two energy levels. In most conventional EPR measurement, the frequency of the microwave is kept constant and magnetic field is varied.

3.3.4.1 Electron paramagnetic resonance spectroscopy: experimental details

In a continuous wave EPR spectrometer, microwaves are produced from an oscillator (Figure 3.8), a klystron, which is a vacuum tube well, at a frequency of approximately 9.6 GHz, also called X-band. The microwaves are then passed via an attenuator which can control the intensity. A directional coupler splits the incoming microwave photons into two parts, one goes directly to the detector as a standard for comparison with the intensity of the radiation after interaction with the sample. The other part is incident on to the sample which is adjusted in a resonant cavity (resonator) or sample cavity. The resonant cavity is placed under a static magnetic field and the strength of which is increased linearly by changing the current in

electromagnetic coils. The frequency of the source is tuned to the frequency of the resonant cavity. A field modulation unit imposes an AC component on the static magnetic field, and this results in an AC signal at the microwave detector which is then amplified. The detector is a crystal rectifier diode which converts AC signal to DC current. The absorption of photons is recorded by a change in the detector current. Rectangular waveguides are used for the transmission of microwave photons to and from the cavity.

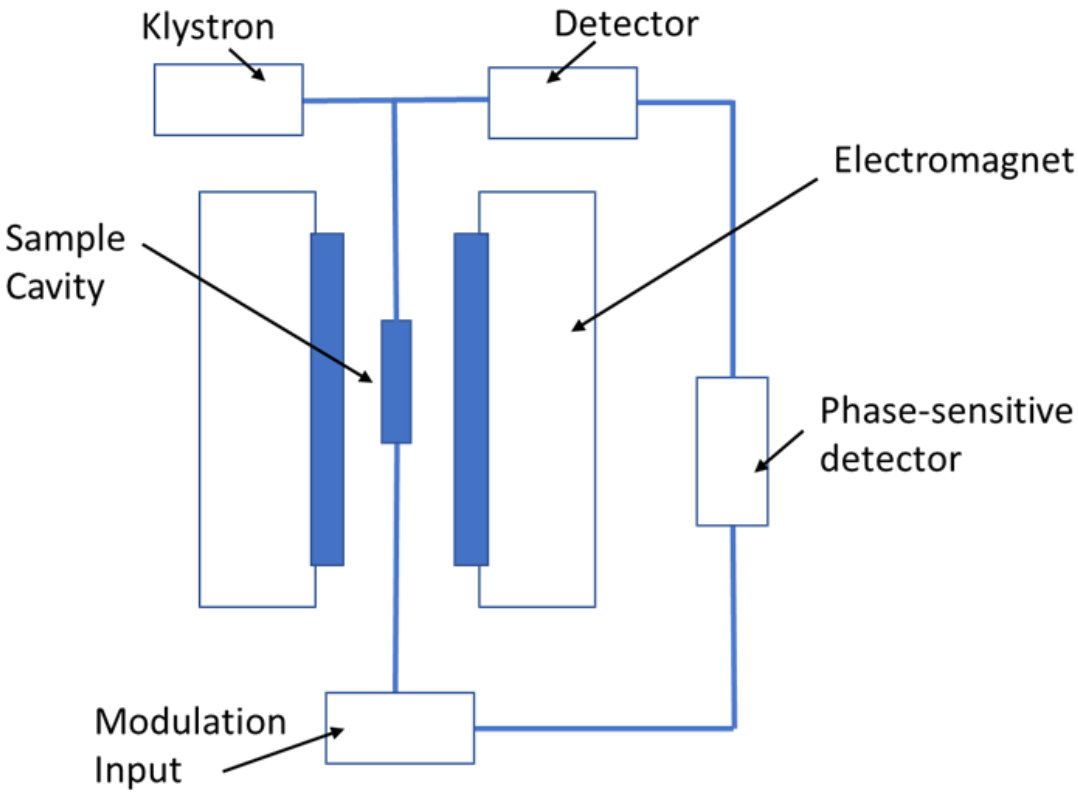

Figure 3. 8 Schematic diagram of an EPR spectrometer (modified from [220])

The samples for investigation can be powder or monoliths. The EPR spectrometer used for measurement was called a Bruker EXM-nano EPR spectrometer (Figure 3.9) [221]. Data acquisitions were performed using software package called Bruker-Xenon. Data was processed using Origin software package. The centre field and sweep width used for EPR measurement under this study was 250 and 370 mT, respectively. The microwave power used was 0.3162 mW, modulation amplitude 0.4 mT and magnetic field modulation was 100 kHz.

Figure 3. 9 EXM-nano EPR spectrometer (Source:[222])

3.3.5 Mössbauer spectroscopy: background

Mössbauer spectroscopy can be used to provide information about the oxidation state, coordination number or the local environment of the atom in a complex material. ^{57}Fe Mössbauer spectroscopy was used in this study to determine the oxidation state, coordination of Fe and redox ratio of (Fe^{2+}/Fe^{3+}) in Fe doped glasses. The measurements were taken at room temperature using a ^{57}Co in Rh spectrometer. A ^{57}Co radioactive source decays to an excited state of ^{57}Fe by electron capture and γ-photon emission. The excited state of ^{57}Fe decays to its ground state by emitting a γ-photon of energy 14.4 keV energy.

Nuclear energy levels are influenced by their local environment. They can change or split depending on their surrounding environment, both electronic and magnetic. These transitions or changes in the energy levels can provide information about atom's local environment within a material. These changes are observed using resonance and fluorescence. However, there are two problems which prevent obtaining this information being obtained: the interactions between the nucleus and its local environment are very small, so-called hyperfine interactions, and resonance does not happen due to the recoil of nuclei (to conserve momentum) when a gamma photon is emitted or absorbed. To resolve the first issue (hyperfine interactions), miniscule variations of the original gamma-photon are achieved by using the Doppler

effect (refers to the effect change in the frequency and hence energy during the relative motion between a source and an observer) [223]. This is achieved by oscillating our radiation source towards and away from absorber with a velocity of a few mm/sec modulating the energy of gamma photons in very small increments. The spectrum is recorded in discrete velocity shifts, and minute energy shifts are thus achieved, necessary to observe the hyperfine interactions. When emitting and absorbing nuclei are of the same isotope and present in a solid matrix, the mass of the recoil nuclei during emission and absorption is very small relative to the effective mass of the whole solid matrix, making the event a recoil-free event and this leads to resonant emission and absorption. This resolves the issue of recoil of nuclei preventing resonance and fluorescence and this phenomenon is called the Mössbauer effect [100,223].

3.3.5.1 Mössbauer spectroscopy: experimental details

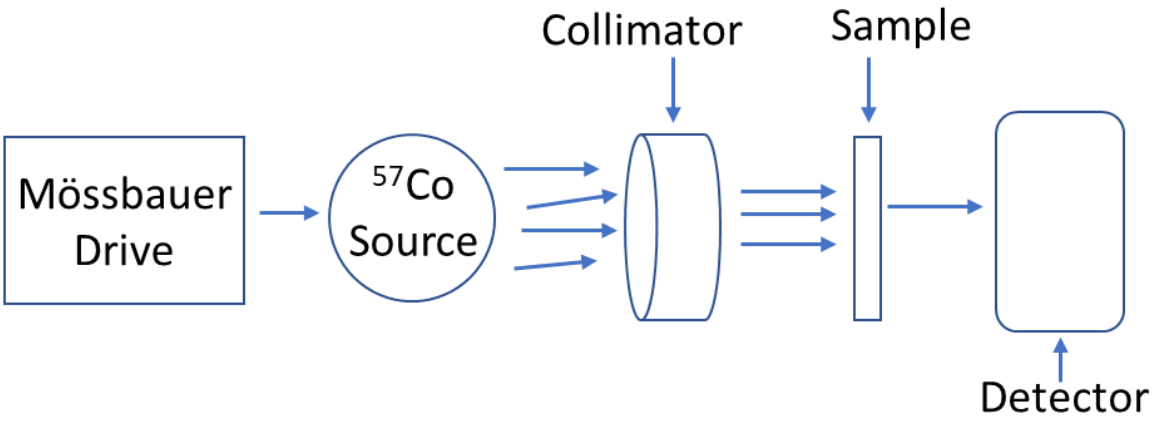

Figure 3. 10 Schematic diagram of an Mössbauer spectrometer (modified from [100])

In Figure 3.10 a Mössbauer drive is used to oscillate the ^{57}Co source with a velocity of few mm/sec towards and away from the absorber. A beam of γ-rays passes through a collimator and then through the absorber or the sample. When the energy of the emitted γ-ray photon matches the splitting energy due to the local environment in the absorber materials, resonant absorption takes place. The transmitted intensity of the beam through the sample is recorded by a detector. The nuclear energy levels in the absorber nuclei due to their local environment can split in three main ways [224,225]:

Isomer Shift: this shift is also known as centre shift, and it arises due to difference in the electron charge density due to the s-electrons in the emitter (source) and the absorber [100,223,226,227].

Quadrupole Splitting: This splitting arises due to the asymmetrical electric field or the electric field gradient [100,223,226,227].

Hyperfine Splitting: In the presence of a magnetic nuclei or the magnetic field, the nuclear energy splits which is called as hyperfine splitting [100,223,226,227]. It occurs when an electron spin interacts with the magnetic nuclei in the sample. A magnetic nucleus with quantum number I splits a single ESR peak (line) into 2I + 1 peaks.

The measurements were recorded using a room temperature ^{57}Fe Mössbauer spectrometer (Figure 3.11) that uses 14.4 keV gamma rays supplied by 25 mCi source of ^{57}Co in Rh over a velocity range of ±6 mm/sec using a constant acceleration driving unit. The spectrometer was calibrated relative to α-Fe (natural Fe). The spectral analysis was carried out using Recoil software package [228].

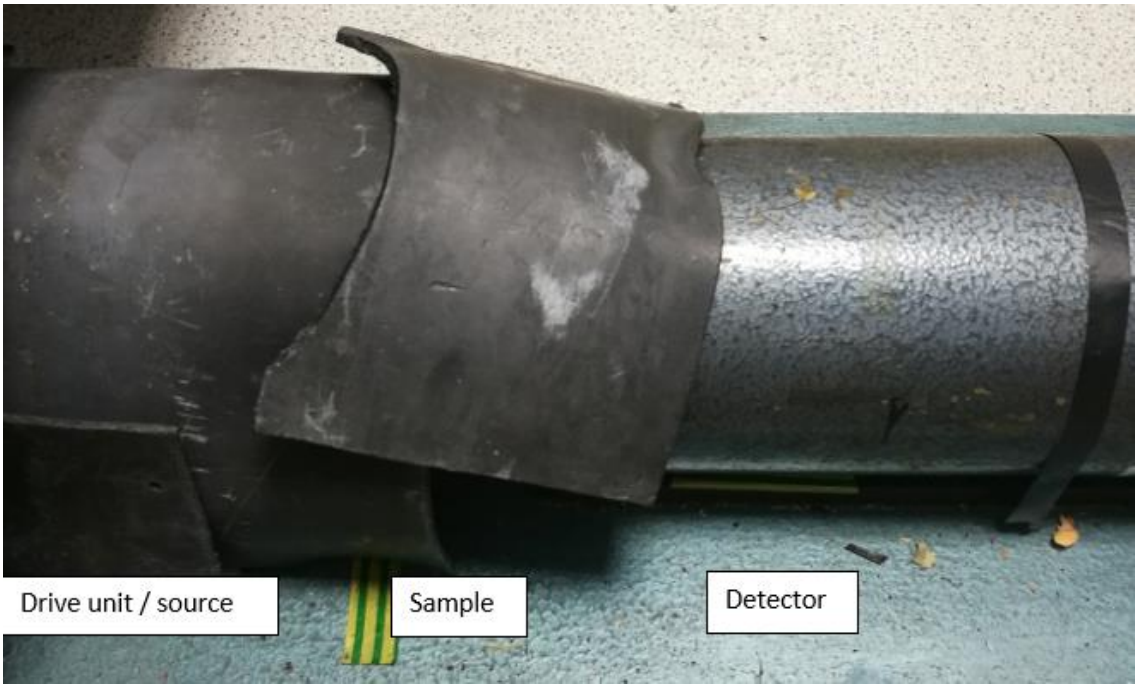

Figure 3. 11 57-Fe Mössbauer Spectrometer (picture captured at the Mössbauer lab, Sheffield Hallam University)

Sample preparation for Mössbauer spectroscopy requires powdered glass sample to be mixed with graphite powder and placing it in a disc shaped sample holder. The

data is processed using a software package Recoil [228]. A α-Fe sample is used for calibration of the instrument.

3.3.6 UV-Vis-nIR spectroscopy: background

UV-Vis-nIR spectroscopy provides information about the radiation induced paramagnetic centres. It is a technique that measures the absorption of radiation as a function of wavelength. It is a type of optical absorption technique in which the light of UV-Vis-nIR region (UV 190-400 nm, visible 400-800 nm, and near infrared 780-3300 nm) is absorbed or transmitted by the material [194,229,230]. This absorption results in the excitation of the electrons from the ground state to a higher energy state. The energy absorbed is equal to energy different between the two energy states and is given by $\Delta E = h\nu$ [229]. The most favoured transitions are from the highest occupied molecular orbital (HOMO) to the lowest occupied molecular orbital (LOMO) such as in transition metal ions (*d-d* transitions and also ligand-to-metal or metal-to-ligand transitions) [231]. These paramagnetic centres absorb electromagnetic radiation in UV, visible and near infrared range and undergo electronic transitions. The optical absorption bands reveal information about the characteristic and concentration of the paramagnetic centres formed when materials (glass here) are subjected to irradiation [232].

3.3.6.1 UV-Vis-nIR optical absorption spectroscopy: experimental details

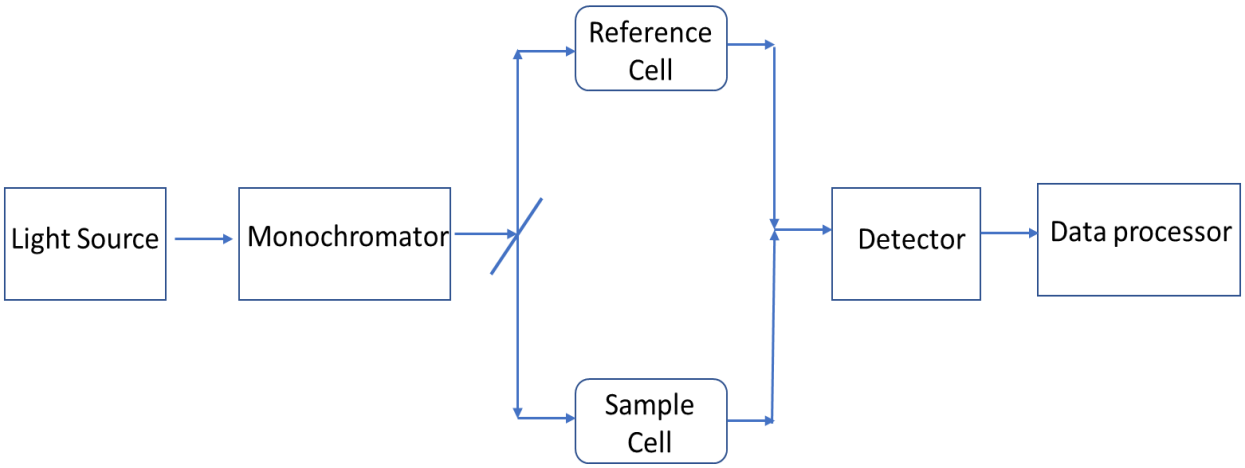

Figure 3.12 Schematics of a UV-Vis-nIR spectrophotometer (modified from [230])

In Figure 3.12 the source of the light is a Xenon flash lamp which produces light in the wavelength range 200 to 1100 nm (50,000 to 9090 cm^{-1} in wavenumbers). A monochromator then separates out the visible light. A beam splitter splits the

monochromatic wave in to two parts one passes to the reference cell and the other interacts with the sample. A detector measures the intensity after interaction with the sample relative to the intensity through the reference and that gives an indication of the absorbance by the sample. A detector then passes it to a data processing unit.

All the UV-Vis-nIR optical absorption measurements in the study were carried out on using a Varian Cary 50 scan spectrophotometer. The glass samples were polished and reduced to a thickness of ~ 1 mm. Data was collected in the absorption mode with a dual beam scan rate of 60 nm/min. Baseline corrections were done using an in-built software package called Scan and the data were corrected to a path length of 1 mm.

3.4 Irradiation experiments

In this study glass samples were irradiated with gamma rays and He-ions. Gamma irradiations were performed using a Foss Therapy Services 812 ^{60}Co Gamma irradiator, using 1.17-1.33 MeV energy photons from a ^{60}Co source at the Dalton Cumbrian Facility, The University of Manchester [221]. The dose rates were measured using Radcal Corporation Accu-Dose+ a base unit equipped with an ionization chamber for in beam measurements of high-intensity gamma irradiation. The name of the model for the high-dose rate ionization chamber was 10x6-0.18, and Accu-Dose+ base unit, and both were supplied by Radcal. All the simple and doped glasses were irradiated with 5 MGy of gamma dose, and in addition to 5 MGy NaBaBSi and LiNaBSi were also irradiated with 0.5 MGy using ^{60}Co.

He-ion irradiations were performed using the Low Energy Ion Beam Facility (LEIBF), at the Inter-University Accelerator Centre (IUAC), Delhi, India. The ion beam parameters and energy loss calculations were carried out using a software package called SRIM-2013 (stopping and range of ions in matter) [233]. LiNaBSi and NaBaBSi glasses were also implanted with 650 keV He^{2+} with fluences of 1 x 10^{15}, 1 x 10^{16}, 5 x 10^{16}, and 1 x 10^{17} ions/cm^2. Figure 3.13 (i), illustrates the image of gamma irradiator located at the Dalton's Cumbrian Facility [221] and (ii), illustrates the image of the LEIBF.

Figure 3. 13 Gamma irradiator, the DCF (Source:[221])

Figure 3. 14 the Low Energy Ion Beam Facility, IUAC (Source:[234])

Chapter 4. Simulation of Alpha-damage

4.1 Introduction and background

This chapter discusses the aspects of this study which were conducted with the aims of simulating the damaging effects of alpha decay in radioactive waste glasses. Actinides present in HLW are the alpha emitters and have very long half-lives (e.g., 2.15 million years for ^{237}Np). Alpha decay of actinides results in the emission of alpha particles and alpha-recoil nuclei. While alpha particles interact with the glass structure mainly by electronic interaction [22,24], recoil-nuclei of alpha decay interact by ballistic processes or elastic collisions [21,22]. Due to their long half-lives, radiation effects due to alpha will become dominant after ~500 years of geological disposal [3,24,128]. Whilst the damage will be accumulated over geological disposal periods (~10^4 years), it is critical to understand the evolution of glasses under self-irradiation due to alpha particles for predicting the long-term performance of the glass waste forms. The most common method used to simulate the damage from alpha particles is to use ion-implantation [3]. The same method was employed for this study, details of which are given in Section 3.4.

Mir *et al.* [45] studied BS3 glass (SiO_2, $B2O_3$ and Na_2O) implanted with 2 MeV He-ion implanted. BS3 glass was given a fluence of 2 x 10^{16} He cm^{-2}. They reported a decrease in hardness by about 17 ± 2% and saturation thereafter. They also reported an overall increase in the area of the Q^3 band (3-bridging oxygen) suggesting a depolymerization (Q^4 is decreased) using Raman spectroscopy [45]. Karakurt *et al.* [128] studied a simulated SON68 glass implanted with 7 MeV Au^{5+} and 1 MeV He^+ to study the effects of alpha recoil nuclei and alpha particles, respectively. For a better understanding of the structural modifications, they studied a 6-oxide borosilicate glass, simplified version of SON68 (ISG) [128]. The He^+ fluences given to both ISG and SON68 glass specimens were 1.75 x 10^{15} and 3.45 x 10^{16} at/cm^2. The Au^{5+} fluences given to both the glass specimens were between the range 1 x 10^{12} to 3 x 10^{14}. Both the ion-irradiations induced a decrease in volume change (-0.7% for alpha particle and -2.7% for Au ions) of both the glasses and a decrease in the polymerization degree of the silica network was reported. Mir *et al.* [36] reported mono and sequential ion irradiation effects in BS3 and simulated SON68 glasses. They used heavy (U, Kr, Au) and light ions (He,O) to study the

variations in hardness when irradiated with single ion and double ion beams [36]. For the heavy ion irradiations, the hardness diminished and saturated after a decrease by 35 ± 1% and when irradiated with light ion a decrease by 18 ± 1% was seen and then saturation was observed. Glass specimens were implanted with different ions of different energies and fluences which are described in Table 4.1.

Table 4. 1 Ion beam parameters (modified from [36])

Ion	Energy (MeV)	Fluence (ion/cm^2) (± 10%)
^{238}U	109.5	7 x 10^{10} – 3 x 10^{13}
^{84}Kr	25	10^{11}-10^{14}
^{19}Au	14	10^{13}- 5 x 10^{15}
^{4}He	2	4 x 10^{15}-10^{17}
^{18}O	137	5 x 10^{11}- 4x 10^{13}

When glass were first irradiated with heavy ion (Au) and then by a light ion (He), a partial damage recovery was observed and an increase of 10-15% in hardness was reported (see ref. [36]). Yang *et al.* [185] studied irradiation damage by 0.5 MeV He-ions and 1.3 MeV electrons in borosilicate glass (see ref. [185]). The He-ion implantation was carried out with fluence in the range of 5 x 10^{14} to 1 x 10^{17} ions/cm^2. For electrons, the irradiation dose is in the range from 10^7 to 10^9 Gy. It was reported that average hardness was reduced by 14% in He-irradiated glasses due to the nuclear energy deposited while electronic energy depositions by the electron irradiations enhanced the polymerisation of the silicate network [185]. Mohapatra *et al.* [28] studied electron irradiation effects in sodium barium borosilicate glasses using electron paramagnetic resonance spectroscopy and found that boron-oxygen and silicon based hole centers along with E' centers were formed when irradiated with doses 10^5, 10^6 and 10^8 Gy. Section 2.3.3 provides detailed information of the irradiation induced defects in simple and complex (simulated waste doped glasses).

Two simple international glasses, namely UK "MW" lithium-sodium borosilicate (LiNaBSi) and Indian sodium-barium borosilicate (NaBaBSi) were implanted with 650 KeV He^{2+} ions with doses ranging from 10^{15} to 10^{17} ions/cm^2. X-band EPR and

Raman spectroscopies were employed to characterise the glass specimens before and after irradiation. Radiation-induced paramagnetic defects centered around g~2.00 were identified in He-ion implanted glass specimens using results from EPR analyses. Raman spectroscopic results showed notable changes in the glass structure post-irradiation, with the emergence of a broad Raman band at 1560 cm^{-1} upon irradiation with high fluences.

4.2 Experimental procedures

LiNaBSi and NaBaBSi glasses with the following compositions (mol%): 60.5SiO_2-18.5B_2O_3-10.5Na_2O-10.5Li_2O and 41.6SiO_2-20.8B_2O_3-21.8Na_2O-15.6BaO were synthesized using a standard melt-pour-anneal method. Glass melting parameters are given in Section 3.2 in Chapter 3. The glass specimens for ion-implantation were prepared by cutting them using a diamond precision saw to small samples of thickness ~1 cm (see Figure 4.1). They were then polished using SiC pads of grit size of up to 1000 (approximate size of 8.4 μm). They were then polished using an aqueous suspension of CeO_2 to obtain a smooth surface to < 1 μm.

He-ion implantation experiments were performed at the Low Energy Ion Beam Facility (LEIBF) at the Inter-University Accelerator Center, India. NaBaBSi and LiNaBSi glasses were implanted with 650 KeV He^{2+} ions to fluences of $1x10^{15}$, $1x10^{16}$, $5x10^{16}$ and $1x10^{17}$ ions/cm^2. The ion-beam parameters are given in Table 4.1 and energy loss in the glass specimens were calculated using SRIM-2013 software (The Stopping and Range of Ions in Matter) [233].

Table 4. 2 Electronic and nuclear stopping for He^{2+} in NaBaBSi and LiNaBSi glasses.

Glass	Ion type	Energy (keV)	Electronic Stopping (Se) (keV/micron)	Nuclear stopping (Sn) (keV/micron)	Sn/Se
NaBaBSi	He^{2+}	650	414.6	0.711	0.001
LiNaBSi	He^{2+}	650	399.1	0.678	0.001

Figure 4. 1 illustrates the specimen holder for ion-implantation at the LEIBF.

4.3 Results

4.3.1 Electron paramagnetic resonance spectroscopy

To study the effects of alpha particles in NaBaBSi glass the first derivative X-band EPR spectra (Figure 4.2) at room temperature implanted with He^{2+} of 650 keV with a range of fluences was recorded. For all the ion-implanted samples an EPR signal centred at g~2.00 with varying linewidth between ~0.08 to 0.40 mT (for the lowest and the highest fluence -implanted samples, respectively) was observed. There are no EPR signals observed due to the trapped-carriers (electron and hole centres), however the obtained signals have a shape which is similar to as observed for peroxy radicals (POR's) [31] and therefore it could be attributed to peroxy radicals. POR's are also reported to be the more thermal stable [57,187] than other radiation induced paramagnetic centres such as BOHC's, non-bridging oxygen hole centres (NBOHC's), and E' centres [28,31,57]. Figure 4.3 illustrates the first derivative room temperature X-band EPR spectra for LiNaBSi glass specimen implanted with He^{2+} with a range of fluences. As with the NaBaBSi glass, all spectra exhibit EPR resonances at g~2.00, with linewidths ranging from ~0.06 to 0.08 mT (for the lowest and the highest fluence-implanted specimens, respectively).

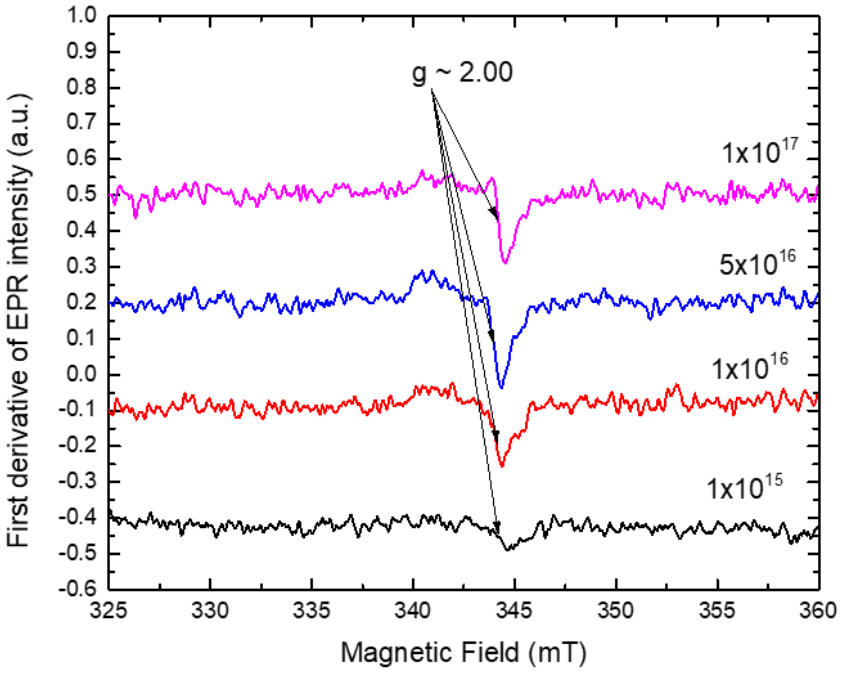

Figure 4. 2 X-band first derivative EPR spectra for He^{2+} implanted NaBaBSi glass.

There is no evidence of EPR signal that would be consistent with trapped charge centres, and the line shape of the g~2.00 resonance is broadly similar to that of a

peroxy-radical, as in the case of LiNaBSi glass. However, the low S/N ratio restricts observation of any underlying signal [28,31,57].

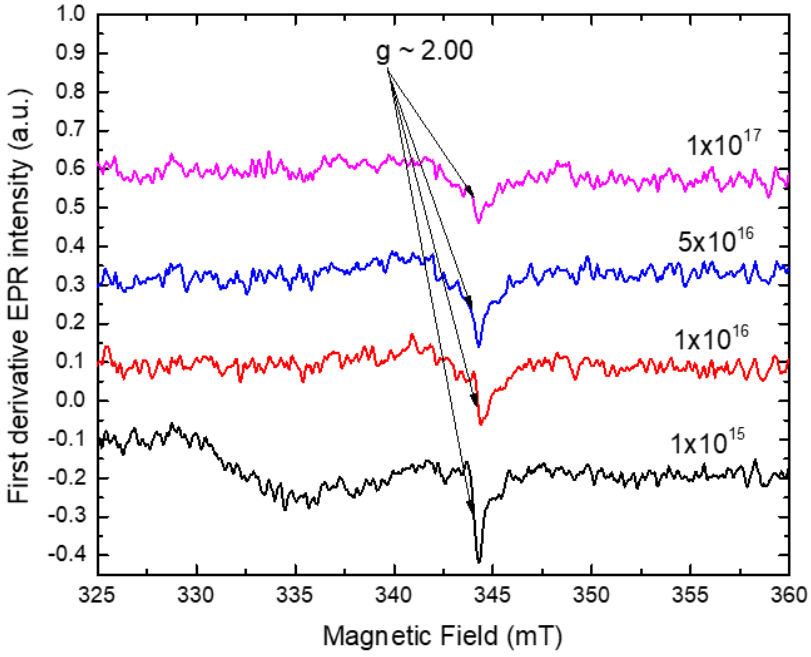

Figure 4. 3 X-band first derivative EPR spectra for He^{2+} implanted LiNaBSi glass.

4.3.2 Raman spectroscopy

Figure 4.4 illustrates stacked Raman spectra of pristine and He^{2+} ion-implanted NaBaBSi simple glass specimens. Unpolarized Raman spectra were acquired and plotted between 100-2000 cm^{-1} and normalisation of the Raman spectra was done using the maximum intensity of the Raman band in the spectrum. The spectra was divided into three main regions: the region between 300 – 550 cm^{-1} is attributed to the mixed stretching and bending modes of Si-O-Si units [37,172,183,195,235]. The band at 630 cm^{-1} could be due to vibrations involving danburite units [235,236], however, this band is debated in literature, therefore, this cannot be considered a confident assignment here [212,236,237]. The band at ~ 750 cm^{-1} could be attributed to 4-coordinated diborate and boroxol ring units [37,128,195,237]. The region between 800-1250 cm^{-1} defines Si-O Q^n-speciation region where *n* is the number of bridging oxygens [100,128,158,173,195,206,212,238,239].The peak at 1450 cm^{-1} could be attributed to B-O vibrational units [195,235–237,240]. The band emerging at 1560 cm^{-1} upon irradiation with high fluences is also notable, literature suggests that molecular oxygen (O-O) vibrations can produce Raman bands at these Raman shifts [31,45,128,171,196] .

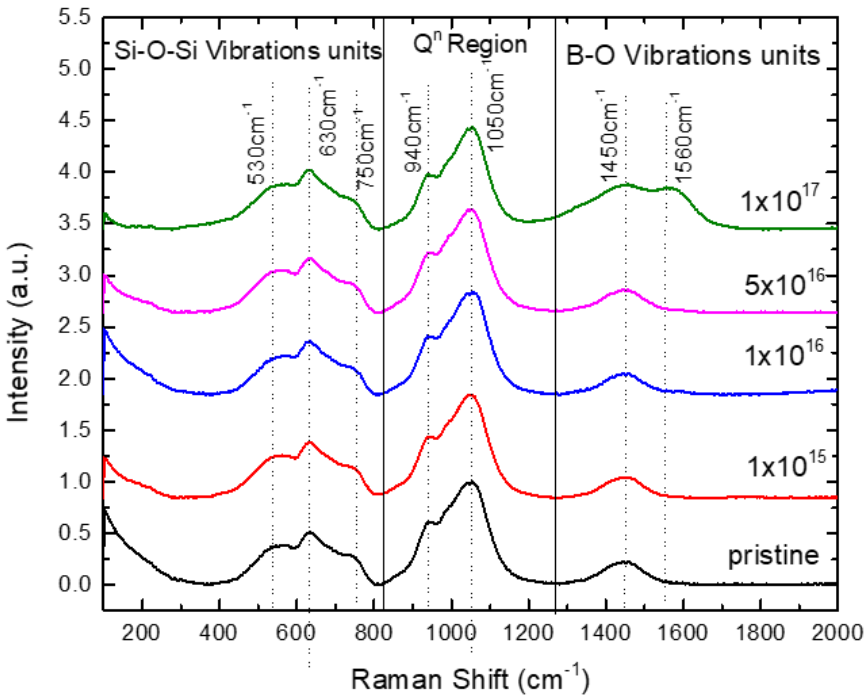

Figure 4. 4 Stacked Raman spectra for NaBaBSi glass implanted with 650 keV He^{2+} to fluences of $1x10^{15}$, $1x10^{16}$, $5x10^{16}$ and $1x10^{17}$ ions/cm^2.

Figure 4.5 illustrates the Raman spectra (stacked) of pristine and He^{2+} ion-implanted LiNaBSi simple glass specimens. The band at 510 cm^{-1} is attributed to Si-O-Si vibrational units and the band at 630 and 750 cm^{-1} is common to both the LiNaBSi and NaBaBSi glasses [32,162,174,185,219]. The band near 1450 cm^{-1} is characteristics of B-O vibration units and is a common band in both the glasses [195,235–237,240]. The Raman band at 1560 cm^{-1} becomes prominent after irradiation with $5x10^{16}$ ions/cm^2 and becomes even more pronounced at a fluence of $1x10^{17}$ ions/cm^2.

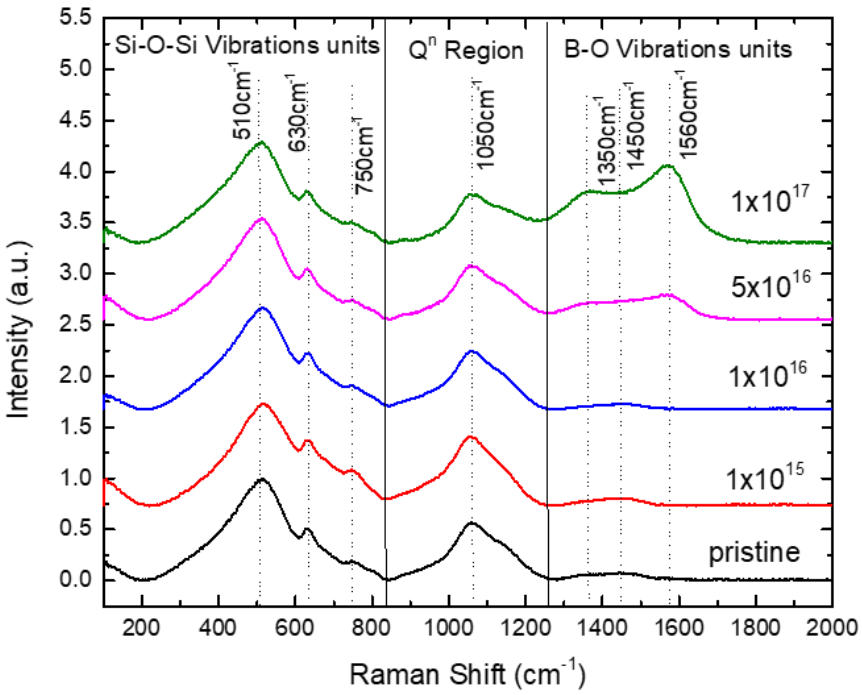

Figure 4. 5 Stacked Raman spectra for LiNaBSi glass implanted with 650 keV He^{2+} to fluences of $1x10^{15}$, $1x10^{16}$, $5x10^{16}$ and $1x10^{17}$ ions/cm^2.

4.4 Discussion

There was no consistent trend observed for the EPR linewidth. There can be a number of different causes for the narrowing of EPR linewidth for NaBaBSi and broadening of LiNaBSi glass specimens with increasing fluence such as non-uniformities in magnetic field, hyperfine interactions, uncertainties in energy levels, inhomogeneities in the sample, different irradiation volume and so on [220]. There is no evidence/signature of EPR signals due to the trapped carriers.

Zhang *et al.* [205] found a narrow Raman band at 1550 cm^{-1} and attributed it to molecular O_2 of the molecular oxygen after Ar-ion irradiation. Abbas *et al.* [172] found an increase in the band associated with molecular oxygen in a Kr-ion irradiated 6-oxide glass. Karakurt *et al.* [128] also reported the presence of a Raman peak at 1550 cm^{-1} in Au-irradiated borosilicate glass and they attributed that to molecular oxygen. However, this band, in all three cases [128,172,205] is far too narrow to fully explain the broad band we observe at high irradiation fluences in both LiNaBSi and NaBaBSi glasses. It is therefore unlikely that the band we observe at 1560 cm^{-1} is due solely to molecular O_2, however, the band due to molecular O_2 could be providing a partial contribution. This new Raman band is also present in

Figure 4.4 but appears only in the spectrum for the NaBaBSi glass sample implanted with the highest (1 x 10^{17} ions/cm^2) He^{2+} fluence. It is notable for both the NaBaBSi and LiNaBSi glasses that the Raman band at 1450 cm^{-1} also increases in intensity (relative to Q^n region) with increasing He^{2+} fluence. Since the band at 1450 cm^{-1} has been widely attributed to B-O units [62,241] , one possible origin for the new band emerging at 1560 cm^{-1} may be that it is associated with changes to the boron units in the glass network [62,241].

4.5 Conclusion

The effects of alpha particles on LiNaBSi and NaBaBSi HLW base glasses were studied using 650 keV He^{2+} implantation with a range of fluences, with the objective of enhancing our understanding of the types of radiation-induced defects that can form in HLW glasses, and how/whether these are affected by glass composition. Room-temperature X-band EPR spectroscopy was carried out to investigate the types of defects forming upon He^{2+} ion implantation. EPR resonance signals showed the formation of defect centres which are broadly consistent with peroxy radicals. There were no signatures of radiation-induced defects due to trapped charge carriers, although it is noted that EPR signal-to-noise ratios were limited by the small volumes of radiation-implanted glasses. Structural studies were performed using Raman spectroscopy. A strong, broad Raman band at 1560 cm^{-1}, accompanied by growth of the nearby B-O band at 1450 cm^{-1}, was observed in both glasses at high irradiation fluence, although fluence corresponding to the onset of this band differs between the two glasses. The structural origins of the new band may be associated with B-O units with partial contribution from the formation of molecular O_2.

Chapter 5. Simulation of Beta-Gamma Damage

5.1 Gamma irradiation

5.1.1 Introduction

As discussed in Chapter 2 in HLW, fission products such as ^{90}Sr and ^{137}Cs will be responsible for the self-irradiation damage in first ~500 years of geological disposal [24,37]. Fission products decay by emitting beta particles with low energy recoil nuclei and gamma rays. Beta-gamma interactions with glass mainly happen in the form of electronic interactions via excitations and ionisations [21,39]. Beta-gamma interactions cause a very few direct atomic displacements (<< 1 per atomic displacement, see ref. [24,37], however, bond-dissociation by them can have several effects such as change in the diffusion properties, depolymerisation of the glass network, mechanical properties change. DeNatale and Howitt [164] studied gamma irradiation effects in high-level waste storage glass from Battelle Laboratories and irradiated it using a ^{60}Co source at Savannah River Laboratories to a total dose of 91 MGy (see ref. [164] for details). El-Alaily *et al.* [242] irradiated barium borosilicate glasses using ^{60}Co gamma source to a dose of 5 kGy. Mohaptara *et al.* [57] studied gamma irradiation effects in Trombay nuclear waste glass doped with Fe_2O_3 (NaBaBSi) irradiated with a dose of 2.5 x 10^5 Gy from a ^{60}Co gamma. In the present study two simple glasses, lithium sodium-borosilicate (LiNaBSi) and sodium barium-borosilicate (NaBaBSi) glasses were irradiated with doses 0.5 and 5 MGy gamma to study the gamma irradiation-induced defects. LiNaBSi and NaBaBSi are glass matrices which are being used to immobilise HLW in UK and India, respectively. A multi-spectroscopic technique approach was used to characterise the samples before and after irradiation. X-band electron paramagnetic resonance (EPR), Raman and UV-Vis-nIR spectroscopies were employed to characterise the glasses. Time-dependent thermal annealing was carried out at a range of temperatures, including temperatures (370 K – 570) K relevant to canister centreline cooling (CCC), to study the thermal stability of gamma-irradiation induced defects [37,41].

5.1.2 Background and literature review

The interaction of high-energy radiation with materials results in the transfer of energy to the solid and can lead to heating, the emission of electromagnetic radiation or structural changes. The electromagnetic radiation can emit in the form of X-rays,

UV or visible light via atomic transitions and is caused by the transfer of energy to the orbital electrons (ionization and excitation) [14,21,22,119,243]. Interaction of these radiations will be the principal sources of heat generation and accumulated damage for the first few hundred years (~500) of storage and geological disposal due to their associated short half-lives ($t_{1/2}$ ^{137}Cs = 30.2 years and $t_{1/2}$ ^{90}Sr = 28.8 years).

The two glasses in the present study were bulk irradiated with gamma photons. Bulk irradiated samples are useful in comparison to samples with a small, irradiated volume as they enable use of more characterisation tools such as EPR, NMR, or Raman spectroscopies to study the microstructural changes in the glass matrix. Bulk irradiation can be carried using radioactive sources such as ^{60}Co or ^{137}Cs which offer realistic simulation doses, however, achieving higher doses can take a very long time. As an example, to attain a few ~5 MGy typically it can take about ~10 days with dose rate of 350 Gy/min as in present study [37,39,58].

In a HLW glass waste form radiation interaction mechanisms will be complex. The interaction of radiation and its effects will be dependent on many factors such as glass structure, composition (concentration of glass formers and modifiers), network bonding, and thermal history of the glass [244]. Macroscopic properties are dependent on microstructure. Radiation induced changes in the microstructure of the HLW glasses can translate into changes in their macroscopic properties. Some of the known microstructural changes due to irradiation can enable release of charge compensators, migration under induced-field, formation of clusters, and molecular oxygen [27,178]. A network modifier cation, for example, in an alkali silicate glass creates non-bridging oxygen (NBO) by breaking up the Si-O-Si network. The cationic field strength of modifier cations dictates the distribution of NBOs within the glass structure and nanoscale inhomogeneities can exist in these glasses [245]. The role of alkali oxides as charge compensators in borosilicate glasses (e.g., conversion of BO_3 to BO_4) or as a network modifier (e.g., formation of NBO), their effects based on their content and type on the structure of the glass, the degree of Si/B mixing associated with bridging oxygen (BO) and NBO, and structural changes based on composition, can all be estimated by many advanced models. Early work by Yun *et al*. [161] and Dell *et al.* [162] based on ^{11}B “wide-line” NMR to study the short-range structure of sodium borosilicate glasses, have led to these advanced models

[146,147,149,246] The mechanical, physical and chemical properties and durability of borosilicate glasses are dependent on the mixing of glass forming structural units (Si/B mixing), the distribution and mixing of modifying species (alkali and alkaline earth), and their role in the structural network alteration [146]. The distribution of alkalis, their content and the degree of Si/B mixing can be more complicated in a borosilicate glass with mixed alkali content and type. Du and Stebbins [149][146] studied mono- and mixed- alkali borosilicate glasses using 3Q-MAS (triple-quantum magic angle spinning) ^{11}B and ^{17}O NMR and reported that there is significant heterogeneity in Li-borosilicate glass in comparison to Na and K containing borosilicate glasses. A lower fraction of tetrahedral boron (BO_4) units, Si-O-B and a higher fraction of NBO's suggested significant heterogeneity in terms of Si/B mixing for mixed Li-Na and Li-K glasses. They also suggested that NBO's are more likely to associate with smaller alkali cations, since heterogeneity increases with increasing cationic field strength. Mishra *et al.* [134] studied Na-Ba borosilicate glasses and suggested that sodium acts as a charge compensator at a ratio of Na/B > 0.5. The ratio Na/B > 0.5 facilitates increased Si/B mixing by charge compensating BO_4 units. The increasing concentration of alkali (sodium) enables the formation of NBO's by breaking Si-O-Si and Si-O-B bonds. The Na^+ cations have higher cationic field strengths and smaller ionic radii than Ba^{2+} which enables Na^+ to occupy sites closer to BO_4^-.

Mohapatra *et al*. [17,57] studied gamma irradiation induced changes in NaBaBSi glass, also called Trombay nuclear waste glass. The LiNaBSi glass, which is also known as UK-MW (Mixture Windscale) glass was studied by McGann *et.al.* [206] to investigate the effects of gamma irradiation. There are only a few reports in the literature for these simple/base glasses (without the addition of HLW waste or inactive surrogate waste).

This study aimed to contribute to developing an enhanced fundamental understanding of the nature of gamma irradiation-induced defects in two simple (4-oxide) representative HLW host (base) glasses at two different doses (0.5 MGy / low and 5 MGy / high). To achieve these aims a multi-spectroscopic approach was used, it included EPR, UV-Vis-nIR optical absorption and Raman spectroscopies. The secondary aim of this study was to determine the compositional effects (if there are any) on the abundances and variations in types of radiation-induced defect.

Furthermore, this study aimed to uncover the mechanisms of creation of any nano/micro structural changes which were not present in un-irradiated glasses. A thermal annealing study at different temperatures and times was conducted to examine the stability / “healing” of the underlying gamma irradiation-induced defect centres in each glass. It was anticipated that this research would provide new insight into the longer-term interim storage and geological repository behaviour of UK and Indian HLW waste forms.

5.2 Experimental procedures

Both of the glasses in this study were synthesised using the melt-quench and anneal method as explained in detail in Chapter 3. Glass specimens were irradiated with doses of 0.5 and 5 MGy at the Dalton Cumbrian Facility in a gamma irradiator with ^{60}Co sources which supply 1.17 -1.33 MeV energy photons with a dose rate of 0.5 to 350 Gy/min [221]. Detailed description of the gamma irradiation method is provided in Chapter 3. Temperature-calibrated electric ovens were used to anneal irradiated glass specimens at 5 different temperatures between 373 K and 773 K for 16 and 24 hours. To perform the annealing experiments at 5 different temperatures and 2 different times, 40 samples were synthesised and irradiated.

5.3 Results

5.3.1 X-ray diffraction

X-ray diffraction measurements were done for both glass samples to assess their X-ray amorphous nature. An X-pert Pro diffractometer equipped with a monochromated Cu-$K_{\alpha 1}$ x-ray source and a PIXcel 3D detector was used to perform the measurements. Data were collected in a theta-theta or theta-2theta geometry in the 2θ range of 10-70° with a step size of 0.016°. Figure 5.1 illustrates that both the glasses were X-ray amorphous and there were no crystalline phases detected.

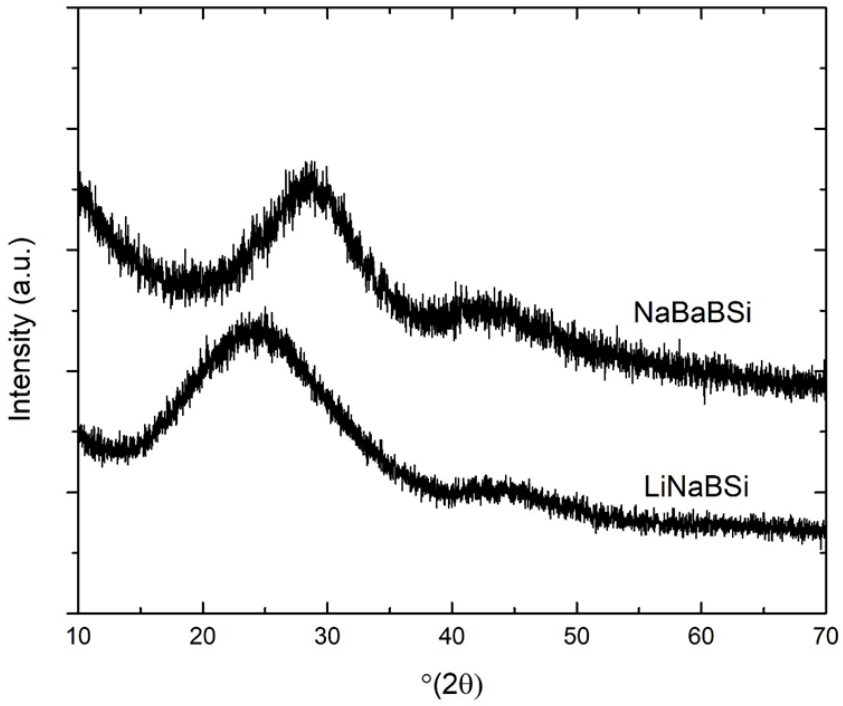

Figure 5. 1 X-ray diffraction pattern for NaBaBSi and LiNaBSi glasses.

5.3.2 Glass coloration

Changes in the visible coloration of the glasses, due to gamma-irradiation, are shown in Table 5.1. The LiNaBSi glass, which was initially transparent, turned brown and the NaBaBSi glass, which was initially slightly yellow in colour, turned blue, following irradiation with a dose of 5 MGy. Similar discoloration happened in the two glasses when irradiated at lower doses (0.5 MGy) but the colour was less pronounced since these specimens had lower thicknesses of 3 – 4 mm whereas the specimens irradiated with 5 MGy were ~ 10 mm thick. The NaBaBSi glass irradiated with 5 MGy (~10 mm thick) and the LiNaBSi glass irradiated with 5 MGy (~ 10 mm thick) showed pronounced colour changes which are easier to observe due to the different lighting conditions used for capturing images.

Table 5. 1 Changes in the visible coloration of the glasses post irradiation.

NaBaBSi Glass		
0 MGy (~ 10 mm)	**0.5 MGy (~3-4 mm)**	**5 MGy (~ 10 mm thick)**
	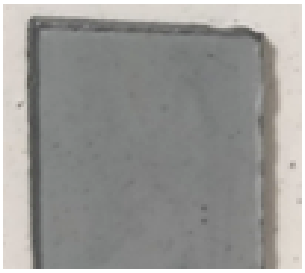	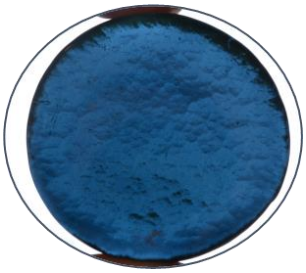
LiNaBSi Glass		
0 MGy (~ 10 mm)	**0.5 MGy (~3-4 mm)**	**5 MGy (~ 10 mm thick)**
		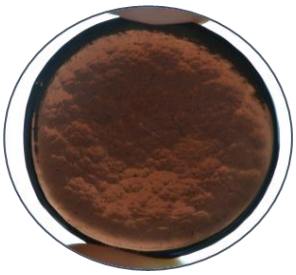

5.3.3 Electron paramagnetic resonance spectroscopy

Figure 5.2 illustrates the first derivative X-band (~9.6 GHz) room temperature EPR spectra for NaBaBSi and LiNaBSi pristine and glasses irradiated with 0.5 and 5 MGy ^{60}Co *γ*-radiation. EPR spectra for pristine glasses show no resonance signals near to g~2. The EPR spectrum for pristine NaBaBSi glass were noisy (no resonance signal were observed) because it was measured from different EPR spectrometer, however, measurement parameters were kept same. There is an EPR resonance signal present in irradiated glass samples, centred at around the free electron value of g~2.00. This signal in both NaBaBSi and LiNaBSi glasses is a four shoulder/peak (quartet structure), which is due to the convolution of radiation-induced paramagnetic centres and can be attributed due to boron oxygen hole centres (BOHCs) [57,68,174,247]. Radiation induced breaking of B-O-B bonds is responsible for creation of BOHCs. In a borosilicate glass a BOHC can be defined as a hole trapped at the non-bridging oxygen (NBO) atom in trigonal boron (=B-O•) units [56,68,248,249]. An EPR signal centred around a magnetic field of ~348 mT with experimental value of g~1.974 ± 0.002 and 1.972 ± 0.002 at 0.5 and 5 MGy, respectively, can be attributed to the E^{-} or polaron centre [27,176,179]. There are no

observable / clear differences in this signal for two different doses. An E^- or polaron centre can be defined as an electron trapped at an alkali cation. There is another shoulder which has been attributed to ET centres, with g~1.991 in the NaBaBSi glass (present at both studied gamma doses). This signal, with g ~ 1.99, was observed by Mohapatra *et al.* [28,57] and they defined it as an electron trapped at a cation. An ET centre is either an F^+ centre or an electron trapped at a cation [28,57]. Two weak isotropic signals for 0.5 and 5 MGy irradiated LiNaBSi glass, centred at g~1.997 and 1.996, respectively, can be attributed to ET centres [28,57].

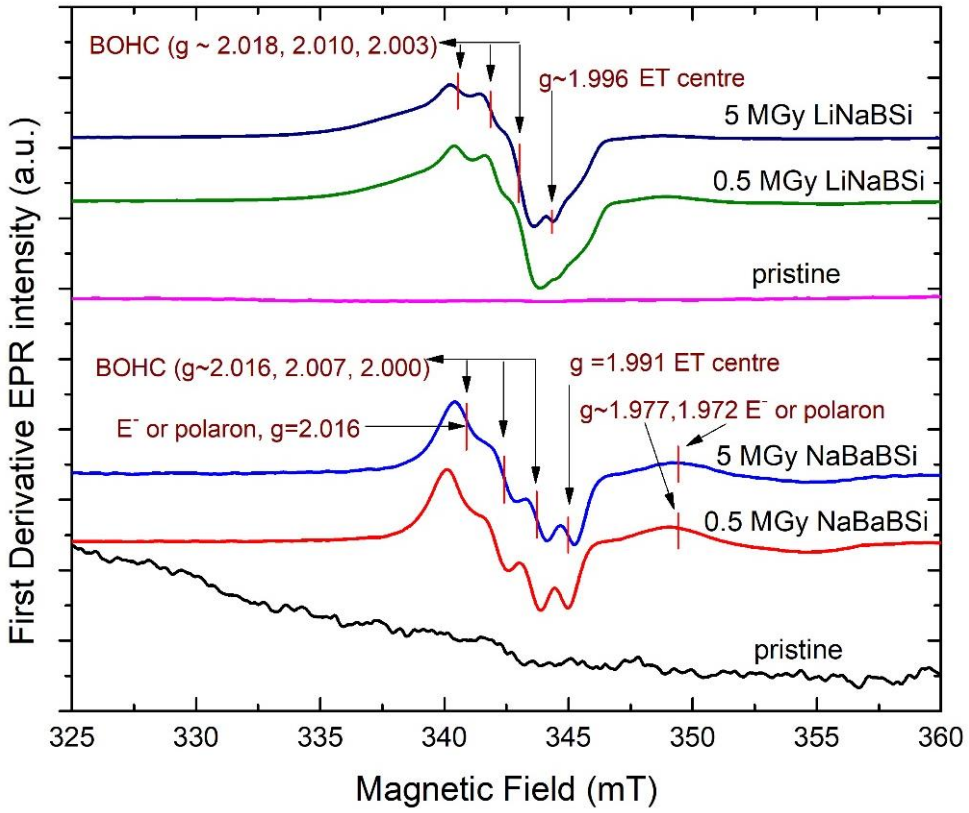

Figure 5. 2 First-derivative, intensity normalised EPR spectra for LiNaBSi and NaBaBSi glasses irradiated with 0.5 and 5 MGy of gamma radiation.

Figure 5.3 illustrates the second-derivative X-band EPR spectra for LiNaBSi and NaBaBSi glasses irradiated with doses of 0.5 and 5 MGy ^{60}Co *γ*-radiation. Since the first-derivative EPR spectra were convoluted due to the presence of different overlapping paramagnetic defect centres, second-derivative spectra were plotted to enhance the definition and further deconvolute the spectra, and to help investigate any underlying signals due to radiation-induced paramagnetic centres. The convoluted EPR resonance signal centred at g~2.00, the four-line/quartet hyperfine

structure which was attributed to BOHC's as illustrated from the first derivative spectra, is slightly better resolved in the second-derivative spectra for NaBaBSi glasses. The EPR signal attributed to E^- centres in the first derivative EPR spectra at g~1.974 ± 0.002 and g ~1.972 ± 0.002 is also present in the second-derivative spectra. There is an additional signal identified in the second-derivative spectra at around g~ 2.018 and g~2.016 for 0.5 and 5 MGy irradiation, respectively, having a linewidth of 1.4 – 1.5 mT and centred at a magnetic field of ~341 mT. This is an isotropic signal and is attributed to E^- centres: paramagnetic centres which are responsible for formation of sodium metallic colloids [28,176,250]. The second-derivative EPR spectra for LiNaBSi irradiated glass samples are a combination of six lines, four for BOHC's and two shoulders. This was anticipated from the first derivative spectra. The four-line shape and structure for BOHC is reported by many researchers through simulations and it matches our first-derivative experimental EPR spectra [27,28,232]. There are no additional signals identified in the second-derivative EPR spectra for LiNaBSi glass. The two signals at g~1.997 and g~1.996 at 0.5 and 5 MGy, respectively, can be attributed to ET centres [176,177].

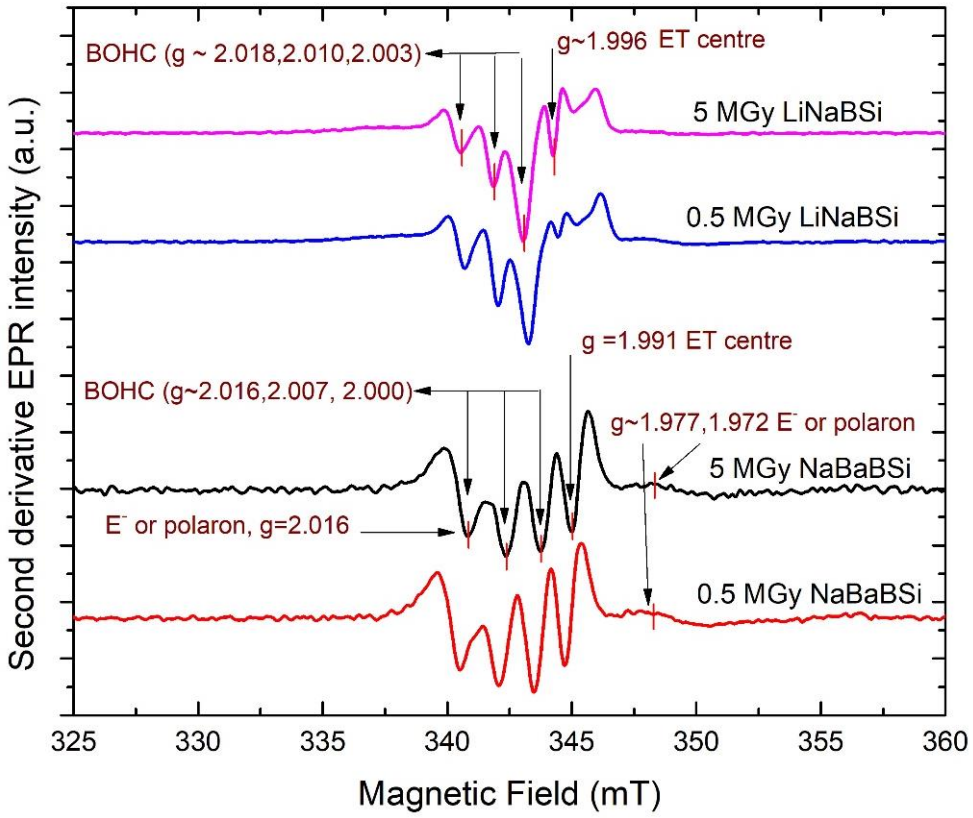

Figure 5. 3 Second-derivative intensity normalised EPR spectra for LiNaBSi and NaBaBSi glasses irradiated with 0.5 and 5 MGy of gamma radiation.

Table 5. 2 The g-values calculated from experiments using the centre of the magnetic field where second derivative becomes negative [28,31,57,173,206].

NaBaBSi 0.5 MGy		NaBaBSi 5 MGy		LiNaBSi 0.5 MGy		LiNaBSi 5 MGy	
g value	Defect	g value	Defect	g value	Defect	g value	Defect
2.018	E^- polaron/BOHC	2.016	E^- polaron/BOHC	2.019	BOHC	2.018	BOHC
2.009	BOHC	2.007	BOHC	2.011	BOHC	2.010	BOHC
2.001	BOHC	2.000	BOHC	2.004	BOHC	2.003	BOHC
1.993	ET	1.991	ET	1.997	ET	1.996	ET
1.974	E^- polaron	1.972	E^- polaron	-	-	-	-

Figures 5.4 – 5.7 illustrate the intensity-normalised first-derivative spectra for NaBaBSi glass specimens irradiated with 0.5 and 5 MGy of ^{60}Co gamma radiation and thermally annealed at temperatures ranging from 373 K to 773 K for 16 and 24 hours. Individual spectrum was normalised with peak-to-peak intensity / height of EPR signal at g~2.00. This was done to compare the annihilation / reduction of EPR signal when annealed at different temperature relative to the rest of the signal. First-derivative spectra give convoluted radiation-induced signals.

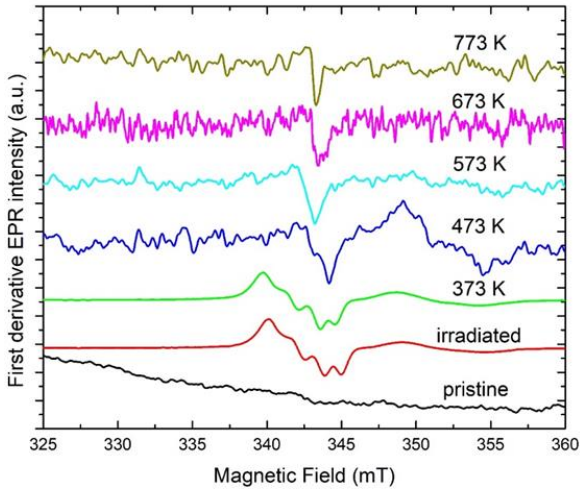

Figure 5. 4 Peak-to-peak first derivative for spectra for NaBaBSi pristine and irradiated glass with 0.5 MGy and annealed for 16 hours at 373-773 K.

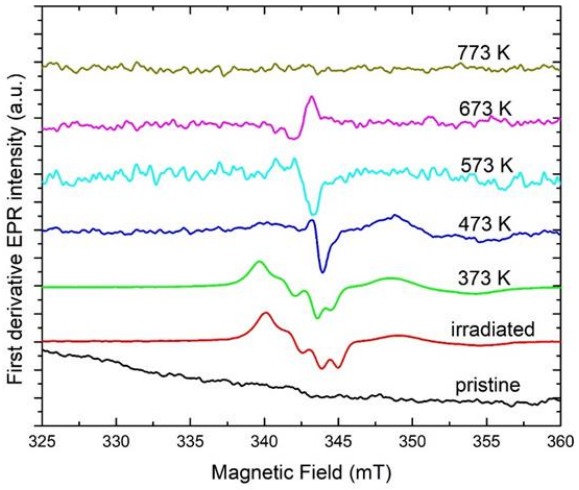

Figure 5. 5 Peak-to-peak first derivative for spectra for NaBaBSi pristine and irradiated glass with 0.5 MGy and annealed for 24 hours at 373-773 K.

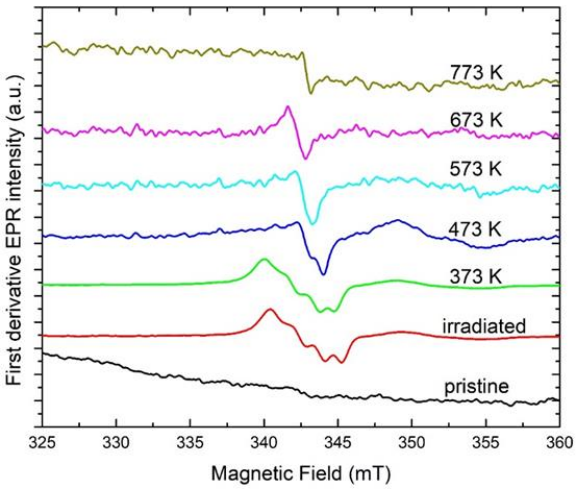

Figure 5. 6 Peak-to-peak first derivative for spectra for NaBaBSi pristine and irradiated glass with 5 MGy and annealed for 16 hours at 373-773 K.

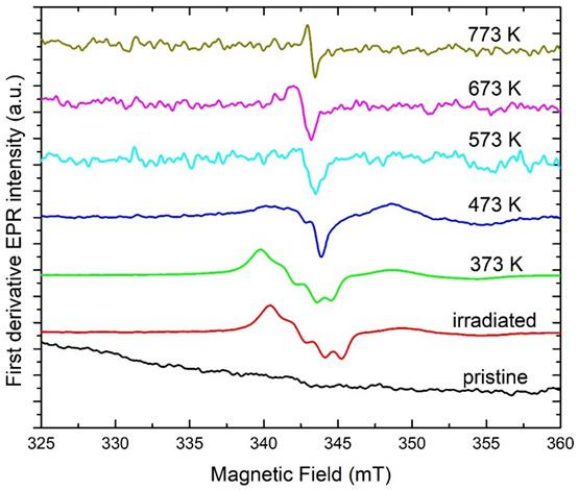

Figure 5. 7 Peak-to-peak first derivative for spectra for NaBaBSi pristine and irradiated glass with 5 MGy and annealed for 24 hours at 373-773 K.

Figures 5.8 – 5.9 illustrate the intensity normalised second-derivative spectra for NaBaBSi glass specimens irradiated with 0.5 and 5 MGy of ^{60}Co gamma radiation and thermally annealed at temperatures ranging from 373 K - 773 K for 16 and 24 hours. In Figure 5.8 EPR resonance signals from the NaBaBSi glass specimen irradiated with 0.5 MGy and thermally annealed at 373 K are the same as in an unannealed irradiated glass specimen. This shows that the radiation-induced paramagnetic defects are reasonably stable at temperatures of up to 373 K. When annealed at temperatures greater than 373 K, some EPR signals disappeared due to possible defect recombination / annihilation. There is an underlying signal revealed from EPR spectra when the same glass type irradiated with the same dose of 0.5 MGy was annealed for 24 hours at 473 K, as illustrated from Figure 5.9. This signal appears to arise from a convolution of two paramagnetic centres. This EPR signal has a value of g~1.998 calculated from experimental second-derivative spectra (Figure 5.9) and can be attributed to E' centres plus a shoulder nearby (not assigned to any defect) [27,57,174]. This signal was not present in the unannealed specimen, which was annealed at 473 K for 16 hours, suggesting that electrons may be trapped at a different site by gaining thermal energy from annealing. The signal at g~1.97 attributed to E^- centres remains stable at 473 K but disappears due to thermal annealing at higher temperatures, as illustrated from the first-derivative spectra in Figure 5.6 - 5.7 [27,176,179].

In Figure 5.10 intensity normalised second-derivative EPR spectra for NaBaBSi glass irradiated with 5 MGy of gamma radiation, when annealed at temperatures of 373 – 773 K for 16 hours, show that radiation-induced paramagnetic defects are stable after annealing at 373 K. After annealing at 473 K for 16 hours the signal due to BOHC's recombined and a new signal appeared. This signal, from its line shape in Figure 5. 6, appears to be due to peroxy-radicals (POR's) or interstitial O_2^- ions. The g-values calculated from second-derivative spectra (Figure 5.10) are g ≈ 2.005, 1.999. The POR is reported by many authors in the literature [27,57,174,232]. It is defined as a hole trapped on a non-bridging oxygen or O_2^- bonded to one Si atom in the glass matrix, and sometimes it is also known as the oxy-defect [27,28,31,32,56,57,168,249]. It has a molecular structure, (≡Si-O-O•). This defect is formed by either breakage of the peroxy-linkage (≡Si-O-O-Si≡) in a glass structure or when an O_2^- ion is captured on a three-fold coordinated Si ion. Figures 5.6 and 5.10 show that the EPR signal due to POR's is unstable at 573 K, since its abundance / concentration starts to decrease - as indicated by the low S/N peak-to-peak intensity [28,31,57].

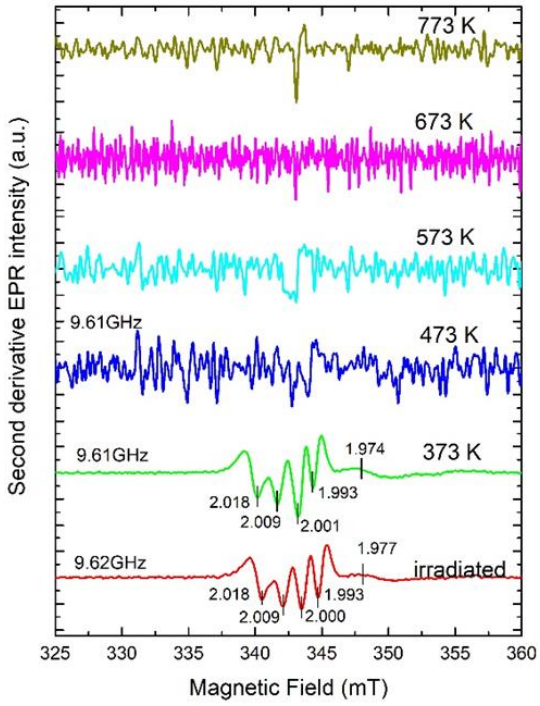

Figure 5.8 Peak-to-peak second derivative for spectra for NaBaBSi pristine and irradiated glass with 0.5 MGy and annealed for 16 hours at 373-773 K.

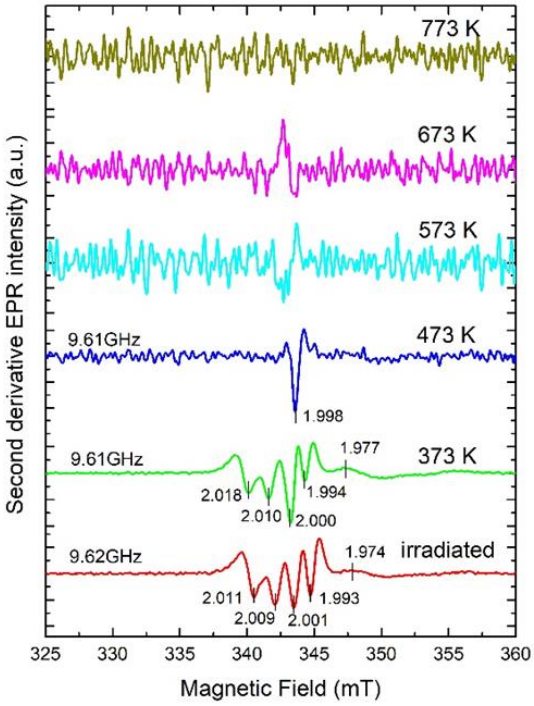

Figure 5.9 Peak-to-peak second derivative for spectra for NaBaBSi pristine and irradiated glass with 0.5 MGy and annealed for 24 hours at 373-773 K.

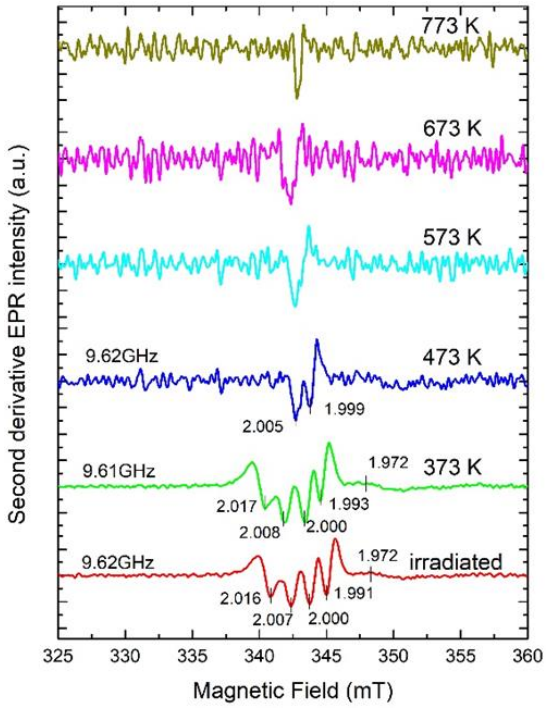

Figure 5.10 Peak-to-peak second derivative for spectra for NaBaBSi pristine and irradiated glass with 5 MGy and annealed for 16 hours at 373-773 K.

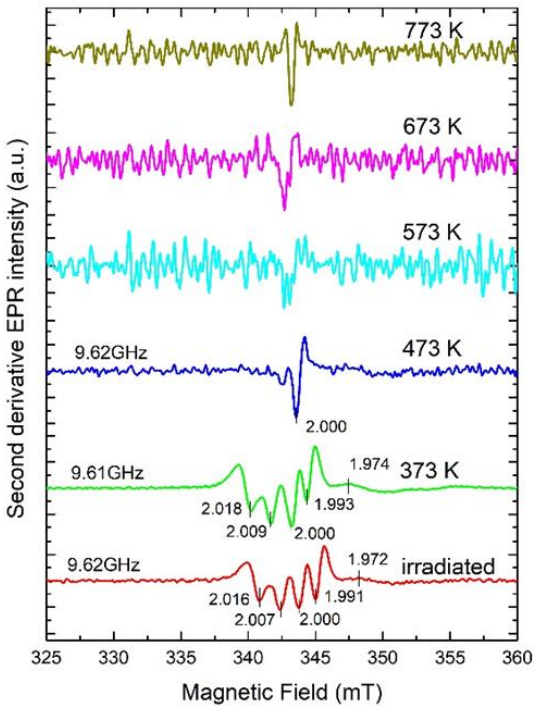

Figure 5.11 Peak-to-peak second derivative for spectra for NaBaBSi pristine and irradiated glass with 5 MGy and annealed for 24 hours at 373-773 K.

In Figure 5.11, the EPR signal for the NaBaBSi glass irradiated with 5 MGy is attributed to POR's and remains stable after annealing at 473 K for 24 hours. The S/N peak-to-peak intensity decreases at temperatures higher than 473 K [28,57,187]. This may be due to recombination/annihilation. The signal attributed to E^- centres (g~1.97) remains stable at 473 K and disappears at higher temperatures [27,176,179].

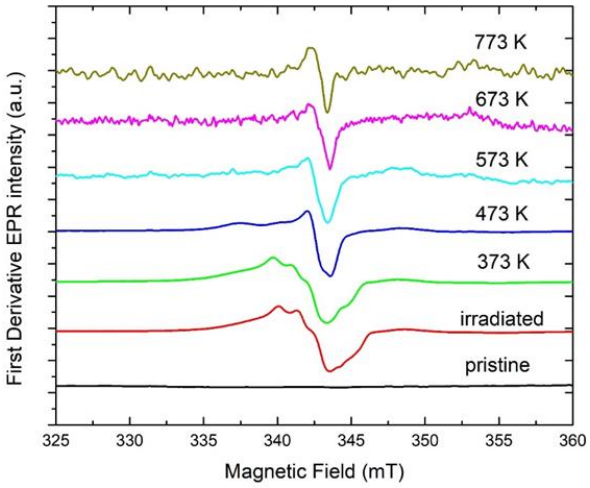

Figure 5. 12 Peak-to-peak first derivative for spectra for LiNaBSi pristine and irradiated glass with 0.5 MGy and annealed for 16 hours at 373-773 K.

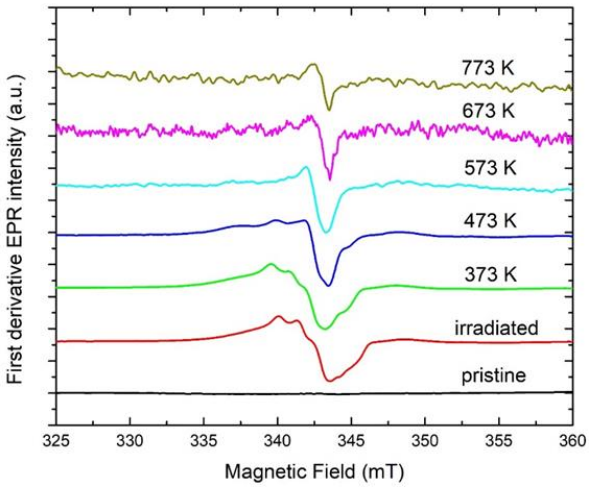

Figure 5. 13 Peak-to-peak first derivative for spectra for LiNaBSi pristine and irradiated glass with 0.5 MGy and annealed for 24 hours at 373-773 K.

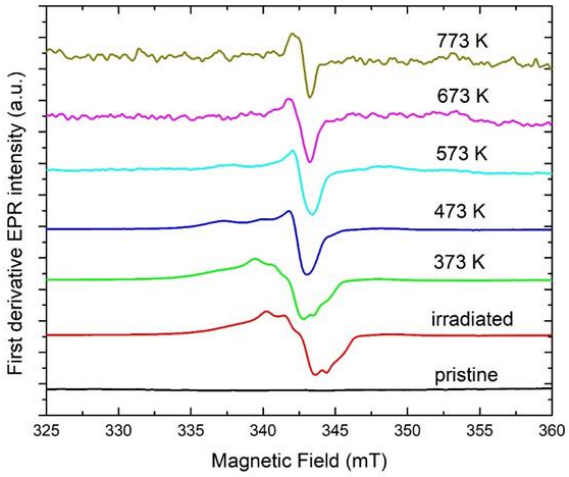

Figure 5. 14 Peak-to-peak first derivative for spectra for LiNaBSi pristine and irradiated glass with 5 MGy and annealed for 16 hours at 373-773 K.

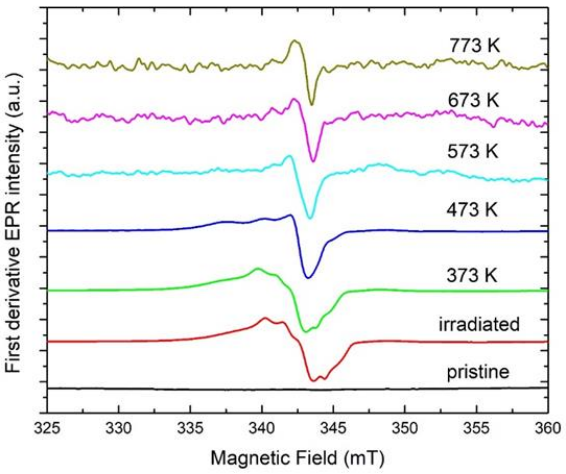

Figure 5. 15 Peak-to-peak first derivative for spectra for LiNaBSi pristine and irradiated glass with 5 MGy and annealed for 24 hours at 373-773 K.

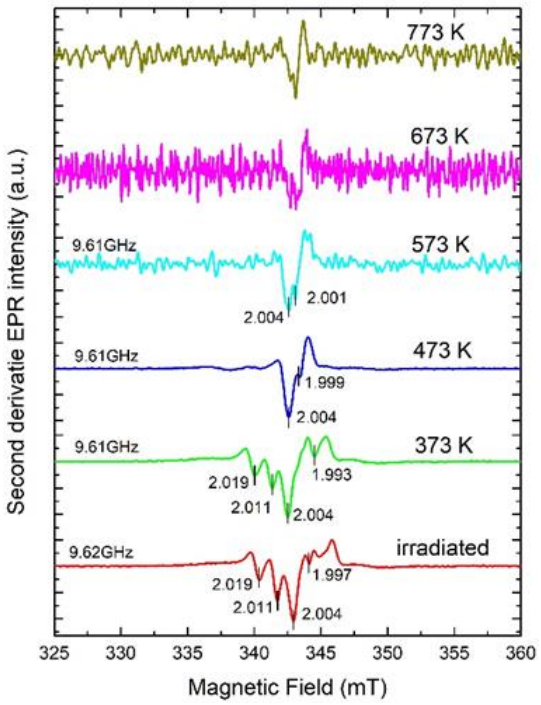

Figure 5.16 Peak-to-peak second derivative for spectra for LiNaBSi pristine and irradiated glass with 0.5 MGy and annealed for 16 hours at 373-773 K.

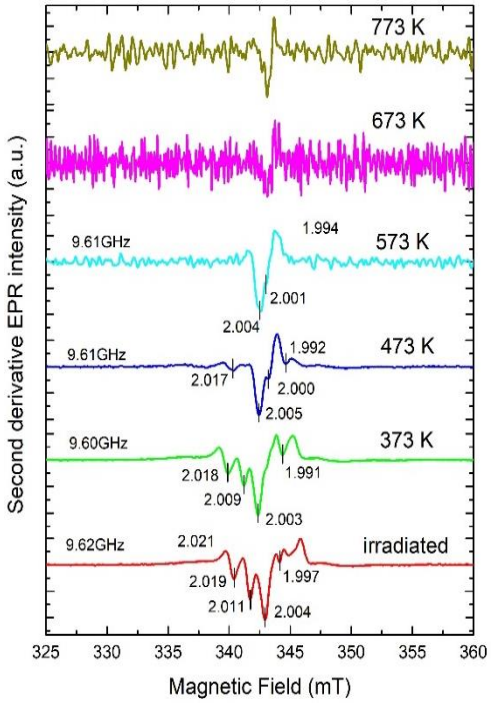

Figure 5.17 Peak-to-peak second derivative for spectra for LiNaBSi pristine and irradiated glass with 0.5 MGy and annealed for 24 hours at 373-773 K.

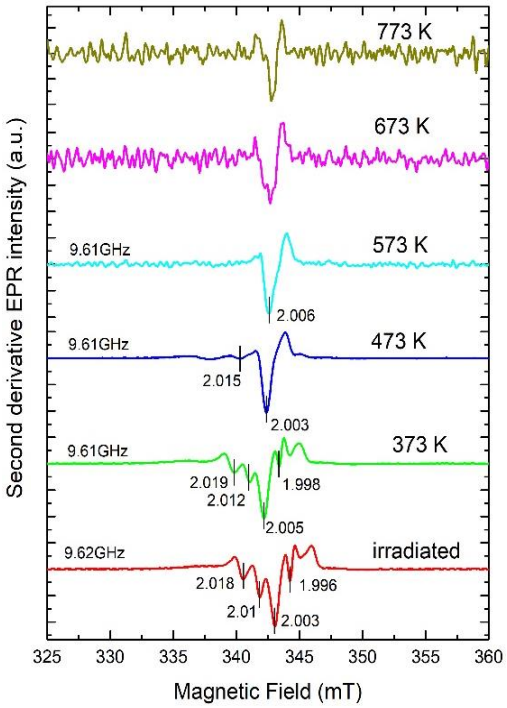

Figure 5.18 Peak-to-peak second derivative for spectra for LiNaBSi pristine and irradiated glass with 5 MGy and annealed for 16 hours at 373-773 K.

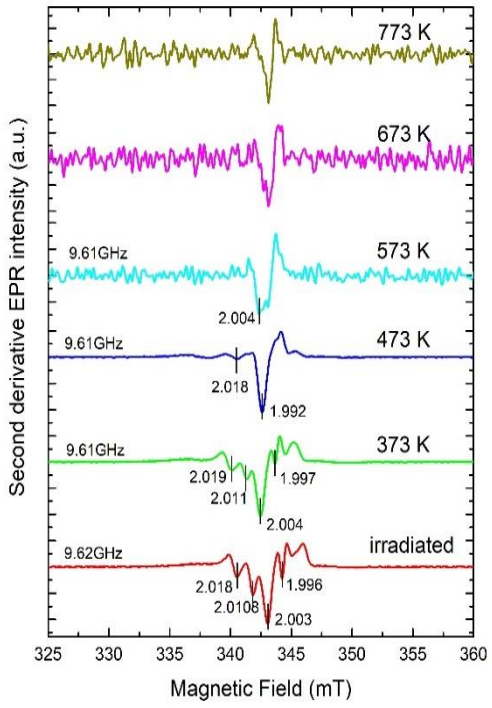

Figure 5.19 Peak-to-peak second derivative for spectra for LiNaBSi pristine and irradiated glass with 5 MGy and annealed for 24 hours at 373-773 K.

Figures 5.12 – 5.15 illustrate the first derivative peak-to-peak absorption intensity versus the magnetic field (in mT) of the EPR spectra for LiNaBSi glasses irradiated with 0.5 and 5 MGy at room temperature and annealed at 373 - 773 K for 16 and 24 hours. The second-derivative peak-to-peak absorption intensity versus the magnetic field of EPR spectra for these glasses is given in Figures 5.16 – 5.19. A shoulder at about g~1.997 disappears after annealing LiNaBSi glasses irradiated with 0.5 MGy at 373 K for 16 and 24 hours as illustrated in Figure 5.16 and 5.17, respectively. Except for this signal at g~1.997, all the other paramagnetic centres which are present in the irradiated unannealed glasses remain after annealing at 373 K for 16 and 24 hours. In Figure 5.16, a new EPR resonance signal arises with values of g ≈2.004, 1.999 along with a low-intensity signal near to them after annealing at 473 K. This signal could be due to POR's [27,57,174,232]. The peak-to-peak intensity for this signal after annealing at higher than 573 K decreases, indicating decreased abundance due to recombination / annihilation or different stages of annealing of POR's as discussed previously in this section. The line shape after annealing at temperatures higher than 573 K resembles that for E' centres (electrons trapped at silicate tetrahedra) as shown in Figure 5.12, but with a broader linewidth than has been reported in literature for E' (0.25 mT [27,57]). At g values ≈ 2.017, 2.005, 2.000 the EPR signal can be attributed to the POR's shown in Figure 5.13 and a low-intensity signal at g ~1.992 is also observed near to it when annealed at 473 K for 24 hours, which can be attributable to ET centre [28,57,251]. These two EPR resonances remain after annealing at 573 K, however, the S/N peak-to-peak intensity decreases at higher temperatures indicating gradual recombination / annihilation.

In Figures 5.18 and 5.19, EPR signals for LiNaBSi glass irradiated with 5 MGy and annealed at 373 K at 16 and 24 hours, respectively, remain stable. EPR resonance for these glasses when annealed at 473 K has a shape (refs [28,57] for the shape of PORs) which is consistent with PORs (Figure 5.14 and 5.15). The EPR signal for PORs remains at 573 K and S/N peak-to-peak intensity decreases with increasing with no or minimal effects of the duration of annealing on the types of defects and their stability.

Figures 5.20 – 5.23 show a decreasing trend in the integrated spectral area with increasing temperature (temperature versus log integrated spectral area) for

NaBaBSi and LiNaBSi glasses irradiated with 0.5 and 5 MGy and annealed at 373-773 K for 16 and 24 hours. This decrease in log (area) indicates decrease in the concentration of paramagnetic defects due to annealing with increasing temperatures. It can be inferred that within the temperature range 373-573 K most of the defects are destroyed/annealed while there are defects such as POR's which are not destroyed/annealed (S/N peak-to-peak intensity become low though) even at temperatures which are closer to glass transition temperatures for both LiNaBSi an NaBaBSi glasses [129,137]. We suggest based on our results that if the annealing time is increased then all the defects can be destroyed.

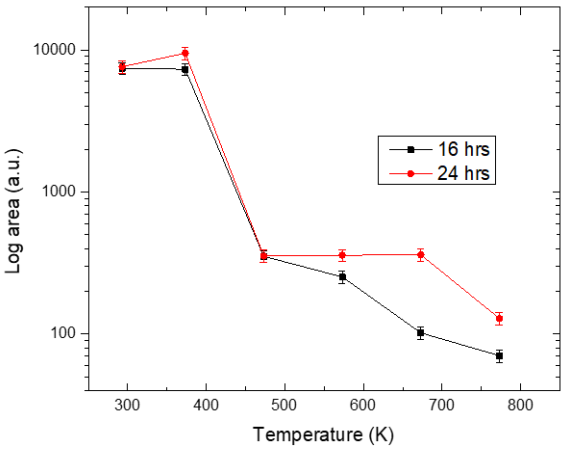

Figure 5. 20 Integral (Temp. vs Log area) for the first derivative EPR intensity curve for NaBaBSi glass irradiated with 0.5 MGy gamma and annealed at 16 and 24 hours.

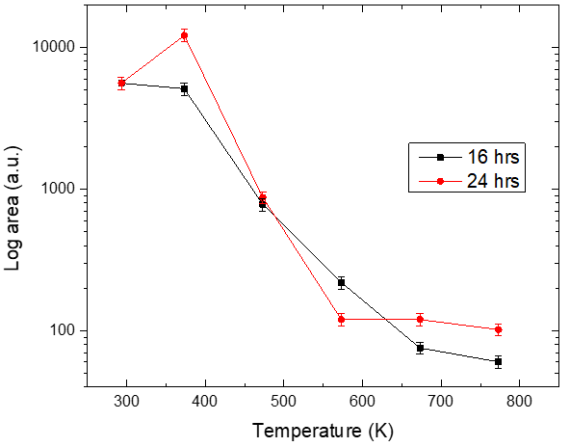

Figure 5. 21 Integral (Temp. vs Log area) for the first derivative EPR intensity curve for NaBaBSi glass irradiated with 5 MGy gamma and annealed at 16 and 24 hours.

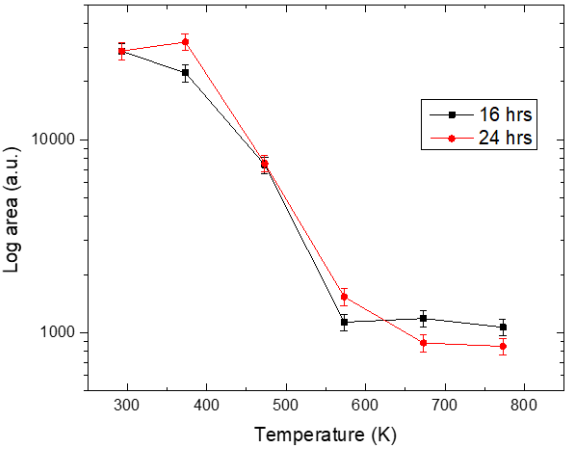

Figure 5. 22 Integral (Temp. vs Log area) for the first derivative EPR intensity curve for LiNaBSi glass irradiated with 0.5 MGy gamma and annealed at 16 and 24 hours.

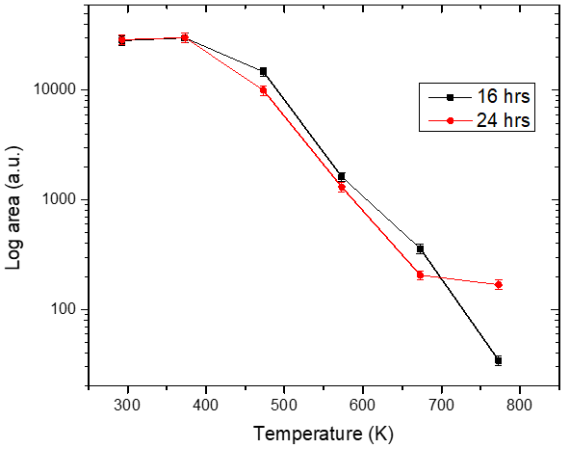

Figure 5. 23 Integral (Temp. vs Log area) for the first derivative EPR intensity curve for LiNaBSi glass irradiated with 5 MGy gamma and annealed at 16 and 24 hours.

5.3.4 Raman spectroscopy

Figure 5.24 illustrates stacked Raman spectra for NaBaBSi pristine and gamma-irradiated glasses with doses of 0.5 and 5 MGy. In each Figure spectra are divided into three regions. Region between 200 and 850 cm^{-1} is the first region and it mainly consists of breathing modes of borate or borosilicate structural ring unit groups and mixed stretching and bending modes of Si-O-Si vibrational units [37,172,183,195,235]. There is a broad band present for pristine as well as irradiated glasses at ~ 530 cm^{-1} is due to bending and stretching vibration modes of Si-O-Si units [236,252,253]. The band at 630 cm^{-1} could be due to vibrations involving danburite units [235,236], however, this band is debated in literature, therefore, as stated before this cannot be considered a confident assignment here [212,236,237]. The band at ~ 750 cm^{-1} could be attributed to 4-coordinated diborate and boroxol ring units [37,128,195,237]. Region 2 is marked between 850-1250 cm^{-1}, can be referred to as the Si Q-speciation region and it includes peaks from Q^n silicon vibrational modes (where Q^n denotes a silicate tetrahedron and *n* is the number of bridging oxygens) [100,128,158,173,195,206,212,238,239]. In this region there are peaks at ~ 940 and ~1050 cm^{-1} which can be attributed to Q^2 and Q^3 (2 and 3 bridging oxygens, respectively) units [60,158,172,195,252] . Region 3, from 1200 to 1600 cm^{-1}, is the region of B-O vibrations units and includes a peak at about ~ 1450 cm^{-1} which is attributed to B-O vibrational units [195,235–237,240].

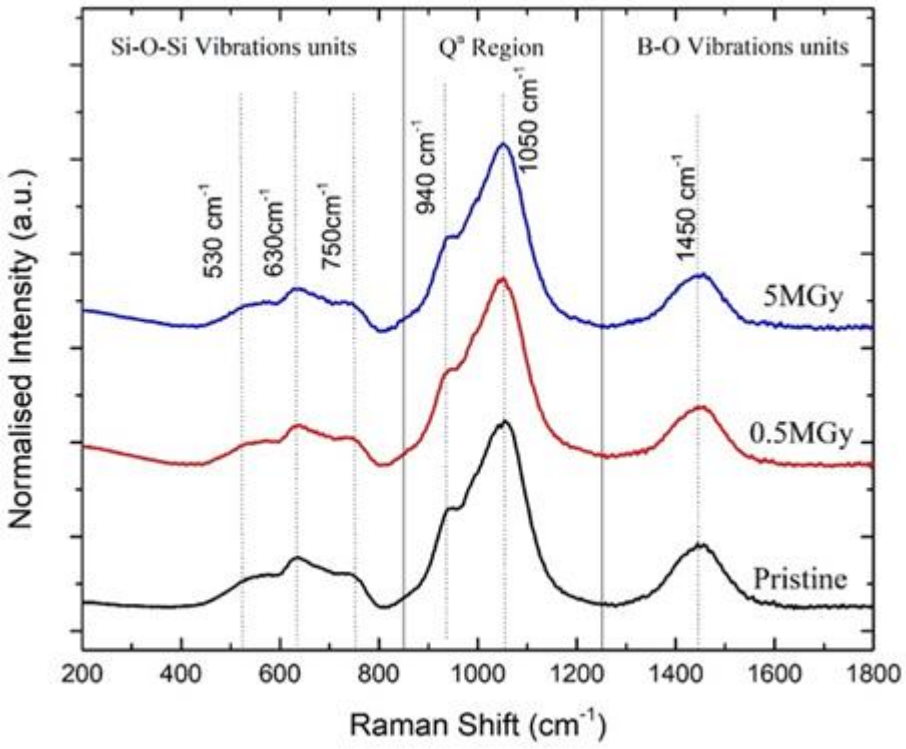

Figure 5.24 Raman spectra for NaBaBSi glasses: pristine and gamma irradiated with doses of 0.5 and 5MGy.

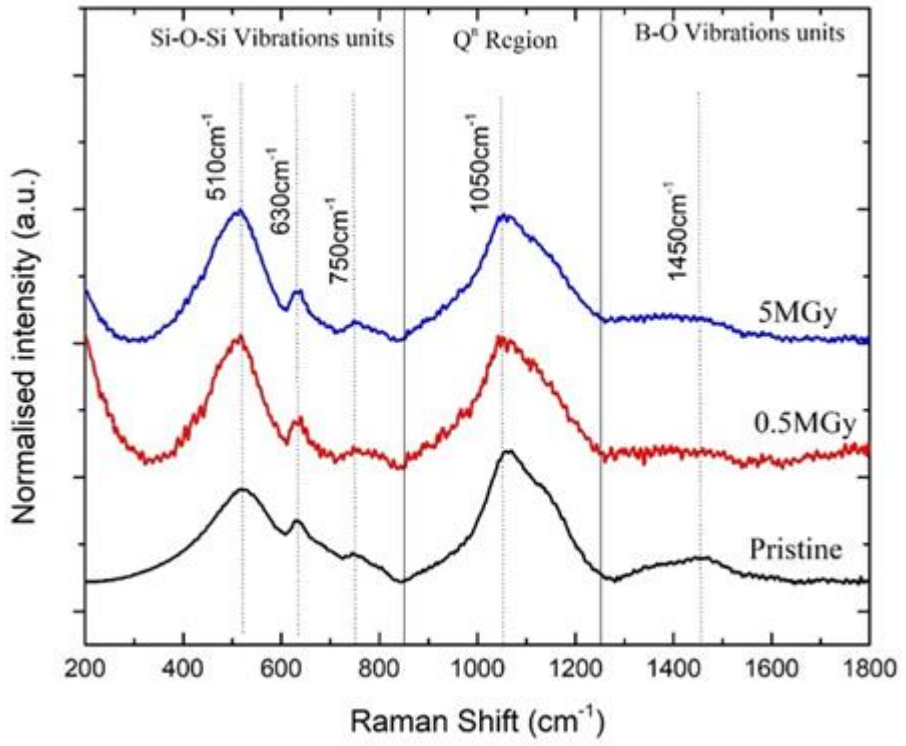

Figure 5. 25 Raman spectra for LiNaBSi glasses: pristine and gamma irradiated with doses of 0.5 and 5MGy.

Figure 5.25 illustrates Raman stacked spectra for pristine and gamma irradiated LiNaBSi glasses. Spectra have been normalised to the intensity of the highest peak in the pristine glass. Raman spectra were acquired and plotted between 100-2000 cm^{-1} and spectra have also been divided into three regions similar to the spectra for NaBaBSi glasses. A comparison with Raman spectra for NaBaBSi glasses has been made and suggests that notable differences in the Raman spectra of LiNaBSi glasses are: (1) increased intensities of peaks in region 1 and also an increase in the Si-O-Si vibration modes in the region 1 and as well as increase in the 4-coordinated diborate and boroxyl rings indicating network polymerisation; (2) a distinct shoulder at ~ 1150 cm^{-1} which could be attributed to Q^4 units [195,212,235]; and (3) decreased intensity of the peak at ~ 1450 cm^{-1} which indicates a decrease in the proportion of 3-coordinated boron [60,254].

5.3.5 UV-Vis-nIR optical absorption spectroscopy

In Figures 5.26 and 5.27 UV-Vis-nIR optical absorption spectra for pristine and irradiated glasses for NaBaBSi and LiNaBSi, respectively, are plotted Both spectra indicate that the pristine glasses are transparent in the UV-visible region. Broad optical absorption bands arise between 560-660 nm and 500-640 nm for the NaBaBSi and LiNaBSi gamma irradiated glass specimens, respectively. Gamma photons cause the breaking of the glass structural 3D network units [21,24,39,57,194]. This interaction with the glass structure causes the conversion of bridging oxygens (BOs) to non-bridging oxygen (NBOs) [57,194,232] .

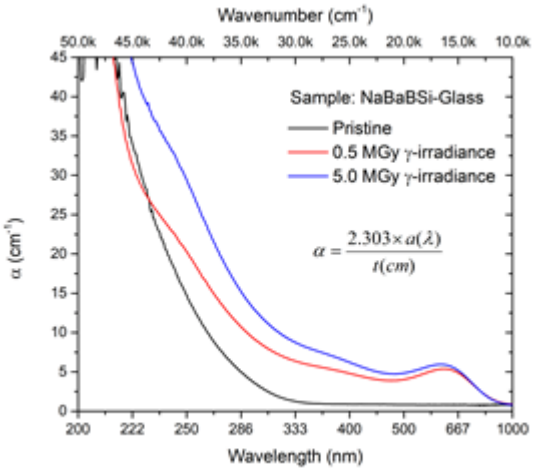

Figure 5.26 UV-Vis-nIR optical absorption spectra for pristine and irradiated NaBaBSi glasses.

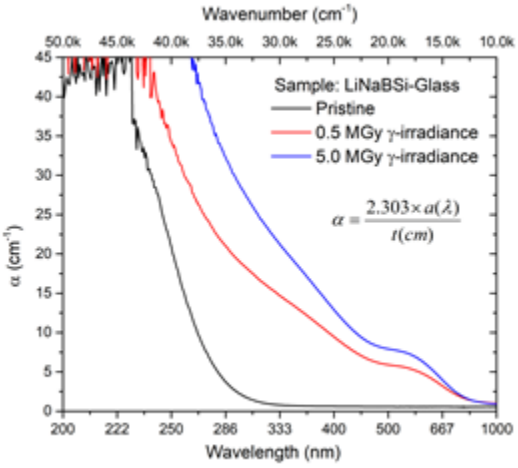

Figure 5.27 UV-Vis nIR optical absorption spectra for pristine and irradiated LiNaBSi glasses.

Table 5.3 gives the optical band gap energies calculated from Tauc-Plots. The relation between photon energy ($h\nu$) and absorption coefficient (α) is given by the equation $(\alpha h\nu)^{1/n} = \beta(h\nu - E_g)$, known as the Davis and Mott equation [255]. In this equation β is a constant, E_g is called the energy of the band gap and *n* is the factor of the transition mode, which is material dependent, and *n* equals 2 (with indirect gap) for glass systems [255,256]. When $(\alpha h\nu)^{1/n}$ is plotted versus the photon energy ($h\nu$), it gives a straight line and when this line is extrapolated the point where it intercepts the ($h\nu$)-axis gives the value of the optical energy gap [256,257]. The plot is called the Tauc-plot [257]. This method is not the most accurate methods to get the optical band gaps energy, however, a decrease in the optical band gap energy as calculated using this method can be associated with defect centres formation as a result of irradiation. Figures 5.28 and 5.29 illustrate the optical band gap energies for 0 (pristine), irradiated with 0.5 MGy and 5 MGy NaBaBSi and LiNaBSi glass specimens, respectively. The transformation of BOs to NBOs as a consequence of interaction of gamma photons with the glass structure is another reason for decrease in the optical band gap energies with increasing gamma radiation dose as discussed.[194,258]. This decreasing band gap energies is an indication that glass network becomes compact after irradiation, this includes electronic defects and breaking of the B-O bonds. The compaction allows the structure to relax and fill the large interstices in the interconnected network of boron and oxygen [194].

Table 5. 3 Optical band gap energies for pristine and irradiated NaBaBSi and LiNaBSi glass specimens calculated from Tauc-plots.

	Band gap / eV	
Dose (MGy)	NaBaBSi	LiNaBSi
0	3.50	3.90
0.5	2.90	2.20
5	2.70	1.50

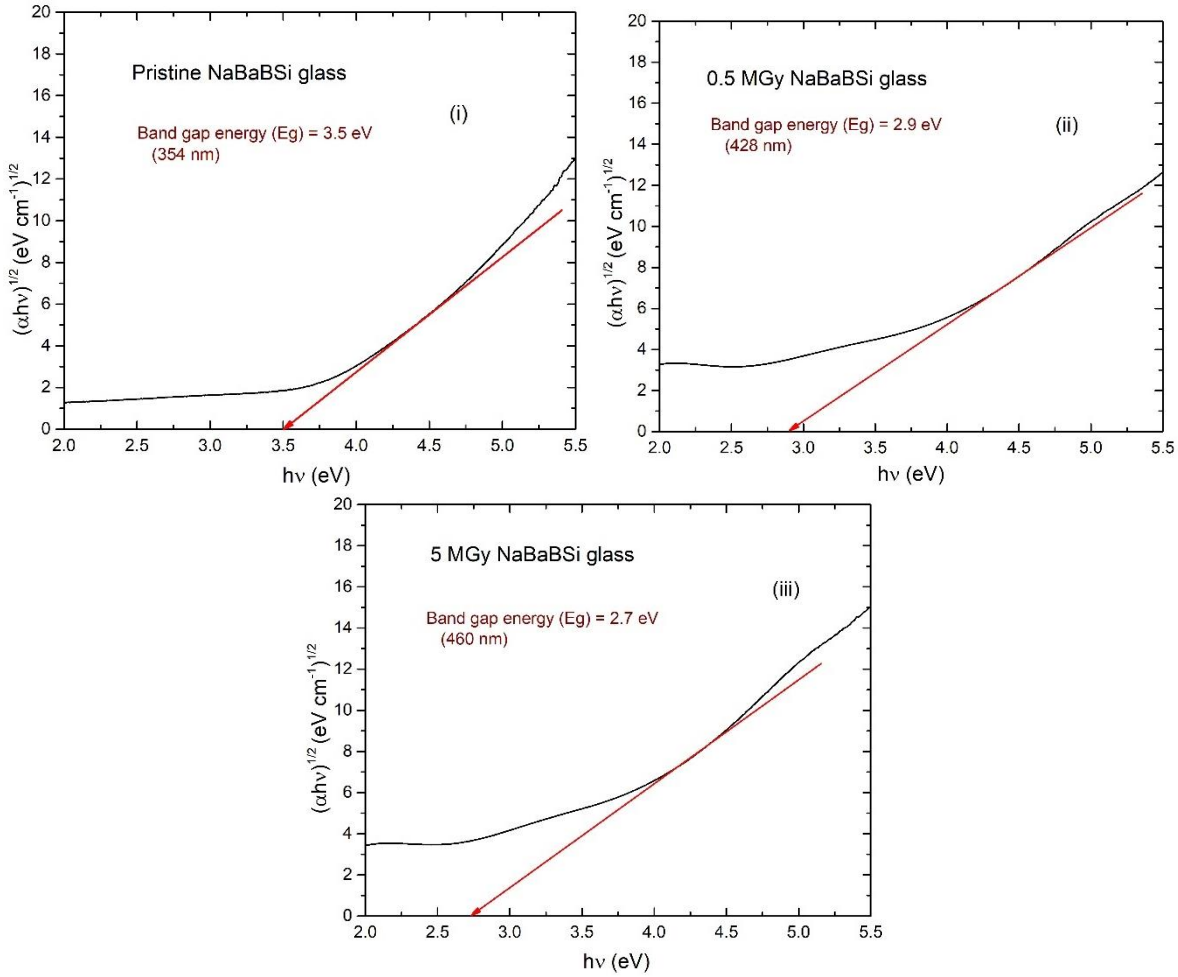

Figure 5. 28 Tauc-plots for (i) pristine and irradiated with (ii) 0.5 MGy and (iii) 5 MGy NaBaBSi glass specimens.

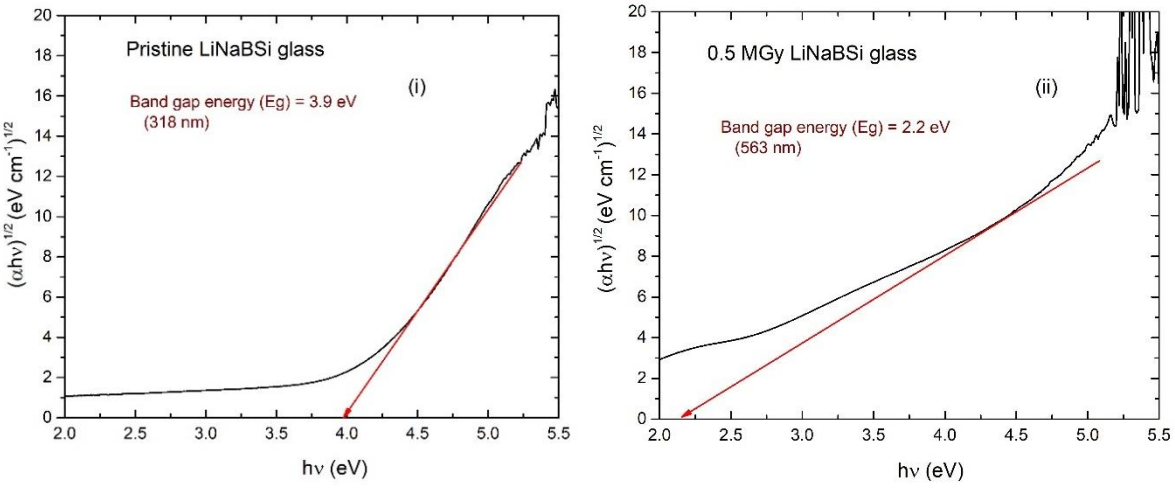

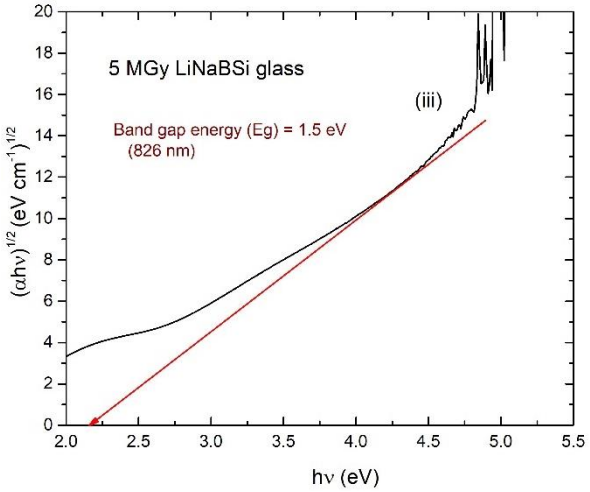

Figure 5. 29 Tauc-plots for (i) pristine and irradiated with (ii) 0.5 MGy and (iii) 5 MGy LiNaBSi glass specimens.

Deconvoluted UV-Vis-nIR optical absorption spectra for irradiated NaBaBSi and LiNaBSi glass specimens are illustrated in Figure 5.30 and 5.31, respectively. For both 0.5 and 5 MGy irradiated glass specimens four Gaussian peaks were fitted to spectra. Fitting parameters are given in Table B1 in Appendix B. There are two absorption bands at 639 nm and 657 nm fitted for NaBaBSi glass irradiated with 0.5 and 5 MGy, respectively, and these could be attributed to an overlapping paramagnetic defect centres comprising of E^- and POR's [259,260]. An absorption band at 629 nm was reported by Griscom *et al.* [259] which he attributed to PORs and another band at 566 nm which was attributed to non-bridging oxygen hole centres (NBOHC) in fused silica. In another study Mackey *et al.* [260] reported optical absorption bands for high-purity SiO_2-Na_2O glass irradiated with X-rays, in the range 600-730 nm and these were attributed to E^- centres. Fayad *et al.* [68] reported optical absorption bands between 500 and 600 nm in gamma-irradiated borosilicate glasses which they attributed to BOHC's and similarly absorption bands fitted to spectra for the NaBaBSi glasses in Figure 5.30 at 527 nm and 568 nm can also be attributed to BOHC's or hole trapped centres [261]. Jiang *et al.* [262] and Mackey *et al.* [263] have reported absorption bands due to Na^+ ions or electrons trapped at alkali ions and, based on their results, we can attribute the absorption bands present at 319 and 324 nm to trapped electrons of alkali or Na^+ ions (plasmon band); furthermore bands at 249 and 253 nm may be due to Fe trace impurities [65,242,261]. An optical absorption band at 568 nm for LiNaBSi glass irradiated with 0.5 MGy can be attributed to a combination of BOHC's and POR's and a band at 622

nm for the sample irradiated with 5 MGy is also attributed to BOHC's [261,264]. There are absorption bands fitted at 354, 376 and 551 nm which are also attributed to BOHC's [263,264]. The two absorption bands are attributed to ET centres at 274 and 289 nm and a band at 263 nm is attributed to Fe impurities [65,261,263,264].

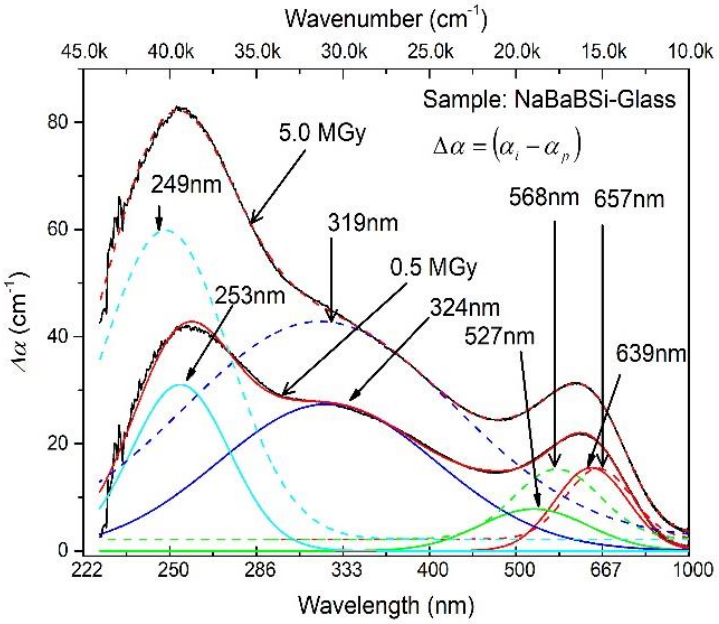

Figure 5. 30 Deconvoluted absorption spectra for NaBaBSi pristine and irradiated glass specimens.

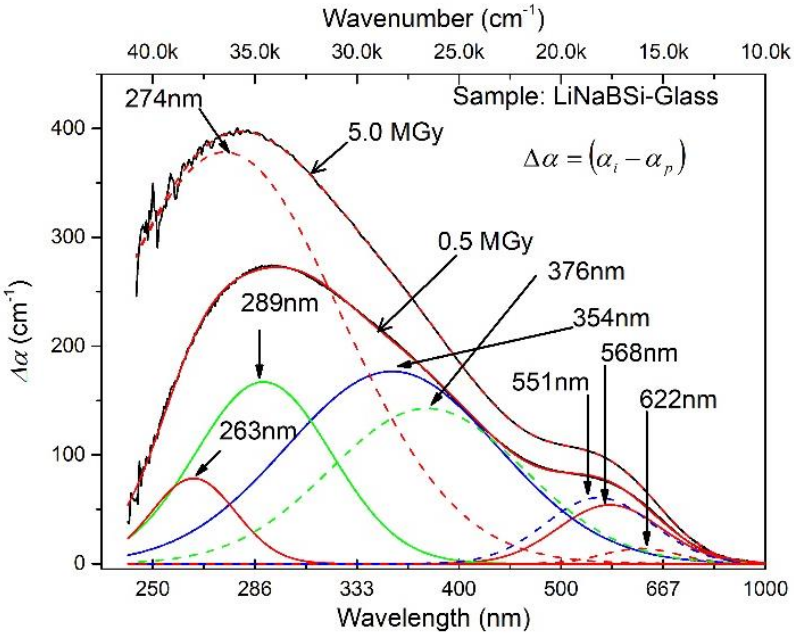

Figure 5. 31 Deconvoluted absorption spectra for LiNaBSi pristine and irradiated glass specimens.

Table 5. 4 Optical absorption bands fitted for NaBaBSi and LiNaBSi irradiated glass spectra and their corresponding defect types.

NaBaBSi		LiNaBSi	
0.5 MGy	**5 MGy**	**0.5 MGy**	**5 MGy**
639 nm (E^- centres + PORs) [259,260]	657 nm (E^- centres + PORs) [259,260]	568 nm (BOHC+ PORs) [259,261,264]	622 nm (BOHC) [264]
527 nm (BOHC)[261]	568 nm (BOHC)[261]	354 nm (BOHC)[264]	551 nm (BOHC)[261]
324 nm (E^- centre)[265]	319 nm (E^- centre)[265]	289 nm (ET centres)[263]	376 nm (BOHC) [264]
253 nm (Fe impurity)[242,261]	249 nm (Fe impurity)[242,261]	263 nm (Fe impurity)[242,261]	274 nm (ET centres) [263]

5.4 Discussion

5.4.1 Radiation-induced defects at room temperature

The fundamental interactions of gamma photons with glass produce electrons and hole pairs. Their mobility and dynamics within the glass structure depends on several factors such as composition (alkali, alkaline earths, rare earths, and transition metals), thermal annealing etc. [26,31,171,266,267]. Weber *et al*. [39] and Boizot *et al.* [26] suggested that these electrons can trap on alkali ions present in the base glasses and can cluster in the form of metallic colloids via similar mechanisms as have been reported and known for alkali halide crystals such as NaCl [39,250,268,269]. Agglomeration of radiation-induced defects can also happen when submitted to high irradiation doses or under induced magnetic fields [179]. In a study carried out by Howitt *et al.* [166], they proposed some mechanisms which could be responsible for the formation of metallic sodium in sodium silicate glasses. On this basis it is suspected that metallic sodium clusters can also form in borosilicate glasses via similar mechanism as reported for alkali halide crystals. The following three equations explain the mechanisms by which metallic sodium colloids might form in the glass:

Si-O-Si or B-O-B (formation of NBOs by irradiation by modifier or radiation) (1)

$Si\text{-}O\cdots\ Na^{+} + hv \rightarrow Si\text{-}O: + Na^{+}$ (breaking of ionic or electrostatic bond) (2)

$Si\text{-}O: + Na^{+} + hv \rightarrow Si\text{-}O\cdot + Na$ (creation of oxide radical and metallic Na) (3)

An evidence found by EPR was given by Hassib *et al.* [270], they measured a resonance signal at g = 2.011 due to sodium colloids formed by the collapse of F-centres in sodalite ($Na_8(Al_6Si_6O_{24})Cl_2$). In a different study by Zatsepin *et al.* [176] also presented evidence of metallic colloids/E^- centres at g = 1.97 at higher magnetic fields (~345-350 mT), in Na/K silicate glasses.

Optical absorption spectroscopy has also long been a key technique to study radiation-induced defects or “colour centres” and is often used as a complimentary technique to EPR. UV-Vis-nIR optical absorption spectroscopy gives absorption bands in UV, visible and near infrared region when electrons and hole trapped at defect sites within the glass structure undergo electronic transition following absorption [269]. Atomically dispersed metallic/colloidal sodium in different materials gives a plasmon absorption band and this is a strong evidence along with a blue colour which is often induced by the presence of atomically dispersed metallic sodium within the glass structure [26,31,171,266,271]. There are several reports in the literature confirming the presence of metallic sodium in different materials using a range of techniques along with the most used EPR and optical absorption. The location of the plasmon absorption band can be at different wavelengths depending on the size and shape of the metallic colloids [266,267]. In a series of studies, Groote *et al.* [269,272–274] investigated electron irradiated NaCl crystal and reported a broad optical absorption band centred at 550-600 nm. They further suggested, based on differential scanning calorimetry (DSC) results that metallic sodium if present in different shapes and sizes within the crystal shows different melting behaviour. Wesełucha-Birczyńska *et al.* [268] investigated natural halite and reported a plasmon band at 629 nm for navy blue single crystals and at 621 nm for blue samples (see ref [268] for detailed study). Tsai *et al.* [177] investigated silicate glasses irradiated with gamma radiation and found an EPR signal at g~2.01 and an absorption band in the range 360-540 nm. Jiang *et al.* [275] investigated electron irradiated sodium silicate glass and used electron energy loss spectroscopy (EELS) and showed the formation of metallic sodium which they identified by bulk plasmon band at 5.8 eV. Bochkareva *et al.* [266] investigated Na doped silicate glasses and

reported a plasmon resonance absorption band around 405-410 nm. Mackey *et al.* [260,263] also reported the presence of Na nanoparticles using a resonance plasmon absorption band at 680 nm. The list in Table B2 in Appendix B is not exhaustive but presents a summary of evidence confirming the formation of metallic colloids in irradiated alkali-halide crystals and different glass systems, identified using mainly EPR and optical absorption spectroscopies along with a range of other techniques. While BOHCs and ET centres are common defect centres in both NaBaBSi and LiNaBSi glasses irradiated with 0.5 and 5 MGy gamma, a broad isotropic signal at g~2.011 and other signal at g ~1.97 is attributed to metallic sodium colloids in the NaBaBSi glass alone. The difference in the peak intensity for samples irradiated with two different doses suggest different concentration of defects. Optical absorption bands fitted for both the base glasses irradiated with 0.5 and 5 MGy gamma, assigned to BOHCs, PORs and ET centres as common defect centres in both the glasses (details are given in Table 5.4). Optical absorption band at 319 and 324 nm has been assigned to E^- centres present in only NaBaBSi glass [263,265]. This defect centre is also identified at higher wavelengths, 639 and 675 nm [259,260]. Characteristics optical absorption band for Fe are present at 249, 253 and 263 nm [242,261].

5.4.2 Effects of glass composition and structure

Mixed alkali effects in glass are defined as a deviation from linearity between physical properties of a glass and composition when the relative proportion of alkalis is changed in a mixed alkali glass [276,277]. Mixed alkali effects in a glass may have several impacts on glass modifier mixing (homogenous or clustered), cation diffusivities and agglomeration or nucleation of crystals [146]. The concentration of Na is lower in LiNaBSi glass than in NaBaBSi glass (concentration of Na in NaBaBSi glass is about double the concentration of Na in LiNaBSi glass) and Li^+ has higher cationic field strength than Na^+ which could be a reason of greater association of Li^+ with NBOs in within the glass structure than Na^+ as suggested by Mishra *et al.* [134] Kaushik *et al.* [136] and Mishra *et al.* [278]. Clustering of defects or alkali ions is also hindered by the heterogeneity and nanoscale immiscibility due to the mixed-alkali effect in LiNaBSi glass. Similarly in NaBaBSi glass, the concentration of Na^+ is higher than Ba^{2+}, the cationic field strength of Na^+ is also higher than Ba^{2+} and ionic radius of Na^+ is a smaller than Ba^{2+}, all these conditions favour the formation and

segregation of metallic sodium colloids via the trapping/capture of electrons by Na^+ [134,136,146,149]. These observations are further supported by results from the UV-Vis-nIR optical absorption measurements. A broad optical absorption band within the range 560-660 indicates the presence of sodium colloid particles in different sizes and shapes, inducing a blue colour to the glass. Compositional differences and more specifically the environment around the Na metallic sodium colloids could be the causes for different sizes and shapes and therefore, the different positions for plasmon resonance absorption band are reported by different authors for different materials. Due to the short spin-grid associated with ionic electron trapping defect centres, it is difficult to observe an evidence of them using room temperature EPR measurements as suggested by Kordas *et al.* [180]. In a study by Griscom *et al.* [248], they suggested that electrons in sodium and potassium borate glasses can be trapped at alkali ions and alkali clusters at temperatures ≤ 77K, however, in the present study, EPR signals due electrons trapped at sodium ions are measured at room temperature. The reason which can explain this phenomenon at room temperature is the resonance absorption of microwaves by conduction electrons that have formed sodium metallic colloids/nanoparticle of small size.

5.4.3 Effects of thermal annealing on radiation induced defects

In Figure 5.8 and 5.9, no EPR signals in NaBaBSi glass irradiated with 0.5 MGy, remain stable at temperatures higher than 473 K when annealed for 16 and 24 hours, respectively. This suggests electron-hole recombination or annihilation is enabled by the thermal energy, and at higher temperatures no paramagnetic defects generated at 0.5 MGy remain stable [279]. The two resonance EPR signal at g~1.97 (due to E^- centres) and g~2.011 both may be due to sodium colloids. After annealing at 473 K the signal due to E^- centres at g~1.97 remains stable whereas the broad, isotropic signal at g~2.011 disappeared after annealing at 373 K. The difference in the thermal stability of the defect centres suggest that sodium colloids of different shape and size have different melting temperatures [272] or this indicates that there are different sized metallic sodium colloids present/forming in the glass.

Thermal energy provided to irradiated glass specimens can enable the charged particle to undergo a transition or move and occupy different sites and because of this new defect centres can appear as we have observed in the form of a combination of signals due to E' and ET centres after thermal annealing. The

appearance of an underlying signal due to PORs in glass specimen irradiated at the higher dose of 5 MGy when annealed at 473 K for 16 hours as well as 24 hours is another observation of thermal-energy enabled revelation of simpler signals from a combination of multiple signals (complex signals) [31,57]. This signal is due to POR's remains stable at 573 K, and when annealed at higher temperatures their abundance becomes low due to possible recombination/annihilation and hence the S/N peak-to-peak intensity decreases. The following reaction shows the mechanism of formation of POR's in the glass structure; gamma photons interact and break the peroxy linkage [184], as shown in (4).

$$\text{Si-O-O-Si} + h\nu \rightarrow \text{Si-O-O}\cdot + \cdot\,\text{Si} \quad (4)$$

A further interaction of POR's with a gamma photon can result in the formation of an E' (Si·) centre and molecular oxygen as shown in (5).

$$\text{Si-O-O}\cdot + h\nu \rightarrow \text{Si}\cdot + O_2 \quad (5)$$

Reaction 5 suggests that thermal energy can possibly remove POR's by converting them to E' and molecular oxygen at higher temperature [164,173]. In Figure 5.16 LiNaBSi glass specimens irradiated with low dose (0.5 MGy) the underlying resonance signals after annealing at 473 K are due to POR's [31,57]. The S/N peak-to-peak intensity decreases when annealed at higher temperatures. The S/N peak-to-peak intensity is higher when irradiated at higher temperatures for glass specimen irradiated at higher does (5 MGy) indicating the increased concentration of number of defects with increased dose.

Peroxy radicals (POR's) are thermally stable at CCC temperatures and can be the precursors for molecular oxygen and E' centres, in both studied glasses. These CCC temperatures may be of relevance to geological repository disposal in future technical assessments that may consider higher temperatures [131]. The thermal energy enables these microstructural changes to relax with time as demonstrated here by the decreasing intensities of EPR signals after thermal annealing at a range of temperatures. However, the microstructural changes can lead to permanent changes, in addition to cumulative effects from ionisation and collisional interactions by beta and alpha particles. These permanent changes may have deteriorating impacts on structural integrity, performance, and long-term durability of the waste form. Investigations in the literature have shown that glass structure settles down

much below the glass transition temperature and there are no decoupled vibrating modes from the glass structural network, however, some modes can exist and remain active and continue to be active in the glassy state during cooling of the glass [21]. The glass network stabilises near the glass transition temperature (T_g) and annihilation and migration of the radiation-induced defects is reduced which allows them to persist at higher temperatures, as shown by this work.

Boizot *et al.* [183] investigated three simple glass compositions under beta irradiation. Raman spectroscopic results reported an increase in silicate network polymerisation due to relative increase of the Q^3/Q^2 species concentration, increase in the concentration of molecular oxygen (O_2) and decrease in the average Si-O-Si bond angle for beta irradiated samples in comparison to unirradiated samples. They suggested that this structural change occur due to the migration and aggregation of sodium ions under beta irradiation. Abbas *et al.* [172] investigated structural evolution of two simple glasses upon alpha and Kr-ion implantation. No evidence of molecular oxygen or any substantial structural changes or any new bands that could be attributed to the formation of molecular oxygen or no significant changes in the boron region were noted using Raman spectroscopic study.

We propose, based on the outcomes of this study, that a further investigation of Q^n units (n is number of bridging oxygens in Si tetrahedron) using other techniques such as ^{29}Si and ^{11}B MAS-NMR may provide more information structural evolution under gamma irradiation. Other techniques such as TEM can give information at nanoscale or other techniques uses bulk-irradiated samples for both the glasses would be useful to develop further understanding of the characteristics of metallic sodium colloids.

5.4.4 Effects of multivalent elements on radiation-induced defects

Many multivalent elements that form a part of the final HLW composition arise at different stages of nuclear fuel cycle and by different processes involved in nuclear power production. Their redox chemistry is very complex within a glass [67]. Their behaviour during and after melting depends on the stable oxidation state, they exist within a glass. While some of these for e.g., Mo, Ru, S etc. can be problematic in terms of their solubility, processing, leachability, foaming and so on, many are responsible for mitigation of defect centres or act as defect trapping centres [67].

Many research studies present in the literature that have reported the mitigation of radiation-induced defects by trapping of free electrons and holes by multivalent cations such as rare earths (Yb, Gd, Eu) and transition metals (Fe, Mn, Cr) [6,134,206,279–281]. This defect-hopping or electron/holes trapping process can also occur in NaBaBSi and LiNaBSi glasses loaded with HLW under optimum redox conditions. The formation of radiation-induced Na colloids may also be mitigated or hindered in NaBaBSi glass doped with actual HLW waste components [104].

5.5 Conclusions

Gamma irradiation induced defect were studied in NaBaBSi and LiNaBSi glasses and both the glasses were irradiated with 0.5 and 5 MGy of gamma. This study was conducted with the objective to improve the fundamental understanding of the types of radiation-induced defects and to establish a study of their thermal stability at geological repository relevant temperatures. A further aim of this study was to investigate how/whether these are affected by glass compositions. The techniques employed to perform this study were X-band EPR spectroscopy, UV-Vis-nIR optical absorption and Raman spectroscopies. In NaBaBSi glass irradiated at low (0.5 MGy) and high (5 MGy) doses, the paramagnetic defect centres identified are BOHC's, E^- centres (g~1.97) and isotropic signal at g~2.011 both due to the colloidal metallic sodium particles. UV-Vis-nIR optical absorption bands for NaBaBSi glass due to E^- centres at 639 and 657 nm, confirms the presence of metallic sodium colloids and the blue colour of the irradiated samples. These investigations were supported by evidence from the literature. In addition, optical absorption bands due to POR's, BOHC's and electron trapped centres were also observed. In LiNaBSi glass BOHC's, ET centres were found at both the doses. Thermal annealing of both the glasses above 373 K enables the annihilation / recombination of the defects, whereas in the LiNaBSi glass, POR's are stable at 473 K and show decreasing S/N peak-to-peak intensity with increasing temperature. POR's or O_2^- interstitials are stable in the LiNaBSi glass irradiated with 5 MGy at temperatures higher than 573 K, whereas the NaBaBSi glass irradiated with 5 MGy showed comparatively low S/N peak-to-peak intensity at higher temperatures. The presence of sodium metallic colloids of differing sizes is a strong indication of radiation-induced formation of nanoparticles.

Chapter 6. Gamma Irradiated – SON68, ISG, CaZn and Waste Loaded and Fe_2O_3-doped Glasses

6.1 Introduction and background

This chapter discusses the beta-gamma radiation effects in three simple glasses: SON68, International Simple Glass (ISG) and CaZn. SON68 glass is an inactive version of French R7T7 [23,24] as discussed in Section 3.1.1.1. ISG is a reference glass proposed by six collaborating nations to undertake chemical durability and glass corrosion related studies [23,24,55]. CaZn, also called as MWCZ is the modified version of MW glass containing Ca and Zn [132,203,204]. This glass is also discussed in Section 3.1.1.1. All three simple glasses were irradiated using ^{60}Co gamma source to a dose of 5 MGy at the Dalton Cumbrian Facility, the University of Manchester [221] with the objective to develop a fundamental understanding of the radiation-induced paramagnetic defects in simple glasses with different compositions. Results obtained from room temperature EPR, UV-Vis-nIR optical absorption, and Raman spectroscopic characterisation techniques which were employed to investigate the glass samples before and after irradiations are discussed in Section 6.3. Section 6.4 presents result on simulated/non-active waste loaded NaBaBSi, LiNaBSi and SON68 glasses. Section 6.5 presents results from the gamma irradiation studies performed on Fe_2O_3 (in concentrations of 0.19, 0.99, 4.76 and 9.09 mol% Fe_2O_3) doped NaBaBSi and LiNaBSi simple glasses. This includes room temperature EPR and Mössbauer spectroscopic results. Section 6.6 discusses density measurements for NaBaBSi and LiNaBSi simple and doped with Fe_2O_3 glass samples before and after irradiations.

Mir *et al.,* [190] studied beta irradiation effects in a three-oxide sodium borosilicate (BS3) and a thirty oxide borosilicate glass (SON68). To simulate the beta-irradiations effects, electron beam of 2.3 MeV energy was used to implant doses ranging from 0.15 to 4.6 GGy at 350 K. Raman results [190] for highest dose (4.57 GGy) sample showed the silica network depolymerisation indicated by a relative decrease in the high-frequency side (>1140 cm^{-1}), an increase in the mid (>1050 cm^{-1}) and low frequency side (<1050 cm^{-1}), formation of molecular oxygen was suggested by a band at 1552 cm^{-1} [172,240], and the changes in the region from 750 to 780 cm^{-1} suggested an increase in the BO_3 population (the transformation of 4-coordinated

boron to 3-coordinated boron) (see ref. [190]). For low dose samples mild structural variations were observed and all the low dose irradiated samples showed similar trends (for detail see ref. [190]). Mir *et al.,* [37] carried out a different study for investigating radiation effects in BS3 glass. Glass was irradiated with 2.3 MeV electrons with doses of 0.15 and 4.6 GGy and subsequently with 96 MeV Xe ions. Raman spectroscopic results for pristine BS3 irradiated with 0.15 GGy did not show any visible structural changes. BS3 when irradiated with 4 x 10^{13} Xe.cm^{-2} and with 0.15 GGy + 4 x 10^{13} Xe.cm^{-2} showed similar Raman spectra. The relative intensity of the peak at 630 cm^{-1} [212,235,236] (could be due to danburite like configuration;4-coordinated boron atoms surrounded by 3-silicon atoms and 1 boron atom) decreased. There was an increase in the R-band (R-band is about ~490 cm^{-1} which gives an idea about average Si-O-Si and Si-O-B angles) position by 10 cm^{-1} in 4 x 10^{13} Xe.cm^{-2} irradiated glass from pristine glass [37,212]. An increase in the high-frequency side at 1460 cm^{-1} suggested an increase in the population of the BO_3 units with NBOs [37,212]. When BS3 glass sample was irradiated with higher electron (4.57 GGy) dose, significant structural changes were observed. The relative intensity of the broad band between 850 and 960 cm^{-1} increased and there was a decrease in the peak at 610 cm^{-1} [37]. This same sample was subsequently irradiated with 4 x 10^{13} Xe.cm^{-2}. A new peak emerged at 960 cm^{-1}. The intensity of the region close to 760 cm^{-1} (bands between 750 to 770 cm^{-1} [37,282,283] in borosilicate glasses are associated with symmetric breathing vibration of six-membered rings containing two and one BO_4 tetrahedra respectively) decreased and region close to 800 cm^{-1} (corresponds to boroxol rings [37,284], which are rings of BO_3 units) increased. There was a decrease in the peak at 630 cm^{-1}. Boizot *et al.,* [183] studied beta-irradiation effects in zirconium bearing three simple glasses, sodium borosilicate, sodium aluminoborosilicate and sodium-calcium aluminoborosilicate glasses also referred to as 4-,5- and 6-oxide glasses, respectively. Electrons with energy 2.5 MeV were used to irradiate the samples with three doses (3 x 10^8, 6 x10^8 and 10^9 Gy). Key findings of this study are discussed in Section 5.4.3. Boizot *et al.* [25] studied dose, dose rate and irradiation temperature effects in beta-irradiated 4-, 5- and 6-oxide glasses (aforementioned glasses) using EPR spectroscopy. Key findings of this study are discussed in Section 2.3.3.2.

There are no beta-gamma irradiation studies in ISG, however, there are few studies which reported the effects of ion irradiation to simulate the effects of alpha particle and alpha recoil in an alpha decay, in ISG glass. Peuget *et al.,* [55] investigated radiation effects in ISG glass. Irradiation were carried out by externally implanting Au-ions and by doping ISG glass with 0.7 wt% ^{244}Cm. Au-ions with multiple energies (see ref. [55]) and fluences ranging from 1.9 x 10^{12} to 5.5 x 10^{14} ions/cm^2 were used to irradiated ISG samples. Alpha-decay produces an alpha particle of energy around 5.8 MeV and a recoil nucleus of ^{240}Pu of 97 keV. Alpha decay dose increases periodically (reaches around 6 x 10^{18} alpha/g for the source used in this study, for more details ref. [55]). Pristine and irradiated samples were investigated for structural evolution using Raman spectroscopy. Both types of irradiation induce same structural changes except above 1250 cm^{-1} where the B-O stretching band is covered by a luminescence signal from Cm [55]. The band at 490 cm^{-1} was assigned to the bending and stretching modes of Si-O-Si bands and is shifted to higher wavenumbers for irradiated samples [36,55,235]. The contribution at around 600 cm^{-1} was assigned to vibration modes due to three membered SiO_4 rings [36,55,235], this band is also called as the D_2 band, and it was increased for both the irradiation conditions. A few studies on irradiation effects on SON68 and ISG are discussed in Section 4.1 [128,201].

6.2 Materials and methods

All the three simple glasses were synthesised using melt-quench and anneal method. The detailed process, melting parameters as well as the glass compositions are presented in Chapter 3. Glasses were cast in disc forms of thickness ~10 mm by pouring onto pre-heated steel plate. Glass specimens were irradiated with a single dose of 5 MGy at the Dalton Cumbrian Facility in a gamma irradiator with ^{60}Co sources which supply 1.17 -1.33 MeV energy photons with a dose rate of 0.5 to 350 Gy/min [221].

Figure 6.1 illustrates stacked diffraction pattern for SON68, ISG, CaZn glasses as well as for NaBaBSi and LiNaBSi glasses for a comparison. Detailed information on the diffractometers, geometry, and measurement parameters to record diffraction pattern for these glasses are given in Section 5.3.1. Stacked diffraction pattern for all five simple glasses show that these are X-ray amorphous and no crystalline phases

detected. Diffraction pattern for non-active waste loaded NaBaBSi, LiNaBSi and SON68 glasses are illustrated in Appendix E.

Multi-spectroscopic characterisation approach was used to characterise the glass specimens before and after irradiation. Raman and UV-Vis-nIR spectroscopies were used to characterise and investigate gamma-radiation induced structural, optical changes, respectively. Room temperature X-band EPR spectroscopy was employed to obtain information about the radiation-induced paramagnetic defects in glass samples before and after irradiation.

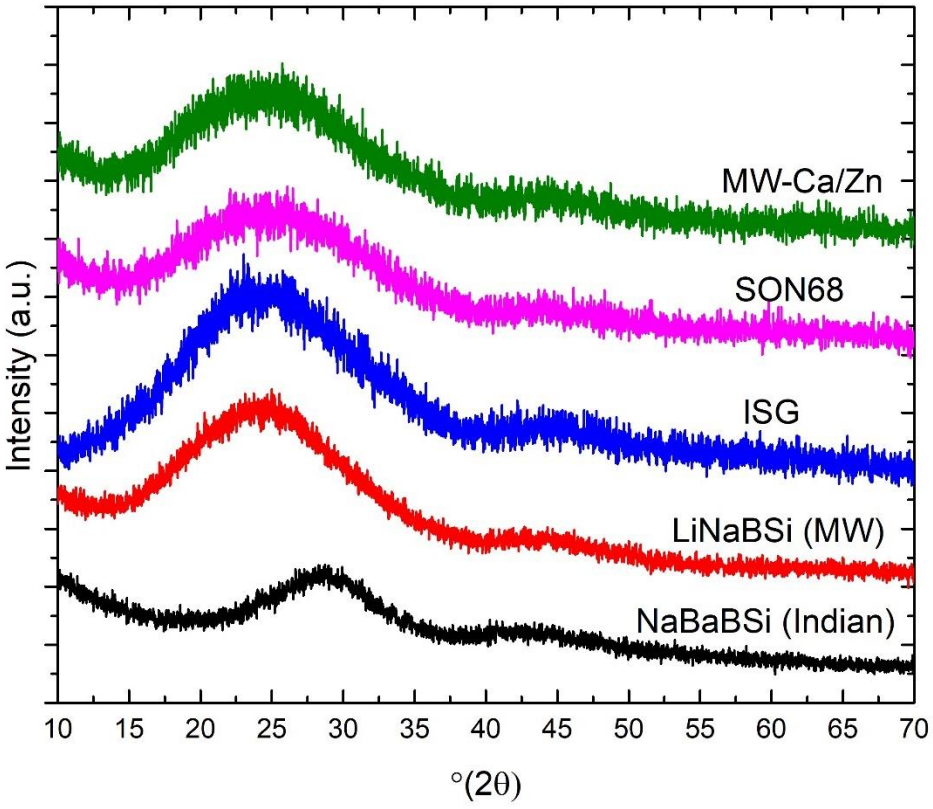

Figure 6. 1 Stacked XRD spectra for NaBaBSi (Indian), LiNaBSi (UK-MW), International simple glass (ISG), SON68 (French), and MW-CaZn (modified MW) pristine glasses.

Table 6. 1 Images of simple and waste loaded glasses.

Glass Type	SON68	ISG	CaZn
Image		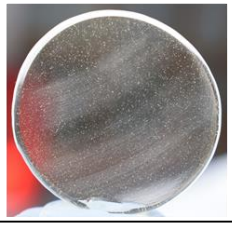	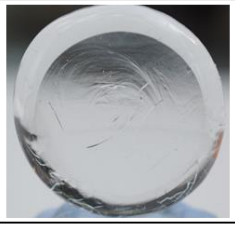
Thickness	~ 1 cm	~ 1 cm	~ 1cm
Glass Type	SON68 waste loaded	NaBaBSi waste loaded	LiNaBSi waste loaded
Image	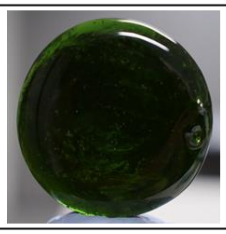		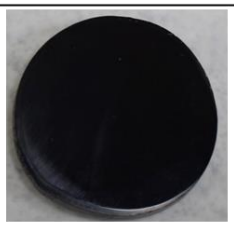
Thickness	~ 1 cm	~ 1 cm	~ 1 cm

6.3 Results – Simple glasses

6.3.1 Raman spectroscopy

Figures 6.2, 6.3 and 6.4 illustrate Raman stacked spectra for pristine and 5 MGy gamma irradiated SON68, ISG and MW-CaZn simple, respectively. Spectra for all the three samples are divided into three regions. First region is divided between the 200 and 850 cm^{-1}. This region mainly consists of breathing modes of borate or borosilicate structural ring unit groups and mixed stretching and bending modes of Si-O-Si vibrational units [37,172,183,195,235]. There is a band at 490 cm^{-1}, common in Raman spectra for both pristine and irradiated SON68 and ISG glasses illustrated by Figure 6.2 and 6.3, respectively. This band is attributed to bending and stretching modes of Si-O-Si vibrational units [36,37,55,203,206,235]. This similar band is located at 500 cm^{-1} in the Raman spectra for CaZn pristine and irradiated glass as illustrated from Figure 6.4 [36,37,55,203,206,235].

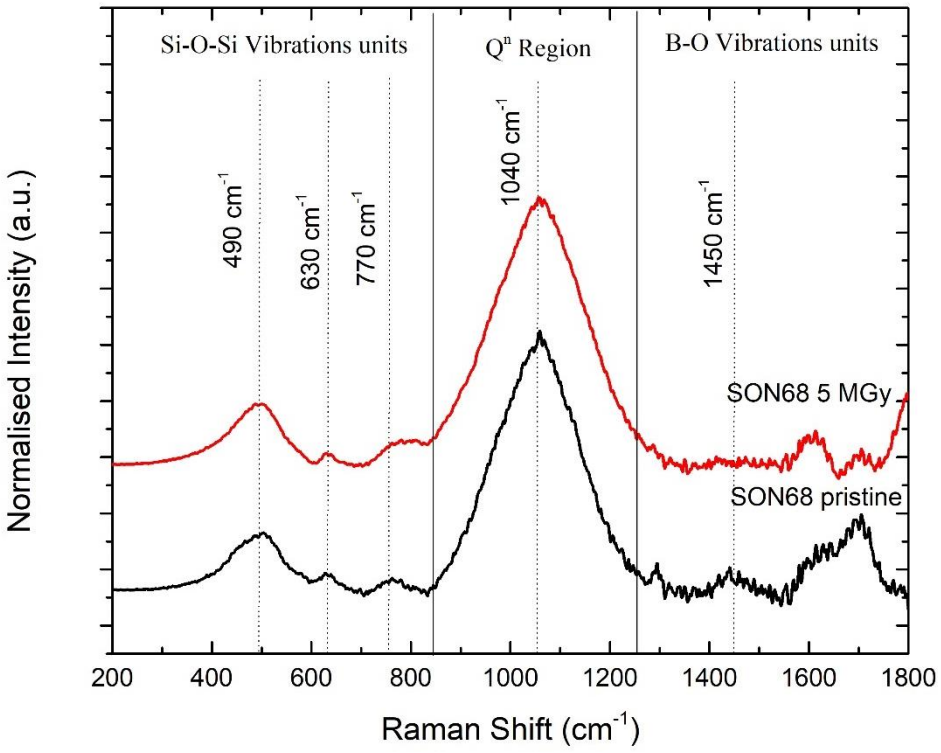

Figure 6. 2 Raman spectra for pristine and gamma irradiated with a dose of 5 MGy SON68 glass.

Raman peak at 630 cm^{-1} in all the three Raman spectra could be due to vibrations involving danburite units [235,236], however, this band is debated in literature, therefore, this cannot be considered a confident assignment here as previously discussed in Section 5.3.4. [212,236,237]. There is a notable difference in the intensities of this band for pristine and irradiated ISG glass Raman spectra (see Figure 6.3), however, there is no shift in the position of the band observed for pristine and irradiated Raman spectra for all the three glasses. Raman band at 770 cm^{-1} is also common in all the three spectra and this is associated with symmetric breathing vibrations of six member rings containing one BO_4 tetrahedra [37,128,195,237,282,283]. There is a change noted in the intensity of this band in pristine and irradiated Raman spectra for SON68 glass (see Figure 6.2).

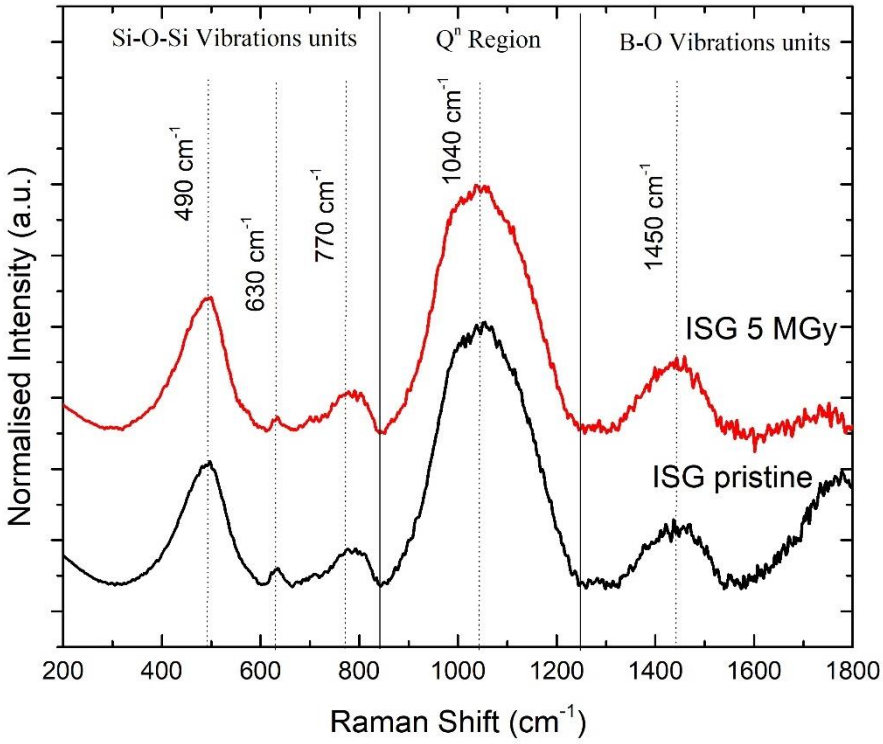

Figure 6. 3 Raman spectra for pristine and gamma irradiated with a dose of 5 MGy ISG glass.

The second region is between 850-1250 cm^{-1}, it is referred to as the Si Q-speciation region and includes peaks from Q^n silicon vibrational modes (where Q^n denotes a silicate tetrahedron and *n* is the number of bridging oxygens and $0 \leq n \leq 4$) [100,128,285,158,173,195,205,206,212,238,239]. Raman peak at 1040 cm^{-1} for Raman spectra for both SON68 and ISG is attributed to Q^3 silicon vibrational units [60,158,172,195,252].

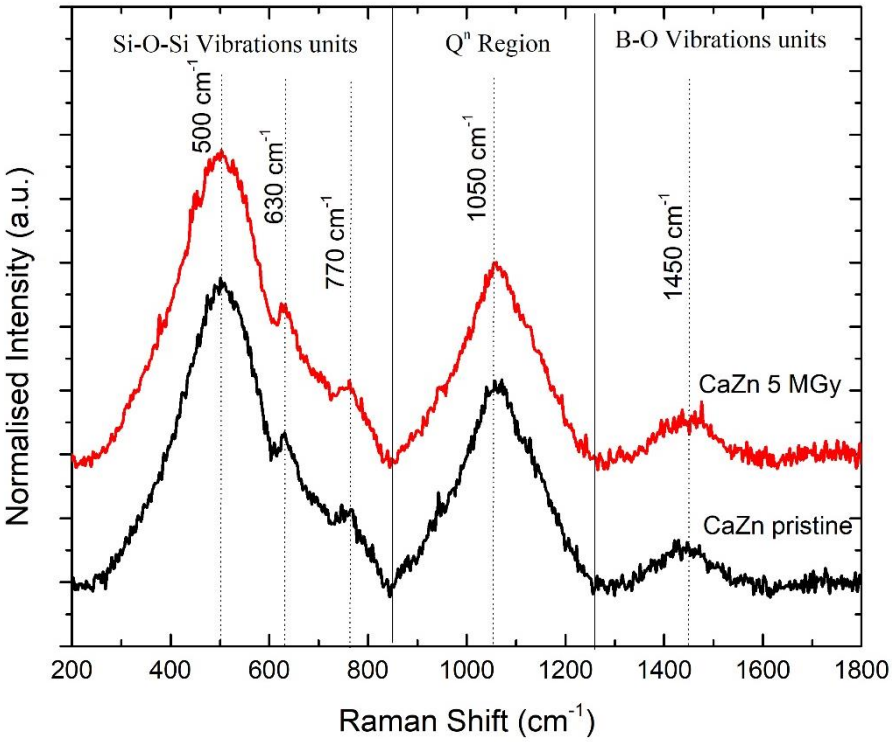

Figure 6. 4 Raman spectra for pristine and gamma irradiated with a dose of 5 MGy CaZn glass.

6.3.2 Electron paramagnetic resonance spectroscopy

Figure 6.5, 6.6 and 6.7 illustrate first derivative X-band (~9.6 GHz) room temperature EPR spectra for SON68, ISG and CaZn pristine and irradiated glasses with 5 MGy ^{60}Co gamma radiation, respectively. There is no EPR resonance signal observed for the pristine glass specimens. There is an EPR resonance signal present for irradiated glass samples which is centred at around g~2.00. From the first derivative EPR absorption signal for all the three simple glasses it can be inferred that these are complex signals that could be due to a contribution from multiple radiation induced paramagnetic centres. Thus, second derivative EPR spectrum for each glass type is produced to enhance the definition and further deconvolute the spectra, and to help investigate any underlying signals due to radiation-induced paramagnetic centres. Figures 6.8, 6.9 and 6.10 illustrate second derivative spectra for SON68, ISG and CaZn irradiated with 5 MGy ^{60}Co gamma radiation, respectively. The common defect centres found from second derivative EPR spectra for SON68, ISG and CaZn glasses were BOHCs which are centred around g~2.00 and ET centres which are centred around g~1.9. There is a signal at g~1.98 for EPR spectrum for CaZn glass (Figure 6.8) which could not be identified. Table 6.2 gives the g-values

calculated from experimental data and corresponding defect types for SON68, ISG and CaZn glasses.

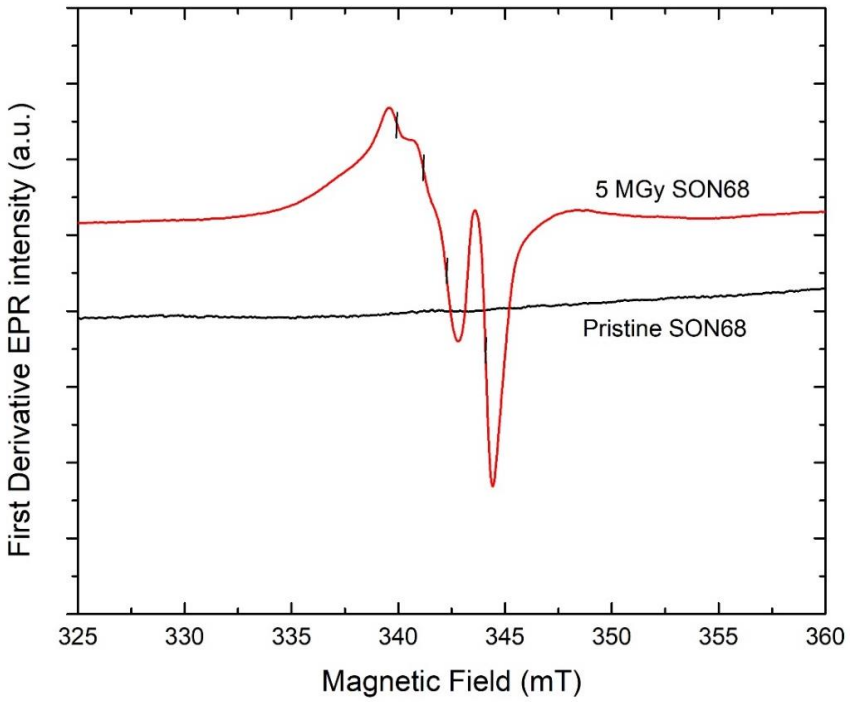

Figure 6. 5 First derivative room temperature X-band EPR spectra for SON68 pristine and gamma irradiated glass.

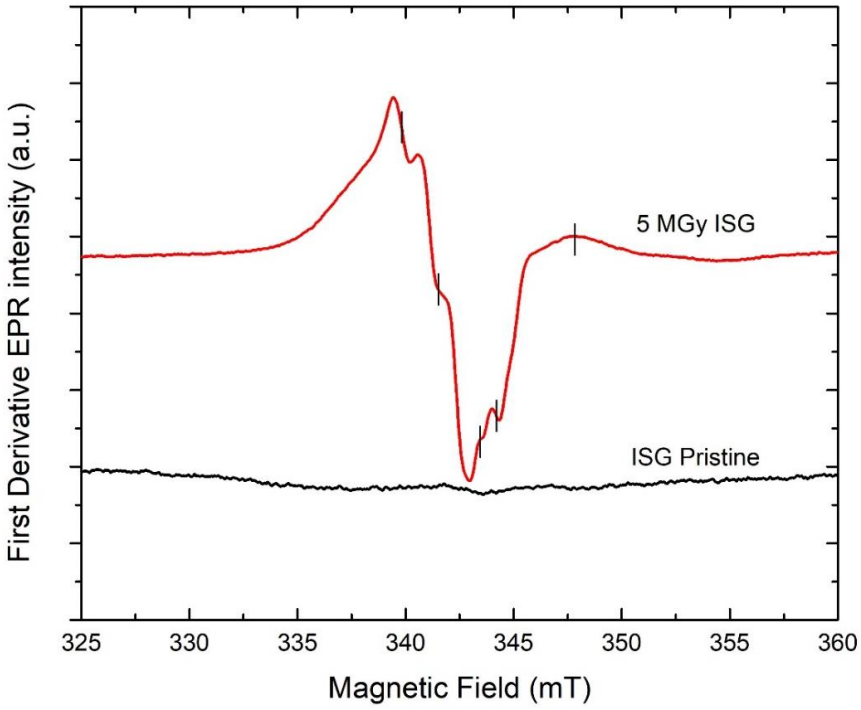

Figure 6. 6 First derivative room temperature X-band EPR spectra for ISG pristine and gamma irradiated glass.

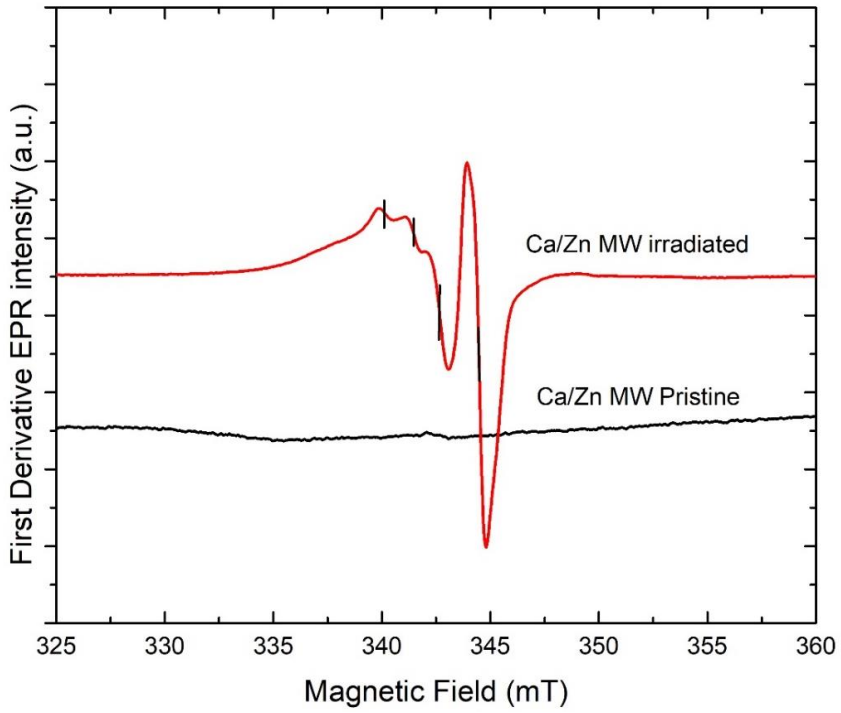

Figure 6. 7 First derivative room temperature X-band EPR spectra for CaZn pristine and gamma irradiated glass.

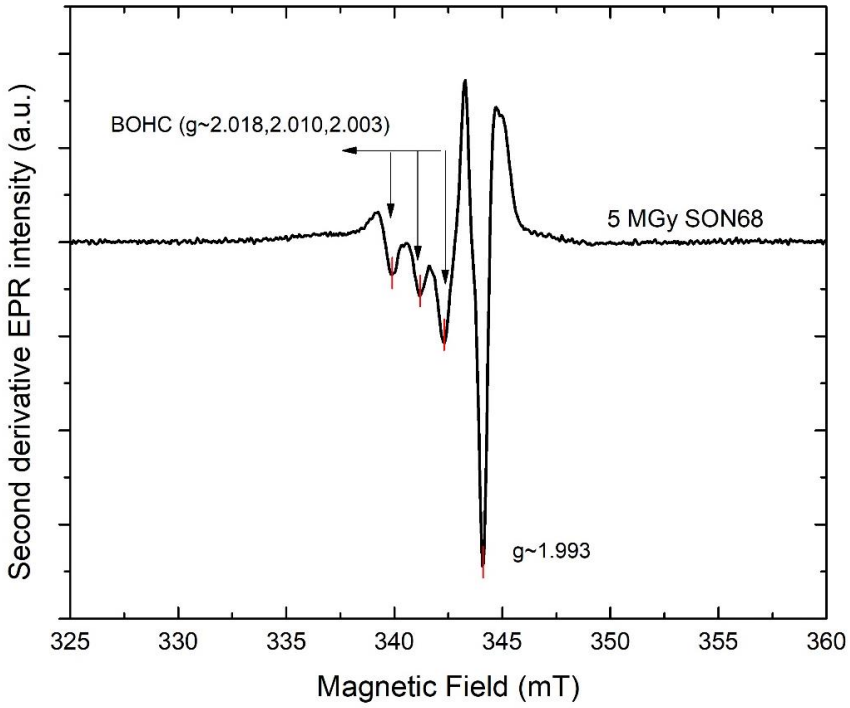

Figure 6. 8 Second derivative room temperature X-band EPR spectra for SON68 gamma irradiated glass.

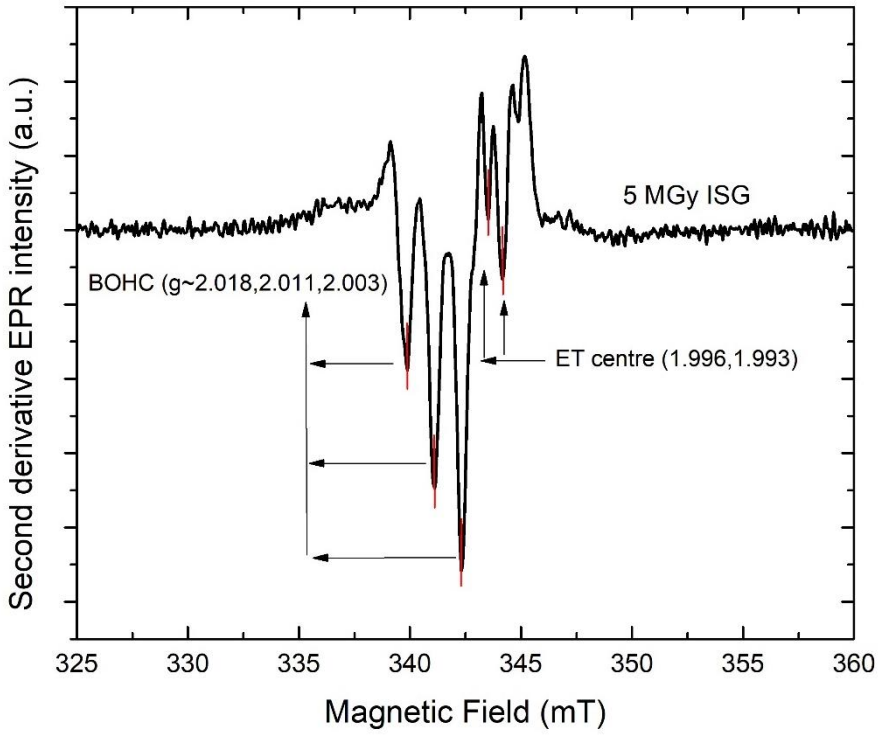

Figure 6. 9 Second derivative room temperature X-band EPR spectra for ISG gamma irradiated glass.

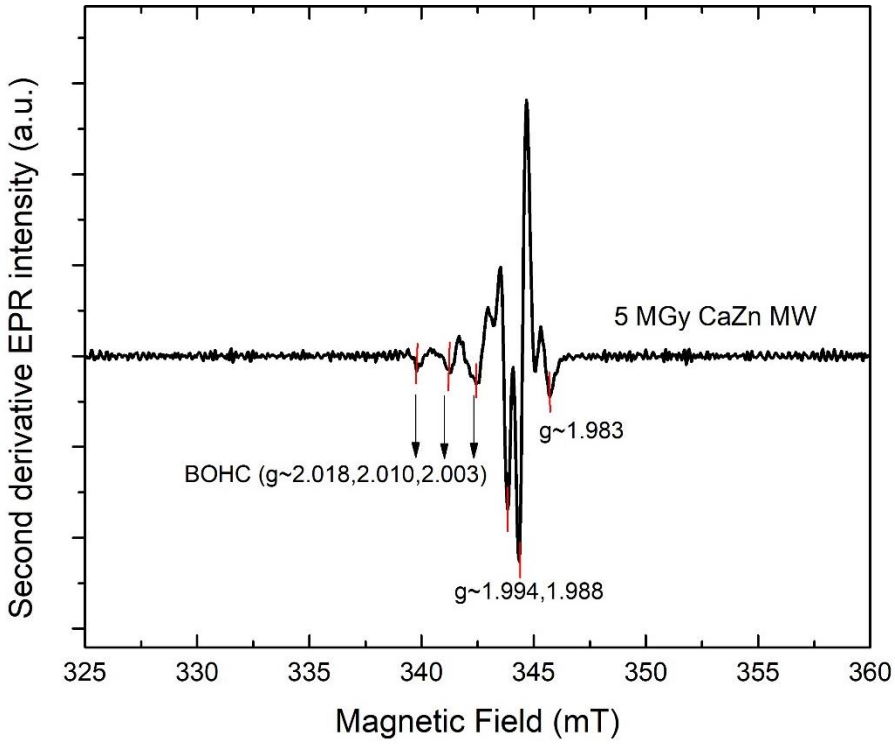

Figure 6. 10 Second derivative room temperature X-band EPR spectra for CaZn gamma irradiated glass.

Table 6. 2 The g-values calculated from experiments using the centre of the magnetic field where second derivative becomes negative [28,31,57,173,206].

SON68		ISG		CaZn	
g-value	**defect**	**g-value**	**defect**	**g-value**	**defect**
2.018	BOHC	2.018	BOHC	2.018	BOHC
2.010	BOHC	2.011	BOHC	2.010	BOHC
2.003	BOHC	2.003	BOHC	2.003	BOHC
1.993	ET	1.996	ET	1.994	ET
		1.993	ET	1.980	?

6.3.3 UV-Vis-nIR optical absorption spectroscopy

Figures 6.11, 6.12 and 6.13 illustrate UV-Vis-nIR optical absorption spectra for SON68, ISG and MW-CaZn pristine and irradiated glasses. It can be seen from three spectra that the pristine glasses are transparent in the UV-visible region. Broad optical absorption bands arise between 560-700 nm, 450-50 nm, and 500-650 nm for SON68, ISG and CaZn gamma irradiated glass specimens, respectively. Interactions of gamma photons result in the breaking of the glass structural 3D network units [21,24,39,57,194]. This leads to the conversion of bridging oxygens (BOs) to non-bridging oxygen (NBOs) [57,194,232].

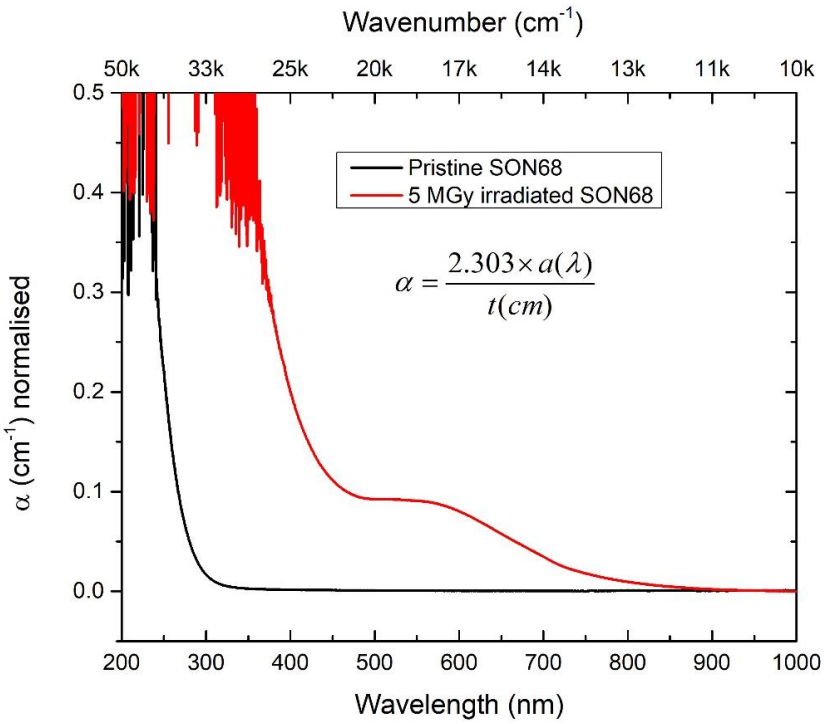

Figure 6. 11 UV-Vis-nIR optical absorption spectra for pristine and irradiated SON68 glass.

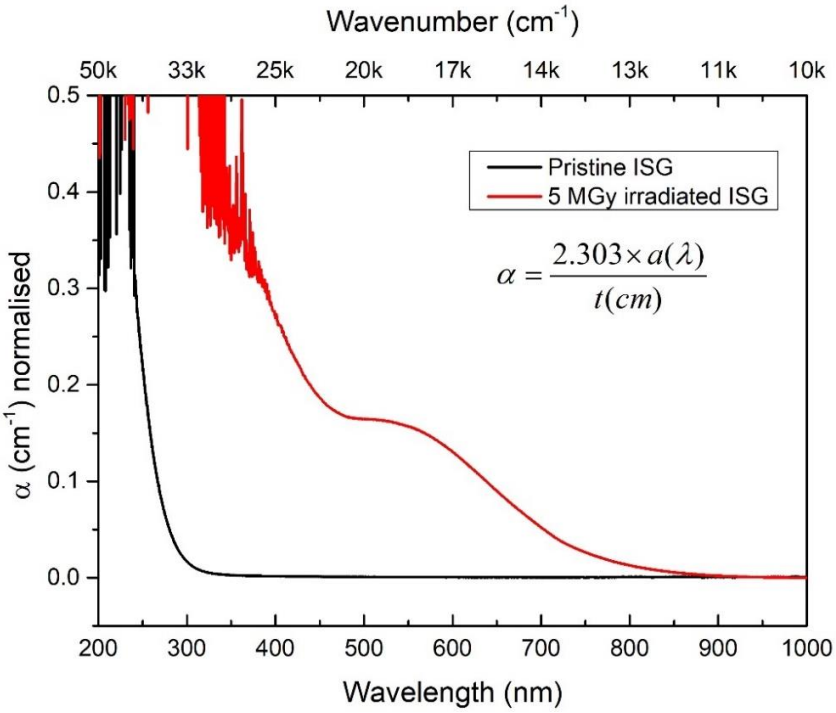

Figure 6. 12 UV-Vis-nIR optical absorption spectra for pristine and irradiated ISG glass.

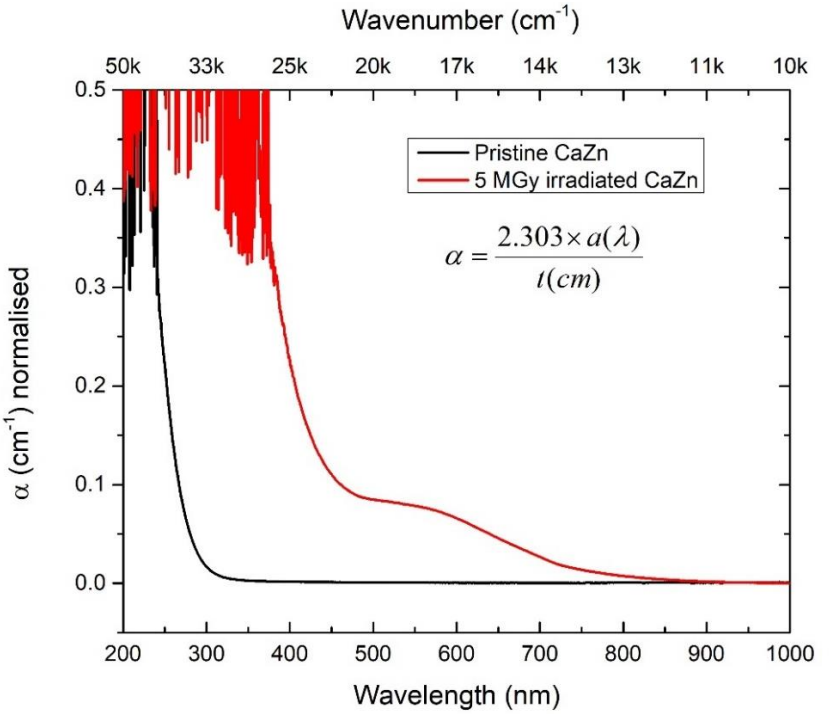

Figure 6. 13 UV-Vis-nIR optical absorption spectra for pristine and irradiated CaZn glass.

Deconvoluted UV-Vis-nIR optical absorption difference spectra for irradiated SON68, ISG and CaZn glass specimens are illustrated in Figure 6.14, 6.15 and 6.16,

respectively. For 5 MGy irradiated SON68 glass (Figure 6.11) specimen three Gaussian peaks are fitted to the spectra. The characteristic optical band of Fe impurities are generally located around 200 nm [242,261,264]. Optical absorption band at 201.62 nm, thus, could be attributed to Fe trace impurities [206,242,264]. Band at 532.64 nm and 604 nm could be attributed to absorption band due to BOHCs [31,206,242,264].

For 5 MGy irradiated ISG glass (Figure 6.12) specimen two Gaussian peaks were fitted to spectra. The optical absorption band at 325.15 nm could be attributed to ET centres, which is electron trapped on alkali cations [28,206,242,264,286]. The band at 568.80 nm could be attributed to BOHCs [31,206,242,264].

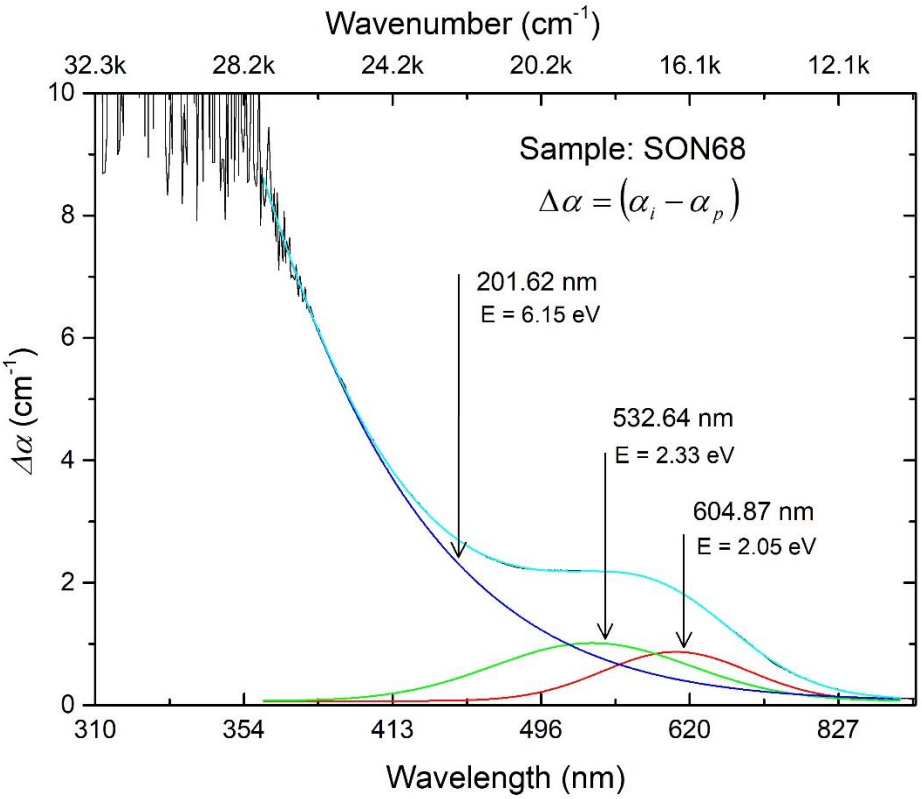

Figure 6. 14 Deconvoluted absorption difference spectra for SON68 glass.

For 5 MGy irradiated CaZn glass (Figure 6.13) specimen two Gaussian peaks were fitted to the spectra. The optical absorption band at 566.21 nm could be attributed to BOHCs [31,206,242,264]. The origin of band at 169.40 nm is unknown and hence it has not been assigned.

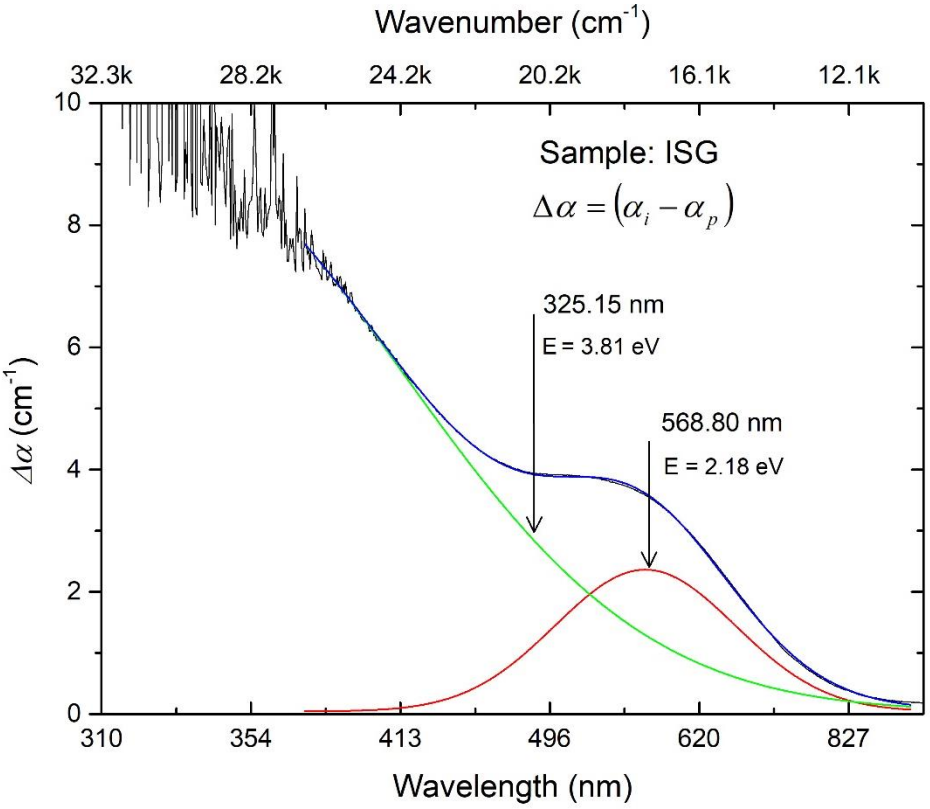

Figure 6. 15 Deconvoluted absorption difference spectra for ISG glass.

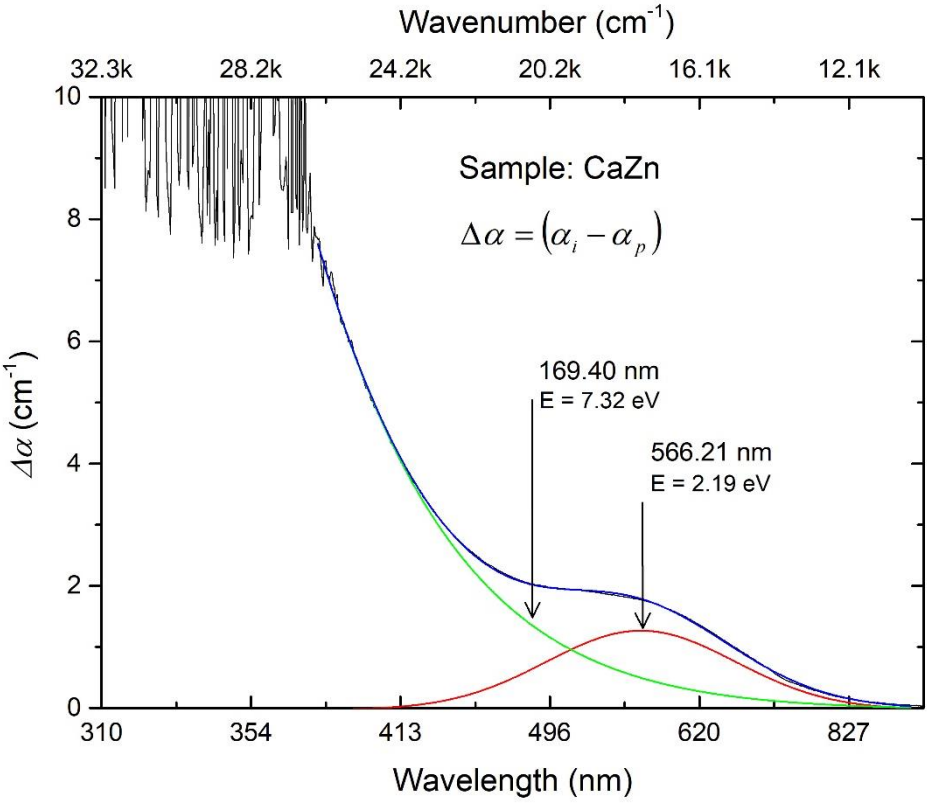

Figure 6. 16 Deconvoluted absorption spectra for CaZn glass.

Table 6. 3 Optical absorption bands fitted for SON68, ISG and CaZn irradiated glass spectra and their corresponding defect types.

SON68	ISG	CaZn
5 MGy	**5 MGy**	**5 MGy**
201.62 nm (Fe trace impurity)[242,261,264]	**325.15 nm (ET centre)** [242,261,264]	**169.40 nm (unknown)**
532.64 nm (BOHC) [242,261,264]	**568.80 nm (BOHC)** [242,261,264]	**566.21 nm (BOHC)** [242,261,264]
604.87 nm (BOHC) [242,261,264]	-	-

6.4 Results – Fe_2O_3 doped NaBaBSi and LiNaBSi glasses

6.4.1 Mössbauer spectroscopy

^{57}Fe Mössbauer spectroscopy was used to study potential changes in the oxidation state post gamma irradiations. Figures 6.17 and 6.18 illustrate stacked Mössbauer spectra for pristine and 5 MGy gamma irradiated NaBaBSi glass specimens (formed in oxidising melting conditions and thus are referred as oxidised glasses) doped with 4.76 and 9.09 mol% Fe_2O_3, respectively. All the measurements were recorded using a room temperature ^{57}Fe Mössbauer spectrometer that employs 14.4 keV gamma rays supplied by 25 mCi source of ^{57}Co in Rh over a velocity range of ±6 mm/sec using a constant acceleration driving unit. Details on experimental setup and sample preparation methods are presented in Section 3.3.5. Spectra were fitted with Lorentzian doublets using Recoil software package [228], centre shift (CS), quadrupole splitting parameters, FWHM, and absorption area (in %) are given in Table 6.4. Fitted spectra parameters were used to determine the possible change in the environment and average Fe-coordination induced by gamma-irradiations. Mössbauer spectra are also fitted using an extended Voigt/Voigtian based method (xVBF) which provides a Gaussian distribution of independent isomer shift and quadrupole splitting parameters for each Fe site. The analysis using xVBF is provided in the Appendix C. In Figure 6.17 two Lorentzian doublets are fitted with CS values (Table 6.4) with mean absolute error of ±.04 indicative of a little difference in the s-electron density around the Fe nuclei for both 4.76 and 9.09 mol% Fe_2O_3

doped NaBaBSi glass [100], similarly, in Figure 6.18 two Lorentzian doublets are fitted.

Figures 6.19 and 6.20 illustrate stacked Mössbauer spectra for pristine and 5 MGy gamma irradiated NaBaBSi glass specimens (formed in reducing melting conditions by mixing graphite with glass batch and thus are referred as reduced glasses) doped with 4.76 and 9.09 mol% Fe_2O_3, respectively. Spectra were fitted with two Lorentzian doublets, each representing a Fe^{2+} and Fe^{3+} environment, values of CS and QS (Table 6.5) obtained by fitting the spectra are used to determine the oxidation state [287,288]. The relative area (in %) obtained for each doublet is considered to be equal to the relative abundance of these oxidation state [206].

Figures 6.21 and 6.22 illustrate stacked Mössbauer spectra for pristine and 5 MGy gamma irradiated LiNaBSi glass specimens formed in oxidising environment doped with 4.76 and 9.09 mol% Fe_2O_3, respectively. Each spectrum was fitted with two Lorentzian doublets (Table 6.6).

In Figure 6.23 and 6.24 Mössbauer spectra for LiNaBSi glass specimen formed with in reducing environment doped with 4.76 and 9.09 mol% Fe_2O_3, respectively, were fitted with two Lorentzian doublets, each representing a Fe^{2+} and Fe^{3+} environment, values of CS and QS (Table 6.7) obtained by fitting the spectra are used to determine the oxidation states [287,288].

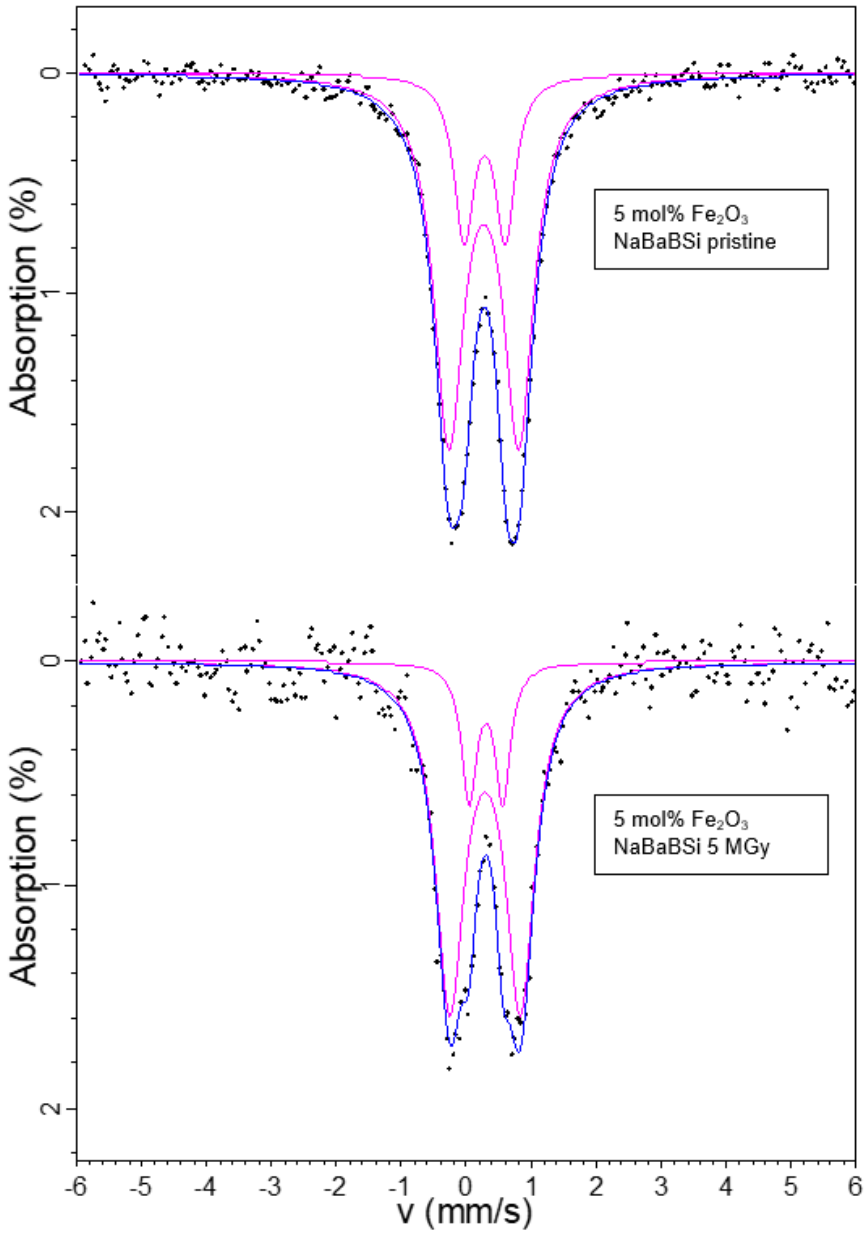

Figure 6. 17 Mössbauer spectra for NaBaBSi doped with 4.76 mol% Fe_2O_3 pristine and 5 MGy irradiated oxidised glass.

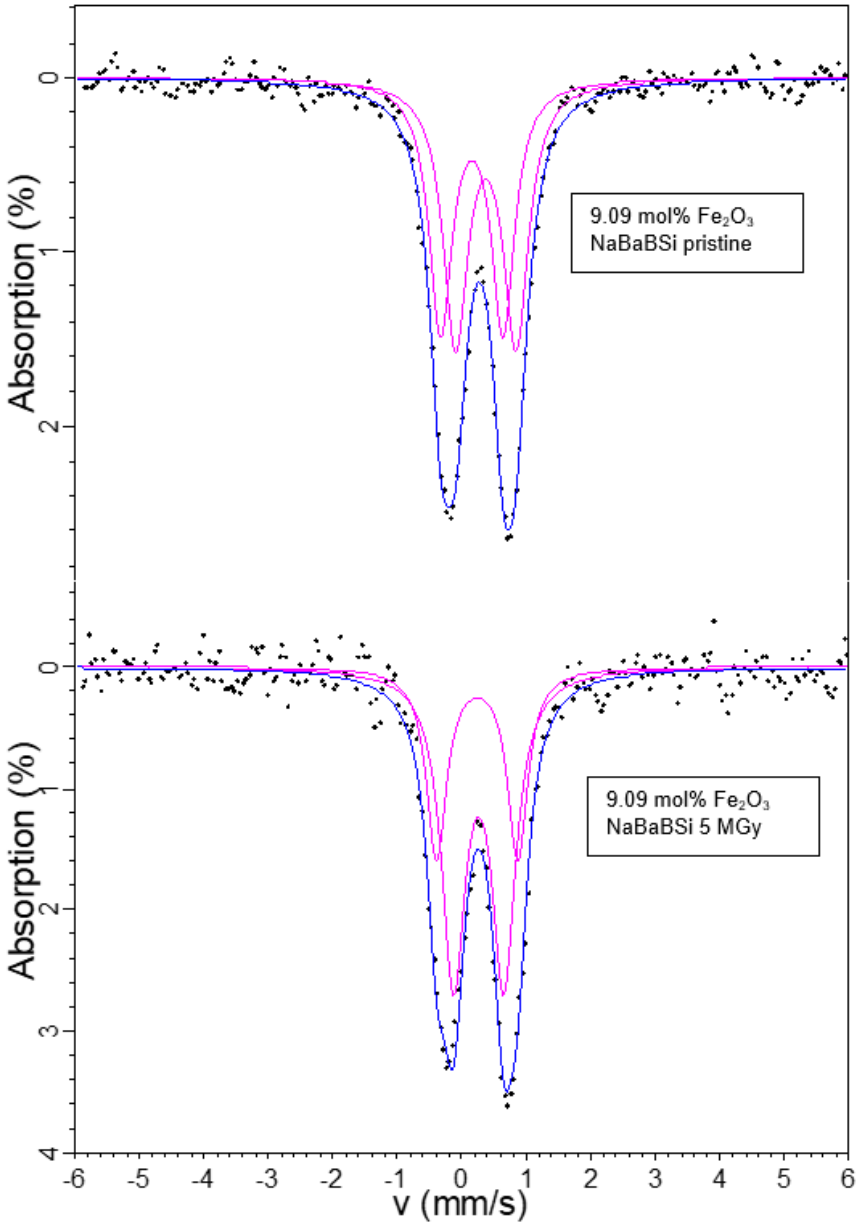

Figure 6. 18 Mössbauer spectra for NaBaBSi doped with 9.09 mol% Fe_2O_3 pristine and 5 MGy gamma irradiated oxidised glass.

Table 6. 4 Fitted parameters for Mössbauer spectra for NaBaBSi doped with 4.76 and 9.09 mol% Fe_2O_3 pristine and 5 MGy irradiated oxidised glass.

Glass		CS (mm/s)	QS (mm/s)	FWHM(mm/s)	Relative Area (%)
4.76 mol% Fe_2O_3 pristine oxidised	Doublet 1 (Fe^{3+})	0.28	0.63	0.18	23
	Doublet 2 (Fe^{3+})	0.26	1.07	0.28	77
4.76 mol% Fe_2O_3 5 MGy oxidised	Doublet 1 (Fe^{3+})	0.30	0.52	0.14	17
	Doublet 2 (Fe^{3+})	0.28	1.09	0.26	83
9.09 mol% Fe_2O_3 pristine oxidised	Doublet 1 (Fe^{3+})	0.15	0.96	0.21	47
	Doublet 2 (Fe^{3+})	0.37	0.93	0.23	53
9.09 mol% Fe_2O_3 5 MGy oxidised	Doublet 1 (Fe^{3+})	0.26	0.78	0.22	65
	Doublet 2 (Fe^{3+})	0.23	1.25	0.18	35

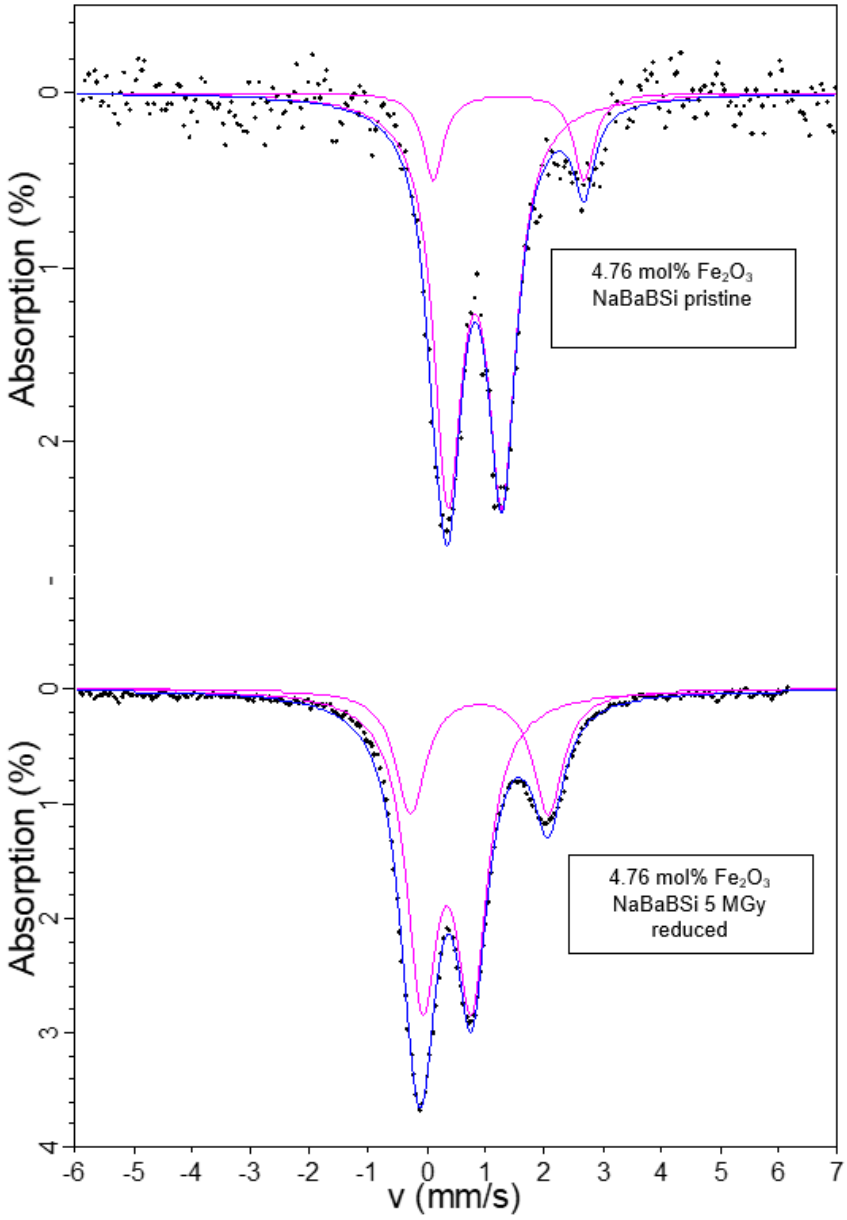

Figure 6. 19 Mössbauer spectra for NaBaBSi doped with 4.76 mol% Fe_2O_3 pristine and 5 MGy gamma irradiated reduced glass.

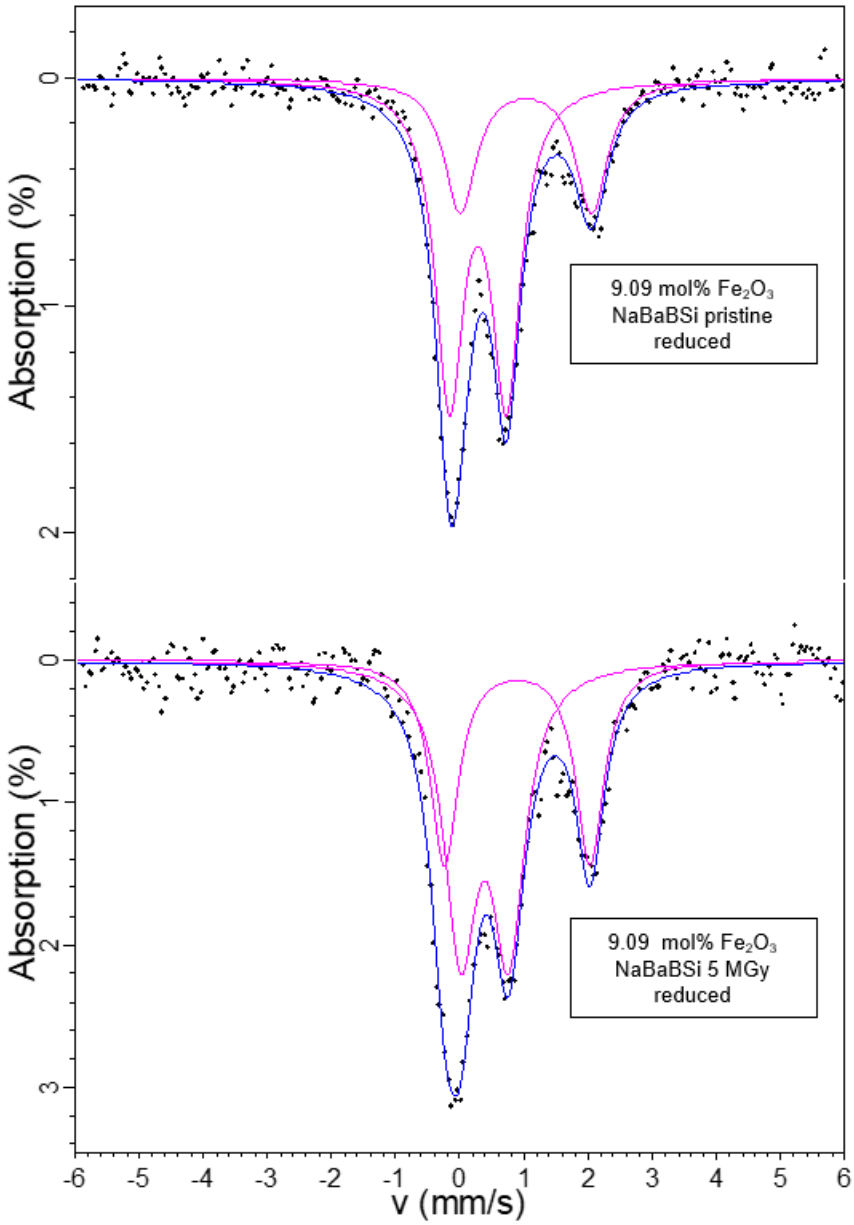

Figure 6. 20 Mössbauer spectra for NaBaBSi doped with 9.09 mol% Fe_2O_3 pristine and 5 MGy gamma irradiated reduced glass.

Table 6. 5 Fitted parameters for Mössbauer spectra for NaBaBSi doped with 4.76 mol% and 9.09 mol% Fe_2O_3 irradiated with 5 MGy gamma reduced glass.

Glass		CS (mm/s)	QS (mm/s)	FWHM(mm/s)	Relative Area (%)
4.76 mol% Fe_2O_3 pristine reduced	Doublet 1 (Fe^{3+})	0.29	0.85	0.27	86
	Doublet 2 (Fe^{2+})	0.83	2.37	0.19	14
4.76 mol% Fe_2O_3 5 MGy reduced	Doublet 1 (Fe^{3+})	0.34	0.83	0.32	71
	Doublet 2 (Fe^{2+})	0.89	2.34	0.31	29
9.09 mol% Fe_2O_3 pristine reduced	Doublet 1 (Fe^{3+})	0.27	0.88	0.26	68.
	Doublet 2 (Fe^{2+})	1.02	2.04	0.30	32
9.09 mol% Fe_2O_3 5 MGy reduced	Doublet 1 (Fe^{3+})	0.38	0.74	0.30	61
	Doublet 2 (Fe^{2+})	0.89	2.27	0.26	39

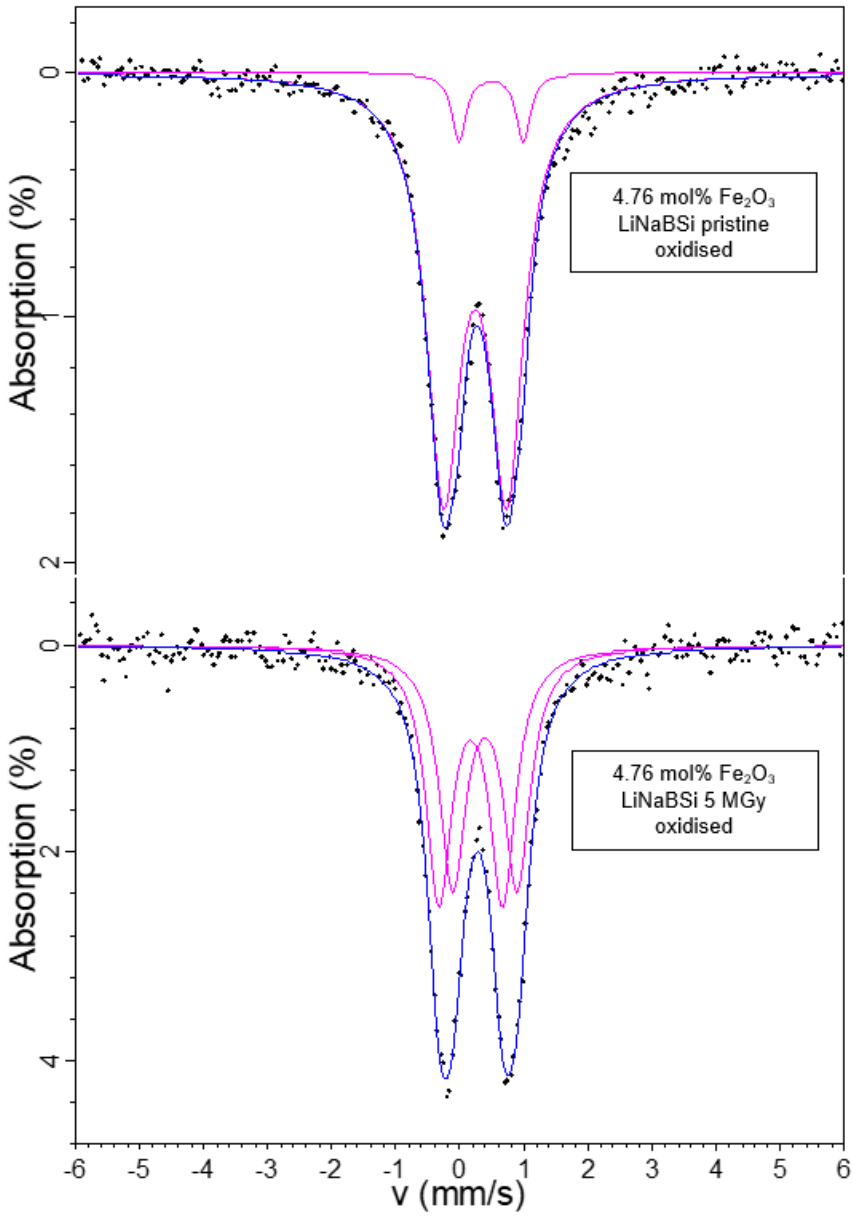

Figure 6. 21 Mössbauer spectra for LiNaBSi doped with 4.76 mol% Fe_2O_3 oxidised pristine and 5 MGy gamma irradiated glass.

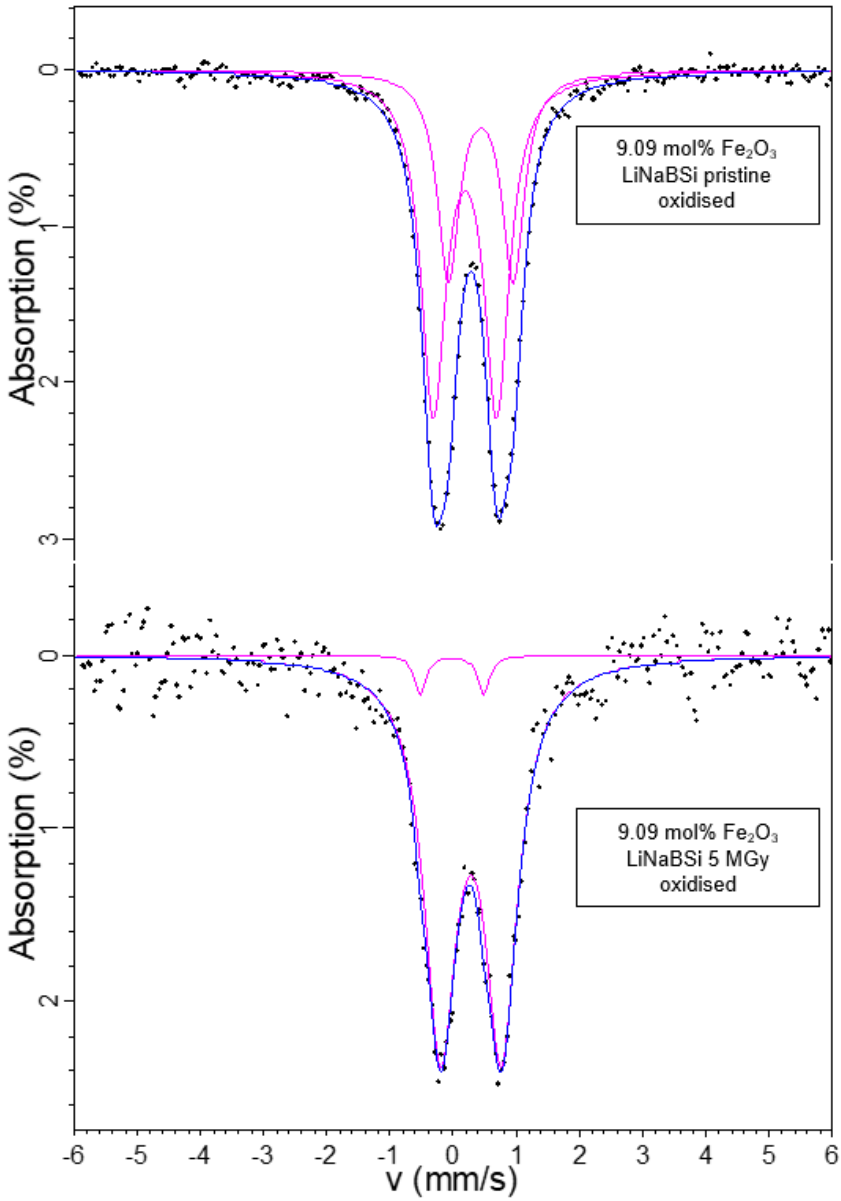

Figure 6. 22 Mössbauer spectra for LiNaBSi doped with 9.09 mol% Fe_2O_3 oxidised pristine and 5 MGy gamma irradiated glass.

Table 6. 6 Fitted parameters for Mössbauer spectra for LiNaBSi doped with 4.76 and 9.09 mol% Fe_2O_3 oxidised pristine glass.

Glass		CS (mm/s)	QS (mm/s)	FWHM(mm/s)	Relative Area (%)
4.76 mol% Fe_2O_3 pristine oxidised	Doublet 1 (Fe^{3+})	0.23	0.98	0.32	93
	Doublet 2 (Fe^{3+})	0.48	1.00	0.13	7
4.76 mol% Fe_2O_3 5 MGy oxidised	Doublet 1 (Fe^{3+})	0.16	0.99	0.24	51
	Doublet 2 (Fe^{3+})	0.38	1.00	0.25	49
9.09 mol% Fe_2O_3 pristine oxidised	Doublet 1 (Fe^{3+})	0.18	1.00	0.23	65
	Doublet 2 (Fe^{3+})	0.43	1.02	0.21	35
9.09 mol% Fe_2O_3 5 MGy oxidised	Doublet 1 (Fe^{3+})	0.26	0.93	0.3	96
	Doublet 2 (Fe^{3+})	0.26	1.57	0.10	4

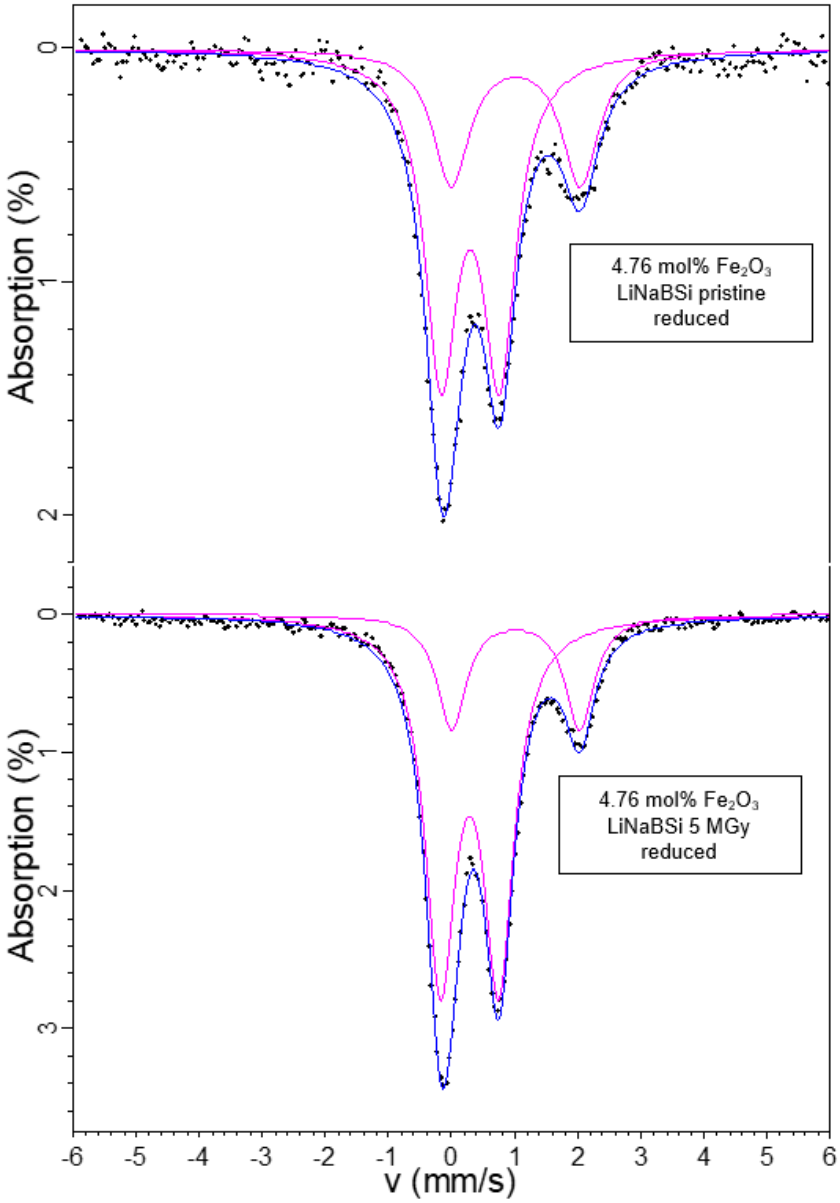

Figure 6. 23 Mössbauer spectrum for LiNaBSi doped with 4.76 and 9.09 mol% Fe_2O_3 reduced pristine and 5 MGy gamma irradiated glass.

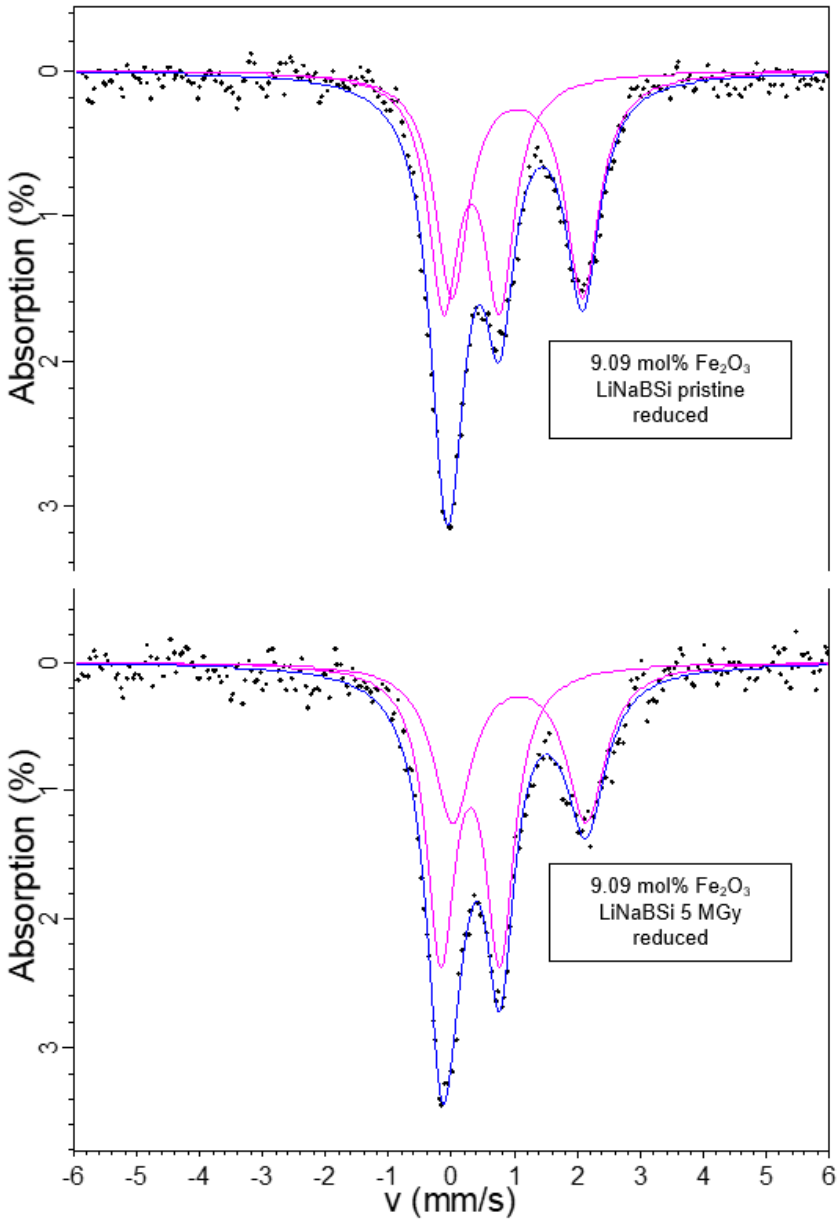

Figure 6. 24 Mössbauer spectra for LiNaBSi doped with 9.09 mol% Fe_2O_3 reduced pristine and 5 MGy gamma irradiated glass.

Table 6. 7 Fitted parameters for Mössbauer spectra for LiNaBSi doped with 4.76 and 9.09 mol% Fe_2O_3 reduced pristine and 5 MGy gamma irradiated glass.

Glass		CS (mm/s)	QS (mm/s)	FWHM(mm/s)	Relative Area (%)
4.76 mol% Fe_2O_3 pristine reduced	Doublet 1 (Fe^{3+})	0.29	0.92	0.31	68
	Doublet 2 (Fe^{2+})	1.01	2.04	0.35	32
4.76 mol% Fe_2O_3 5 MGy reduced	Doublet 1 (Fe^{3+})	0.28	0.92	0.29	77
	Doublet 2 (Fe^{2+})	1.01	2.02	0.27	24
9.09 mol% Fe_2O_3 pristine reduced	Doublet 1 (Fe^{3+})	0.31	0.88	0.29	47
	Doublet 2 (Fe^{2+})	1.04	2.07	0.32	53
9.09 mol% Fe_2O_3 5 MGy reduced	Doublet 1 (Fe^{3+})	0.29	0.93	0.27	57
	Doublet 2 (Fe^{2+})	1.07	2.11	0.37	43

.

6.4.2 Electron paramagnetic resonance spectroscopy

Figures 6.25-6.27 illustrate first derivative room temperature X-band EPR spectra for 0.19, 0.99 and 4.76 mol% Fe_2O_3 doped NaBaBSi pristine and 5 MGy gamma irradiated glasses, respectively. The centre field and sweep width used for EPR measurement under this study was 250 and 370 mT, respectively. The microwave power used was 0.3162 mW, modulation amplitude 0.4 mT and magnetic field modulation was 100 kHz. In Figure 6.25 EPR spectrum for pristine samples there is only intense signal at g~4.3. There are two resonance signals at g~4.3 and g~2.0 observed for irradiated EPR spectrum in 0.19 mol% Fe_2O_3 doped NaBaBSi glass specimen. For 0.99 mol% Fe_2O_3 doped specimen (Figure 6.26), the resonance signal at g~4.3 becomes broad, there is a broad signal present at g~2.0 for the pristine and irradiated samples. In Figure 6.27 the signal at g~4.3 becomes broad with low intensity and the rest of the signal saturates. A similar observation was noted for pristine and gamma irradiated LiNaBSi glass specimens with 0.19, 0.99 and 4.76 mol% Fe_2O_3 doped as shown in Figure 6.28-6.30, respectively, except for the irradiated 4.76 mol% Fe_2O_3 doped specimen where the EPR signal saturates and no distinct signal at either g~4.3 or g~2.0 was observed. EPR spectra was also recorded for pristine and 5 MGy gamma irradiated 9.09 mol% Fe_2O_3 doped NaBaBSi and LiNaBSi glass specimens and are given in Appendix D.

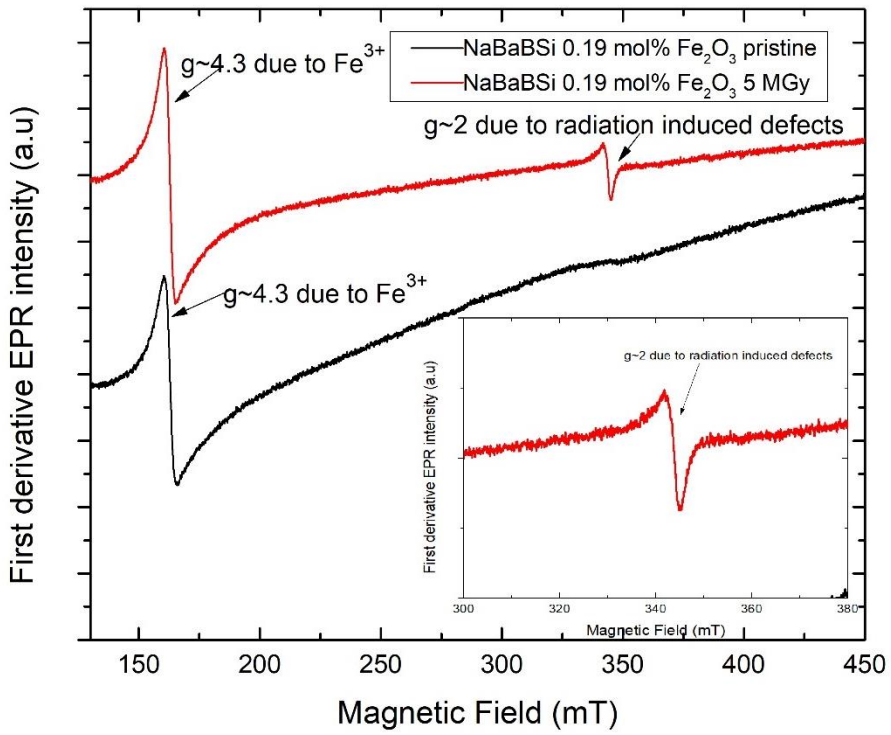

Figure 6. 25 First derivative room temperature X-band EPR spectra for 0.19 mol% Fe_2O_3 doped NaBaBSi pristine and 5 MGy gamma irradiated glass.

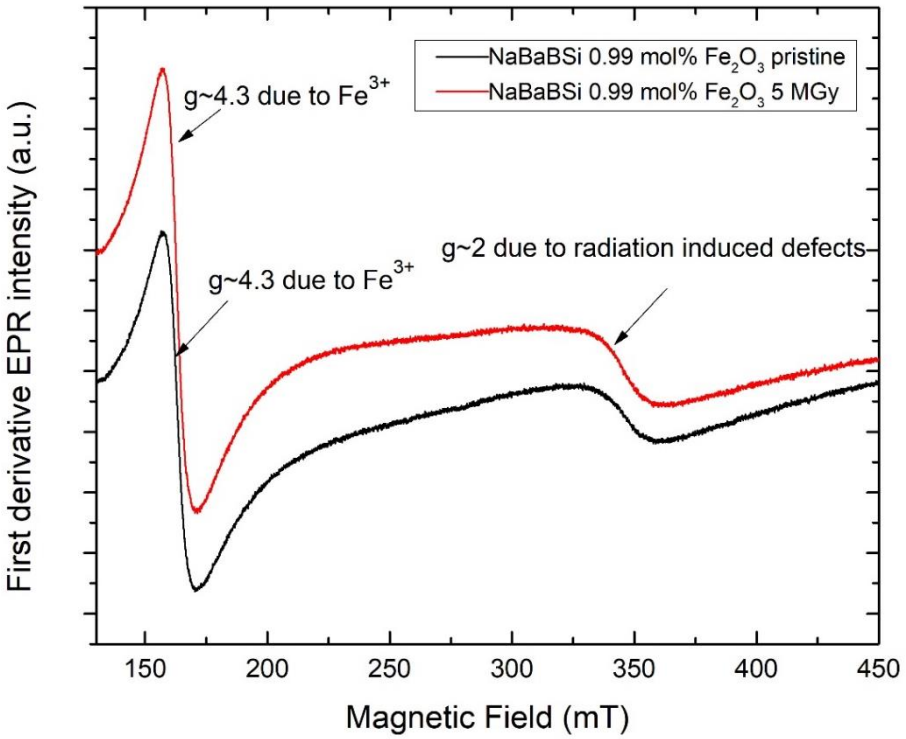

Figure 6. 26 First derivative room temperature X-band EPR spectra for 0.99 mol% Fe_2O_3 doped NaBaBSi pristine and 5 MGy gamma irradiated glass.

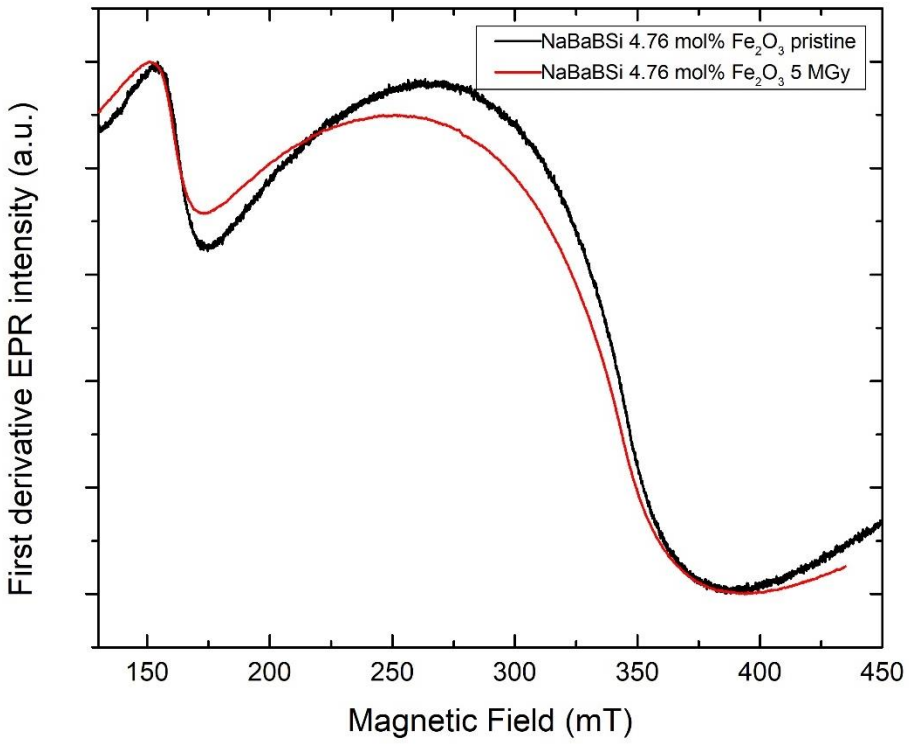

Figure 6. 27 First derivative room temperature X-band EPR spectra for 4.76 mol% Fe_2O_3 NaBaBSi doped pristine and 5 MGy gamma irradiated glass.

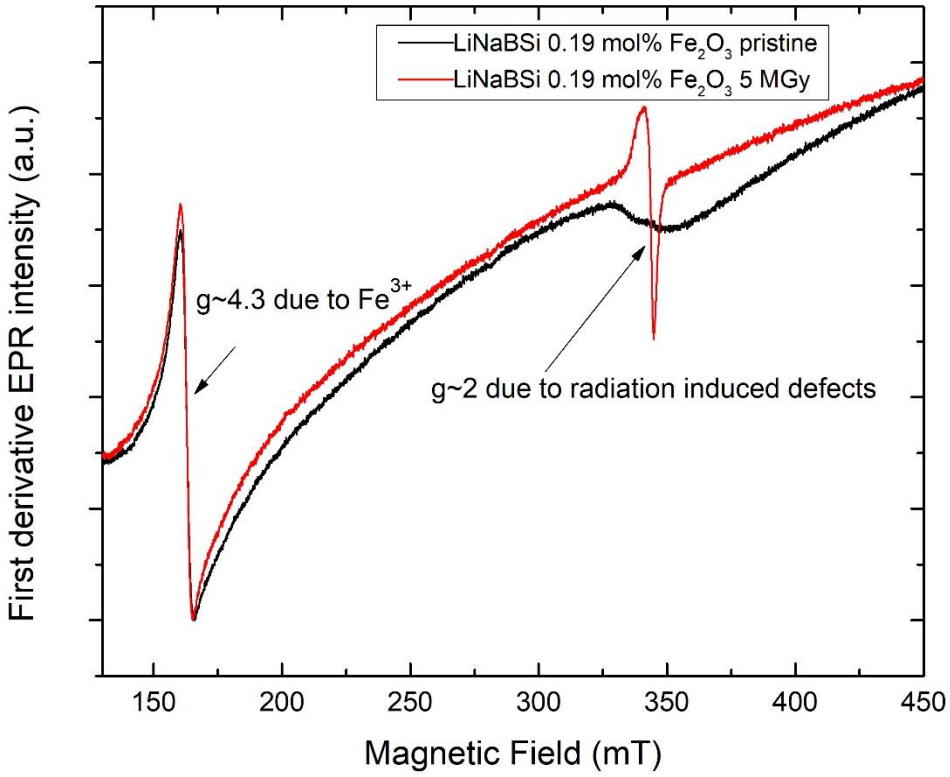

Figure 6. 28 First derivative room temperature X-band EPR spectra for 0.19 mol% Fe_2O_3 doped LiNaBSi pristine and 5 MGy gamma irradiated glass.

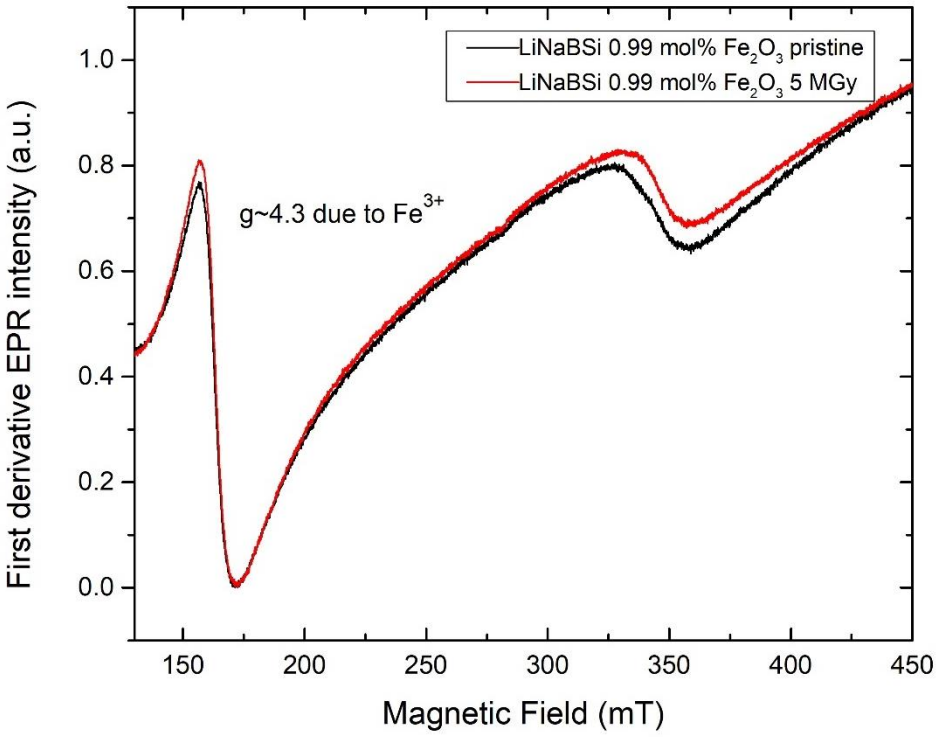

Figure 6. 29 First derivative room temperature X-band EPR spectra for 0.99 mol% Fe_2O_3 doped LiNaBSi pristine and 5 MGy gamma irradiated glass.

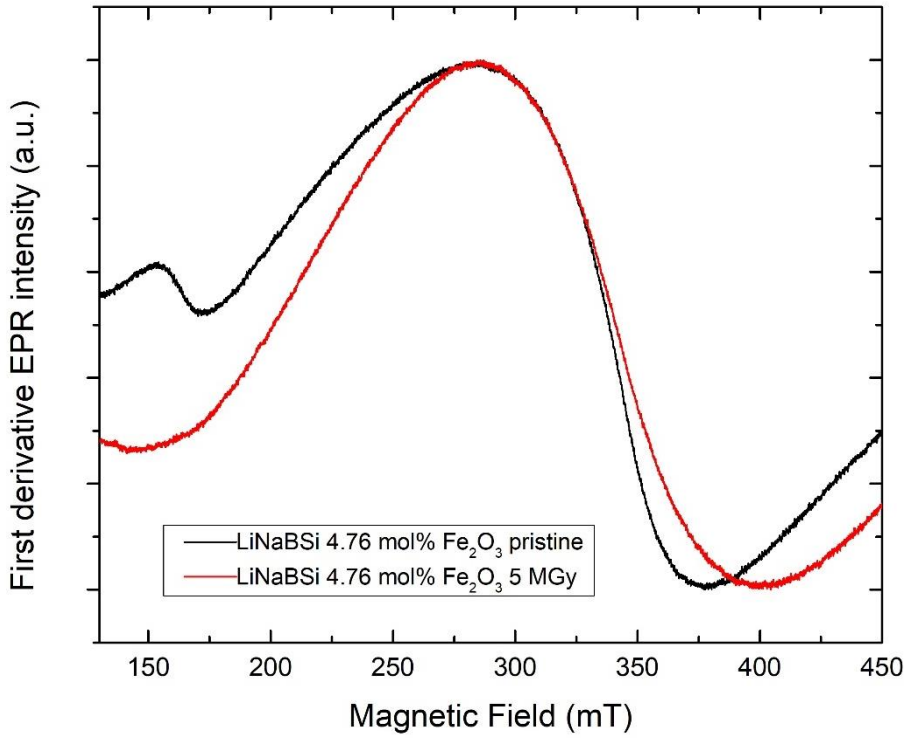

Figure 6. 30 First derivative room temperature X-band EPR spectra for 4.76 mol% Fe_2O_3 doped LiNaBSi pristine and 5 MGy gamma irradiated glass.

6.5 Results – Non-active waste simulated glasses

First derivative X-band room temperature EPR spectra was recorded for NaBaBSi, LiNaBSi and SON68 waste simulated pristine and 5 MGy irradiated as illustrated by Figure 6.31-6.33, respectively. Composition for the waste for each glass type is given in Section 3.1.1.3.

There is a resonance signal at g~4.3 which is common in all three glasses and can be observed for both pristine and irradiated glasses (discussed in Section 6.7). There is a broad resonance at g~2.0 in Figure 6.31 for NaBaBSi glass which decreases in the intensity for irradiated specimen. This band can be a convolution of gamma irradiated induced defects or any paramagnetic species in the glass [31,60,68,248]. The EPR spectra for LiNaBSi glass are a complex one which is difficult to deconvolute. For SON68 g~4.3 and g~2.0 resonances are clearly distinct.

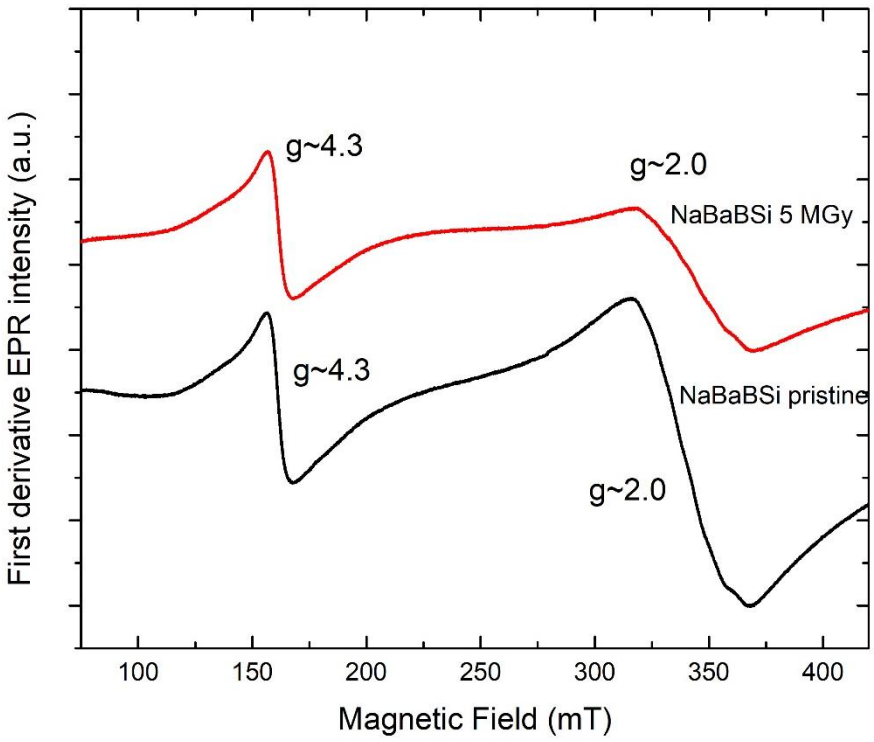

Figure 6. 31 First derivative EPR spectra for pristine and 5 MGy gamma irradiated NaBaBSi waste loaded glass specimen.

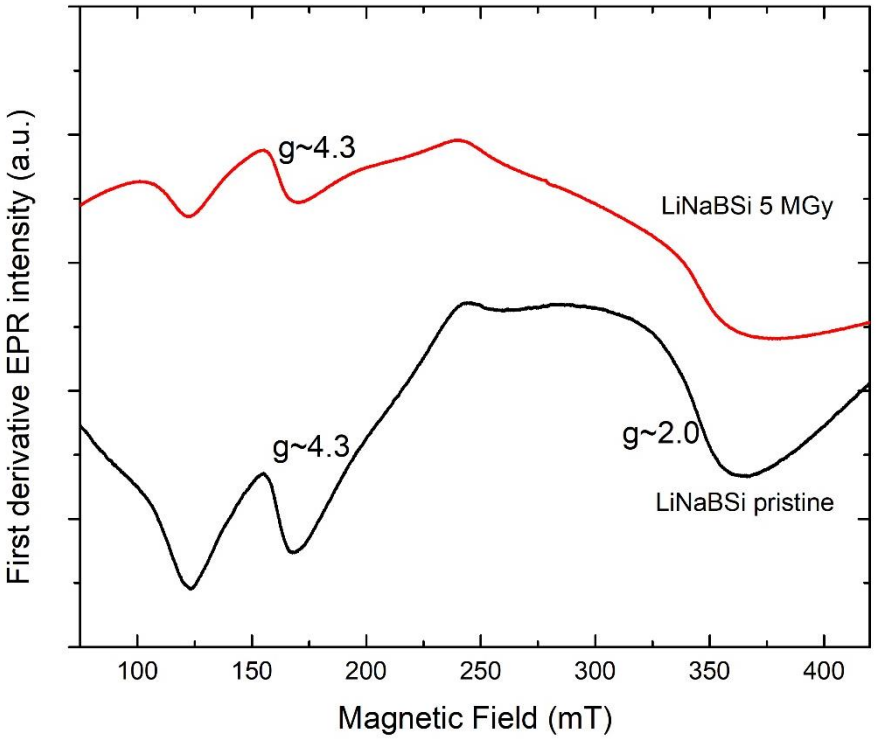

Figure 6. 32 First derivative EPR spectra for pristine and 5 MGy gamma irradiated waste loaded LiNaBSi glass specimen.

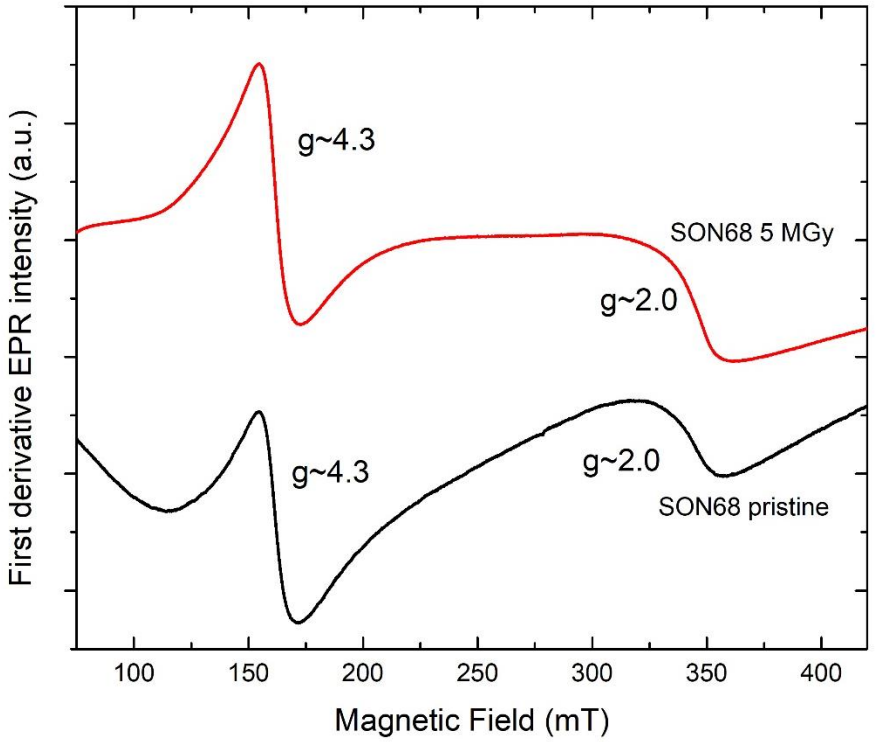

Figure 6. 33 First derivative EPR spectra for pristine and 5 MGy gamma irradiated waste loaded SON68 glass specimen.

6.6 Results – Density measurements

Density measurements were carried out for monolithic pristine and irradiated simple and Fe_2O_3 doped (both oxidised and reduced) NaBaBSi and LiNaBSi glasses. Averages of five independent measurements were taken using Archimedes' method to minimise the uncertainties. The detailed principle, procedure and setup is explained and discussed in Section 3.3.3. Densities recorded (average of five measurements) for pristine and 5 MGy gamma irradiated simple NaBaBSi and LiNaBSi glasses are presented in Table 6.8. There is a percentage increase post irradiation of 0.13 for both the glasses. Densities recorded (average of five measurements) for pristine and 5 MGy gamma irradiated doped NaBaBSi and LiNaBSi glasses are presented in Table 6.9 and Table 6.10, respectively.

Table 6. 8 Density measurements for NaBaBSi and LiNaBSi simple glasses for pristine and 5 MGy irradiated samples.

Sample ID	0 MGy/ pristine (g/cm^3)	Stdev	5 MGy (g/cm^3)	Stdev	% change
NaBaBSi	3.1022	0.0019	3.1063	0.0011	↑0.132
LiNaBSi	2.463	0.0006	2.4664	0.0006	↑0.138

Table 6. 9 Density measurements recorded for pristine and 5 MGy gamma irradiated oxidised NaBaBSi glass doped with 0.19, 0.99, 4.76 and 9.09 mol% Fe_2O_3.

NaBaBSi + *x* mol% Fe_2O_3		0 MGy /pristine (g/cm^3)	Stdev	5 MGy (g/cm^3)	Stdev	% change
x	**0**	3.1022	0.0019	3.1063	0.0011	↑0.132
x	**0.19**	3.1116	0.0001	3.1144	0.0004	↑0.138
x	**0.99**	3.1220	0.0004	3.1261	0.0004	↑0.131
x	**4.76**	3.1744	0.0004	3.1747	0.0003	↑0.009
x	**9.09**	3.2302	0.0004	3.2222	0.0004	↓0.247

Table 6. 10 Density measurements recorded for pristine and 5 MGy gamma irradiated oxidised LiNaBSi glass doped with 0.19, 0.99, 4.76 and 9.09 mol% Fe_2O_3.

LiNaBSi + *x* mol% Fe_2O_3		0 MGy /pristine (g/cm^3)	Stdev	5 MGy (g/cm^3)	Stdev	% change
x	**0**	2.463	0.0006	2.4664	0.0006	↑0.138
x	**0.19**	2.4733	0.0002	2.4811	0.0003	↑0.315
x	**0.99**	2.4845	0.0009	2.4884	0.0005	↑0.157
x	**4.76**	2.5518	0.0002	2.6251	0.0003	↑2.872
x	**9.09**	2.6174	0.0006	2.5552	0.0001	↓2.376

6.7 Discussion

6.7.1 Electron paramagnetic resonance spectroscopy for SON68, ISG and CaZn simple glasses

Figure 6.8 shows the deconvoluted (in practice 2nd derivative spectra) EPR resonance signal centred at g~2.00, the four-line/quartet hyperfine structure for SON68 glass, which is attributed to BOHCs [28,57,60,187]. From second derivative spectra, g-values calculated for BOHCs are (g~ 2.018,2.010,2.003) (ref Table 6.2). There is another signal present at g~1.993 corresponding to a magnetic field of ~344.07 mT which can be attributed to ET centres [28,57,177]. By looking at the line shape for the first derivative spectrum for irradiated SON68 glass it can be inferred that the signal is due to BOHCs with maximum contribution to the overall signal along with the other underlying signals [28,173,185]. The EPR spectrum is better resolved in the second-derivative form for SON68 glass. BOHCs and ET centres are common radiation-induced paramagnetic centres in EPR spectra for all three glass types.

In Figure 6.9, the double derivative EPR spectrum for ISG shows a signal which is attributed to BOHCs with g values g~2.018,2.011,2.003 [28,57,60,187]. There is another signal at g~1.996 and 1.993 which is attributed to ET centres [28,57,177]. Similarly, in Figure 6.10, the corresponding g values in CaZn EPR second derivative

spectrum for BOHCs are g~2.018,2.010,2.003 and for ET centres [28,57,177] it is g~1.994. There is another signal with g~1.988±.005 which could be either due to ET centre [28,57,177] or any trace impurity.

6.7.2 Mössbauer spectroscopy

The CS values in Table 6.4 show that iron predominantly exists as Fe^{3+} form for both 4.76 and 9.09 mol% Fe_2O_3 doped NaBaBSi pristine and 5 MGy gamma irradiated glass specimens (Figure 6.17 and 6.18) [226,287,288]. There could be two different sites at which Fe may be bound to other atoms either octahedrally or tetrahedrally [289–292] as indicated with two different values for QS (see Table 6.4). There is an increase of 0.11 ± 0.04 mm/s in CS from pristine to irradiated 9.09 mol% Fe_2O_3 NaBaBSi for Doublet 1 and decrease of 0.14 ± 0.04 for Doublet 2 which may be an indicative of a change in coordination as a result of gamma irradiation as reported by Eissa *et al.,* [293], however, this difference for CS values for both the doublet sites is also observed when fitted using xVBF method. This suggests that in 9.09 mol% Fe_2O_3 doped NaBaBSi oxidised glass, there are some gamma irradiation induced effects that result in change in the Fe coordination. McGann *et. al*. [206] reported a decrease in average population of Fe^{3+} in 6-fold coordination and in increase in 4-fold coordination as a result of gamma irradiation in MW and G73 glass.

In Figure 6.19 and 6.20 the Doublet 1 for both 4.76 and 9.09 mol% Fe_2O_3 doped pristine and irradiated reduced glasses corresponds to iron in Fe^{3+} environment which are determined by the values of CS and QS [227,287,288,293]. And the Doublet 2 for both 4.76 and 9.09 mol% Fe_2O_3 doped pristine and irradiated reduced glasses corresponds to iron in Fe^{2+} environment. The relative area obtained from fitting the spectra for ion in Fe^{3+} decreases by 17.58% and 9.09% for 4.76 and 9.09 mol% Fe_2O_3 doped glasses, respectively, when irradiated with 5 MGy of gamma. The relative area for iron in Fe^{2+} environment increases by 109% and 20.7% 4.76 and 9.09 mol% Fe_2O_3 doped glasses, respectively, when irradiated with 5 MGy of gamma. This relative decrease in the Fe^{3+} environment and increase in the Fe^{2+} environment can be attributed to a mechanism which was initially proposed by Debnath *et al.* [294] and suggested by Brown [295] which is given by the equation 6.1 for the remediation of gamma radiation induced defects. This mechanism is also called defect hopping [63,206,226,294].

$Fe^{3+} + e- \rightarrow Fe^{2+}$ and $Fe^{2+} + h^{+} \rightarrow Fe^{3+}$ (6.1)

The shift of 0.14 ± 0.04 mm/s in QS (Fe^{3+}) for 9.09 mol% Fe_2O_3 doped (Doublet 1) gamma irradiated sample is consistent with Eissa *et al.,* [293] and Forder *et al.,* [227]. This shift indicates an increase in $^{[4]}Fe^{3+}/^{[6]}Fe^{3+}$ [226,227,293].

In Figure 6.21 and 6.22 two Lorentzian doublets are fitted with CS values (Table 6.6) with mean absolute error of ±.04 indicative of a little difference in the s-electron density around the Fe nuclei for both 4.76 and 9.09 mol% Fe_2O_3 doped LiNaBSi glass [100]. The CS values show that iron predominantly exists as Fe^{3+} form in the glass specimens [226,287,288]. There is no notable shift in the QS except a shift ~ 0.5 mm/s for Doublet 2 for 9.09 mol% Fe_2O_3 doped LiNaBSi irradiated glass which can be attributed to change in the Fe^{3+} coordination due to irradiation [63,206,226,294].

In Figure 6.23 and 6.24, the relative area obtained from fitting the spectra (Table 6.7) for iron in Fe^{3+} environment increases by 12.99 % and 20.2% for 4.76 and 9.09 mol% Fe_2O_3 doped LiNaBSi reduced glasses, respectively, when irradiated with 5 MGy of gamma. The relative area for iron in Fe^{2+} environment decreases by 27.2% and 18.25% for 4.76 and 9.09 mol% Fe_2O_3 doped glasses, respectively, when irradiated with 5 MGy of gamma. This is again due to the mechanism initially proposed by Debnath *et al.* [294] and suggested by Brown [295], however, for LiNaBSi glass Fe^{2+} is getting converted to Fe^{3+} by capturing of holes and hence the relative area for Fe^{3+} is increasing after gamma irradiations. This is opposite to what is observed in NaBaBSi glass where Fe^{3+} was getting reduced to Fe^{2+} by capture of electrons.

6.7.3 Electron paramagnetic resonance spectroscopy for Fe_2O_3 doped NaBaBSi and LiNaBSi oxidised glasses

EPR spectra for pristine and 5 MGy gamma irradiated NaBaBSi glass specimen doped with 0.19 mol% Fe_2O_3 showed a common sharp and intense signal at g~4.3 signals. This signal can be attributed to isolated Fe^{3+} ions at tetrahedral or rhombic (lower) symmetric sites [60,68,251,296]. There is a very small shoulder at g~2.0 in pristine sample which can be attributed to Fe^{3+} ions sites of less distorted octahedral field [57,60,251,292]. There is a sharp and intense resonance signal at g~2.0 observed for irradiated 0.19 mol% Fe_2O_3 doped NaBaBSi which can be attributed to gamma irradiation induced defect which has also shown by the inset in Figure 6.25

[59,68,176,206,242]. Now, when the Fe_2O_3 concentration is increased to 0.99 mol%, the resonance signal at g~2.0 becomes broad. The appearance of a broad resonance signal at g~2.0 for pristine sample can be attributed to the Fe^{3+} ions at tetrahedral or rhombic (lower symmetric sites) may be due to clustering of iron Fe^{3+} ions [57,60,251,292]. The intense and sharp gamma irradiation induced resonance signal disappear possibly due to $Fe^{3+} + e^- + Fe^{2+}$ reaction (defect recombination) [57,60,66,68,226,227] which is also reported by Mohapatra *et al.,* [28,57] (ref Figure.6.34) and a broad signal similar to the signal in pristine sample due Fe^{3+} ions at tetrahedral or rhombic (lower symmetric sites) appears. Similarly, there are two resonance signal observed for LiNaBSi glass specimens, one at g~4.3 and other at g~2.0 for 0.19 and 0.99 0.19 mol% Fe_2O_3 doped pristine and irradiated specimens. The signal at g~2.0 is broad for 0.19 mol% Fe_2O_3 doped pristine specimen. For 4.76 mol% Fe_2O_3 doped NaBaBSi and LiNaBSi we observe that there is no irradiation induced defects and signal at g~2.00 saturates and signal at g~4.3 almost disappears. This may be due to the majority of Fe^{3+} becoming clustered [57,60,66,68,226,227].

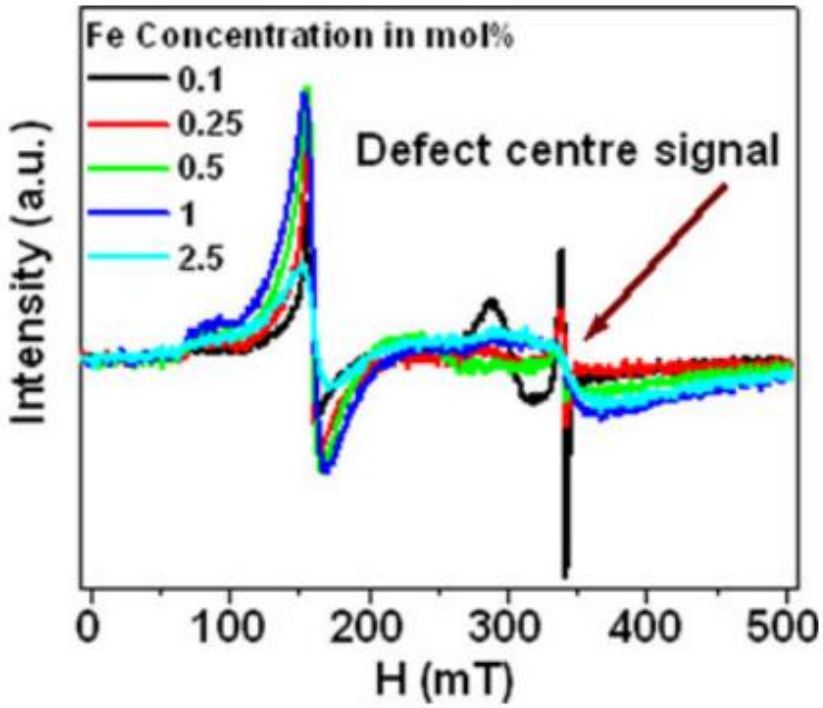

Figure 6. 34 Room temperature EPR spectra for NaBaBSi glass doped with different concentration of Fe_2O_3 (Source: [57])

Chapter 7. Summary of the Key Conclusions and Future Work

The overall aim of this study was to enhance our fundamental understanding of radiation-induced defects in simple and doped glasses which are being used commercially as HLW immobilisation glass matrices, as well as to compare how/whether the defects are affected by the glass composition. In addition, this study aimed to develop further on effects of multivalent species (rare earths and transition metals) that are present in actual HLW, on radiation induced defects. There has been modest amount of work published on iron doped nuclear waste glasses, therefore, to build on these studies, we aimed to investigate the effects of doping Fe_2O_3 in controlled redox in glasses with different compositions.

7.1 Radiation effects due to alpha (He^{2+}) – Simulation of alpha damage

In this study two simple glasses, namely LiNaBSi and NaBaBSi were chosen for investigating the effects of alpha-particle damage. To simulate the same, 650 keV He^{2+} ions with a range of fluences were implanted in these two simple glasses. This study was carried out with the objective to enhance our understanding of the types of alpha-particle induced defects that can form in simple glasses used to as HLW glass matrices, and how/whether these are affected by glass composition. Glass characterisation post ion-implantation revealed resonance signal which are broadly consistent with peroxy radicals, other than no resonance signal due to trapped carriers were observed. There was no consistent trend in EPR linewidth for two glass types irradiated with different fluences. Since He^{2+} due to their large mass, charge state and columbic interactions cannot penetrate deeper in the matter and deposits their energy in a very short range. This resulted in small volumes of ion-implanted glass and hence EPR S/N ratio were limited for two glass types. Raman spectroscopy revealed a strong, broad Raman band at 1560 cm^{-1}, accompanied by growth of the nearby B-O band at 1450 cm^{-1}. The onset of band at 1560 cm^{-1} for LiNaBSi glass was observed at fluence of 5 x 10^{16} ions/cm^2 whereas in NaBaBSi glass the band was observed for highest fluence (1 x 10^{17} ions/cm^2). This band could be attributed to B-O units with less likely but partial contribution from the formation of molecular O_2. Zhang *et al*. [205] Abbas *et al*. [172] and Karakurt *et al.* [128] have

reported Raman bands related to molecular oxygen at about 1550 cm^{-1} and B-O units have been reported by many authors in the literature [36,45,190].

7.2 Radiation effects due to gamma rays – Simulation of gamma damage

7.2.1 Gamma irradiation effects in NaBaBSi and LiNaBSi simple glasses

In both NaBaBSi and LiNaBSi glass irradiated at low (0.5 MGy) and high (5 MGy) doses, BOHC's and POR's are common defect centres found by X-band room temperature EPR spectroscopy. Another paramagnetic defect centre identified in NaBaBSi glass are E^- centres (g~1.97) and isotropic signal at g~2.011 which could be related to the colloidal metallic sodium particles. This assignment was done based on a thorough literature review; a list of reports on formation of sodium colloids in glasses and alkali halide crystals is presented in Table B2 in Appendix B. Absorption bands at 639 and 657 nm in NaBaBSi glass were identified as band due to E^- centres and confirms the presence of metallic sodium colloids and the blue colour of the irradiated samples using UV-Vis-nIR optical absorption spectroscopy. Brow [181] reported the formation metallic sodium on the surface of irradiated binary sodium silicate glass. Howitt *et al.* [166] proposed mechanisms for the formation of metallic sodium in binary SiO_2-Na_2O glasses shown in (1-3) below, and a similar mechanism may arise in borosilicate glasses. Hassib *et al.* found an EPR signal at g = 2.011 due to sodium colloids formed by the collapse of F-centres in sodalite ($Na_8(Al_6Si_6O_{24})Cl_2$). Zatsepin *et al.* [176] reported the presence of E^- centres at g = 1.97 at higher magnetic fields (~345-350 mT) in Na/K silicate glasses.

Si-O-Si or B-O-B (formation of NBOs by irradiation by modifier or radiation) (1)

$Si\text{-}O\cdots Na^+ + h\nu \rightarrow Si\text{-}O: + Na^+$ (breaking of ionic or electrostatic bond) (2)

$Si\text{-}O: + Na^+ + h\nu \rightarrow Si\text{-}O\cdot + Na$ (creation of oxide radical and metallic Na) (3)

In addition to BOHC's, ET centres were found at both the doses for LiNaBSi glass. Thermal stabilities of these defects were investigated by annealing at 373 K – 773 K and results showed that the only paramagnetic defect stable above 373 K in NaBaBSi and above 473 K in LiNaBSi glass are POR's, all other defects were annihilated / recombined due to thermal annealing at 373 K. POR's were also stable in the LiNaBSi glass irradiated with 5 MGy at temperatures higher than 573 K, whereas the NaBaBSi glass irradiated with 5 MGy showed comparatively low S/N

peak-to-peak intensity at higher temperatures. This suggested that electron-hole recombination or annihilation is enabled by thermal energy as discussed in Section 5.4.3. Thermal energy can also enable the formation of new defect centres as it enables electron and hole to undergo transition and occupy different sites within the glass structure. Since some few of the defects are less stable at particular temperatures than the others, thermal annealing can also reveal the underlying defect centres in a more complex and convoluted EPR spectra.

As discussed in Section 5.4.2. formation of radiation induced defects, their abundance and type can be influenced by glass compositions and structure. In NaBaBSi glass Na^+ has higher cationic field strength than Ba^{2+} and Na^+ has smaller ionic radius than Ba^{2+}. This may be the reason of greater association of Na^+ with NBOs and formation of ionic bonds with them. In case of LiNaBSi Li+ is associated with NBOs because of high cationic field strength than Na^+. Gamma photons can break these ionic bond creating electron and hole pairs and ions and thus forming different radiation defects.

7.2.2 Gamma irradiation effects in SON68, ISG and CaZn simple glasses

Three simple glasses namely SON68 (ref Figure 6.8), ISG (ref Figure 6.9) and CaZn (ref Figure 6.10) were irradiated with 5 MGy gamma dose using ^{60}Co. Room temperature X-band EPR spectroscopy revealed the formation of resonance signal at g~2.00 in all three glasses which were attributed due to BOHC's. The other common defect found in all the three glasses was ET centres. UV-Vis-nIR optical absorption spectroscopy revealed bands at 532.64 nm and 604 nm, 568.80 nm, and 566.21 nm due to BOHC's in SON68, ISG and CaZn glasses, respectively. Optical absorption band at 325.15 nm was attributed to ET centres in ISG glass. Band at 201.62 nm in SON68 glass was attributed to iron impurities.

Investigation of gamma irradiation induced defects in simple glasses with different compositions thus revealed that dose of 5 MGy of gamma can enable the formation of different radiation-induced paramagnetic defects, however, some of the defects formed are common in all glass types. These defects may also have different thermal stabilities as shown for NaBaBSi and LiNaBSi glasses.

7.2.3 Gamma irradiation effects in simulated waste doped glasses

Room temperature X-band EPR spectroscopy revealed that there are resonance signals at g~4.3 and g~2.00 present in both pristine and 5 MGy gamma irradiated SON68, ISG and CaZn doped with non-active waste glasses. The resonance signal at g~2.00 can be considered due to a convolution of gamma irradiated induced defects or any paramagnetic species in all the three glasses. The resonance signal at g~4.3 can be considered due to iron (Fe^{3+}) present in the glass as a component of the waste / raw material impurity. The EPR spectra for LiNaBSi glass are a complex one which is difficult to deconvolute, however resonances at g~4.3 and g~2.00 can be clearly observed. For SON68 g~4.3 and g~2.0 resonances are also clearly distinct. No sharp and intense signals indicative of radiation-induced paramagnetic defect centres was observed in the simulated HLW-loaded glasses. This is attributed partly to the complexity of the waste and the many paramagnetic oxides present in the glass; and furthermore, the absence of sharp and intense resonances could also be related to the annihilation / mitigation of defect centres due to the presence of multivalent species in the waste-loaded glass.

7.2.4 Gamma irradiation effects in Fe_2O_3 doped glasses

Room temperature X-band EPR spectroscopy was carried out for NaBaBSi and LiNaBSi glasses doped with 0.19,0.99, 4.76 and 9.09 mol% Fe_2O_3. The results revealed that there are two resonance signals at g~4.3 and g~2.00 found in both the glass samples containing 0.19, 0.99 and 4.76 mol% Fe_2O_3. For 10 mol% Fe_2O_3 doped sample the EPR signal saturates, and no clear sharp resonance peaks/bands were observed. The resonance at g~4.3 is attributed to isolated Fe^{3+} ions at tetrahedral or rhombic (lower) symmetric sites. There is an intense sharp resonance signal observed at g~2.00 for 0.19 mol% Fe_2O_3 irradiated NaBaBSi and LiNaBSi which is due to radiation induced defects and which disappeared in 0.99 and 4.76 mol% Fe_2O_3 doped samples. The resonance signal at g~2.00 in 0.99 mol% Fe_2O_3 doped samples is attributed to the Fe^{3+} ions at tetrahedral or rhombic (lower) symmetric sites may be due to clustering of iron Fe^{3+} ions.

In NaBaBSi and LiNaBSi glass samples synthesised in oxidising environment, Mossbauer spectroscopy study showed that iron predominantly exists as Fe^{3+} form for both 4.76 and 9.09 mol% Fe_2O_3 doped NaBaBSi pristine and 5 MGy gamma irradiated glass specimens. There could be two different sites (tetrahedral and

octahedral) for Fe^{3+} which was indicated by different QS values in NaBaBSi glass but not observed for LiNaBSi glass. Also, the iron oxidation state may have changed after irradiation which is indicated by change in CS values for both the doped glasses.

In NaBaBSi and LiNaBSi glass samples synthesised in reducing environment, Mossbauer spectroscopy study showed that iron oxidation states changed after gamma irradiation. In LiNaBSi glass Fe^{2+} is getting converted to Fe^{3+} by the capture of holes which was observed by the increase in the relative area for Fe^{3+} increasing after gamma irradiations. This is opposite to what was observed in NaBaBSi glass where Fe^{3+} got reduced due to capture of electrons to Fe^{2+}. The two mechanisms observed for two different glasses are given by the following mechanisms:

$Fe^{3+} + e- \rightarrow Fe^{2+}$ (reduction of Fe^{3+}) and $Fe^{2+} + h^{+} \rightarrow Fe^{3+}$ (oxidation of Fe^{2+})

This observation showed that radiation induced defects are different in glasses with different compositions, however, a further investigation of the underlying causes of these observation is required

7.3 Future work

This section presents scope of the future work based on the results obtained and knowledge gained during the course of this study.

1. The presence of sodium elemental colloids in gamma irradiated NaBaBSi glasses will be investigated using microscopic techniques such as TEM to confirm their formation and thus their particle size and distribution. LiNaBSi glass will also be inspected using TEM. This study will also lead to answers about the disappearance of blue color on thermal annealing.
2. Simple glasses will be doped by other transition metals (TM) to investigate their effects and study how/whether they mitigate the radiation-induced defects.
3. HLW glasses doped with multivalent species such as TMs will also be further investigated before and after irradiation to study their effects on radiation-induced defects.
4. It will be attempted to control the redox of Fe as accurately as possible by forming Fe_2O_3 doped glasses in a controlled atmosphere.

5. Glasses will be irradiated to simulate the damage of recoil nuclei (atomic displacements).

References

[1] International Atomic Energy Agency, Management of Spent Fuel from Nuclear Power Reactors, Learning from the Past, Enabling Future, Proceedings of an International Conference, Vienna, Austria, 24-28 June (2019).

[2] W.N. Association, Emerging Nuclear Energy Countries, (2020). https://www.world-nuclear.org/information-library/country-profiles/others/emerging-nuclear-energy-countries.aspx#:~:text=About 30 countries are considering,their first nuclear power plants.

[3] A.H. Mir, S. Peuget, Using external ion irradiations for simulating self-irradiation damage in nuclear waste glasses: State of the art, recommendations and, prospects, J. Nucl. Mater. 539 (2020) 1–30. https://doi.org/10.1016/j.jnucmat.2020.152246. 1-30

[4] NDA, Geological disposal: Generic Specification for waste packages containing high heat generating waste, NDA Rep. NDA/RWMD/0 (2010).

[5] International Atomic Energy Agency, Classification of Radioactive Waste, in: Gen. Saf. Guid. GSG-1, 2009.

[6] V.I. Malkovsky, S. V. Yudintsev, M.I. Ojovan, V.A. Petrov, The Influence of Radiation on Confinement Properties of Nuclear Waste Glasses, Sci. Technol. Nucl. Install. 2020 (2020). 1-14 https://doi.org/10.1155/2020/8875723.

[7] A. Jan, THÈSE POUR OBTENIR LE GRADE DE DOCTEUR DE L ' UNIVERSITÉ DE MONTPELLIER Impact des effets balistiques sur les propriétés de la couche de gel des verres nucléaires simplifiés : une approche de simulation Monte Carlo, (2020).

[8] IAEA, Spent Fuel Reprocessing Options, Vienna, IAEA-TECDOC-1587, ISBN 978-92-0-103808-1 (2008).

[9] C.M. Jantzen, Development of glass matrices for high level radioactive wastes, Woodhead Publishing Limited, 2011. https://doi.org/10.1533/9780857090959.2.230.

[10] C.M. Jantzen, Systems approach to nuclear waste glass development, J. Non. Cryst. Solids. 84 (1986) 215–225. https://doi.org/10.1016/0022-3093(86)90780-5.

[11] D. Caurant, P. Loiseau, O. Majerus, V. Aubin-Chevaldonnet, I. Bardez, A. Quintas, Glasses, Glass-Ceramics and Ceramics for Immobilization of Highly Radioactive Nuclear Wastes, 2008. http://journals.sagepub.com/doi/10.1177/1120700020921110%0Ahttps://doi.org/10.1016/j.reuma.2018.06.001%0Ahttps://doi.org/10.1016/j.arth.2018.03.044%0Ahttps://reader.elsevier.com/reader/sd/pii/S1063458420300078?token=C039B8B13922A2079230DC9AF11A333E295FCD8.

[12] A. Andrews, I. Policy, I. Division, Radioactive Waste Streams : Updated December 13 , 2006 Anthony Andrews Specialist in Industrial Engineering and Infrastructure Policy Resources , Science , and Industry Division N / A

Radioactive Waste Streams : Waste Classification for Disposal, CRS Rep. Congr. (2006).

[13] W.J. Weber, F.P. Roberts, A review of radiation effects in solid nuclear wast forms, Nucl. Technol. 60 (1983) 178–198. https://doi.org/10.13182/NT83-A33073.

[14] C.S. N.Jacquet-Francillon, R. Bonniaud, Glass as a Material for the Final Disposal of Fission Products, Radiochim. Acta. 240 (1979) 231–240.

[15] A.H. Mir, A. Jan, J.-M. Delaye, S. Donnelly, J. Hinks, S. Gin, Effect of decades of corrosion on the microstructure of altered glasses and their radiation stability, Npj Mater. Degrad. 4 (2020) 1–9. https://doi.org/10.1038/s41529-020-0115-0.

[16] E.M. Pierce, P. Frugier, L.J. Criscenti, K.D. Kwon, S.N. Kerisit, Modeling Interfacial Glass-Water Reactions: Recent Advances and Current Limitations, Int. J. Appl. Glas. Sci. 5 (2014) 421–435. https://doi.org/10.1111/ijag.12077.

[17] M. Mohapatra, B.S. Tomar, Spectroscopic investigations of radiation damage in glasses used for immobilization of radioactive waste, Defect Diffus. Forum. 341 (2013) 107–128. https://doi.org/10.4028/www.scientific.net/DDF.341.107.

[18] M. Mohapatra, V.K. Manchanda, Characterization of borosilicate glass as host matrix for high level waste, IOP Conf. Ser. Mater. Sci. Eng. 2 (2009) 012006. https://doi.org/10.1088/1757-899X/2/1/012006.

[19] W.J. Weber, L.R. Corrales, N.J. Ness, R.E. Williford, H.L. Heinisch, S. Thevuthasan, J.P. Icenhower, B.P. McGrail, R. Devanathan, R.M. VanGinhoven, J. Song, B. Park, W. Jiang, B.D. Begg, R.B. Birtcher, X. Chen, S.D. Conradson, Radiation Effects in Nuclear Waste Materials October 2000 Prepared for the U . S . Department of Energy, PNNL-13345. (2000).

[20] K. Sun, L.M. Wang, R.C. Ewing, W.J. Weber, Electron irradiation induced phase separation in a sodium borosilicate glass, Nucl. Instruments Methods Phys. Res. Sect. B Beam Interact. with Mater. Atoms. 218 (2004) 368–374. https://doi.org/10.1016/j.nimb.2003.12.022.

[21] R.C. Ewing, W.J. Weber, F.W. Clinard, Radiation effects in nuclear waste forms for high-level radioactive waste, Prog. Nucl. Energy. 29 (1995) 63–127. https://doi.org/10.1016/0149-1970(94)00016-Y.

[22] W.J. Weber, Radiation and Thermal Ageing of Nuclear Waste Glass, Procedia Mater. Sci. 7 (2014) 237–246. https://doi.org/10.1016/j.mspro.2014.10.031.

[23] S. Gin, A. Abdelouas, L.J. Criscenti, W.L. Ebert, K. Ferrand, T. Geisler, M.T. Harrison, Y. Inagaki, S. Mitsui, K.T. Mueller, J.C. Marra, C.G. Pantano, E.M. Pierce, J. V. Ryan, J.M. Schofield, C.I. Steefel, J.D. Vienna, An international initiative on long-term behavior of high-level nuclear waste glass, Mater. Today. 16 (2013) 243–248. https://doi.org/10.1016/j.mattod.2013.06.008.

[24] S. Gin, P. Jollivet, M. Tribet, S. Peuget, S. Schuller, Radionuclides containment in nuclear glasses: An overview, Radiochim. Acta. 105 (2017) 927–959. https://doi.org/10.1515/ract-2016-2658.

[25] B. Boizot, G. Petite, D. Ghaleb, G. Calas, Dose, dose rate and irradiation

temperature effects in β-irradiated simplified nuclear waste glasses by EPR spectroscopy, J. Non. Cryst. Solids. 283 (2001) 179–185. https://doi.org/10.1016/S0022-3093(01)00338-6.

[26] B. Boizot, G. Petite, D. Ghaleb, N. Pellerin, F. Fayon, B. Reynard, G. Calas, Migration and segregation of sodium under β-irradiation in nuclear glasses, Nucl. Instruments Methods Phys. Res. Sect. B Beam Interact. with Mater. Atoms. 166 (2000) 500–504. https://doi.org/10.1016/S0168-583X(99)00787-9.

[27] B. Boizot, G. Petite, D. Ghaleb, G. Calas, Radiation induced paramagnetic centers in nuclear glasses by EPR spectroscopy, Nucl. Inst. Methods Phys. Res. B. 141 (1998) 580–584.

[28] M. Mohapatra, R.M. Kadam, R.K. Mishra, D. Dutta, P.K. Pujari, C.P. Kaushik, R.J. Kshirsagar, B.S. Tomar, S. V. Godbole, Electron beam irradiation effects in Trombay nuclear waste glass, Nucl. Instruments Methods Phys. Res. Sect. B Beam Interact. with Mater. Atoms. (2011). https://doi.org/10.1016/j.nimb.2011.06.009.

[29] M. Mohapatra, R.K. Mishra, C.P. Kaushik, S. V Godbole, Photoluminescence investigations of rare earth (Eu and Gd) incorporated nuclear waste glass, Phys. B Phys. Condens. Matter. 405 (2010) 4790–4795. https://doi.org/10.1016/j.physb.2010.09.003.

[30] D.L. Griscom, W.J. Weber, Electron spin resonance study of Fe 3 + and Mn 2 + ions in 17-year-old nuclear-waste-glass simulants containing PuO 2 with different degrees of Pu substitution, J. Non. Cryst. Solids. 357 (2011) 1437–1451. https://doi.org/10.1016/j.jnoncrysol.2010.11.017.

[31] D.L. Griscom, C.I. Merzbacher, R.A. Weeks, R.A. Zuhr, Electron spin resonance studies of defect centers induced in a high-level nuclear waste glass simulant by gamma-irradiation and ion-implantation, J. Non. Cryst. Solids. 258 (1999) 34–47. https://doi.org/10.1016/S0022-3093(99)00557-8.

[32] D.A. Dutt, P.L. Higby, D.L. Griscom, An electron spin resonance study of X-irradiated calcium aluminosilicate glasses, J. Non. Cryst. Solids. 130 (1991) 41–51. https://doi.org/10.1016/0022-3093(91)90154-X.

[33] R.C.* and D.L. Griscom, On the structure of defect centers in gamma-irradiated alkali silicate glasses, Nucl. Inst. Methods Phys. Res. B1. (1984) 503–510.

[34] D.L. Griscom, Self-trapped holes in pure-silica glass: A history of their discovery and characterization and an example of their critical significance to industry, J. Non. Cryst. Solids.352 (2006). 2601-2617 https://doi.org/10.1016/j.jnoncrysol.2006.03.033.

[35] D.L. Griscom, γ-Ray-induced visible/infrared optical absorption bands in pure and F-doped silica-core fibers: Are they due to self-trapped holes?, in: J. Non. Cryst. Solids, 349 (2004) 139.147. https://doi.org/10.1016/j.jnoncrysol.2004.08.221.

[36] A.H. Mir, I. Monnet, M. Toulemonde, S. Bouffard, C. Jegou, S. Peuget, Mono and sequential ion irradiation induced damage formation and damage recovery in oxide glasses: Stopping power dependence of the mechanical properties, J.

Nucl. Mater. 469 (2016) 244–250. https://doi.org/10.1016/j.jnucmat.2015.12.004.

[37] A.H. Mir, I. Monnet, B. Boizot, C. Jégou, S. Peuget, Electron and electron-ion sequential irradiation of borosilicate glasses: Impact of the pre-existing defects, J. Nucl. Mater. 489 (2017) 91–98. https://doi.org/10.1016/j.jnucmat.2017.03.047.

[38] T. Charpentier, L. Martel, A.H. Mir, J. Somers, C. Jégou, Self-healing capacity of nuclear glass observed by NMR spectroscopy, Nat. Publ. Gr. (2016) 1–6. https://doi.org/10.1038/srep25499.

[39] W.J. Weber, R.C. Ewing, C.A. Angell, G.W. Arnold, A.N. Cormack, J.M. Delaye, D.L. Griscom, L.W. Hobbs, A. Navrotsky, D.L. Price, A.M. Stoneham, M.C. Weinberg, Radiation Effects in Glasses Used for Immobilization of High-level Waste and Plutonium Disposition, J. Mater. Res. 12 (1997) 1948–1978. https://doi.org/10.1557/jmr.1997.0266.

[40] W.J. Weber, Radiation and Thermal Ageing of Nuclear Waste Glass, Procedia Mater. Sci. 7 (2014) 237–246. https://doi.org/10.1016/j.mspro.2014.10.031.

[41] B.F. Dunnett, Review of the Development of UK High Level Waste Vitrified Product (Nexia Solutions (06) 7926), (2007) 11–17.

[42] J. Delaye, S. Peuget, G. Bureau, G. Calas, Molecular dynamics simulation of radiation damage in glasses, J. Non. Cryst. Solids. 357 (2011) 2763–2768. https://doi.org/10.1016/j.jnoncrysol.2011.02.026.

[43] G. Bureau, J.M. Delaye, S. Peuget, G. Calas, Molecular dynamics study of structural changes versus deposited energy dose in a sodium borosilicate glass, Nucl. Instruments Methods Phys. Res. Sect. B Beam Interact. with Mater. Atoms. 266 (2008) 2707–2710. https://doi.org/10.1016/j.nimb.2008.03.217.

[44] G. Calas, L. Galoisy, L. Cormier, J.-M. Delaye, P. Jollivet, S. Peuget, Structural Evolution of Nuclear Glasses under Forcing Conditions (Irradiation, Alteration), Mater. Res. Soc. Symp. Proc. 1265 (2010) 1265-AA03-01. https://doi.org/10.1557/PROC-1265-AA03-01.

[45] A.H. Mir, S. Peuget, M. Toulemonde, P. Bulot, C. Jegou, S. Miro, S. Bouffard, Defect recovery and damage reduction in borosilicate glasses under double ion beam irradiation, Epl. 112 (2015). https://doi.org/10.1209/0295-5075/112/36002.

[46] N. Valle, A. Verney-Carron, J. Sterpenich, G. Libourel, E. Deloule, P. Jollivet, Elemental and isotopic (29Si and 18O) tracing of glass alteration mechanisms, Geochim. Cosmochim. Acta. 74 (2010) 3412–3431. https://doi.org/10.1016/j.gca.2010.03.028.

[47] D. Rébiscoul, F. Rieutord, F. Né, P. Frugier, R. Cubitt, S. Gin, Water penetration mechanisms in nuclear glasses by X-ray and neutron reflectometry, J. Non. Cryst. Solids. 353 (2007) 2221–2230. https://doi.org/10.1016/j.jnoncrysol.2007.03.002.

[48] D. Rébiscoul, F. Bruguier, V. Magnin, S. Gin, Impact of soda-lime borosilicate

glass composition on water penetration and water structure at the first time of alteration, J. Non. Cryst. Solids. 358 (2012) 2951–2960. https://doi.org/10.1016/j.jnoncrysol.2012.07.014.

[49] S. Gin, M. Collin, P. Jollivet, M. Fournier, Y. Minet, L. Dupuy, T. Mahadevan, S. Kerisit, J. Du, Dynamics of self-reorganization explains passivation of silicate glasses, Nat. Commun. 9 (2018) 1–9. https://doi.org/10.1038/s41467-018-04511-2.

[50] M. Tribet, A.H. Mir, C. Gillet, C. Jegou, S. Mougnaud, J.A. Hinks, S.E. Donnelly, S. Peuget, New Insights about the Importance of the Alteration Layer/Glass Interface, J. Phys. Chem. C. 124 (2020) 10032–10044. https://doi.org/10.1021/acs.jpcc.0c02121.

[51] S. Peuget, E.A. Maugeri, T. Charpentier, C. Mendoza, M. Moskura, T. Fares, O. Bouty, C. Jégou, Comparison of radiation and quenching rate effects on the structure of a sodium borosilicate glass, J. Non. Cryst. Solids. 378 (2013) 201–212. https://doi.org/10.1016/j.jnoncrysol.2013.07.019.

[52] A.H. Mir, A. Jan, J.-M. Delaye, S. Donnelly, J. Hinks, S. Gin, Effect of decades of corrosion on the microstructure of altered glasses and their radiation stability, Npj Mater. Degrad. 4 (2020) 0–9. https://doi.org/10.1038/s41529-020-0115-0.

[53] G. Geneste, F. Bouyer, S. Gin, Hydrogen-sodium interdiffusion in borosilicate glasses investigated from first principles, J. Non. Cryst. Solids. 352 (2006) 3147–3152. https://doi.org/10.1016/j.jnoncrysol.2006.04.023.

[54] R. Hellmann, S. Cotte, E. Cadel, S. Malladi, L.S. Karlsson, S. Lozano-Perez, M. Cabié, A. Seyeux, Nanometre-scale evidence for interfacial dissolution-reprecipitation control of silicate glass corrosion, Nat. Mater. 14 (2015) 307–311. https://doi.org/10.1038/nmat4172.

[55] S. Peuget, M. Tribet, S. Mougnaud, S. Miro, C. Jégou, Radiations effects in ISG glass: from structural changes to long-term aqueous behavior, Npj Mater. Degrad. 2 (2018) 1-9. https://doi.org/10.1038/s41529-018-0044-3.

[56] E.J. Friebele, D.L. Griscom, M. Stapelbroek, R.A. Weeks, Fundamental defect centers in glass: The peroxy radical in irradiated, high-purity, fused silica, Phys. Rev. Lett. 42 (1979) 1346–1349. https://doi.org/10.1103/PhysRevLett.42.1346.

[57] M. Mohapatra, R.M. Kadam, R.K. Mishra, C.P. Kaushik, B.S. Tomar, S. V. Godbole, Gamma Radiation-Induced Changes in Trombay Nuclear Waste Glass Containing Iron, Int. J. Appl. Glas. Sci. 4 (2013) 53–60. https://doi.org/10.1111/j.2041-1294.2012.00094.x.

[58] B. Boizot, N. Ollier, F. Olivier, G. Petite, D. Ghaleb, E. Malchukova, Irradiation effects in simplified nuclear waste glasses, Nucl. Instruments Methods Phys. Res. Sect. B Beam Interact. with Mater. Atoms. 240 (2005) 146–151. https://doi.org/10.1016/j.nimb.2005.06.105.

[59] N. Ollier, V. Pukhkaya, Point defect stability in gamma irradiated aluminoborosilicate glasses: Influence of Yb 3+ doping ions, Nucl. Instruments Methods Phys. Res. Sect. B Beam Interact. with Mater. Atoms. 277 (2012)

121–125. https://doi.org/10.1016/j.nimb.2011.12.053.

[60] F.Y. Olivier, B. Boizot, D. Ghaleb, G. Petite, Raman and EPR studies of β-irradiated oxide glasses: The effect of iron concentration, J. Non. Cryst. Solids. 351 (2005) 1061–1066. https://doi.org/10.1016/j.jnoncrysol.2005.01.018.

[61] E. Malchukova, B. Boizot, Reduction of Eu3+ to Eu2+ in aluminoborosilicate glasses under ionizing radiation, Mater. Res. Bull. 45 (2010) 1299–1303. https://doi.org/10.1016/j.materresbull.2010.04.027.

[62] E. Malchukova, B. Boizot, G. Petite, D. Ghaleb, Optical properties and valence state of Sm ions in aluminoborosilicate glass under β-irradiation, J. Non. Cryst. Solids. 353 (2007) 2397–2402. https://doi.org/10.1016/j.jnoncrysol.2007.04.003.

[63] N.J. Cassingham, P. Bingham, R.J. Hand, S. Forder, Property modification of a high level nuclear waste borosilicate glass through the addition of Fe2O3, Glas. Technol. Eur. J. Glas. Sci. Technol. A, Febr. 2008, 49 (1), 21–26. 49 (2008) 21–26. http://www.societyofglasstechnology.org.uk/cgi-bin/open.cgi?page=journal&sessionid=85597106.

[64] K.J. Rao, B.G. Rao, Electron spin resonance of transition metal ions in glasses, Proc. Indian Acad. Sci. - Chem. Sci. 95 (1985) 169–188. https://doi.org/10.1007/BF02839726.

[65] T.T. Volotinen, J.M. Parker, P.A. Bingham, Concentrations and site partitioning of Fe2+ and Fe3+ ions in a soda-lime-silica glass obtained by optical absorbance spectroscopy, Phys. Chem. Glas. Eur. J. Glas. Sci. Technol. Part B. 49 (2008) 258–270.

[66] R.P. Sreekanth Chakradhar, A. Murali, J.L. Rao, Electron paramagnetic resonance and optical absorption studies of Fe(III) ions in alkali barium borate glasses, Opt. Mater. (Amst). 10 (1998) 109–116.

[67] H.D. Schreiber, A.L. Hockman, Redox Chemistry in Candidate Glasses for Nuclear Waste Immobilization, J. Am. Ceram. Soc. 70 (1987) 591–594. https://doi.org/10.1111/j.1151-2916.1987.tb05712.x.

[68] M. Mohapatra, R.K. Mishra, C.P. Kaushik, B.S. Tomar, Investigation of Radiation Damage in Trombay Nuclear Waste Glasses by ESR and Photoluminescence Techniques, Procedia Mater. Sci. 7 (2014) 247–251. https://doi.org/10.1016/j.mspro.2014.10.032.

[69] R. Michal, Fifty years ago in December : Atomic reactor EBR-I produced first electricity, Nucl. News. (2001) 28–29. http://www2.ans.org/pubs/magazines/nn/docs/2001-11-2.pdf.

[70] International Atomic Energy Agency, Nuclear energy basic principles, IAEA Nucl. Energy Ser. (2008). https://www-pub.iaea.org/MTCD/Publications/PDF/Pub1374_web.pdf.

[71] International Atomic Energy Agency, Energy, Electricity and Nuclear Power Estimates for the Period up to 2050, Ref. Data Ser. No. 1. (2019). https://www-pub.iaea.org/MTCD/Publications/PDF/19-00521_web.pdf.

[72] International Atomic Energy Agency, Demonstrating performance of spent fuel

and related storage system components during very long term storage, IAEA TECDOC Ser. (2019). https://www-pub.iaea.org/MTCD/Publications/PDF/TE-1878web.pdf.

[73] World Nuclear Association, (n.d.). https://www.world-nuclear.org/information-library/nuclear-fuel-cycle/nuclear-wastes/radioactive-waste-management.aspx (accessed October 12, 2020).

[74] IAEA, The nuclear fuel cycle, Int. At. Energy Agency. (2011) 1–24. www.iaea.org/OurWork/ST/NE/NEFW/index.

[75] International Atomic Energy Agency, IAEA Nuclear Energy Series Radioactive Waste Management Objectives, IAEA Nucl. Energy Ser. (2011) 7. https://www-pub.iaea.org/MTCD/Publications/PDF/Pub1521_web.pdf.

[76] L.N. Larson, The Front End of the Nuclear Fuel Cycle : Current Issues The Front End of the Nuclear Fuel Cycle : Current Issues, Congr. Res. Serv. (2019). https://crsreports.congress.gov.

[77] József Kónya and Noémi M. Nagy, Nuclear and Radiochemistry, 2, 2012. ISBN 9780128136447. https://doi.org/10.1016/B978-0-12-405897-2.00021-5.

[78] Worl Nuclear Association, (n.d.). https://www.world-nuclear.org/information-library/nuclear-fuel-cycle/introduction/nuclear-fuel-cycle-overview.aspx (accessed October 14, 2020).

[79] B. Collum, 1 - Nuclear fuel cycle, Elsevier Ltd., n.d. https://doi.org/10.1016/B978-0-08-101938-2.00001-5.

[80] P. Joseph, Introductory course on the Nuclear Fuel Cycle for NA-21 Personnel, Los Alamos Natl. Lab. (2017).

[81] Hore-Lacy, Mining and milling of uranium, Woodhead Publishing Limited, 2012. https://doi.org/10.1533/9780857096388.2.129.

[82] G.M. Mudd, The future of Yellowcake: A global assessment of uranium resources and mining, Sci. Total Environ. 472 (2014) 590–607. https://doi.org/10.1016/j.scitotenv.2013.11.070.

[83] W. Jeff, Uranium conversion and enrichment, Woodhead Publishing Limited, 2012. https://doi.org/10.1533/9780857096388.2.151.

[84] R. Natarajan, Reprocessing of spent nuclear fuel in India: Present challenges and future programme, Prog. Nucl. Energy. 101 (2017) 118–132. https://doi.org/10.1016/j.pnucene.2017.03.001.

[85] P.K. Dey, N.K. Bansal, Spent fuel reprocessing: A vital link in Indian nuclear power program, Nucl. Eng. Des. 236 (2006) 723–729. https://doi.org/10.1016/j.nucengdes.2005.09.029.

[86] K.B. Sorenson, Long-term storage of spent nuclear fuel and high-level radioactive waste: Strategies and implications for package design, in: Safe Secur. Transp. Storage Radioact. Mater., Elsevier, 2015: pp. 311–324. https://doi.org/10.1016/B978-1-78242-309-6.00019-8.

[87] P. Netter, Reprocessing of spent oxide fuel from nuclear power reactors,

Woodhead Publishing Limited, 2012. https://doi.org/10.1533/9780857096388.4.459.

[88] A.P. Paiva, P. Malik, Recent advances on the chemistry of solvent extraction applied to the reprocessing of spent nuclear fuels and radioactive wastes, J. Radioanal. Nucl. Chem. 261 (2004) 485–496. https://doi.org/10.1023/B:JRNC.0000034890.23325.b5.

[89] K.L. Nash, M. Nilsson, Introduction to the reprocessing and recycling of spent nuclear fuels, Elsevier Ltd., 2015. https://doi.org/10.1016/B978-1-78242-212-9.00001-0.

[90] R.C. Ewing, Long-term storage of spent nuclear fuel, Nat. Mater. 14 (2015) 252–257. https://doi.org/10.1038/nmat4226.

[91] T. Storvick, G.J. Suppes, Recycling and Waste Handling for Spent Nuclear Fuel, in: Sustain. Nucl. Power, 2007: pp. 283–317. https://doi.org/10.1016/b978-012370602-7/50028-4.

[92] B.L. Metcalfe, I.W. Donald, Management of radioactive waste (RAW) from nuclear weapons programmes, Radioact. Waste Manag. Contam. Site Clean-Up Process. Technol. Int. Exp. (2013) 775–800. https://doi.org/10.1533/9780857097446.3.775.

[93] J.A.C. Marples, The preparation, properties, and disposal of vitrified high level waste from nuclear fuel reprocessing, Glas. Technol. 29 (1988) 230–47.

[94] R.N.J.Taylor, I. W. DONALD, B. L. METCALFE, The immobilization of high level radioactive wastes using ceramics and glasses, in: J. Mater. Sci., 32 (1997): pp. 5851–5887.

[95] J. Bruno, R.C. Ewing, Spent nuclear fuel, Elements. 2 (2006) 343–349. https://doi.org/10.2113/gselements.2.6.343.

[96] J.P. Ackerman, Chemical Basis for Pyrochemical Reprocessing of Nuclear Fuel, Ind. Eng. Chem. Res. 30 (1991) 141–145. https://doi.org/10.1021/ie00049a022.

[97] T. Koyama, M. Iizuka, Pyrochemical fuel cycle technologies for processing of spent nuclear fuels: Developments in Japan, Elsevier Ltd., 2015. https://doi.org/10.1016/B978-1-78242-212-9.00018-6.

[98] K. Raj, K.K. Prasad, N.K. Bansal, Radioactive waste management practices in India, Nucl. Eng. Des. 236 (2006) 914–930. https://doi.org/10.1016/j.nucengdes.2005.09.036.

[99] P.A. Bingham, A.J. Connelly, N.C. Hyatt, R.J. Hand, Corrosion of glass contact refractories for the vitrification of radioactive wastes: A review, Int. Mater. Rev. 56 (2011) 226–242. https://doi.org/10.1179/1743280410Y.0000000005.

[100] S. Vaishnav, Structure and Characterization of Sulphate Doped Glasses for Radioactive Waste Immobilisation, 2018.Retrieved from: https://doi.org/10.7190/shu-thesis-00114

[101] P. Rose, The Crystallisation and Aqueous Durability of Borosilicate Nuclear Waste Glasses, 2007. Retrieved from:

http://ethos.bl.uk/OrderDetails.do?uin=uk.bl.ethos.489679.

[102] J.M. Schofield, Vitrification of a chloride containing actinide waste surrogate, 2011.

[103] P.B. Rose, D.I. Woodward, M.I. Ojovan, N.C. Hyatt, W.E. Lee, Crystallisation of a simulated borosilicate high-level waste glass produced on a full-scale vitri fi cation line, J. Non. Cryst. Solids. 357 (2011) 2989–3001. https://doi.org/10.1016/j.jnoncrysol.2011.04.003.

[104] C.P. Kaushik, Indian Program for Vitrification of High Level Radioactive Liquid Waste, Procedia Mater. Sci. 7 (2014) 16–22. https://doi.org/10.1016/j.mspro.2014.10.004.

[105] M.J.D. Rushton, Simulations of Glass and Ceramic Systems for Nuclear Waste Applications, 2006. Retrieved from: http://abulafia.mt.ic.ac.uk/publications/theses/rushton_thesis.pdf

[106] N.J. Cassingham, Structure and Durability of UK Simulated High Level Nuclear Waste Glasses, 2013 Retrieved from: https://etheses.whiterose.ac.uk/4131/

[107] U. Kingdom, N. Limited, Identification and Description of UK Radioactive Wastes and Materials Potentially Requiring Long-term Management, 2003.

[108] P.K. Wattal, Back end of Indian nuclear fuel cycle-A road to sustainability, Prog. Nucl. Energy. 101 (2017) 133–145. https://doi.org/10.1016/j.pnucene.2017.03.004.

[109] T.A. Todd, Development of closed nuclear fuel cycles in the United States, Elsevier Ltd., 2015. https://doi.org/10.1016/B978-1-78242-212-9.00019-8.

[110] E.D. Collins, Advanced thermal denitration conversion processes for aqueous-based reprocessing and recycling of spent nuclear fuels, Elsevier Ltd., 2015. https://doi.org/10.1016/B978-1-78242-212-9.00012-5.

[111] J.P. Glatz, P. Souček, R. Malmbeck, Key challenges in advanced reprocessing of spent nuclear fuels, Reprocess. Recycl. Spent Nucl. Fuel. (2015) 49–62. https://doi.org/10.1016/B978-1-78242-212-9.00003-4.

[112] I.W. Donald, B.L. Metcalfe, R.N.J. Taylor, Review The immobilization of high level radioactive wastes using ceramics and glasses, J. Mater. Sci. (1997) 5851–5887.

[113] I.B. Plecas, A.D. Peric, J.D. Drljaca, A.M. Kostadinovic, S.D. Glodic, Immobilization of radioactive waste water residues in a cement matrix, Cem. Concr. Res. 22 (1992) 571–576. https://doi.org/10.1016/0008-8846(92)90007-I.

[114] W. Xuequan, Y. Sheng, S. Xiaodong, T. Minghshu, Y. Liji, Alkali activated slag cement based radioactive waste forms Cem. Concr. Res. 21 (1991) 16–20.

[115] C. Varghese, A.K. Govindan, P.K. Wattal, T.K. Theyyunni, S. Krishnan, B.V.B. Pai, Cementation Matrices for Intermediate Level Aqueous Radioactive Wastes, 27 (1995). 420-423 https://doi.org/10.12935/jvma1951.50.420.

[116] M.I. Ojovan, W.E. Lee, Nuclear Waste Types and Sources, An Introd. to Nucl.

Waste Immobil. (2014) 75–97. https://doi.org/10.1016/b978-0-08-099392-8.00008-5.

[117] K. Raj, C.P. Kaushik, Glass matrices for vitrification of radioactive waste - An update on R & D efforts, IOP Conf. Ser. Mater. Sci. Eng. 2 (2009). https://doi.org/10.1088/1757-899X/2/1/012002.

[118] W.E. Lee, M.I. Ojovan, M.C. Stennett, N.C. Hyatt, M.I. Ojovan, M.C. Stennett, N.C.H. Immobilisation, W.E. Lee, M.I. Ojovan, M.C. Stennett, N.C. Hyatt, Immobilisation of radioactive waste in glasses , glass composite materials and ceramics Immobilisation of radioactive waste in glasses , glass composite materials and ceramics, 6753 (2016). https://doi.org/10.1179/174367606X81669.

[119] W.G. Burns, A.E. Hughes, J.A.C. Marples, R.S. Nelson, A.M. Stoneham, Effects of radiation on the leach rates of vitrified radioactive waste, J. Nucl. Mater. 107 (1982) 245–270. https://doi.org/10.1016/0022-3115(82)90424-X.

[120] I. Bardez, D. Caurant, J.L. Dussossoy, P. Loiseau, C. Gervais, F. Ribot, D.R. Neuville, N. Baffier, C. Fillet, Development and characterization of rare earth-rich glassy matrices envisaged for the immobilization of concentrated nuclear waste solutions, Nucl. Sci. Eng. 153 (2006) 272–284. https://doi.org/10.13182/NSE06-A2613.

[121] N.J. Cassingham, P. Bingham, R.J. Hand, S. Forder, Property modification of a high level nuclear waste borosilicate glass through the addition of Fe2O3, Glas. Technol. Eur. J. Glas. Sci. Technol. A, Febr. 2008, 49 (1), 21–26. (2008) 21–26.

[122] W.J. Weber, A. Navrotsky, S. Stefanovsky, E.R. Vance, E. Vernaz, Materials Science of High-Level Immobilization, MRS Bull. 34 (2009) 46–52. https://doi.org/10.1557/mrs2009.12.

[123] F.A. Lifanov, I.A. Sobolev, S.A. Dmitriev, S.V. Stefanovsky, M.I. Ojovan, W.. Lee, R. Burcl, Vitrification of low and intermediate level waste: Technology and glass performance, Waste Manag. Conf. (2004) 55. http://eprints.uanl.mx/5481/1/1020149995.PDF.

[124] M.J. Plodinec, Borosilicate glasses for nuclear waste imobilisation, Glas. Technol. 41 (2000) 186–192.

[125] É. Vernaz, J. Bruezière, History of Nuclear Waste Glass in France, Procedia Mater. Sci. 7 (2014) 3–9. https://doi.org/10.1016/j.mspro.2014.10.002.

[126] C. Poinssot, B. Boullis, S. Bourg, Role of recycling in advanced nuclear fuel cycles, Elsevier Ltd., 2015. https://doi.org/10.1016/B978-1-78242-212-9.00002-2.

[127] S. Peuget, J.N. Cachia, C. Jégou, X. Deschanels, D. Roudil, V. Broudic, J.M. Delaye, J.M. Bart, Irradiation stability of R7T7-type borosilicate glass, J. Nucl. Mater. 354 (2006) 1–13. https://doi.org/10.1016/j.jnucmat.2006.01.021.

[128] G. Karakurt, A. Abdelouas, J.P. Guin, M. Nivard, T. Sauvage, M. Paris, J.F. Bardeau, Understanding of the mechanical and structural changes induced by alpha particles and heavy ions in the French simulated nuclear waste glass, J.

Nucl. Mater. 475 (2016) 243–254. https://doi.org/10.1016/j.jnucmat.2016.04.022.

[129] M.T. Harrison, Vitrification of High Level Waste in the UK, Procedia Mater. Sci. 7 (2014) 10–15. https://doi.org/10.1016/j.mspro.2014.10.003.

[130] NDA, Nuclear Decommissioning Authority Strategy effective from March 2021, (n.d.). https://www.gov.uk/government/publications/nuclear-decommissioning-authority-strategy-effective-from-march-2021/nuclear-decommissioning-authority-strategy-effective-from-march-2021 (accessed March 18, 2021).

[131] NDA, Geological Disposal An overview of the generic Disposal System Safety Case, 2010.

[132] R. Short, Phase Separation and Crystallisation in UK HLW Vitrified Products, Procedia Mater. Sci. 7 (2014) 93–100. https://doi.org/10.1016/j.mspro.2014.10.013.

[133] P. Sengupta, C.P. Kaushik, G.K. Dey, Immobilization of High Level Nuclear Wastes : The Indian Scenario, On a Sustainable Future of the Earth's Natural Resources XIV (2013) 25-51. https://doi.org/10.1007/978-3-642-32917-3.

[134] R.K. Mishra, S. Kumar, B.S. Tomar, A.K. Tyagi, C.P. Kaushik, K. Raj, V.K. Manchanda, Effect of barium on diffusion of sodium in borosilicate glass, J. Hazard. Mater. 156 (2008) 129–134. https://doi.org/10.1016/j.jhazmat.2007.12.006.

[135] P.B. Jahagirdar, P.K. Wattal, Vitrification of sulphate bearing high level wastes in borosilicate matrix, Waste Manag. 18 (1998) 265–273. https://doi.org/10.1016/S0956-053X(98)00025-7.

[136] C.P. Kaushik, R.K. Mishra, P. Sengupta, A. Kumar, D. Das, G.B. Kale, K. Raj, Barium borosilicate glass – a potential matrix for immobilization of sulfate bearing high-level radioactive liquid waste, J. Nucl. Mater. 358 (2006) 129–138. https://doi.org/10.1016/j.jnucmat.2006.07.004.

[137] R.K. Mishra, K. V. Sudarsan, P. Sengupta, R.K. Vatsa, A.K. Tyagi, C.P. Kaushik, D. Das, K. Raj, Role of sulfate in structural modifications of sodium barium borosilicate glasses developed for nuclear waste immobilization, J. Am. Ceram. Soc. 91 (2008) 3903–3907. https://doi.org/10.1111/j.1551-2916.2008.02773.x.

[138] A.K. Varshneya, Fundamentals of Inorganic Glassmaking, (1994) 507-550. https://doi.org/10.1016/b978-0-08-057150-8.50025-2.

[139] T.M. Nieuwenhuizen, Thermodynamic picture of the glassy state gained from exactly solvable models, Phys. Rev. E. 61 (1998) 267-292.

[140] T.M. Nieuwenhuizen, Thermodynamic picture of the glassy state, J. Phys. Condens. Matter. 12 (2000) 6543–6552. https://doi.org/10.1088/0953-8984/12/29/326.

[141] E.D. Zanotto, J.C. Mauro, The glassy state of matter: Its definition and ultimate fate, J. Non. Cryst. Solids. 471 (2017) 490–495. https://doi.org/10.1016/j.jnoncrysol.2017.05.019.

[142] J.E. Shelby, Introduction to Glass Science and Technology, 2005. https://doi.org/10.1524/zpch.1999.208.part_1_2.292. Pg 4.

[143] G.N. Greaves, K.L. Ngai, Reconciling ionic-transport properties with atomic structure in oxide glasses, Phys. Rev. B. 52 (1995) 6358-6380

[144] G.N. Greaves, S. Sen, Inorganic glasses, glass-forming liquids and amorphizing solids, Adv. Phys. 56 (2007) 1–166. https://doi.org/10.1080/00018730601147426.

[145] D.J. Backhouse, A Study of the Dissolution of Nuclear Waste Glasses in Highly-Alkaline Conditions, 2017.

[146] L.S. Du, J.F. Stebbins, Site preference and Si/B mixing in mixed-alkali borosilicate glasses: A high-resolution 11B and 17O NMR study, Chem. Mater. 15 (2003) 3913–3921. https://doi.org/10.1021/cm034427r.

[147] P. Zhao, S. Kroeker, J.F. Stebbins, Non-bridging oxygen sites in barium borosilicate glasses: Results from 11B and 17O NMR, J. Non. Cryst. Solids. 276 (2000) 122–131. https://doi.org/10.1016/S0022-3093(00)00290-8.

[148] B. Hehlen, D.R. Neuville, Raman response of network modifier cations in alumino-silicate glasses, J. Phys. Chem. B. 119 (2015) 4093–4098. https://doi.org/10.1021/jp5116299.

[149] L.S. Du, J.F. Stebbins, Solid-state NMR study of metastable immiscibility in alkali borosilicate glasses, J. Non. Cryst. Solids. 315 (2003) 239–255. https://doi.org/10.1016/S0022-3093(02)01604-6.

[150] G.N. Greaves, A. Fontaine, P. Lagarde, D. Raoux, S.J. Gurman, Local structure of silicate glasses., Nature. 293 (1981) 611–616. https://doi.org/https://doi.org/10.1038/293611a0.

[151] G.N. Greaves, Exafs and the structure of glass , J. Non. Cryst. Solids. 71 (1985) 203–217.

[152] Wright, A.C., Neutron and X-ray amorphography, J. Non. Cryst. Solids. 106 (1988) 1–16.

[153] W.H. Zachariasen, The atomic arrangement in glass, J. Am. Chem. Soc. 54 (1932) 3841–3851.

[154] B.E. Warren, Summary of Work on Atomic Arrangement in Glass, J. Am. Ceram. Soc. 24 (1941) 256–261. https://doi.org/10.1111/j.1151-2916.1941.tb14858.x.

[155] K. -H Sun, Fundamental Condition of Glass Formation, J. Am. Ceram. Soc. 30 (1947) 277–281. https://doi.org/10.1111/j.1151-2916.1947.tb19654.x.

[156] K.B. Patel, Effects of radiation damage and composition on phase separation in borosilicate nuclear waste glasses, 2018.1-328, Retrieved from: https://www.repository.cam.ac.uk/handle/1810/275693

[157] J. Krogh-Moe, No Title, Phys. Chem. Glas. 3 (1962) 208

[158] B.G. Parkinson, Influence of Composition on Structure and Caesium Volatilisation from Glasses for HLW Confinement, 2007.

[159] H. Doweidar, Consideration of the boron oxide anomaly, J. Mater. Sci. 25 (1990) 253–258. https://doi.org/10.1007/BF00544216.

[160] A.H. Silver, P.J. Bray, Nuclear Magnetic Resonance Absorption in Glass. I. Nuclear Quadrupole Effects in Boron Oxide, Soda-Boric Oxide, and Borosilicate Glasses.pdf, J. Chem. Phys. 29 (1958) 984-990.

[161] Y.H. Yun, P.J. Bray, Nuclear magnetic resonance studies of the glasses in the system Na20-B203-SiO 2, J. Non. Cryst. Solids. 30 (1978) 45–60. https://doi.org/10.1016/0022-3093(78)90055-8.

[162] W.J. Dell, P.J. Bray, S.Z. Xiao, 11B NMR studies and structural modeling of Na2O-B2O3-SiO2 glasses of high soda content, J. Non. Cryst. Solids. 58 (1983) 1–16. https://doi.org/10.1016/0022-3093(83)90097-2.

[163] L. Leay, M.T. Harrison, Bubble formation in nuclear glasses: A review, J. Mater. Res. 34 (2019) 905–920. https://doi.org/10.1557/jmr.2019.29.

[164] J.F. Denatale, D.G. Howitt, The gamma-irradiation of nuclear waste glasses, Radiat. Eff. 91 (1985) 89–96. https://doi.org/10.1080/00337578508222550.

[165] K.B. Patel, B. Boizot, S.P. Facq, G.I. Lampronti, S. Peuget, S. Schuller, I. Farnan, β-Irradiation Effects on the Formation and Stability of CaMoO4 in a Soda Lime Borosilicate Glass Ceramic for Nuclear Waste Storage, Inorg. Chem. 56 (2017) 1558–1573. https://doi.org/10.1021/acs.inorgchem.6b02657.

[166] D.G. Howitt, H.W. Chan, J.F. DeNatale, J.P. Heuer, Mechanism for the Radiolytically Induced Decomposition of Soda–Silicate Glasses, J. Am. Ceram. Soc. 74 (1991) 1145–1147. https://doi.org/10.1111/j.1151-2916.1991.tb04358.x.

[167] S. Peuget, J.M. Delaye, C. Jégou, Specific outcomes of the research on the radiation stability of the French nuclear glass towards alpha decay accumulation, J. Nucl. Mater. 444 (2014) 76–91. https://doi.org/10.1016/j.jnucmat.2013.09.039.

[168] D.L. Griscom, From E′ centers to the “characteristic” resonance: a colleague’s reminiscences on the scientific odyssey of Robert A. Weeks, J. Non. Cryst. Solids. (1994) 22-38. https://doi.org/10.1016/0022-3093(94)90682-3.

[169] D.L. Griscom, Electron spin resonance in glasses, J. Non. Cryst. Solids. 40 (1980) 211–272.

[170] N. Ollier, G. Rizza, B. Boizot, G. Petite, Effects of temperature and flux on oxygen bubble formation in Li borosilicate glass under electron beam irradiation, J. Appl. Phys. 99 (2006) 1-6. https://doi.org/10.1063/1.2189026.

[171] N. Ollier, B. Champagnon, B. Boizot, Y. Guyot, G. Panczer, B. Padlyak, Influence of external β-irradiation in oxide glasses, J. Non. Cryst. Solids. 323 (2003) 200–206. https://doi.org/10.1016/S0022-3093(03)00307-7.

[172] A. Abbas, Y. Serruys, D. Ghaleb, J.M. Delaye, B. Boizot, B. Reynard, G. Calas, Evolution of nuclear glass structure under α-irradiation, Nucl. Instruments Methods Phys. Res. Sect. B Beam Interact. with Mater. Atoms. 166 (2000) 445–450. https://doi.org/10.1016/S0168-583X(99)00695-3.

[173] N. Ollier, B. Boizot, B. Reynard, D. Ghaleb, G. Petite, β irradiation in borosilicate glasses: The role of the mixed alkali effect, Nucl. Instruments Methods Phys. Res. Sect. B Beam Interact. with Mater. Atoms. 218 (2004) 176–182. https://doi.org/10.1016/j.nimb.2003.12.014.

[174] M. Mohapatra, R.M. Kadam, R.K. Mishra, D. Dutta, P.K. Pujari, C.P. Kaushik, R.J. Kshirsagar, B.S. Tomar, S. V Godbole, Nuclear Instruments and Methods in Physics Research B Electron beam irradiation effects in Trombay nuclear waste glass, Nucl. Inst. Methods Phys. Res. B. 269 (2011) 2057–2062. https://doi.org/10.1016/j.nimb.2011.06.009.

[175] R.A. Weeks, Paramagnetic resonance of lattice defects in irradiated quartz, J. Appl. Phys. 27 (1956) 1376–1381. https://doi.org/10.1063/1.1722267.

[176] A.F. Zatsepin, V.B. Guseva, V.A. Vazhenin, M.Y. Artoymov, Paramagnetic defects in gamma-irradiated Na/K-silicate glasses, Phys. Solid State. 54 (2012) 1776–1784. https://doi.org/10.1134/S1063783412090326.

[177] H.S. Tsai, D.S. Chao, Y.H. Wu, Y.T. He, Y.L. Chueh, J.H. Liang, Spectroscopic investigation of gamma radiation-induced coloration in silicate glass for nuclear applications, J. Nucl. Mater. 453 (2014) 233–238. https://doi.org/10.1016/j.jnucmat.2014.07.002.

[178] K.B. Patel, B. Boizot, S.P. Facq, S. Peuget, S. Schuller, I. Farnan, Impacts of composition and beta irradiation on phase separation in multiphase amorphous calcium borosilicates, J. Non. Cryst. Solids. 473 (2017) 1–16. https://doi.org/10.1016/j.jnoncrysol.2017.06.018.

[179] D.L. Griscom, Alkali- Associate Trapped-Electron centers in Alkali borate glasses irradiated at 77 K, J. Non. Cryst. Solids. 6 (1971) 275–282.

[180] G. Kordas, B. Camara, H.J. OEL, Electron spin resonance studies of radiation damage in silicate glasses, J. Non. Cryst. Solids. 50 (1982) 79–95.

[181] R.K. Brow, Electron beam reduction of sodium-containing glass surfaces, J. Non. Cryst. Solids. 175 (1994) 155–159. https://doi.org/10.1016/0022-3093(94)90007-8.

[182] B. Macalik, Optical properties of gamma irradiated soda-lime silicate glasses exchanged with copper, Radiat. Eff. Defects Solids. 158 (2003) 403–406. https://doi.org/10.1080/1042015021000052340.

[183] B. Boizot, G. Petite, D. Ghaleb, B. Reynard, G. Calas, Raman study of beta-irradiated glasses, J. Non. Cryst. Solids. 243 (1999) 268–272.

[184] J.F. DeNatale, D.K. McElfresh, D.G. Howitt, Preliminary observations on the microstructure of nuclear waste glasses, Ceram. Int. 8 (1982) 128–130. https://doi.org/10.1016/0272-8842(82)90002-5.

[185] K.J. Yang, T.S. Wang, G.F. Zhang, H.B. Peng, L. Chen, L.M. Zhang, C.X. Li, F. Tian, W. Yuan, Study of irradiation damage in borosilicate glass induced by He ions and electrons, Nucl. Instruments Methods Phys. Res. Sect. B Beam Interact. with Mater. Atoms. 307 (2013) 541–544. https://doi.org/10.1016/j.nimb.2012.12.113.

[186] C. Mendoza, S. Peuget, T. Charpentier, M. Moskura, R. Caraballo, O. Bouty,

A.H. Mir, I. Monnet, C. Grygiel, C. Jegou, Oxide glass structure evolution under swift heavy ion irradiation, Nucl. Instruments Methods Phys. Res. Sect. B Beam Interact. with Mater. Atoms. 325 (2014) 54–65. https://doi.org/10.1016/j.nimb.2014.02.002.

[187] D.L. Griscom, C.I. Merzbacher, R.A. Weeks, R.A. Zuhr, Electron spin resonance studies of defect centers induced in a high-level nuclear waste glass simulant by gamma-irradiation and ion-implantation, J. Non. Cryst. Solids. (1999) 34-47. https://doi.org/10.1016/S0022-3093(99)00557-8.

[188] J.E. Mendel, W.A. Ross, R.P. Turcotte, J.L. McElroy, Physical properties of glass for immobilization of high level radioactive waste, Nucl. Chem. Waste Manag. 1 (1980) 17–28. https://doi.org/10.1016/0191-815X(80)90025-X.

[189] J.E. Mendel, The Storage and Disposal of Radioactive Waste as Glass in Canisters, Pnl-2764 Uc-70. (1978).

[190] A.H. Mir, B. Boizot, T. Charpentier, M. Gennisson, M.Odorico, R. Podor, C. Jegou, S. Bouffard, S. Peuget, Surface and bulk electron irradiation effects in simple and complex glasses _ Elsevier Enhanced Reader.pdf, J. Non. Cryst. Solids.453 (2016) 141–149.

[191] V.S. Yalmali, D.S. Deshingkar, P.K. Wattal, Chemical Durability of Lead Borosilicate Glass Matrix Under Simulated Geological Conditions, Bhabha At. Res. Cent. (2002). http://www.ghbook.ir/index.php?name= مجموعه مقالات دومین هم اندیشی سراسری رسانه تلویزیون و سکولاریسم&option=com_dbook&task=readonline&book_id=13629&page=108&chkhashk=03C706812F&Itemid=218&lang=fa&tmpl=component.

[192] N.E. Bibler, J.P. Bibler, M.K. Andrews, C.M. Jantzen, Initial demonstration of the vitrification of high-level nuclear waste sludge containing an organic Cs-loaded ion-exchange resin, Mater. Res. Soc. Symp. Proc. 294 (1993) 81–86.

[193] S. Peuget, P.Y. Noël, J.L. Loubet, S. Pavan, P. Nivet, A. Chenet, Effects of deposited nuclear and electronic energy on the hardness of R7T7-type containment glass, Nucl. Instruments Methods Phys. Res. Sect. B Beam Interact. with Mater. Atoms. 246 (2006) 379–386. https://doi.org/10.1016/j.nimb.2005.12.053.

[194] R. Kaur, S. Singh, O.P. Pandey, Gamma ray irradiation effects on the optical properties of BaO-Na 2O-B2O3-SiO2 glasses, J. Mol. Struct. 1048 (2013) 78–82. https://doi.org/10.1016/j.molstruc.2013.05.037.

[195] J. de Bonfils, S. Peuget, G. Panczer, D. de Ligny, S. Henry, P.Y. Noël, A. Chenet, B. Champagnon, Effect of chemical composition on borosilicate glass behavior under irradiation, J. Non. Cryst. Solids. 356 (2010) 388–393. https://doi.org/10.1016/j.jnoncrysol.2009.11.030.

[196] S. Peuget, T. Fares, E.A. Maugeri, R. Caraballo, T. Charpentier, L. Martel, J. Somers, A. Janssen, T. Wiss, F. Rozenblum, M. Magnin, X. Deschanels, C. Jegou, Effects of 10B(n,a)7Li irradiation on the structure of a sodium, Nucl. Inst. Methods Phys. Res. B. 327 (2014) 22.28. https://doi.org/10.1016/j.nimb.2009.09.027.

[197] M.O. Prado, N.B. Messi, T.S. Plivelic, I.L. Torriani, A.M. Bevilacqua, M.A.

Arribére, The effects of radiation on the density of an aluminoborosilicate glass, J. Non. Cryst. Solids. 289 (2001) 175–184. https://doi.org/10.1016/S0022-3093(01)00707-4.

[198] N. Deladerrière, J.M. Delaye, S. Peuget, G. Bureau, Effect of elastic collisions on acoustic wave propagation in simplified nuclear glass: Molecular dynamics simulation, Nucl. Instruments Methods Phys. Res. Sect. B Beam Interact. with Mater. Atoms. 266 (2008) 2687–2690. https://doi.org/10.1016/j.nimb.2008.03.100.

[199] S. Gin, Open Scientific Questions about Nuclear Glass Corrosion, Procedia Mater. Sci. 7 (2014) 163–171. https://doi.org/10.1016/j.mspro.2014.10.022.

[200] J.D. Vienna, J. V. Ryan, S. Gin, Y. Inagaki, Current understanding and remaining challenges in modeling long-term degradation of borosilicate nuclear waste glasses, Int. J. Appl. Glas. Sci. 4 (2013) 283–294. https://doi.org/10.1111/ijag.12050.

[201] S. Mougnaud, M. Tribet, J. Renault, S. Gin, R. Podor, C. Jégou, Heavy ion radiation ageing on long-term glass alteration behaviour, (2018) 1-16. https://doi.org/10.1016/j.jnucmat.2018.07.046..

[202] D.F. Bickford, A. Applewhite-Ramsey, C.M. Jantzen, K.G. Brown, Preliminary General limits at Savannah River, J. Am. Ceram. Soc. (1990) 2896–2902.

[203] N.J. Cassingham, C.L. Corkhill, M.C. Stennett, R.J. Hand, N.C. Hyatt, Alteration layer formation of Ca- and Zn-oxide bearing alkali borosilicate glasses for immobilisation of UK high level waste: A vapour hydration study, J. Nucl. Mater. 479 (2016) 639–646. https://doi.org/10.1016/j.jnucmat.2016.06.009.

[204] E. Curti, J.L. Crovisier, G. Morvan, A.M. Karpoff, Long-term corrosion of two nuclear waste reference glasses (MW and SON68): A kinetic and mineral alteration study, Appl. Geochemistry. 21 (2006) 1152–1168. https://doi.org/10.1016/j.apgeochem.2006.03.010.

[205] H. Zhang, C.L. Corkhill, P.G. Heath, R.J. Hand, M.C. Stennett, N.C. Hyatt, Effect of Zn- and Ca-oxides on the structure and chemical durability of simulant alkali borosilicate glasses for immobilisation of UK high level wastes, J. Nucl. Mater. 462 (2015) 321–328. https://doi.org/10.1016/j.jnucmat.2015.04.016.

[206] O.J. McGann, P.A. Bingham, R.J. Hand, A.S. Gandy, M. Kavčič, M. Žitnik, K. Bučar, R. Edge, N.C. Hyatt, The effects of γ-radiation on model vitreous wasteforms intended for the disposal of intermediate and high level radioactive wastes in the United Kingdom, J. Nucl. Mater. 429 (2012) 353–367. https://doi.org/10.1016/j.jnucmat.2012.04.007.

[207] Indian Barium boroslictae glasses_Waste components.pdf, (n.d.) Indian Nuclear Society News, Vol 5, No 4,Oct-Dec. 2008.

[208] R.K. Brow, Chapter 3: Glass Making, (2012) 1–5 http://web.mst.edu.

[209] C. Lopez, X. Deschanels, J.M. Bart, C. Levrau, Solubility of plutonium surrogates in nuclear glasses , CEA, Marcpule, BP 171, 30207 (n.d.) 2–6.

[210] D.A. Skoog, F.J. Holler, S.R. Crouch, Principles of Instrumental Analysis, 7th ed.,Thomson Brooks/Cole. (2007).

[211] C.K. Saw, T. Lian, S.D. Day, J.C. Farmer, X-ray diffraction techniques for structural determination of amorphous materials, (2006). http://www.osti.gov/servlets/purl/900132

[212] B.G. Parkinson, D. Holland, M.E. Smith, C. Larson, J. Doerr, Quantitative measurement of Q 3 species in silicate and borosilicate glasses using Raman spectroscopy, J. Non. Cryst. Solids. 354 (2008) 1936–1942. https://doi.org/10.1016/j.jnoncrysol.2007.06.105.

[213] Raman spectroscopy-An overiview, Raman products technical note number - 1101, (2001).

[214] D.A. Long, Raman Spectroscopy, McGraw-Hill, New York, 1977.

[215] The Prashant Kamat Laboratory Retrieved from https://www3.nd.edu/~kamatlab/facilities_spectroscopy.html, (n.d.).

[216] Mettler Toledo Balance, (2021). https://www.mt.com/gb/en/home/phased_out_products/Laboratory_Weighing_Solutions/Analytical/AL/AL54.html (accessed January 14, 2021).

[217] Z. E., Spin-magnetic resonance in paramagnetics, J. Phys. E. Sci. Instruments. 9 (1945) 245–249.

[218] J.R.B. John A. Weil, Electron Paramagnetic Resonance, 2nd ed., John Wiley & Sons, INC., Hoboken, New Jersey, 1929.

[219] Y.C. Arango, Electron spin resonance (ESR) spectroscopy of low-dimensional spin systems, 2010.

[220] The University of Texas at Austin, What is EPR? Retrieved from https://sites.cns.utexas.edu/epr_facility/what-epr, (n.d.).

[221] L. Leay, W. Bower, G. Horne, P. Wady, A. Baidak, M. Pottinger, M. Nancekievill, A.D. Smith, S. Watson, P.R. Green, B. Lennox, J.A. Laverne, S.M. Pimblott, Development of irradiation capabilities to address the challenges of the nuclear industry, Nucl. Instruments Methods Phys. Res. Sect. B Beam Interact. with Mater. Atoms. 343 (2015) 62–69. https://doi.org/10.1016/j.nimb.2014.11.028.

[222] Bruker, (2021). https://www.bruker.com/products/mr/epr/emxnano/overview.html (accessed January 14, 2021).

[223] Introduction to Mössbauer Spectroscopy, (n.d.). https://www.rsc.org/membership-and-community/connect-with-others/through-interests/interest-groups/mossbauer/#:~:text=Mössbauer spectroscopy is a versatile,dependent properties of a material. (accessed January 16, 2021).

[224] M.D. Dyar, D.G. Agresti, M.W. Schaefer, C.A. Grant, E.C. Sklute, Mössbauer spectroscopy of Earth and planetary materials, Annu. Rev. Earth Planet. Sci. 34 (2006) 83–125. https://doi.org/10.1146/annurev.earth.34.031405.125049.

[225] H. Muller-Warmuth, W., & Eckert, Nuclear Magnetic Resonance and Mossbauer Spectroscopy of Glasses, (1982).

[226] P.A. Bingham, The Environment Iron of in Silicate Glasses, (2000). Retrieved from: https://etheses.whiterose.ac.uk/12823/

[227] S.D. Forder, P.A. Bingham, O.J. McGann, M.C. Stennett, N.C. Hyatt, Mössbauer studies of materials used to immobilise industrial wastes, Hyperfine Inetractions. (2013) 83–90. https://doi.org/10.1007/s10751-012-0700-x.

[228] D. Rancourt, Mössbauer spectral analysis software, Ottawa Intell. Sci. Appl. Inc. (1998).

[229] W. Meulebroeck, K. Baert, A. Ceglia, P. Cosyns, H. Wouters, K. Nys, H. Terryn, H. Thienpont, The potential of UV-VIS-NIR absorption spectroscopy in glass studies, Integr. Approaches to Study Hist. Glas. 8422 (2012) 842208. https://doi.org/10.1117/12.975684.

[230] B.L. Allsopp, Effects of d 0 and s 2 cations on optical properties of silicate glasses, (2018). Retreived from: https://doi.org/10.7190/shu-thesis-00177

[231] C.J. Chirayil, J. Abraham, R.K. Mishra, S.C. George, S. Thomas, Instrumental Techniques for the Characterization of Nanoparticles, in: Therm. Rheol. Meas. Tech. Nanomater. Charact., 2017: pp. 1–36. https://doi.org/10.1016/B978-0-323-46139-9.00001-3.

[232] T.T. Wang, X.Y. Zhang, M.L. Sun, X. Du, M. Guan, H.B. Peng, T.S. Wang, γ-Irradiation effects in borosilicate glass studied by EPR and UV–Vis spectroscopies, Nucl. Instruments Methods Phys. Res. Sect. B Beam Interact. with Mater. Atoms. 464 (2020) 106–110. https://doi.org/10.1016/j.nimb.2019.12.007.

[233] J.P.B. J.F. Ziegler, The Stopping and Range of Ions in Matter, Pergamon. 2–6 (1985).

[234] Low Energy Ion Beam Facility, (n.d.). https://www.iuac.res.in/low-energy-ion-beam-facility (accessed January 22, 2021).

[235] D. Manara, A. Grandjean, D.R. Neuville, Structure of borosilicate glasses and melts: A revision of the Yun, Bray and Dell model, J. Non. Cryst. Solids. 355 (2009) 2528–2531. https://doi.org/10.1016/j.jnoncrysol.2009.08.033.

[236] D. Manara, A. Grandjean, D.R. Neuville, Advances in understanding the structure of borosilicate glasses: A raman spectroscopy study, Am. Mineral. 94 (2009) 777–784. https://doi.org/10.2138/am.2009.3027.

[237] G.F. Zhang, T.S. Wang, K.J. Yang, L. Chen, L.M. Zhang, H.B. Peng, W. Yuan, F. Tian, Raman spectra and nano-indentation of Ar-irradiated borosilicate glass, Nucl. Instruments Methods Phys. Res. Sect. B Beam Interact. with Mater. Atoms. 316 (2013) 218–221. https://doi.org/10.1016/j.nimb.2013.09.020.

[238] R. Limbach, S. Karlsson, G. Scannell, R. Mathew, M. Edén, L. Wondraczek, The effect of TiO2 on the structure of Na2O-CaO-SiO2 glasses and its implications for thermal and mechanical properties, J. Non. Cryst. Solids. 471 (2017) 6–18. https://doi.org/10.1016/j.jnoncrysol.2017.04.013.

[239] D.R. Neuville, B.O. Mysen, Role of aluminium in the silicate network: In situ, high-temperature study of glasses and melts on the join SiO2-NaAlO2, Geochim. Cosmochim. Acta. 60 (1996) 1727–1737. https://doi.org/10.1016/0016-7037(96)00049-X.

[240] D.R. Neuville, L. Cormier, B. Boizot, A.M. Flank, Structure of β-irradiated glasses studied by X-ray absorption and Raman spectroscopies, J. Non. Cryst. Solids. 323 (2003) 207–213. https://doi.org/10.1016/S0022-3093(03)00308-9.

[241] P.A. Bingham, G. Yang, R.J. Hand, G. Möbus, Boron environments and irradiation stability of iron borophosphate glasses analysed by EELS, Solid State Sci. 10 (2008) 1194–1199. https://doi.org/10.1016/j.solidstatesciences.2007.11.024.

[242] N.A. El-Alaily, E.M.A. Hussein, F.M. Ezz Eldin, Gamma Irradiation and Heat Treatment Effects on Barium Borosilicate Glasses Doped Titanium Oxide, J. Inorg. Organomet. Polym. Mater. 28 (2018) 2662–2676. https://doi.org/10.1007/s10904-018-0934-4.

[243] K. Nordlund, S.J. Zinkle, A.E. Sand, F. Granberg, R.S. Averback, R.E. Stoller, T. Suzudo, L. Malerba, F. Banhart, W.J. Weber, F. Willaime, S.L. Dudarev, D. Simeone, Primary radiation damage: A review of current understanding and models, J. Nucl. Mater. 512 (2018) 450–479. https://doi.org/10.1016/j.jnucmat.2018.10.027.

[244] N. Jiang, J. Silcox, Electron irradiation induced phase decomposition in alkaline earth multi-component oxide glass, J. Appl. Phys. 92 (2002) 2310–2316. https://doi.org/10.1063/1.1496148.

[245] C. Huang, A.N. Cormack, Structural differences and phase separation in alkali silicate glasses, J. Chem. Phys. 95 (1991) 3634–3642. https://doi.org/10.1063/1.460814.

[246] J.W. MacKenzie, A. Bhatnagar, D. Bain, S. Bhowmik, C. Parameswar, K. Budhwani, S.A. Feller, M.L. Royle, S.W. Martin, 29Si MAS-NMR study of the short range order in alkali borosilicate glasses, J. Non. Cryst. Solids. 177 (1994) 269–276. https://doi.org/10.1016/0022-3093(94)90540-1.

[247] D. Forum, M. Mohapatra, B. Atomic, T. Bhabha, P. View, Spectroscopic Investigations of Radiation Damage in Glasses Used for Immobilization of Radioactive Waste, (2013). https://doi.org/10.4028/www.scientific.net/DDF.341.107.

[248] D.L. Griscom, E.S.R. studies of radiation damage and structure in oxide glasses not containing transition group ions: A contemporary overview with illustrations from the alkali borate system, J. Non. Cryst. Solids. 13 (1974) 251–285. https://doi.org/10.1016/0022-3093(74)90095-7.

[249] H. Hosono, Y. Abe, Photosensitivity and structural defects in dopant-free ultraviolet-sensitive calcium aluminate glasses, J. Non. Cryst. Solids. 95–96 (1987) 717–724. https://doi.org/10.1016/S0022-3093(87)80673-7.

[250] H. Annersten, A. Hassib, Blue sodalite, Can. Mineral. 17 (1979) 39–46. http://canmin.geoscienceworld.org/content/17/1/39.extract.

[251] M. Mohapatra, B.S. Tomar, Spectroscopic investigations of radiation damage in glasses used for immobilization of radioactive waste, Defect Diffus. Forum. 341 (2013) 107–128. https://doi.org/10.4028/www.scientific.net/DDF.341.107.

[252] Paul McMillan, Structural studies of silicate glasses and melts-applications and limitations of Raman spectroscopy, Am. Mineral. 69 (1984) 622–644. https://doi.org/10.1007/BF00307725.

[253] S.K.S. and J.A.P. Dean W. Matson, The structure of high-silica alkali-slicate glasses. A Raman spectroscopic investigation, J. Non. Cryst. Solids. 58 (1983) 323–352. https://doi.org/10.1093/jicru_os19.1.1.

[254] J. Ramkumar, S. Chandramouleeswaran, V. Sudarsan, R.K. Mishra, C.P. Kaushik, K. Raj, A.K. Tyagi, Barium borosilicate glass as a matrix for the uptake of dyes, J. Hazard. Mater. 172 (2009) 457–464. https://doi.org/10.1016/j.jhazmat.2009.07.028.

[255] Neville F. Mott, Electronic Processes In Non-Crystalline Materials, 1979. https://doi.org/10.1063/1.2915913.

[256] G. Gupta, S. Balaji, K. Biswas, A. Kalyandurg, Mid-IR transparent TeO2-TiO2-La2O3 glass and its crystallization behavior for photonic applications, J. Am. Ceram. Soc. 101 (2018) 3900–3916. https://doi.org/10.1111/jace.15558.

[257] A.S. Hassanien, A.A. Akl, Influence of composition on optical and dispersion parameters of thermally evaporated non-crystalline Cd50S50-xSex thin films, J. Alloys Compd. 648 (2015) 280–290. https://doi.org/10.1016/j.jallcom.2015.06.231.

[258] J. Du, J. Wu, L. Zhao, L. Song, Color centers of a borosilicate glass induced by 10 MeV proton, 1.85 MeV electron and 60Co-γ ray, Radiat. Phys. Chem. 86 (2013) 59–63. https://doi.org/10.1016/j.radphyschem.2013.01.044.

[259] D.L. Griscom, M. Mizuguchi, Determination of the visible range optical absorption spectrum of peroxy radicals in gamma-irradiated fused silica, J. Alloys Compd. 239 (1998) 66–77. https://doi.org/10.1016/s0022-3093(98)00721-2.

[260] J.H. Mackey, H.L. Smith, A. Halperin, Optical Studies in X-Irradiated High Purity Sodium Silicate Glasses, J. Phys. Chem. Solids. 27 (1966) 1759–1772.

[261] A.M. Fayad, W.M. Abd-Allah, F.A. Moustafa, Effect of Gamma Irradiation on Structural and Optical Investigations of Borosilicate Glass Doped Yttrium Oxide, Silicon. 10 (2018) 799–809. https://doi.org/10.1007/s12633-016-9533-6.

[262] N. Jiang, J. Qiu, J. Silcox, Precipitation of nanometer scale Zn crystalline particles in ZnO-B2O3-SiO2 glass during electron irradiation, Appl. Phys. Lett. 77 (2000) 3956–3958. https://doi.org/10.1063/1.1332829.

[263] J.H. Mackey, H.L. Smith, J. Nahum, Competitive trapping in sodium disilicate glasses doped with Eu+3, J. Phys. Chem. Solids. 27 (1966) 1773–1782. https://doi.org/10.1016/0022-3697(66)90108-9.

[264] Adli Bishay, Radiation Induced Color Centers in Multicomponent Glasses, J. Non. Cryst. Solids. 3 (1970) 54–114.

[265] N. Jiang, B. Wu, J. Qiu, J.C.H. Spence, Precipitation of nanocrystals in glasses by electron irradiation: An alternative path to form glass ceramics?, Appl. Phys. Lett. 90 (2007) 15–18. https://doi.org/10.1063/1.2724898.

[266] E.S. Bochkareva, N. V. Nikonorov, O.A. Podsvirov, M.A. Prosnikov, A.I. Sidorov, The Formation of Sodium Nanoparticles in Alkali-Silicate Glass Under the Action of the Electron Beam and Thermal Treatments, Plasmonics. 11 (2016) 241–246. https://doi.org/10.1007/s11468-015-0046-8.

[267] E. Kolobkova, N. Nikonorov, Metal sodium nanoparticles in fluorophosphate glasses, J. Alloys Compd. 637 (2015) 545–551. https://doi.org/10.1016/j.jallcom.2015.02.148.

[268] A. Wesełucha-Birczyńska, S. Zelek, K. Stadnicka, Blue halite colour centre aggregates studied by micro-Raman spectroscopy and X-ray diffraction, Vib. Spectrosc. 60 (2012) 124–128. https://doi.org/10.1016/j.vibspec.2011.11.001.

[269] J.C. Groote, J.R.W. Weerkamp, J. Seinen, H.W. Den Hartog, Radiation damage in NaCl. I. Optical-absorption experiments on heavily irradiated samples, Phys. Rev. B. 50 (1994) 9781–9786. https://doi.org/10.1103/PhysRevB.50.9781.

[270] A. Hassib, O. Beckman, H. Annersten, Photochromic properties of natural sodalite, J. Phys. D. Appl. Phys. 10 (1977) 771–777. https://doi.org/10.1088/0022-3727/10/5/018.

[271] P. Mahadik, N. Pathak, P. Sengupta, Spectroscopic studies on blue halite, J. Lumin. 194 (2018) 327–333. https://doi.org/10.1016/j.jlumin.2017.10.013.

[272] J. Seinen, J.C. Groote, J.R.W. Weerkamp, H.W. Den Hartog, Radiation damage in NaC1. III. Melting phenomena of sodium colloids, Phys. Rev. B. 50 (1994) 9793–9797.

[273] J. Seinen, J.C. Groote, J.R.W. Weerkamp, H.W. Den Hartog, Radiation damage in NaC1. II. The early stage of F-center aggregation, Phys. Rev. B. 91 (1994). https://doi.org/10.1017/CBO9781107415324.004.

[274] J.C. Groote, J.R.W. Weerkamp, J. Seinen, H.W. Den Hartog, Radiation damage in NaCl. IV. Raman scattering, Phys. Rev. B. 50 (1994) 9798–9802. https://doi.org/10.1103/PhysRevB.50.9798.

[275] N. Jiang, D. Su, J.C.H. Spence, S. Zhou, J. Qiu, Electron energy loss spectroscopy of Na in Na, Na2O, and silicate glasses, J. Mater. Res. 23 (2008) 2467–2471. https://doi.org/10.1557/jmr.2008.0296.

[276] J.O. Isard, The Mixed Alkali Effect in Glass, J. Non. Cryst. Solids. (1969) 235–261. https://doi.org/10.1111/j.1151-2916.1965.tb14784.x.

[277] Y. Tokuda, Y. Takahashi, H. Masai, S. Kaneko, Y. Ueda, S. Fujimura, T. Yoko, Local structure of alkalis in mixed-alkali borate glass to elucidate the origin of mixed-alkali effect, J. Asian Ceram. Soc. 3 (2015) 412–416. https://doi.org/10.1016/j.jascer.2015.09.002.

[278] R.K. Mishra, V. Sudarsan, C.P. Kaushik, K. Raj, S.K. Kulshreshtha, A.K. Tyagi, Effect of BaO addition on the structural aspects and thermophysical properties of sodium borosilicate glasses, J. Non. Cryst. Solids. 353 (2007) 1612–1617.

https://doi.org/10.1016/j.jnoncrysol.2007.01.074.

[279] L.D. Bogomolova, A.A. Deshkovskaya, N.A. Krasil'nikova, G. Battaglin, F. Caccavale, EPR study of structural defects in ion-implanted multicomponent silicate glasses, J. Non. Cryst. Solids. 151 (1992) 23–31. https://doi.org/10.1016/0022-3093(92)90005-5.

[280] O. Pinet, I. Hugon, S. Mure, Redox Control of Nuclear Glass, Procedia Mater. Sci. 7 (2014) 124–130. https://doi.org/10.1016/j.mspro.2014.10.017.

[281] V. Pukhkaya, T. Charpentier, N. Ollier, Study of formation and sequential relaxation of paramagnetic point defects in electron-irradiated Na-aluminosilicate glasses: Influence of Yb, J. Non. Cryst. Solids. 364 (2013) 1–8. https://doi.org/10.1016/j.jnoncrysol.2013.01.021.

[282] D.Maniu, T.Iliescu, I. Ardelean, S.Cinta-Pinzaru, N.Tarcea, W. Kiefer, Raman study on B2O3-CaO glasses, J. Mol. Struct. 651-653 (2003) 485–488.

[283] D.Maniu, I.Ardelean, T.Iliescu, S.Cinta-Pinzaru, V.Nagel, W.Kiefer, Raman spectroscopic investigations on oxide glass system (1-x)[3B2O3.K2O].xTiO2, J. Mol. Struct. 480-481 (1999) 657–659.

[284] W.L. Konijnendijk, J.M. Stevels, The structure of borate glasses studied by Raman scattering, J. Non. Cryst. Solids. 18 (1975) 307–331. https://doi.org/10.1016/0022-3093(75)90137-4.

[285] P. McMillan, Structural studies of silicate glasses and melts-applications and limitations of Raman spectroscopy., Am. Mineral. 69 (1984) 622–644.

[286] D.L. Griscom, On the natures of radiation-induced point defects in GeO_2-SiO_2 glasses: reevaluation of a 26-year-old ESR and optical data set, Opt. Mater. Express. 1 (2011) 400-412. https://doi.org/10.1364/OME.1.000400.

[287] MD Dyar, A review of Mössbauer data on inorganic glasses: the effects of composition on iron valency and coordination, Am. Mineral. 70 (3-4) (1985) 304-316.

[288] K. Ed. Uhlmann, D. R., G. Tomandl in Glass: Science and Technology, Academic Press, New York, 1990, ch. 5, Glas. Sci. Technol. 4B (1990).

[289] P. Cochain, B., Neuville, D. R., Henderson, G. S., McCammon, C. A., Pinet, O., & Richet, Effects of the Iron Content and Redox State on the Structure of Sodium Borosilicate Glasses: A Raman, Mössbauer and Boron K-Edge XANES spectroscopy study, J. Am. Ceram. Soc. 95(3) (2012) 962–971.

[290] J. McCloy, J. Washton, N., Gassman, P., Marcial, J., Weaver, R. Kukkadapu, Nepheline crystallization in boron-rich alumino-silicate glasses as investigated by multi-nuclear NMR, Raman, & Mössbauer spectroscopies., J. Non. Cryst. Solids. 409 (2015) 149–165.

[291] C.J. Roca, A. G., Marco, J. F., Morales, M. del P., & Serna, Effect of nature and particle size on properties of uniform magnetite and maghemite nanoparticles., J. Phys. Chem. C. 111(50) (2007) 18577–18584.

[292] M. Mohapatra, R.M. Kadam, S.N. Tripathy, A.R. Dhobale, R.K. Mishra, C.P. Kaushik, B.S. Tomar, K. Raj, S. V. Godbole, V.K. Manchanda, Spectroscopic

investigation of transition metal (Cr, Cu, Fe, and Mn) containing Trombay waste base glass, Phys. Chem. Glas. Eur. J. Glas. Sci. Technol. Part B. 51 (2010) 217–225.

[293] N.A. Eissa, N.H. Sheta, W.M. El-Meliga, S.M. El-Minyawi, H.A. Sallam, Mossbauer effect study of the effect of gamma irradiation on the behaviour of iron in sodium silicate glasses, Radiat Phys. Chem. 44 (1994) 35–38.

[294] R.Debnath, Thermally reversible γ-ray-induced redox reaction between substitutional iron and aluminum impurity centers in a silica glass, J. Mater. Res. Vol 16 issue 1 (2001).

[295] G. Brown, An esr study of electron and hole trapping in gamma-irradiated Pyrex, J. Mater. Sci. (1975) 1841–18448.

[296] P.A. Bingham, J.M. Parker, T.M. Searle, I. Smith, Local Structure and Medium Range Ordering of Tetrahedrally Coordinated Fe3+ Ions in Alkali–Alkaline Earth–Silica Glasses, J. Non. Cryst. Solids. 353 (2007) 2479–2494.

[297] A. Manara, M. Antonini, P. Camagni, P.N. Gibson, Radiation Damage in Silica-Based Glasses: Point Defects, Microstructural Changes and Possible Implications on Etching and Leaching., Nucl. Instruments Methods Phys. Res. Sect. B Beam Interact. with Mater. Atoms. 229 (B1) (1983) 475–480.

Appendix A

Table A. 1 Composition for NaBaBSi and LiNaBSi glass doped with graphite/C in mol%

Oxide	NaBaBSi base glass + Fe_2O_3 + C in mol%	
SiO_2	39.68	37.88
B_2O_3	19.38	18.93
Na_2O	20.83	19.89
BaO	14.87	14.20
Fe_2O_3	4.76	9.09
C	4	8
Total	104	108

Oxide	LiNaBSi base glass + Fe_2O_3 + C in mol%	
SiO_2	57.62	55.00
B_2O_3	17.62	16.81
Na_2O	9.99	9.54
Li_2O	10.00	9.54
Fe_2O_3	4.76	9.09
C	4	8
Total	104	108

Appendix B

Table B. 1 Fitting parameters for the deconvoluted UV-Vis-nIR optical absorption spectra

Parameter		LiNaBSi		NaBaBSi	
		0.5 MGy	**5.0 MGy**	**0.5 MGy**	**5.0 MGy**
Reduced χ^2		0.40202	0.24107	2.46828	4.50537
R^2		0.99629	0.9993	0.99962	0.99967
	v_1	17620 cm^{-1}	16084 cm^{-1}	15636 cm^{-1}	15224 cm^{-1}
	λ_1	568 nm (BOHC + peroxy radicals)	622 nm (BOHC)	639 nm (E- centre + peroxy radicals)	657 nm (E-centre + peroxy radicals)
	A_1	341412 (7.69%)	64983 (0.86%)	81602 (10.27%)	62725 (4.27%)
	Δv_1	5936 cm^{-1}	4380 cm^{-1}	4945 cm^{-1}	4444 cm^{-1}
	v_2	28274 cm^{-1}	16161 cm^{-1}	18969 cm^{-1}	17618 cm^{-1}
	λ_2	354 nm (BOHC)	551 nm (BOHC)	527 nm (BOHC)	568 nm (BOHC)
	A_2	2298160 (51.73%)	397338 (5.72%)	61154 (7.70%)	82003 (5.58%)
	Δv_2	12215 cm^{-1}	6145 cm^{-1}	7367 cm^{-1}	5864 cm^{-1}
	v_3	34580 cm^{-1}	26565 cm^{-1}	30883 cm^{-1}	31321 cm^{-1}
	λ_3	289 nm (Trapped electrons)	376 nm (BOHC)	324 nm (E- centre)	319 nm (E-centre)
	A_3	1397460 (31.46%)	1701740 (22.58%)	432366 (54.44%)	795898 (54.19%)
	Δv_3	7861 cm^{-1}	11194 cm^{-1}	14823 cm^{-1}	18375 cm^{-1}
	v_4	38002 cm^{-1}	36465 cm^{-1}	39388 cm^{-1}	40230 cm^{-1}
	λ_4	263 nm (Trace Fe impurity)	274 nm (Trapped electrons)	253 nm (Trace Fe impurity)	249 nm (Trace Fe impurity)
	A_4	405291 (9.12%)	5370910 (71.28%)	219076 (27.58%)	528043 (35.95%)
	Δv_4	4856 cm^{-1}	5661 cm^{-1}	6663 cm^{-1}	8588 cm^{-1}

Table B2. Summary of the results obtained in different materials with different irradiations conditions where formation of atomically dispersed metallic/colloidal sodium is discussed.

Study	Material	Radiation type	Result	Analysis
Hassib *et al.* (1977) [270]	Sodalite	X-ray	Formation of colloidal aggregates (Na), blue coloration, EPR signal at 2.011	EPR, Optical transmission
Groote *et al*.(I) (1994) [269]	NaCl	Electron beam	F-defect centres T<65˚C, Na colloids at higher T, absorption band b/w 550-600nm	Optical absorption spectroscopy
Groote *et al.* (II) (1994) [273]	NaCl	Electron beam	Na colloids of different shape and size	Optical absorption spectroscopy
Groote *et al*. (III) (1994) [272]	NaCl	Electron beam	Different melting T is linked with different size of Na colloid	Differential scanning calorimetry
Wesełucha-Birczyńska *et al.* (2011) [268]	Single crystals of natural blue halite	N/A	Plasmon band at 629 for navy blue and 621 nm for blue samples	Optical absorption spectroscopy
Tsai *et al*. (2014) [177]	Silicate glass	Gamma	Absorption band in the range 360-540, HC1 and HC2 defect centre, EPR signal at 2.01	EPR, Optical transmission spectroscopy
Zatsepin *et al.* (2012) [176]	Sodium silicate glass	Gamma	HC1, HC2, and E^- centre (g~1.97)	EPR
Mahadik *et al*. (2018) [271]	Natural halite	N/A	F-centres, Na colloids	Photoluminescence, Micro-Raman spectroscopy
Jiang *et al.* (2008) [275]	Sodium silicate glass	Electron beam	Formation of metallic sodium identified by plasmon at 5.8 eV	Electron energy loss spectroscopy
Manara *et al.* (1984) [297]	Borosilicate glass	Electron beam	Na moves towards the periphery, concentrated in a possible colloidal form	Energy dispersive X-ray analysis
Fayad *et al.* (2018) [261]	Borosilicate glass doped with yttrium oxide	Gamma	Absorption band at 229 nm related to Fe impurities and visible band b/w 500-600 due to BOHC or NBOHC	XRD, FTIR, optical absorption spectroscopy
El-Alaily *et al*. (2018) [242]	Barium borosilicate glass doped with titanium oxide	Gamma and heat treatment	Absorption band at 240 nm due to trace Fe impurity	SEM, Infrared, optical absorption, and transmission spectroscopy
Kolobkova *et al.* (2015) [267]	Sodium fluorophosphate glasses	Heat treatment	Surface plasmon b/w 400-450 nm	Heat treatment
Bochkareva *et al.* (2016) [266]	Na containing silicate glasses	Electron beam and subsequent heat	Na nanoparticles characterised by plasmon resonance band at 405-410 nm	Optical absorption spectroscopy

		treatment		
Jiang *et al.* (2007) [265]	Na silicate glasses	Electron beam	Bulk plasmon band at 5.8 eV (214 nm) and surface plasmon at 3.9 eV (318 nm)	TEM and EELS
Griscom *et al.* (1998) [259]	Fused silica	Gamma	Combination of band due to peroxy radicals and NBOHC at ~620 nm	Differential optical absorption spectroscopy
A.Bishay (1969) [264]	Alkali silicate glass	Gamma	Hole centre at 590-620, 427-450 nm	EPR, Optical absorption spectroscopy
Mackey *et al.* (1966) [260]	Sodium silicate glass	X-ray	Absorption band b/w 600-730 nm (E- centre), 326-413 nm due to trapped holes	Optical absorption spectroscopy
Mackey *et al.* (1966) [263]	Sodium disilicate glass doped with Eu^{3+}	X-ray	Absorption band 305 nm trapped electrons, 460 and 620 nm due to trapped holes	Optical absorption spectroscopy

Appendix C

Mössbauer spectroscopy xVBF fitted spectra for Fe_2O_3 doped NaBaBSi and LiNaBSi glasses.

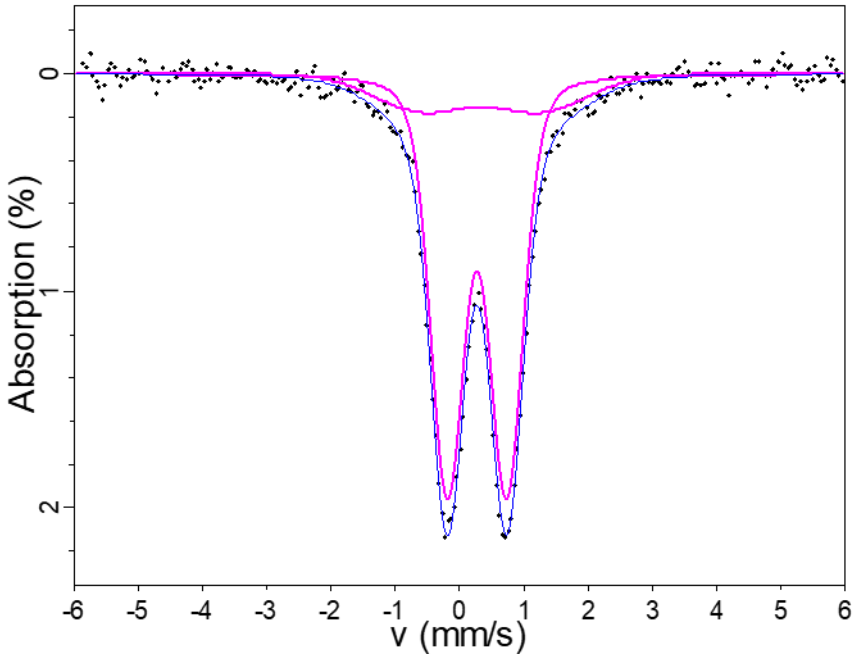

Figure C. 1 Mössbauer spectrum for NaBaBSi doped with 4.76 mol% Fe_2O_3 pristine oxidised glass.

Table C. 1 Fitting parameters for NaBaBSi doped with 4.76 mol% Fe_2O_3 pristine oxidised glass.

Sample ID		CS (mm /s)	QS (mm/s)	stdev (mm/s)	Relative area (%)
NaBaBSi 4.76 mol% Fe_2O_3 pristine oxidised glass	**Doublet 1 (Fe^{3+})**	0.268	0.924	0.286	81.1
	Doublet 2 (Fe^{3+})	0.33	1.86	0.944	18.9

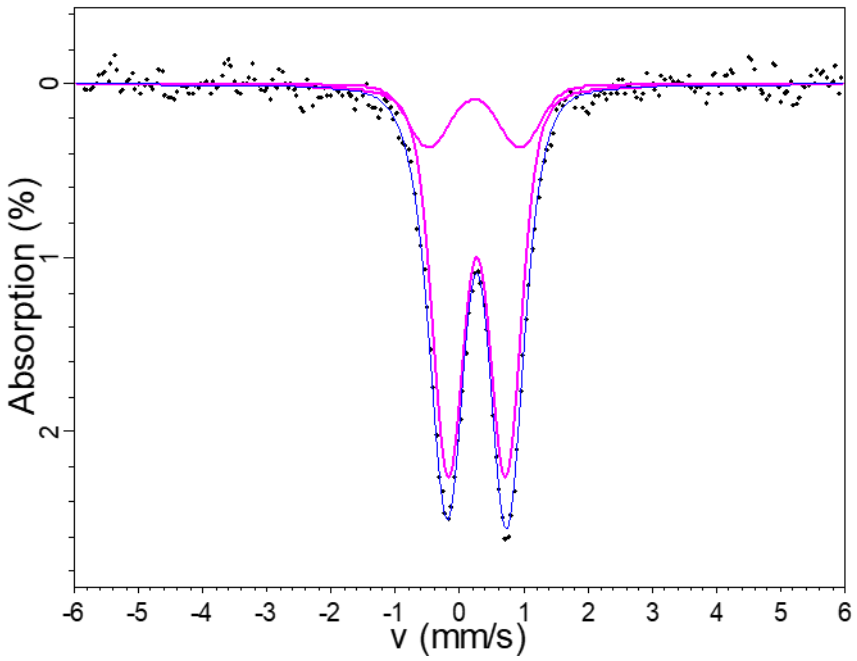

Figure C. 2 Mössbauer spectrum for NaBaBSi doped with 9.09 mol% Fe_2O_3 pristine oxidised glass.

Table C. 2 Fitting parameters for NaBaBSi doped with 9.09 mol% Fe_2O_3 pristine oxidised glass.

Sample ID		CS (mm/s)	QS (mm/s)	stdev (mm/s)	Relative area (%)
NaBaBSi 9.09 mol% Fe_2O_3 pristine oxidised glass	**Doublet 1 (Fe^{3+})**	0.267	0.894	0.286	83
	Doublet 2 (Fe^{3+})	0.225	1.41	0.411	17

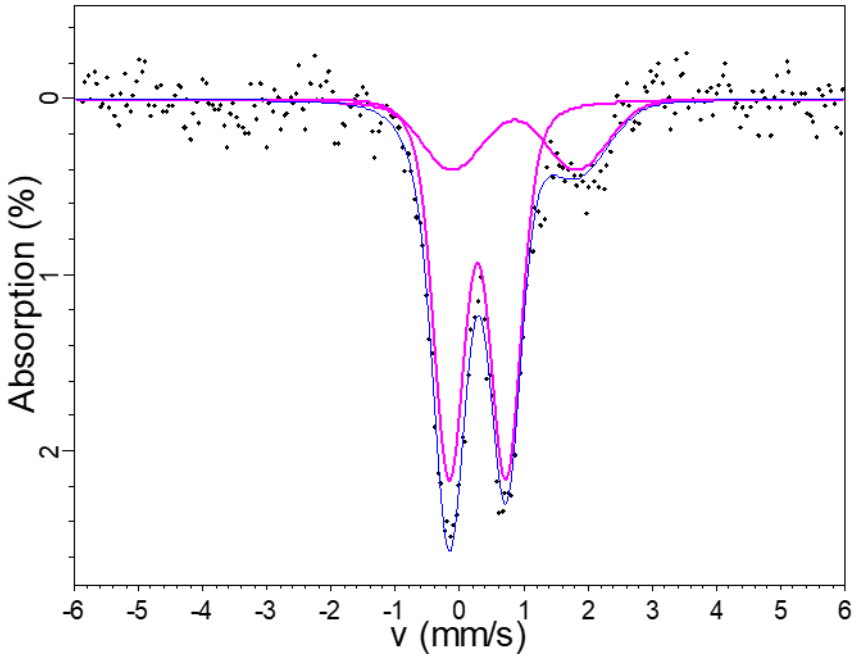

Figure C. 3 Mössbauer spectrum for NaBaBSi doped with 4.76 mol% Fe_2O_3 pristine reduced glass.

Table C. 3 Fitting parameters for NaBaBSi doped with 4.76 mol% Fe_2O_3 pristine reduced glass.

Sample ID		CS (mm/s)	QS (mm/s)	stdev (mm/s)	Relative area (%)
NaBaBSi 4.76 mol% Fe_2O_3 pristine reduced glass	**Doublet 1 (Fe^{3+})**	0.27	0.88	0.26	73.8
	Doublet 2 (Fe^{2+})	0.85	1.94	0.61	26.2

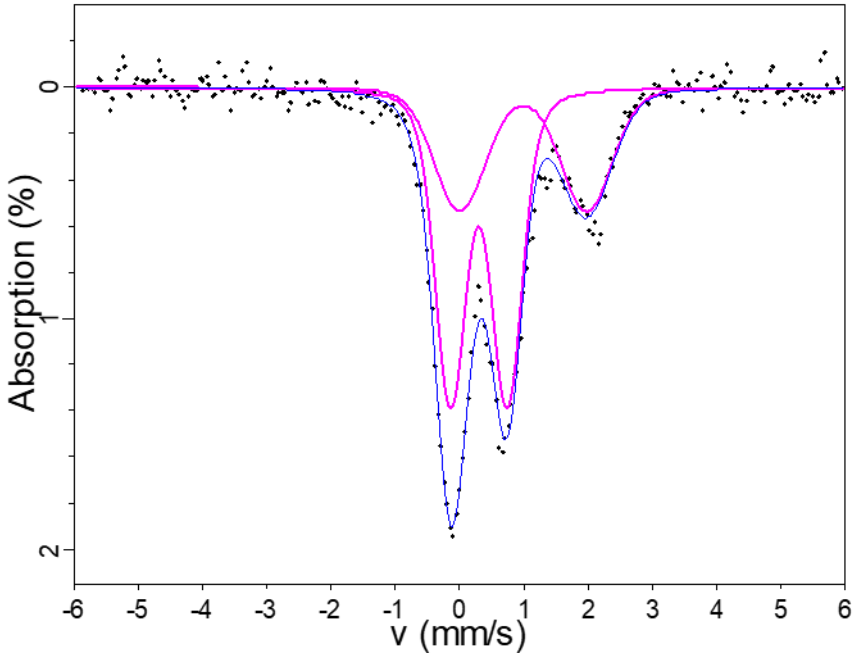

Figure C. 4 Mössbauer spectrum for NaBaBSi doped with 9.09 mol% Fe_2O_3 pristine reduced glass.

Table C. 4 Fitting parameters for NaBaBSi doped with 9.09 mol% Fe_2O_3 pristine reduced glass.

Sample ID		CS (mm/s)	QS (mm/s)	stdev (mm/s)	Relative area (%)
NaBaBSi 9.09 mol% Fe_2O_3 pristine reduced glass	**Doublet 1 (Fe^{3+})**	0.296	0.882	0.262	61.8
	Doublet 2 (Fe^{2+})	0.991	1.975	0.496	38.2

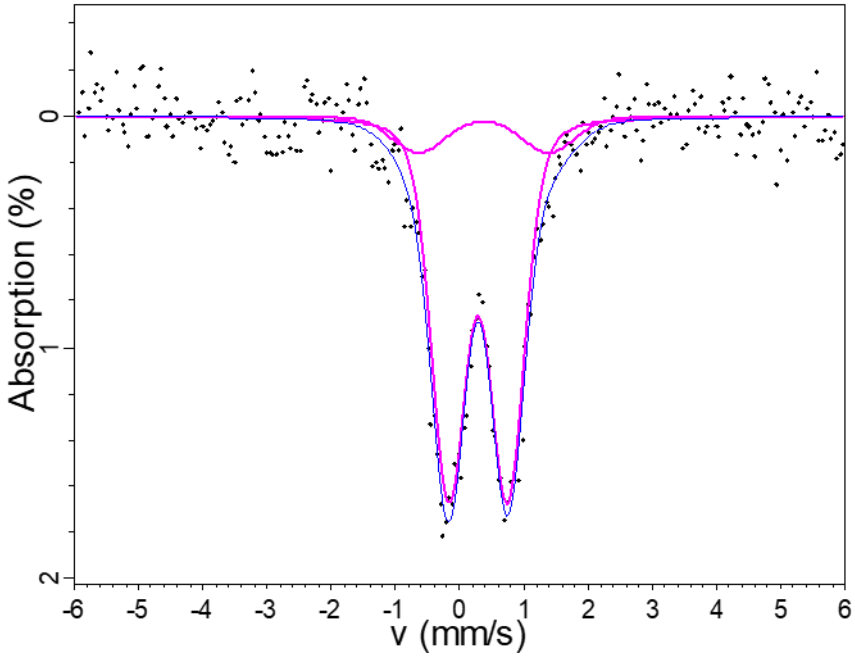

Figure C. 5 Mössbauer spectrum for NaBaBSi doped with 4.76 mol% Fe_2O_3 irradiated oxidised glass.

Table C. 5 Fitting parameters for NaBaBSi doped with 4.76 mol% Fe_2O_3 irradiated oxidised glass.

Sample ID		CS (mm/s)	QS (mm/s)	stdev (mm/s)	Relative area (%)
NaBaBSi 4.76 mol% Fe_2O_3 irradiated oxidised glass	**Doublet 1 (Fe^{3+})**	0.37	2.030	0.479	12
	Doublet 2 (Fe^{3+})	0.285	0.913	0.301	88

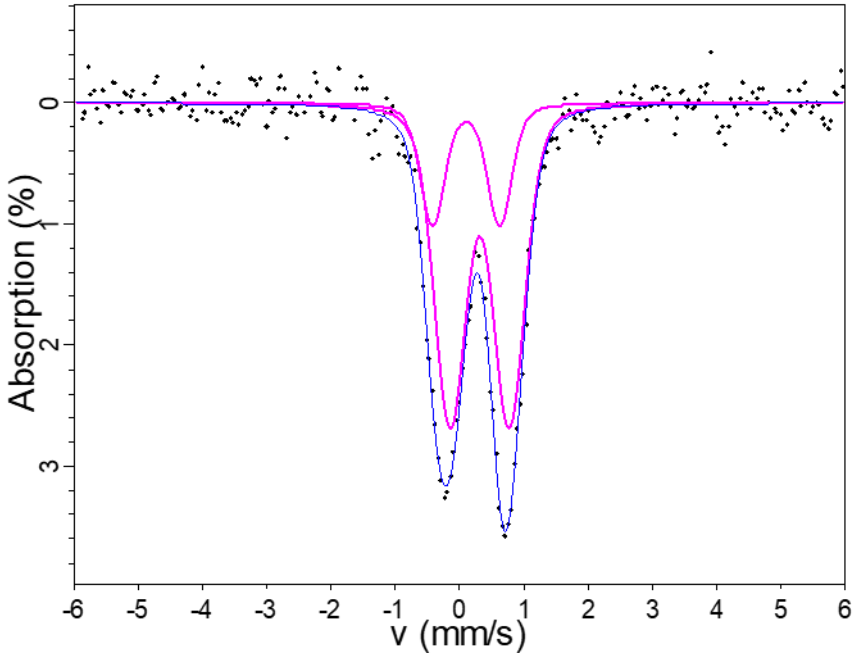

Figure C. 6 Mössbauer spectrum for NaBaBSi doped with 9.09 mol% Fe_2O_3 irradiated oxidised glass.

Table C. 6 Fitting parameters for NaBaBSi doped with 9.09 mol% Fe_2O_3 irradiated oxidised glass.

Sample ID		CS (mm/s)	QS (mm/s)	stdev (mm/s)	Relative area (%)
NaBaBSi 9.09 mol% Fe_2O_3 irradiated oxidised glass	**Doublet 1 (Fe^{3+})**	0.311	0.923	0.262	76
	Doublet 2 (Fe^{3+})	0.100	1.047	0.171	24

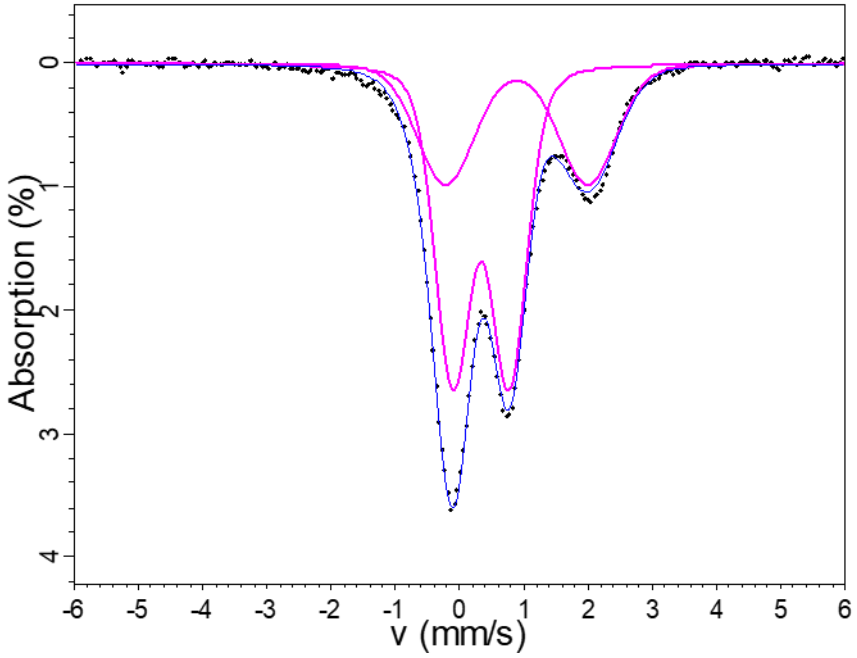

Figure C. 7 Mössbauer spectrum for NaBaBSi doped with 4.76 mol% Fe_2O_3 irradiated reduced glass.

Table C. 7 Fitting parameters for NaBaBSi doped with 4.76 mol% Fe_2O_3 irradiated reduced glass.

Sample ID		CS (mm/s)	QS (mm/s)	stdev (mm/s)	Relative area (%)
NaBaBSi 4.76 mol% Fe_2O_3 irradiated reduced glass	**Doublet 1(Fe^{2+})**	0.888	2.217	0.579	36.8
	Doublet 2 (Fe^{3+})	0.331	0.876	0.335	63.2

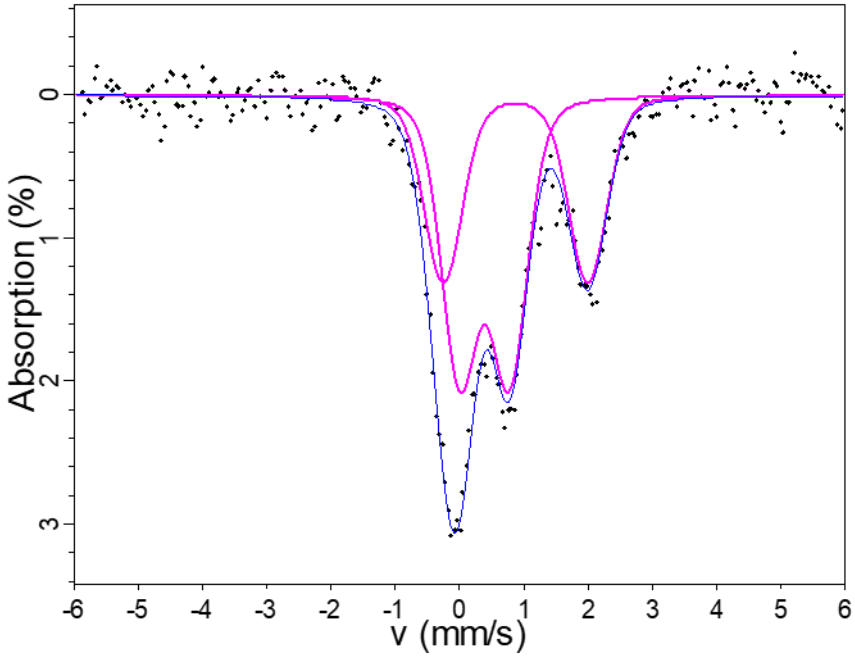

Figure C. 8 Mössbauer spectrum for NaBaBSi doped with 9.09 mol% Fe_2O_3 irradiated reduced glass.

Table C. 8 Fitting parameters for NaBaBSi doped with 9.09 mol% Fe_2O_3 irradiated reduced glass.

Sample ID		CS (mm/s)	QS (mm/s)	stdev (mm/s)	Relative area (%)
NaBaBSi 9.09 mol% Fe_2O_3 irradiated reduced glass	**Doublet 1 (Fe^{3+})**	0.387	0.772	0.327	58.8
	Doublet 2 (Fe^{2+})	0.870	2.25	0.354	41.2

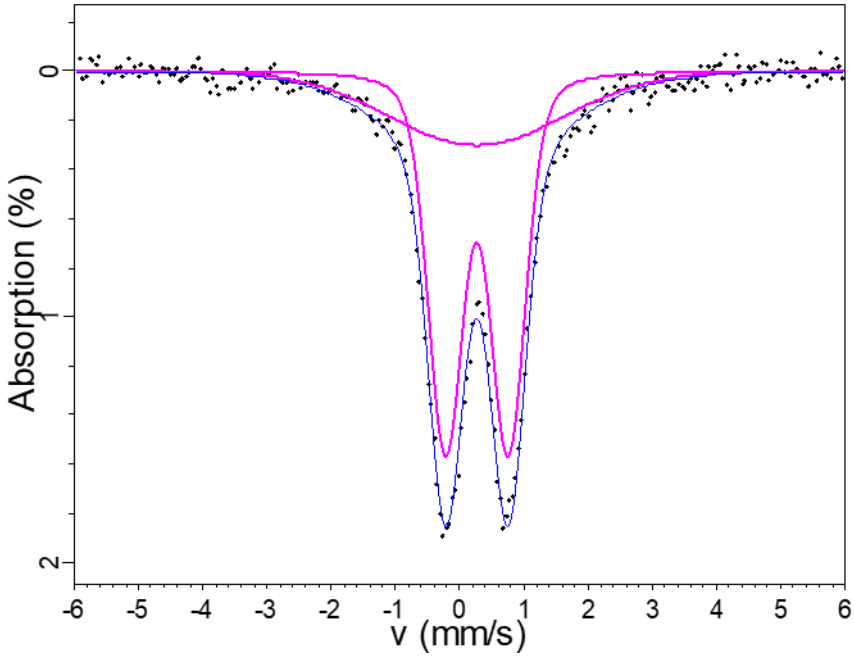

Figure C. 9 Mössbauer spectrum for LiNaBSi doped with 4.76 mol% Fe_2O_3 pristine oxidised glass.

Table C. 9 Fitting parameters for LiNaBSi doped with 4.76 mol% Fe_2O_3 pristine oxidised glass.

Sample ID		CS (mm/s)	QS (mm/s)	stdev (mm/s)	Relative area (%)
LiNaBSi 4.76 mol% Fe_2O_3 pristine oxidised glass	**Doublet 1 (Fe^{3+})**	0.266	0.976	0.312	68.8
	Doublet 2 (Fe^{3+})	0.265	2.12	1.602	31.2

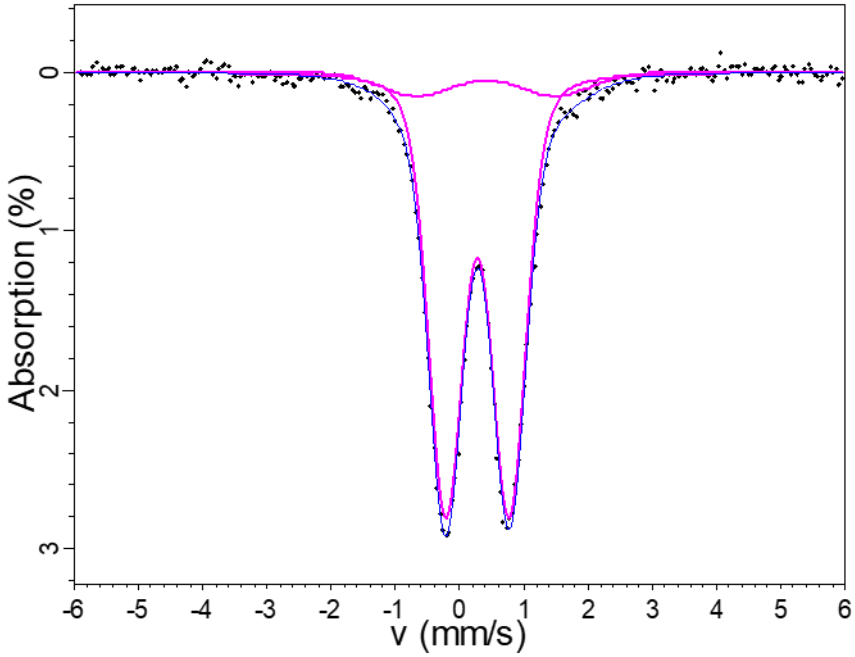

Figure C. 10 Mössbauer spectrum for LiNaBSi doped with 9.09 mol% Fe_2O_3 pristine oxidised glass.

Table C. 10 Fitting parameters for LiNaBSi doped with 9.09 mol% Fe_2O_3 pristine oxidised glass.

Sample ID		CS (mm/s)	QS (mm/s)	stdev (mm/s)	Relative area (%)
LiNaBSi 9.09 mol% Fe_2O_3 pristine oxidised glass	**Doublet 1 (Fe^{3+})**	0.275	0.989	0.299	90.2
	Doublet 2 (Fe^{3+})	0.412	2.16	0.699	9.8

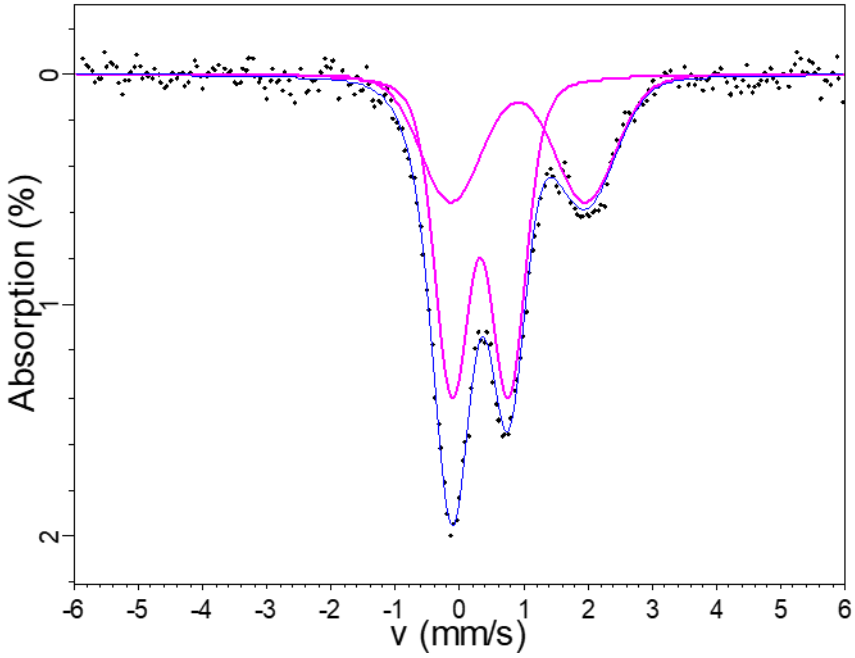

Figure C. 11 Mössbauer spectrum for LiNaBSi doped with 4.76 mol% Fe_2O_3 pristine reduced glass.

Table C. 11 Fitting parameters for LiNaBSi doped with 4.76 mol% Fe_2O_3 pristine reduced glass.

Sample ID		CS (mm/s)	QS (mm/s)	stdev (mm/s)	Relative area (%)
LiNaBSi 4.76 mol% Fe_2O_3 pristine reduced glass	**Doublet 1 (Fe^{3+})**	0.320	0.879	0.272	60.0
	Doublet 2 (Fe^{2+})	0.910	2.091	0.602	40.0

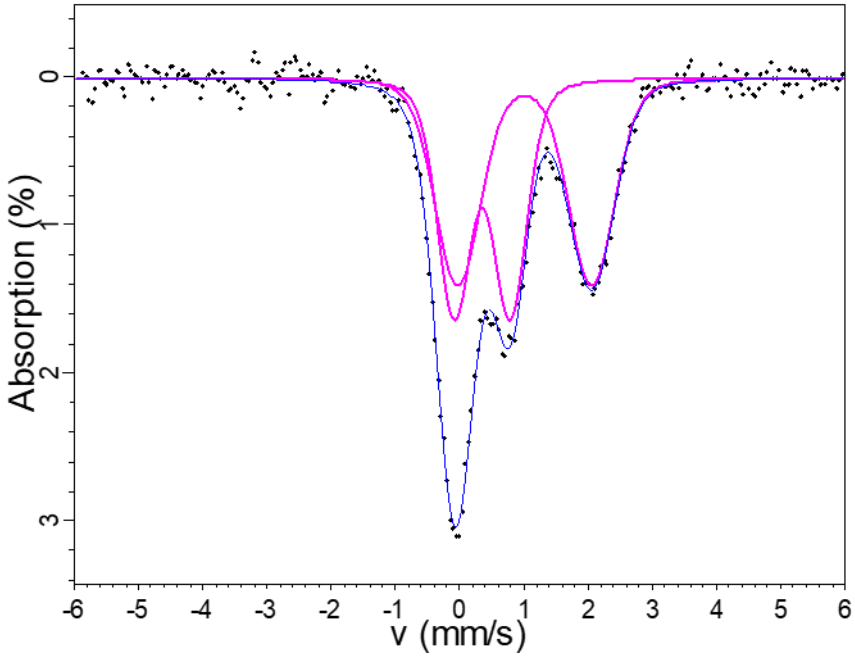

Figure C. 12 Mössbauer spectrum for LiNaBSi doped with 9.09 mol% Fe_2O_3 pristine reduced glass.

Table C. 12 Fitting parameters for LiNaBSi doped with 9.09 mol% Fe_2O_3 pristine reduced glass.

Sample ID		CS (mm/s)	QS (mm/s)	stdev (mm/s)	Relative area (%)
LiNaBSi 9.09 mol% Fe_2O_3 pristine reduced glass	**Doublet 1 (Fe^{3+})**	0.350	0.872	0.297	46.3
	Doublet 2 (Fe^{2+})	1.012	2.089	0.436	53.7

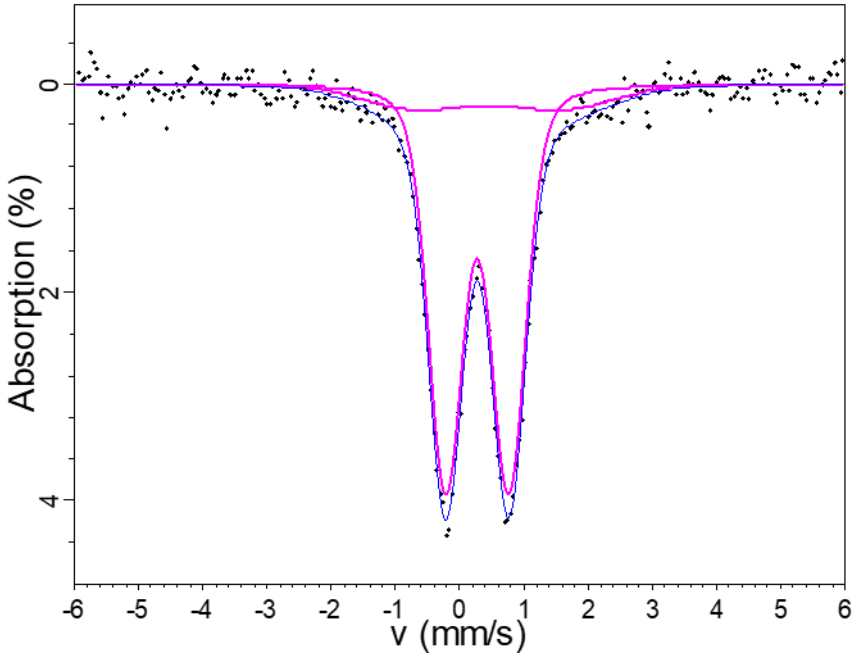

Figure C. 13 Mössbauer spectrum for LiNaBSi doped with 4.76 mol% Fe_2O_3 irradiated oxidised glass.

Table C. 13 Fitting parameters for LiNaBSi doped with 4.76 mol% Fe_2O_3 irradiated oxidised glass.

Sample ID		CS (mm/s)	QS (mm/s)	stdev (mm/s)	Relative area (%)
LiNaBSi 4.76 mol% Fe_2O_3 irradiated oxidised glass	**Doublet 1 (Fe^{3+})**	0.271	0.983	0.297	84.3
	Doublet 2 (Fe^{3+})	0.452	2.252	1.099	15.7

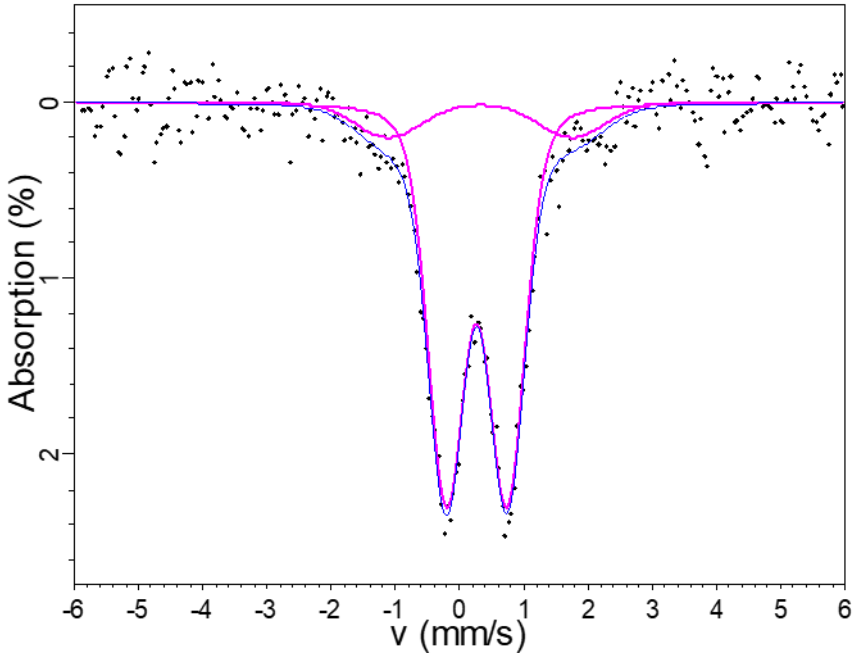

Figure C. 14 Mössbauer spectrum for LiNaBSi doped with 9.09 mol% Fe_2O_3 irradiated oxidised glass.

Table C. 14 Fitting parameters for LiNaBSi doped with 9.09 mol% Fe_2O_3 irradiated oxidised glass.

Sample ID		CS (mm/s)	QS (mm/s)	stdev (mm/s)	Relative area (%)
LiNaBSi 9.09 mol% Fe_2O_3 irradiated oxidised glass	**Doublet 1 (Fe^{3+})**	0.262	0.944	0.346	87
	Doublet 2 (Fe^{3+})	0.322	2.862	0.689	13

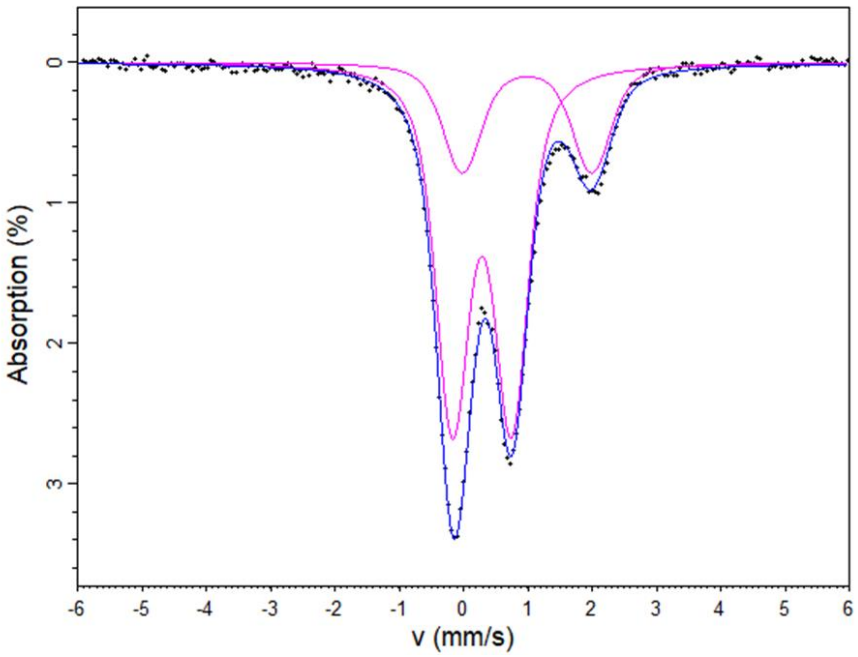

Figure C. 15 Mössbauer spectrum for LiNaBSi doped with 4.76 mol% Fe_2O_3 irradiated reduced glass.

Table C. 15 Fitting parameters for LiNaBSi doped with 4.76 mol% Fe_2O_3 irradiated reduced glass.

Sample ID		CS (mm/s)	QS (mm/s)	stdev (mm/s)	Relative area (%)
LiNaBSi 4.76 mol% Fe_2O_3 irradiated reduced glass	**Doublet 1 (Fe^{3+})**	0.289	0.920	0.207	74.29
	Doublet 2 (Fe^{2+})	0.991	2.014	0.269	25.71

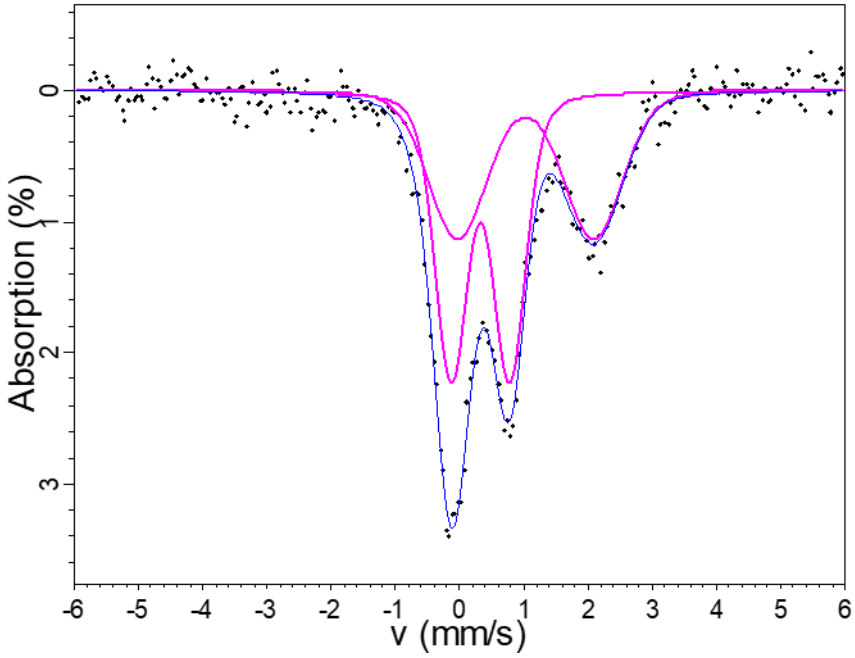

Figure C. 16 Mössbauer spectrum for LiNaBSi doped with 9.09 mol% Fe_2O_3 irradiated reduced glass.

Table C. 16 Fitting parameters for LiNaBSi doped with 9.09 mol% Fe_2O_3 irradiated reduced glass.

Sample ID		CS (mm/s)	QS (mm/s)	stdev (mm/s)	Relative area (%)
LiNaBSi 9.09 mol% Fe_2O_3 irradiated reduced glass	**Doublet 1 (Fe^{3+})**	0.321	0.910	0.280	53.3
	Doublet 2 (Fe^{2+})	1.025	2.124	0.581	46.7

Appendix D

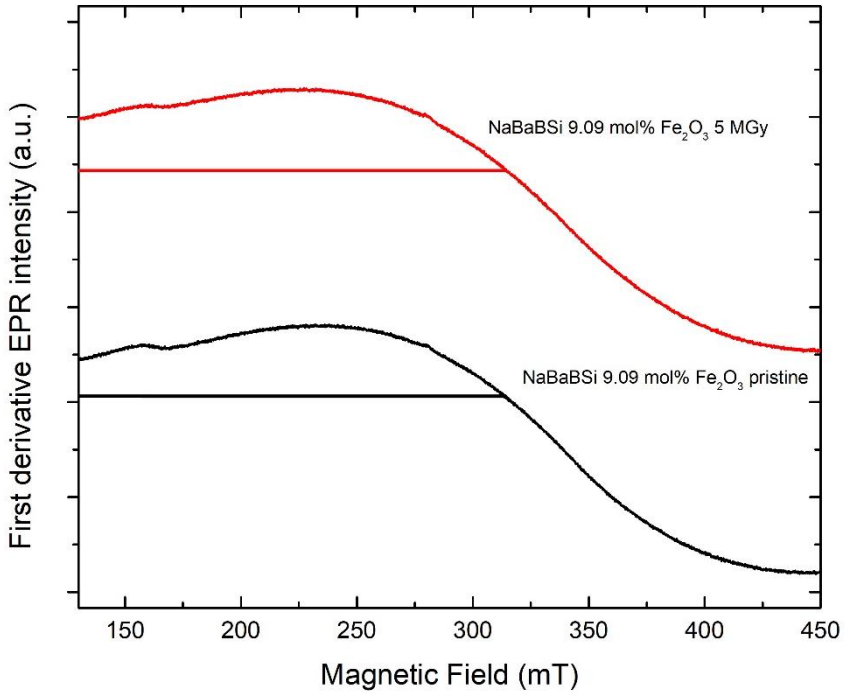

Figure D. 1 First derivative EPR spectra for pristine and gamma irradiated 9.09 mol% Fe_2O_3 doped NaBaBSi glass.

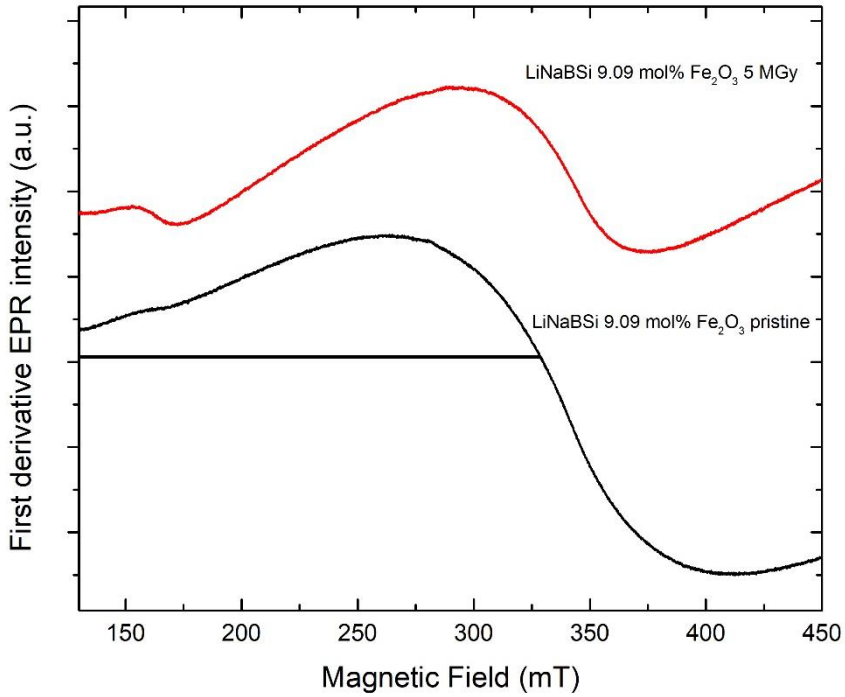

Figure D. 2 First derivative EPR spectra for pristine and gamma irradiated 9.09 mol% Fe_2O_3 doped LiNaBSi glass.

Appendix E

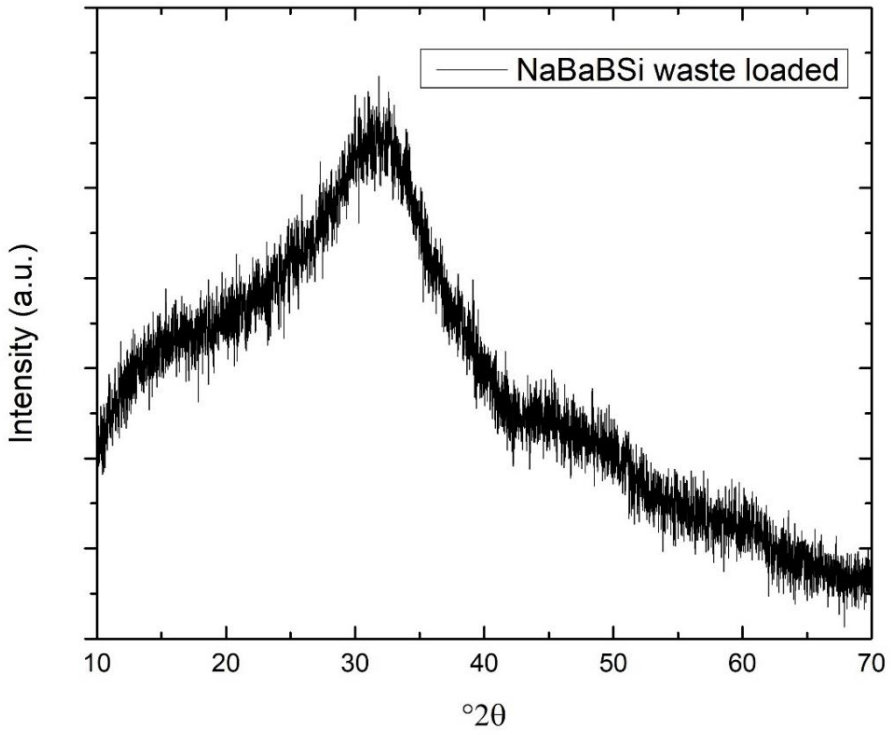

Figure E. 1 XRD pattern for NaBaBSi non-active waste loaded glass.

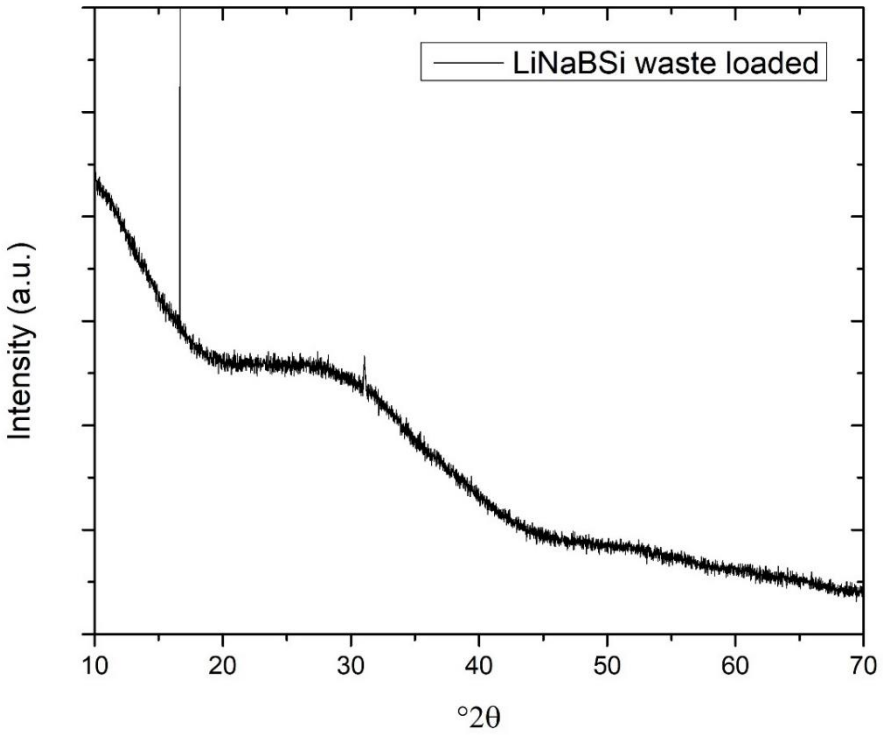

Figure E. 2 XRD pattern for LiNaBSi non-active waste loaded glass.

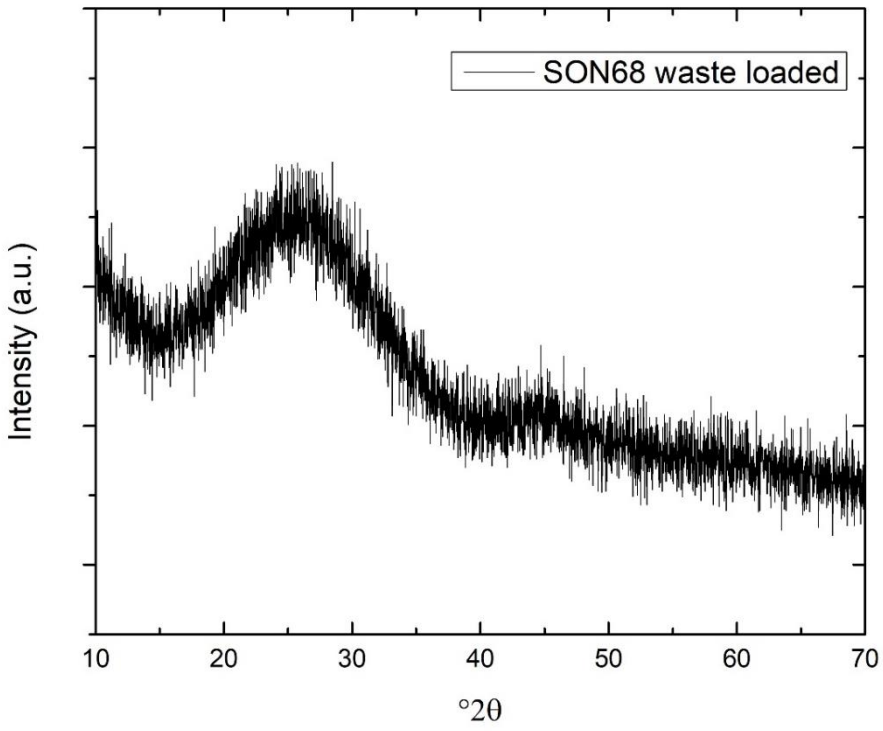

Figure E. 3 XRD pattern for SON68 non-active waste loaded glass.

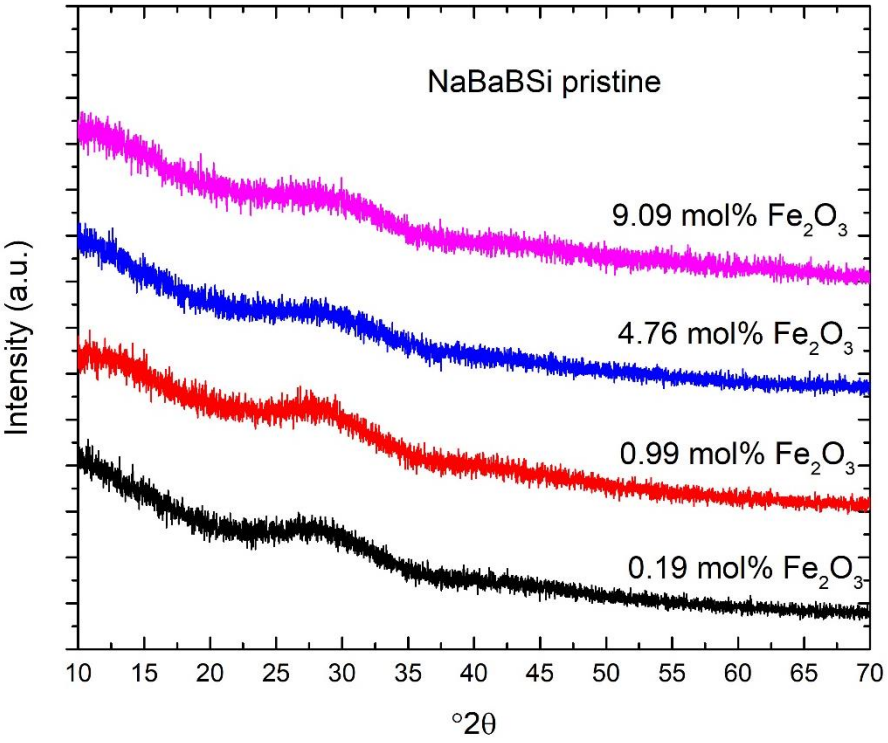

Figure E. 4 XRD pattern for NaBaBSi doped with 0.19, 0.99, 4.76 and 9.09 mol% Fe_2O_3 pristine glasses.

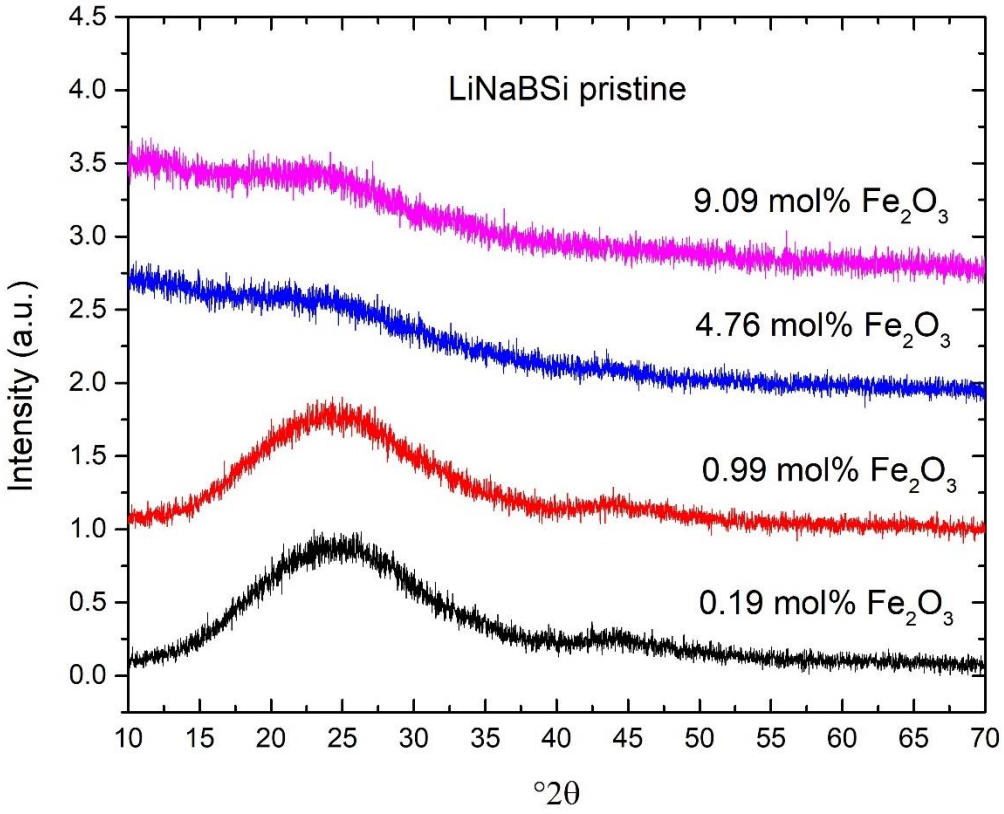

Figure E. 5 XRD pattern for LiNaBSi doped with 0.19, 0.99, 4.76 and 9.09 mol% Fe_2O_3 pristine glasses.